Semiconductors, Vol. 37, No. 11, 2003, pp. 1243–1246. Translated from Fizika i Tekhnika Poluprovodnikov, Vol. 37, No. 11, 2003, pp. 1281–1284.
Original Russian Text Copyright © 2003 by Medvedeva, Yur'eva, Ivanovskiĭ.

ELECTRONIC AND OPTICAL PROPERTIES OF SEMICONDUCTORS

Electronic Structure of Cubic Silicon Carbide with Substitutional *3d* Impurities at Si and C Sites

N. I. Medvedeva, E. I. Yur'eva, and A. L. Ivanovskiĭ

Institute of Solid State Chemistry, Ural Branch of Russian Academy of Sciences, Yekaterinburg, 620219 Russia

e-mail: medvedeva@ihim.uran.ru

Submitted January 20, 2003; accepted for publication January 25, 2003

Abstract—The full-potential linear muffin-tin orbital method is used to calculate the electronic structure and cohesive energies for cubic silicon carbide doped with transition 3*d* metal impurities (Me = Ti, V, Cr, Mn, Fe, Co, Ni), substituting Si or C at the corresponding sublattice of the atomic matrix. It is established that all 3*d* impurities mainly occupy silicon sites. For the Ti ⟶ Si substitution, dopant impurity levels are located in the conduction band of SiC, whereas doping silicon carbide with other 3*d* impurities gives rise to additional donor or acceptor levels in the band gap. For 3*C*-SiC the effect of impurities on the lattice parameter (with the substitutions Me ⟶ Si) and on the impurity local magnetic moments (with the substitutions Me ⟶ Si, C) is studied. *© 2003 MAIK "Nauka/Interperiodica".*

Silicon carbide is a promising material for extremal electronics. Using intentional doping with atoms of 3*d* metals (Me), one can appreciably vary the electrical, magnetic, and mechanical properties of SiC [1–6]. For example, the introduction of vanadium atoms compensates for the uncontrollable presence of oxygen and nitrogen atoms, resulting in improvement in the dielectric performance of the material [1]. The introduction of titanium and nickel atoms improves the SiC strength characteristics [2, 3], whereas the iron and cobalt atoms are the catalysts for the process of thin wire fabrication from crystals of cubic silicon carbide [4]. The chrome and manganese impurities are promising for producing magnetic materials on the basis of doped silicon carbide [5, 6].

Information on the mechanism of the effect of 3*d* elements on the properties of a SiC:Me system can be obtained by studying how the electronic spectrum of the atomic matrix is modified by impurity states and then how the impurity type (donor or acceptor) depends on the possible impurity sites in the lattice. These studies are closely related to the problems of forecasting changes in lattice and cohesive properties of the matrix: the effects of structural relaxation, doping-induced variation in the stability of the system, etc.

Recently, the solution of these problems for impurity systems on the basis of cubic silicon carbide (3*C*-SiC) doped with 3*d* metals has attracted considerable attention [7–13]. For example, the energy states of isolated 3*d* impurities in the silicon sublattice in the 3*C*-SiC:Me (Me = Ti, V,…, Ni, Cu) system were calculated by using the method of linear muffin-tin orbitals (LMTOs) and Green functions [7, 8]. It was concluded that the system is minimally destabilized by the atoms at the beginning and at the end of the 3*d* series [7]. Calculations of spin polarization by the full-potential augmented plane wave method (APW) showed that, for the states of an isolated Ti atom in 3*C*-SiC, the relaxation phenomena play an important role in formation of the parameters of hyperfine interactions; moreover, the substitutional defect (Ti ⟶ Si) is stabler than the interstitial defect [9]. The LMTO and tight binding calculations were performed for SiC:Me systems, where Me=Ti, V [10] and Me = Cr, Mn, Fe, Co [11]. According to [11], Cr, Fe, and Co predominantly replace carbon, whereas Mn atoms mainly occupy silicon sites. For doping of SiC with Ti, V, and Ni, the effect of relaxation of carbon atoms was considered in [12]. It was found that the substitution Me ⟶ Si is accompanied by radial displacement of carbon atoms away from the impurity center and that the substitution energy is positive; it is lowest for titanium and increases with the atomic number of the impurity. The possibility of double defects forming (Me and a lattice vacancy) in SiC was also considered using theoretical calculations in the context of the cluster model [13].

The aim of this study is to analyze the tendencies in the variation of structural, electronic, and energy properties of cubic silicon carbide as a result of doping with 3*d* metals and to establish how these properties depend on the type and position of the substitutional impurity. The metals Me = Ti, V, Cr, Mn, Fe, Co, Ni were chosen as impurities; they could be introduced to the sites in both of Si and C sublattices.

The SiC:Me systems (of formal stoichiometry $Si_{0.875}Me_{0.125}C$ and $SiC_{0.875}Me_{0.125}$ with substitutions Me ⟶ Si and Me ⟶ C, respectively) were simulated by the 16-atom supercells $MeSi_7C_8E_8$ and $MSi_8C_7E_8$; eight "empty" spheres (E) were introduced into each cell to accomplish close packing. Such a choice of the

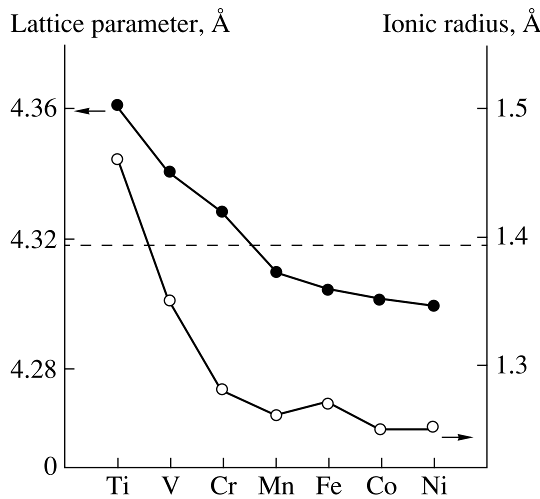

Fig. 1. Impurity-type dependence of the calculated lattice parameters and ionic radii for the 3*C*-SiC:Me system [16]. The dashed line corresponds to the theoretical lattice parameter for the 3*C*-SiC lattice.

cell is optimal, since it allows one to include the effects of structural relaxation of the nearest atoms without substantial increase in computing time. The use of the supercell model implies the ordering of impurities in the calculation, whereas in doped materials disorder can affect the matrix properties. However, for low impurity concentrations, impurity–impurity interaction is weak, and the effect of disorder in impurity positions on the electronic spectrum is negligible. The calculations were performed by the self-consistent spin-unbounded scalar-relativistic full-potential method [14], with an exchange–correlation potential of the form suggested in [15].

We calculated the total and partial densities of electronic states, atomic magnetic moments (MM), total energies (E_t), and cohesion energies (E_c). The effects of structural relaxation were evaluated using the equilibrium values of lattice parameters a; the latter were obtained from the minimality condition on E_t for the optimized SiC:Me system, where the coordinates of the atoms nearest to the impurity were varied without breaking the total symmetry of the crystal (we described the results on local relaxation in [12]). We drew our conclusions concerning the preferential position of the substitutional atom (Me ⟶ Si or Me ⟶ C) by comparing the corresponding energies E_c(E_c^{Si} and E_c^{C}) defined as the difference of the total energy E_t of SiC:Me and the sum of the energies of the corresponding free atoms.

Cohesion energy E_c, density of states at the Fermi level $N(E_F)$, (energy band gap E_g), and 3*d* impurity magnetic moment (MM)

3*C*-SiC : Me	E_c, eV/atom	$N(E_F)$, eV^{-1}	MM
3*C*-SiC	7.39	(E_g = 2.4 eV)	0
Ti ⟶ Si	7.30	(E_g = 2.4 eV)	0
Ti ⟶ C	5.88	9.07	0
V ⟶ Si	7.19	4.17	0.9
V ⟶ C	6.07	4.84	0
Cr ⟶ Si	6.90	0.11	2.0
Cr ⟶ C	6.61	10.78	1.3
Mn ⟶ Si	6.95	4.05	1.1
Mn ⟶ C	6.66	7.87	1.0
Fe ⟶ Si	7.02	0.41	0
Fe ⟶ C	6.75	(E_g = 0.08 eV)	0
Co ⟶ Si	7.03	8.16	0
Co ⟶ C	6.63	3.23	0
Ni ⟶ Si	7.04	4.40	0
Ni ⟶ C	6.51	3.24	0

Note: Magnetic moments are expressed in Bohr magnetons μ_B.

The results of the calculation are shown in Figs. 1 and 2 and in the table. The parameters of the electronic spectrum, namely, the total density of states at the Fermi level $N(E_F)$, the band gap E_g, E_c, and the MMs of 3*d* atoms in SiC:Me (see table), are found to be quite different for different substitutions.

Since E_c (Me ⟶ Si) > E_c (Me ⟶ C) for all impurity atoms (see table), the impurities considered must predominantly replace silicon atoms. This is the basic difference from [11], where it was concluded that, for Cr, Fe, and Co, the most probable sites are those of carbon. For substitution of silicon atoms, the largest values of E_c^{Si} correspond to Ti and V impurities, for which the energy (E_c^{C}) is lowest. For these impurities, the preference energy ΔE, defined as the difference between E_c^{Si} and E_c^{C}, is highest. In contrast, ΔE is minimal for Cr, Mn, and Fe. Therefore, under certain conditions, one can expect the impurities Cr, Mn, and Fe to be located at both Si and C sites; this, however, is improbable for Ti and V atoms.

Analysis of the calculated effects of lattice relaxation [dependence of lattice parameter a on impurity type at the Si site for SiC:Me systems (see Fig. 1)] shows that the replacement of silicon by titanium, vanadium, and chrome must result in an increase in the lattice parameter compared to undoped 3*C*-SiC and that the replacement of Si by Fe, Co, and Ni should lead to a slight decrease in the lattice parameter; this behavior indicates a correlation with the ionic radii of Me. The general tendency also manifests itself in the decrease in a with increasing atomic number N of the impurity: at the beginning of the series (Ti, V, and Cr atoms), the slope of curve a/N is greater than at the end of the series (Mn, Fe, Co, and Ni atoms).

Let us consider the changes in electronic structure produced by substitution effects. For Ti, Cr, and Co impurities, the electronic densities of state at the Fermi

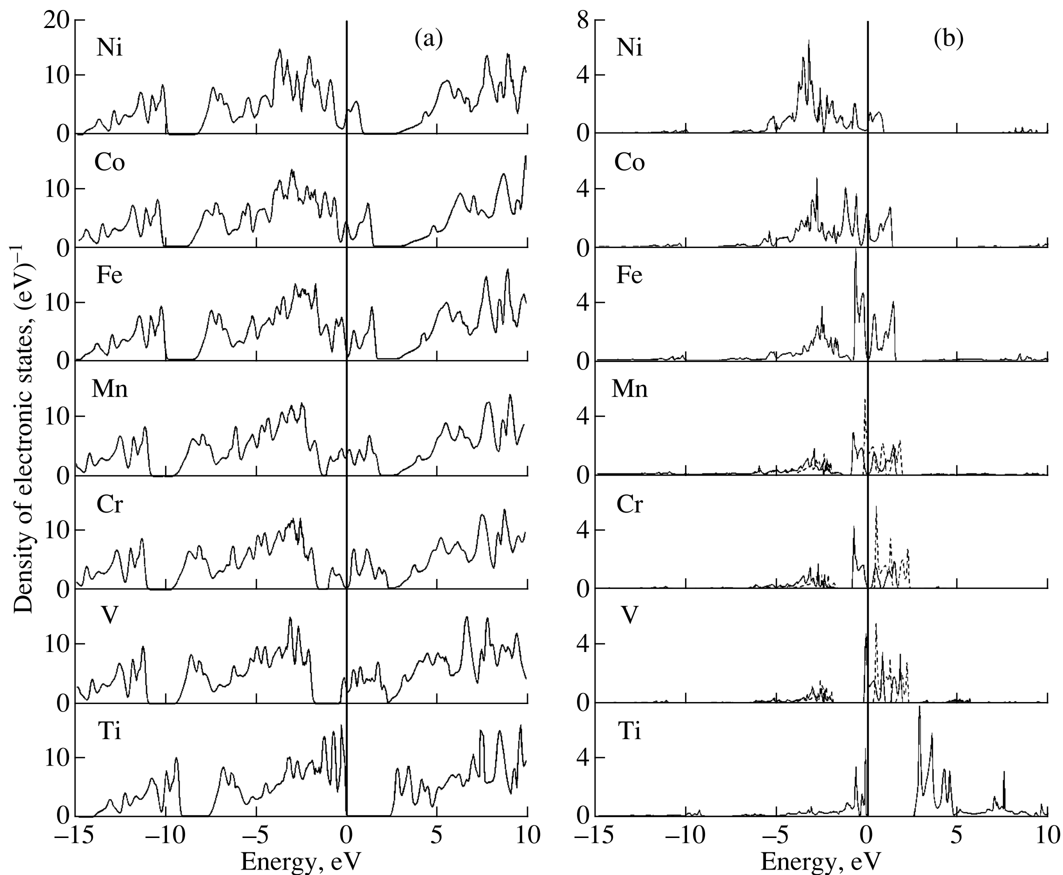

Fig. 2. Total (a) and partial (b) densities of 3*d* states for 3*C*-SiC:Me.

level, to a great extent, are determined by the substitution position, whereas for V, Mn, Fe, and Ni atoms, this dependence is not so significant.

Figure 2 shows the total (*a*) and partial (*b*) densities of 3*d* states in SiC:Me with Me impurities in the silicon sublattice. It is well known (e.g., see [12]) that the spectrum of "pure" 3*C*-SiC has two filled bands of C2*s*, Si3*s* and Si3*s*, Si3*p*, C2*p* states; these bands have widths of about 5 eV and 8 eV, respectively, and are separated by an energy gap of about 2 eV. The band gap between the valence and conduction bands (formed by Si3*s*, Si3*p*, Si3*d*, and antibonding C2*p* states) is about 2.4 eV, in agreement with previous calculations [17–19]. In Fig. 2 we see that only the titanium impurity does not affect the basic features of the spectrum of SiC: the Ti3*d* levels are admixed to the edges of the valence and conduction bands; no new impurity bands appear in the band gap of the matrix, and the gap remains practically unchanged.

A different situation occurs for vanadium doping of SiC. For the system under consideration, a band of impurity V3*d* levels splits off from the bottom of the conduction band by 0.1 eV and is found to be half-filled. It follows that for SiC:V a filled donor state appears nearly at midgap, whereas most of the empty V3*d* states lie near the edge of the conduction band. Partial filling of states (of type *e* with spin up) gives rise to local magnetic moments of about $1\mu_B$ at vanadium atoms. The gap between the valence band and conduction bands decreases to about 1.42 eV.

The chrome and manganese impurities are also magnetic. Since for the SiC:Cr system the states of *e* type with spin up are completely filled and the states with spin down lie about 1.2 eV higher and are empty, it follows that the MM at chrome atoms is about $2\mu_B$. The Fermi level lies in the pseudogap between the subbands of types *e* and t_2 with spin up, and $N(E_F)$ almost vanishes. For SiC:Mn, *e* states with spin up are filled, *e* states with spin down are half-filled, and t_2 states are empty. The magnetic moment of manganese is $1\mu_B$, and the quantity $N(E_F)$ is close to that for SiC:V. The binding energy for impurity levels increases with impurity atomic number; for Cr and Mn these states lie near the midgap of the matrix.

Impurity Fe3*d* levels lie close to the edge of the valence band. The iron impurity is nonmagnetic: all *e* levels are filled and t_2 levels are empty. The Fermi level lies within the pseudogap between the *e* and t_2 lev-

els and $N(E_F)$ is small. The cobalt and nickel impurities are also nonmagnetic. Their 3*d* levels are shifted into the valence band: for example, the highest Ni3*d* peak lies about 4 eV below the Fermi level. For the systems considered, a number of acceptor levels near the edge of the valence band appears. The gap increases from 1.1 eV for SiC:Fe to 1.7 eV for SiC:Ni.

Summarizing the results of the calculations, we can draw the following conclusions.

(1) For doping of SiC with metals of 3*d* series under equilibrium conditions, the impurity atoms mainly occupy the sites in the Si sublattice of the matrix. For Cr, Mn, and Fe one can expect that the C sublattice sites are partially filled. The substitution of this type is least probable for Ti and V.

(2) A correlation exists between the variation in the lattice parameter of SiC:Me and the Me impurity ionic radius.

(3) The vanadium magnetic state manifests itself only if V atom is localized at silicon sites. The Cr and Mn atoms are magnetic at both Si and C sites. For the substitution Cr $\longrightarrow$ Si, the chrome MM is two times greater than that for the substitution Cr $\longrightarrow$ C, whereas the manganese MMs for both sublattice positions are close to each other. The Ti, Fe, and Co atoms have no localized MMs for any of the sites considered.

(4) Depending on the type of the substitution position (Si or C site), $N(E_F)$ for 3*C*-SiC:Me can change by almost an order of magnitude (for Me = Cr) or remain unchanged (for Me = V, Ni). For a Ti impurity substituting silicon, the band gap does not change. In other cases, donor (at the beginning of the 3*d* series) or acceptor (at end of the 3*d* series) states appear in the gap.

ACKNOWLEDGMENTS

This study was supported by the Russian Foundation for Basic Research, project no. 01-03-33175.

REFERENCES

1. S. A. Reshanov, Diamond Relat. Mater. **9**, 480 (2000).
2. R. Alexandrescu, E. Borsella, S. Botti, *et al.*, J. Mater. Sci. **32**, 5629 (1997).
3. Y. T. Pei, J. H. Ouyang, T. C. Lei, and Y. Zhou, Mater. Sci. Eng. A **194**, 219 (1995).
4. Y. Q. Zhu, W. B. Hu, W. K. Hsu, *et al.*, J. Mater. Chem. **9**, 3173 (1999).
5. N. T. Son, A. Ellison, B. Magnusson, *et al.*, J. Appl. Phys. **86**, 4348 (1999).
6. N. Theodoropoulou, A. F. Hebart, S. N. G. Chu, *et al.*, Electrochem. Solid-State Lett. **4**, G119 (2001).
7. R. F. Sabiryanov, A. L. Ivanovskiĭ, and G. P. Shveĭkin, Zh. Neorg. Khim. **38**, 1572 (1993).
8. H. Overhof, Mater. Sci. Forum **258**, 677 (1997).
9. K. O. Barbosa, W. V. M. Machado, and L. V. C. Assali, Physica B (Amsterdam) **308–310**, 726 (2001).
10. N. I. Medvedeva, Zh. I. Gertner, V. V. Kraskovskaya, *et al.*, Neorg. Mater. **31**, 55 (1995).
11. V. A. Gubanov, C. Boekema, and C. Y. Fong, Appl. Phys. Lett. **78**, 216 (2001).
12. N. I. Medvedeva, É. I. Yur'eva, and A. L. Ivanovskiĭ, Fiz. Tekh. Poluprovodn. (St. Petersburg) **36**, 805 (2002) [Semiconductors **36**, 751 (2002)].
13. É. I. Yur'eva and A. L. Ivanovskiĭ, Zh. Strukt. Khim. **43**, 220 (2002).
14. M. Methfessel and M. Scheffler, Physica B (Amsterdam) **172**, 175 (1991).
15. S. H. Vosko, L. Wilk, and M. Nusair, Can. J. Phys. **58**, 1200 (1980).
16. W. B. Pearson, *Crystal Chemistry and Physics of Metals and Alloys* (Wiley, New York, 1972; Mir, Moscow, 1977).
17. A. R. Lubinsky, D. E. Ellis, and G. S. Painter, Phys. Rev. B **11**, 1537 (1975).
18. K. J. Chang and M. L. Cohen, Phys. Rev. B **35**, 8196 (1987).
19. M. Causa, R. Dovesi, and C. Roetti, Phys. Rev. B **43**, 11937 (1991).

Translated by I. Zvyagin

Semiconductors, Vol. 37, No. 11, 2003, pp. 1247–1251. Translated from Fizika i Tekhnika Poluprovodnikov, Vol. 37, No. 11, 2003, pp. 1285–1289.
Original Russian Text Copyright © 2003 by Bodnar'.

Optical and Thermal Properties of $CuAl_xIn_{1-x}Te_2$ Solid Solutions

I. V. Bodnar'

Belarussian State University of Informatics and Radioelectronics, ul. Brovki 17, Minsk, 220072 Belarus

e-mail: chemzav@gw.bsuir.unibel.by

Submitted January 22, 2003; accepted for publication January 28, 2003

Abstract—The optical and thermal properties of crystals of $CuAl_xIn_{1-x}Te_2$ solid solutions grown by the Bridgman–Stockbarger method were studied for the first time. From the transmission and reflection spectra in the region of the intrinsic-absorption edge, the band gap (E_g) was determined for the $CuInTe_2$ and $CuAlTe_2$ compounds and for their solid solutions; the concentration dependence of E_g was plotted. The E_g value was found to vary nonlinearly with x and can be described by the quadratic dependence. Dilatometry was used to study the thermal expansion of these solid solutions. The coefficient of thermal expansion (α_L) was shown to have a λ-shaped temperature dependence in the region of phase transitions. The isotherms are plotted for the concentration dependence of α_L. The thermal conductivity was investigated and its concentration dependence was plotted. The dependence of the thermal conductivity on x was established to have a minimum in the region of medium compositions. *© 2003 MAIK "Nauka/Interperiodica".*

1. INTRODUCTION

The tellurides $CuInTe_2$ and $CuAlTe_2$ belong to a large class of I–III–VI_2 ternary compounds, which are crystallized in the chalcopyrite structure (the D_{2d}^{12}–$I\bar{4}2d$ space group) [1]. These compounds are characterized by direct band-to-band transitions and by an optical-absorption coefficient > 10^4 cm^{-1}, which makes them promising materials for manufacturing solar cells and devices of nonlinear optics and polarization electronics. The properties of these compounds have by mow been adequately studied [2–7]; at the same time, there are no published data on the properties of solid solutions based on $CuInTe_2$ and $CuAlTe_2$. In this paper, for the first time we report the results of investigations of the optical and thermal properties of $CuAl_xIn_{1-x}Te_2$ solid solutions.

2. EXPERIMENTAL

$CuAlTe_2$ and $CuInTe_2$ ternary compounds and $CuAl_xIn_{1-x}Te_2$ solid solutions were grown by the horizontal Bridgman–Stockbarger method using the phase diagram of the $CuInTe_2$–$CuAlTe_2$ system [8]. The metal components (in a graphitized quartz boat) and tellurium were placed in different sections of an evacuated quartz cell. The cell was placed in a two-zone horizontal furnace. The temperature of the zone with metal components was maintained at 20–40 K above the melting point of the compound or the liquidus temperature of the corresponding solid solution. The temperature of the zone with tellurium was increased at a rate of ~100 K/h up to 1000–1100 K and held for 3 h so that the reaction between the metal components and tellurium vapors could proceed. After the indicated time had elapsed, we performed the planar crystallization of the melt, decreasing the temperature at a rate of ~2 K/h. To ensure that the alloys obtained were homogeneous, they were annealed at 950 K for 720 h. The ingots obtained after annealing had a coarse-block structure, and the average sizes of individual blocks were $5 \times 4 \times 3$ mm^3.

The composition and homogeneity of the solid solutions were determined by X-ray diffraction (a DRON-3M diffractometer, CuK_α radiation, nickel filter). In all the diffraction patterns obtained, there was a system of lines corresponding to the chalcopyrite structure in which the original $CuAlTe_2$ and $CuInTe_2$ compounds were crystallized. The resolution for large-angle lines in the diffraction patterns indicated that the grown crystals were homogeneous. The composition of solid solutions was determined on the basis of validity of the Vegard law in the $CuInTe_2$–$CuAlTe_2$ system with an accuracy of ±1 mol % [8].

3. RESULTS AND DISCUSSION

The $CuAlTe_2$ and $CuInTe_2$ crystals and $CuAl_xIn_{1-x}Te_2$ solid solution obtained were used to investigate the transmission and reflection spectra in the region of the intrinsic-absorption edge. The spectra were recorded by a Beckman-5240 spectrophotometer in the wavelength range 0.5–2.0 μm at 80 and 293 K. For the measurements, we cut single crystal blocks, which were ground and polished mechanically on both sides down to a thickness of ~20 μm. Immediately before the measurements, the samples were treated in the $Br_2 : C_2H_5OH$ = 1 : 3 etchant.

From the transmission (T) and reflection (R) spectra, we calculated the absorption coefficient (α) from a for-

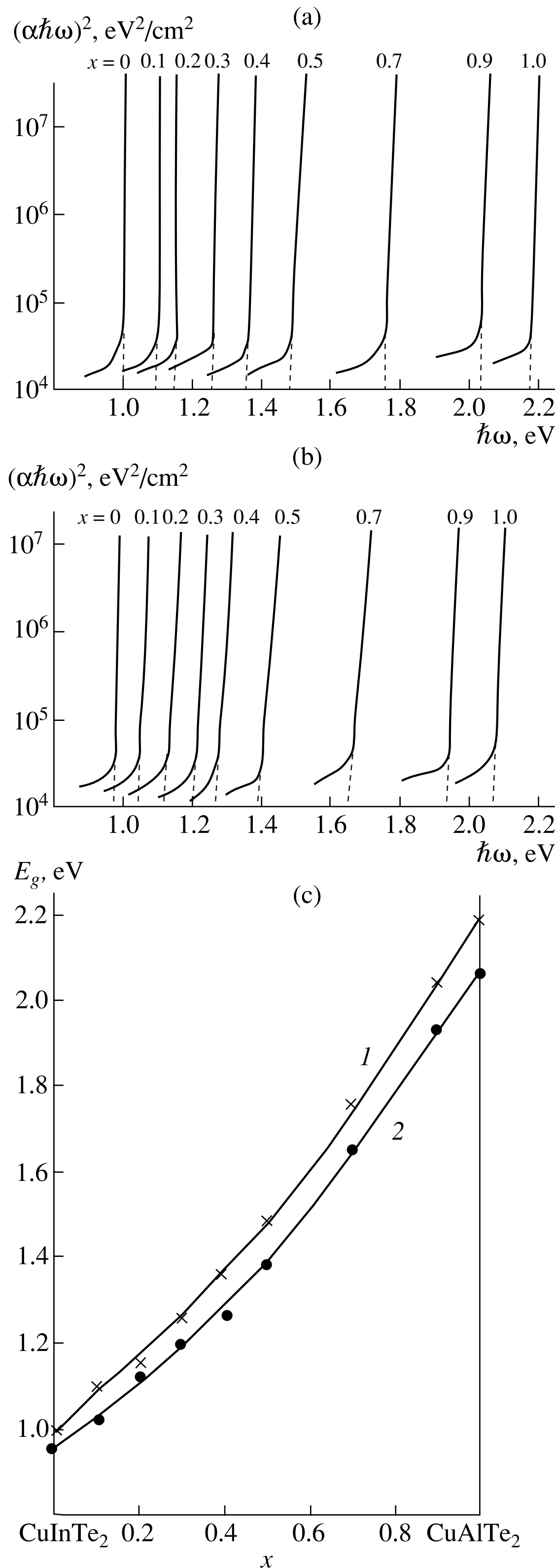

Fig. 1. Spectral dependences of the absorption coefficient in the form of the dependence of $(\alpha\hbar\omega)^2$ on $\hbar\omega$ at (a) 80 and (b) 293 K and the concentration dependences $E_g(x)$ of the band gap at (*1*) 80 and (*2*) 293 K for the $CuAl_xIn_{1-x}Te_2$ solid solutions.

mula that accounted for the multiple internal reflection in a plane-parallel sample; i.e.,

$$\alpha = (1/d)\ln\left\{(1-R)^2/2T + \sqrt{[(1-R)^2/2T]^2 + R^2}\right\}, \quad (1)$$

where d is the sample thickness and the reflection coefficient R is equal to 0.25–0.27 for various compositions.

It is well known that the I–III–VI_2 compounds are materials with direct band-to-band transitions; therefore, the band gap (E_g) was determined by extrapolating the rectilinear portion of the dependence of $(\alpha\hbar\omega)^2$ on the photon energy ($\hbar\omega$) to the intersection with the abscissa axis both for ternary compounds and for their solid solutions.

In Fig. 1, we show the indicated dependences at 80 and 293 K. They have pronounced rectilinear portions, which (like the X-ray data) is indicative of the homogeneity and uniformity of the grown crystals. The energies E_g for the original compounds are equal to 0.97 ± 0.01 eV (293 K) and 1.00 ± 0.01 eV (80 K) for $CuInTe_2$; 2.06 ± 0.01 eV (293 K) and 2.18 ± 0.01 eV (80 K) for $CuAlTe_2$. The band-gap temperature coefficients are $\partial E_g/\partial T = 1.4 \times 10^{-4}$ eV/K for $CuInTe_2$ and 5.6×10^{-4} eV/K for $CuAlTe_2$. In Fig. 1c, we show the concentration dependences of E_g for the $CuAl_xIn_{1-x}Te_2$ solid solution. As can be seen, E_g varies nonlinearly with x, which is characteristic of solid solutions formed by the I–III–VI_2 ternary compoonds [9–12].

Nowadays, two approximations are used to explain the deviations of $E_g(x)$ from linearity: the dielectric model and the pseudopotential model [13–15]. The former model is based on the fact that the determining role in the deviation of E_g from linearity in solid solutions is played by the fluctuations of the crystal potential induced by the random arrangement of substituting atoms. The latter model assumes that the deviation is a consequence of the properties of the crystal field.

In order to describe $E_g(x)$, we used a quadratic dependence of the following form:

$$E_g(x) = E_g(1) + [E_g(2) - E_g(1) - c]x + cx^2. \quad (2)$$

Here, $E_g(1)$ and $E_g(2)$ are the band gaps for $CuInTe_2$ and $CuAlTe_2$, respectively, and c is the nonlinearity parameter characterizing the degree of deviation of E_g from the linear dependence for $x = 0.5$, which can be determined from the expression

$$c = 2[E_g(1) + E_g(2)] - 4E_g(x = 0.5). \quad (3)$$

The values of the band gap for solid solutions calculated from expression (2) are shown in Fig. 1c by solid lines. It can be seen that the calculated and experimental values are in good agreement.

The concentration dependences $E_g(x)$ at 80 and 295 K for the $CuAl_xIn_{1-x}Te_2$ solid solutions are described by the following functions:

$$E_g^{80}(x) = 1.00 + 0.74x + 0.44x^2,$$

$$E_g^{295}(x) = 0.97 + 0.59x + 0.50x^2. \quad (4)$$

The crystals of $CuInTe_2$ and $CuAlTe_2$ ternary compounds and $CuAl_xIn_{1-x}Te_2$ solid solutions were used to investigate the temperature dependences of the coefficients of thermal expansion α_L. The investigations were performed with a quartz dilatometer [16]. The temperature dependence of relative extension ($\Delta l/l$) was measured for samples $3 \times 3 \times 8$ mm^3 in size. The coefficient of thermal expansion α_L was calculated using the formula from [16]. The temperature was measured using a Chromel–Alumel thermocouple. The error in the measurements was less than 5%. To eliminate the sample oxidation, the measurements were performed in an inert-gas atmosphere. The heating rate was 3–5 K/min.

In Fig. 2, we show the temperature dependences of the coefficients of thermal expansion α_L for the $CuInTe_2$ and $CuAlTe_2$ compounds and for the $CuAl_xIn_{1-x}Te_2$ solid solutions. It can be seen that, both for the ternary compounds and for the solid solutions based on them, α_L increases linearly in the range T = 80–290 K. Later, the dependence α_L(T) levels of up to the phase-transformation temperature. In the phase-transformation region, a λ-shaped variation in the coefficient of thermal expansion takes place.

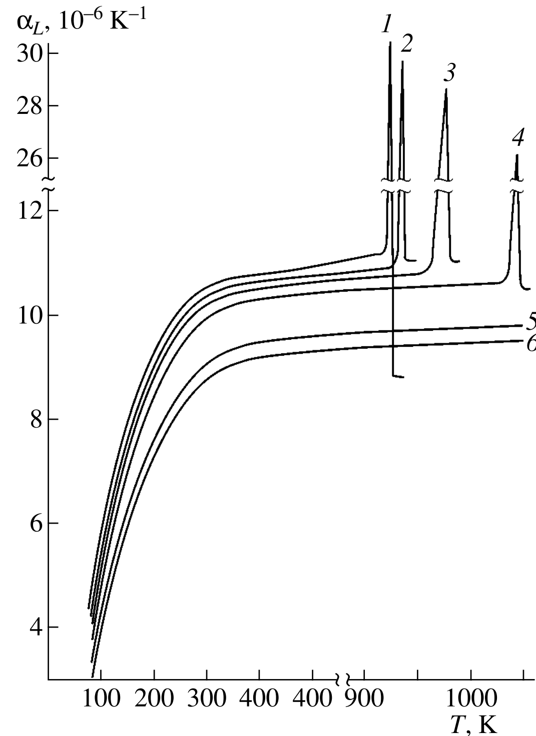

Fig. 2. Temperature dependences of the coefficient of thermal expansion for the $CuAl_xIn_{1-x}Te_2$ solid solutions with x = (*1*) 0.0, (*2*) 0.1, (*3*) 0.2, (*4*) 0.4, (*5*) 0.7, and (*6*) 1.0.

Thus, according to the data of differential thermal analysis [8] and from the experimental dependence $\alpha_L = f(T)$, we may conclude that the transitions observed in the $CuAl_xIn_{1-x}Te_2$ ($0 \le x \le 0.5$) solid solutions are the first-order phase transitions because they are realized with thermal effects. However, in contrast to typical first-order phase transitions, which occur at a constant temperature, these transitions are close to the second-order phase transitions because they proceed in the temperature interval with the λ-shaped variation of α_L.

At the same time, it is known that two types of phase transformation are possible in the I–III–VI_2 ternary compounds [17]; these transformations are induced by the cation–cation and cation–anion disorder. In [18], high-temperature X-ray investigations showed that these ternary compounds undergo a transition from the chalcopyrite structure to the sphalerite structure as a result of cation–cation disordering. By analogy with the I–III–VI_2 ternary compounds, the same transition can be assumed also for the $CuAl_xIn_{1-x}Te_2$ ($0 \le x \le 0.5$) solid solutions (the chalcopyrite–sphalerite structural transition).

The physial essence of the solid-phase transitions that take place in the materials under investigation can be perceived as follows. Under the cation–cation disordering that occurs in the temperature interval of 10–30 K, the atoms in the cation sublattice exchange their sites. Until the probability of cations occurring at various sites is the same, these sites remain inequivalent, and the structure is unchanged and remains as before (chalcopyrite). When these probabilities become identical and all the sites in the cation sublattice become equivalent, the chalcopyrite structure transforms into a sphalerite structure, and the crystal symmetry increases. To verify this statement, we quenched the crystals (by immersing in liquid nitrogen) of both the $CuInTe_2$ ternary compound and the $CuAl_xIn_{1-x}Te_2$ solid solutions, which were previously heated above the temperature of the phase transitions corresponding to the cation–cation disordering. We failed to find the high-temperature modifications corresponding to the sphalerite structure in any of these substances. This also indicates that the phase transformations under study are similar to second-order phase transitions, because the existence of overheating and overcooling phenomena are impossible for such transitions.

In Fig. 3, we show the isotherms of the concentration dependence of the coefficients of thermal expansion. It can be seen that α_L linearly increases with the content of indium atoms in the solid solutions.

The obtained experimental values of melting points (for compounds), liquidus temperatures (for solid solutions), and coefficients of thermal expansion were used to calculate the characteristic Debye temperatures (Θ) and the root-mean-square dynamic displacements

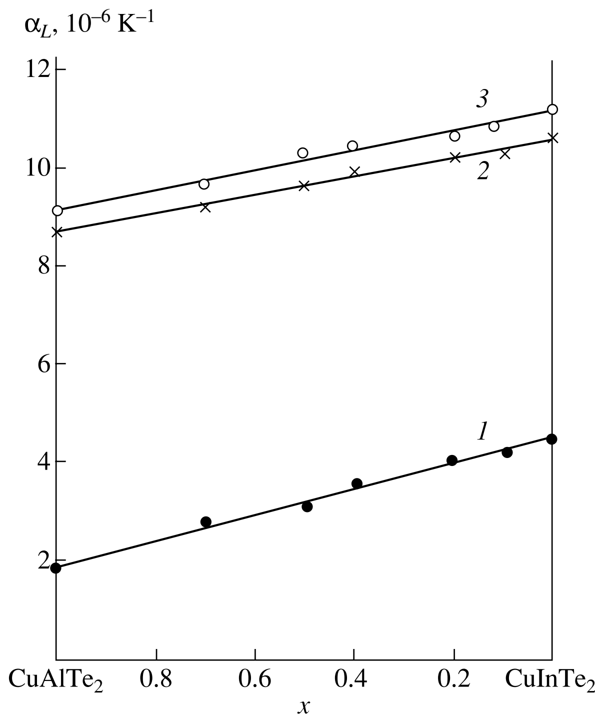

Fig. 3. Concentration dependences of the coefficient of thermal expansion for the $CuAl_xIn_{1-x}Te_2$ solid solutions at (*1*) 80, (*2*) 300, and (*3*) 900 K.

$(\sqrt{\bar{u}^2})$ of atoms (parameters characterizing the features of atomic interaction) from the following relationships [19, 20]:

$$\Theta^{\alpha_L} = 14.3/\alpha_L^{1/2}\bar{A}^{1/2}V^{1/3}, \quad (5)$$

$$\Theta^{T_m} = 137T_m/\bar{A}^{1/2}V^{1/3}, \quad (6)$$

$$\overline{u^2} = 4.3\times 10^{-14}[D(\Theta/T)/(\Theta/T) + 1/4]/\bar{A}\Theta. \quad (7)$$

Here, Θ^{α_L} and Θ^{T_m} are the Debye temperatures determined from the coefficient of thermal expansion and the melting point, $\bar{A}$ is the averaged atomic mass, V is the averaged atomic volume, T_m is the melting point, and $D(\Theta/T)$ is the Debye function.

Debye temperatures and the root-mean-square dynamic displacements of atoms for the $CuAlTe_2$ and $CuInTe_2$ ternary compounds and the $CuAl_xIn_{1-x}Te_2$ solid solutions

x	$\bar{A}$, g	V, cm^3	Θ^{α_L}, K	Θ^{T_m}, K	$\sqrt{\overline{u^2}}$, Å
1.0	86.43	16.37	204	200	0.190
0.7	93.02	16.69	191	188	0.197
0.5	97.10	17.04	181	179	0.202
0.4	99.61	17.22	176	176	0.205
0.2	104.00	17.48	169	170	0.208
0.1	106.20	17.66	166	166	0.212
0.0	108.39	17.81	163	165	0.214

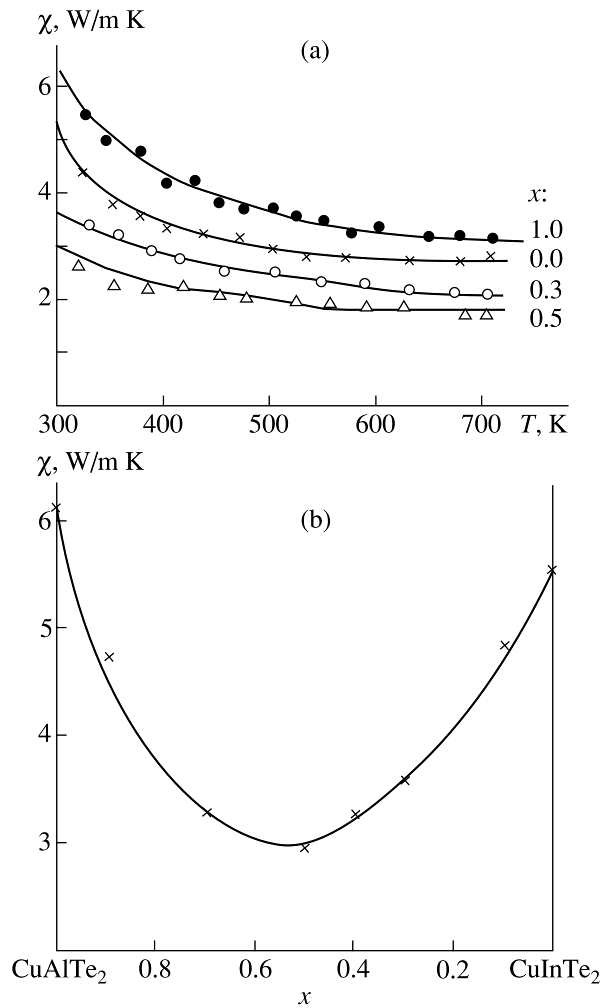

Fig. 4. (a) Temperature and (b) concentration dependences of the thermal conductivity for the $CuAl_xIn_{1-x}Te_2$ solid solutions.

The results of calculations are listed in the table, from which it can be seen that an increase in the indium-atom content in solid solutions results in a decrease in the Debye temperature, while the root-mean-square dynamic displacements in the crystal lattice increase. Such behavior of the indicated values indicates that the chemical bonds in the $CuAl_xIn_{1-x}Te_2$ solid solutions are weakened as the indium-atom concentration increases.

The thermal conductivity (χ) of the indicated compounds and their solid solutions was measured by an absolute steady-state method [21] in the temperature range T = 300–700 K using the samples, whose sizes are listed above. THe accuracy of the measurements is ~6%. The temperature dependence of χ is shown in Fig. 4a for the materials under investigation. The ther-

mal conductivity of the ternary compounds varies proportionally to T^{-1} in the range 300–400 K, which is characteristic of three-phonon scattering processes. The results obtained are consistent with the Peierls theory, according to which χ must be inversely proportional to temperature [22] above the Debye temperature. In this case, phonon–phonon scattering takes place in the course of which the energy exchange occurs between three phonons (the three-phonon process). As a result of such processes, one phonon annihilates and two new phonons appear, or two phonons annihilate and the third phonon appears. At higher temperatures, χ is described by an expression in the form of $\chi \propto T^{-n}$ $(0 < n < 1)$, which is indicative of the predominance of scattering processes at impurities and defects of the crystal lattice at such temperatures. A consequence of this circumstance is the weak temperature dependence of χ. In solid solutions, we observed the power-low dependence $\chi \propto T^{-n}$ for the thermal conductivity within the entire temperature range, which indicated that the scattering by the crystal-lattice defects was predominant.

In Fig. 4b, we show the concentration dependence of the thermal conductivity for the $CuAl_xIn_{1-x}Te_2$ solid solutions. It can be seen that the dependence of χ on x has a minimum corresponding to the content, which is almost equimolar. Such behavior of χ (a substantial reduction in χ for the solid solutions as compared with the original compounds) is related to the violation of periodicity in the crystal lattice of solid solutions due to the statistical distribution of atoms over the equivalent sites.

It is known that, although the atoms occupy the correct sites in the solid-solution crystal lattice, no order in the arrangement of various atoms is observed in this lattice. As a result, the atomic masses and the force constants vary randomly from site to site, which leads to the phonon scattering. In this context, the solid solutions can be considered as transition substances between the crystal state (conservation of the crystal lattice) and the amorphous state (due to the disordering in the arrangement of atoms). For the solid solutions, the highest disordering corresponds to medium compositions; therefore, the thermal conductivity is also lowest for them.

4. CONCLUSION

The horizontal Bridgeman–Stockbarger method was used to grow coarse-block crystals of $CuInTe_2$ and $CuAlTe_2$ ternary compounds and $CuAl_xIn_{1-x}Te_2$ solid solutions. From the transmission and reflection spectra in the region of the intrinsic-absorption edge for these compounds and their solid solutions, E_g was determined. It was established that E_g varies nonlinearly with the Al content x. The thermal expansion and the thermal conductivity of the indicated materials were investigated. It was found that the coefficient α_L of thermal expansion varied linearly, and the thermal conductivity had a minimum in the region of medium contents.

REFERENCES

1. N. A. Goryunova, *Diamond-Like Compound Semiconductors* (Sovetskoe Radio, Moscow, 1968).
2. M. Iqbol, J. Galibert, S. M. Wasim, *et al.*, Phys. Status Solidi B **219**, 351 (2000).
3. S. Roy, P. Guha, S. Chaudhuri, and A. K. Pal, Phys. Status Solidi A **189**, 209 (2002).
4. I. V. Bodnar', Zh. Neorg. Khim. **46**, 655 (2001).
5. V. Yu. Rud', Yu. V. Rud', V. F. Gremenok, *et al.*, Fiz. Tekh. Poluprovodn. (St. Petersburg) **33**, 824 (1999) [Semiconductors **33**, 757 (1999)].
6. V. M. Glazov, M. S. Mirgalovskaya, and L. A. Petrakova, Izv. Akad. Nauk SSSR, Otd. Tekh. Nauk **7**, 68 (1957).
7. H. Miyake, M. Hibi, K. Sugiyama, and K. Hiramatsu, Jpn. J. Appl. Phys., Suppl. **39** (1), 54 (2000).
8. I. V. Bodnar', Zh. Neorg. Khim. **47**, 1038 (2002).
9. S. Shirakata, S. Chichibu, R. Sudo, *et al.*, Jpn. J. Appl. Phys. **32**, L1304 (1993).
10. S. Shirakata, A. Ogawa, S. Isomura, and T. Kariya, Jpn. J. Appl. Phys., Suppl. **32** (3), 588 (1993).
11. I. V. Bodnar', V. A. Ivanov, V. A. Gaĭsin, and B. S. Kulinkin, Opt. Spektrosk. **82**, 430 (1997) [Opt. Spectrosc. **82**, 393 (1997)].
12. K. Yoshino, N. Mitani, M. Sugiyama, *et al.*, Physica B (Amsterdam) **302–303**, 349 (2001).
13. J. A. Van-Vechten and T. K. Bergstresser, Phys. Rev. B **1**, 3351 (1970).
14. R. Hill and D. Richardson, J. Phys. C **6**, L115 (1973).
15. R. Hill, J. Phys. C **7**, 521 (1974).
16. S. I. Novikova, *Thermal Expansion of Solids* (Nauka, Moscow, 1974).
17. L. S. Palatnik, V. M. Koshkin, and L. P. Gal'chinetskiĭ, Fiz. Tverd. Tela (Leningrad) **4**, 2365 (1962) [Sov. Phys. Solid State **4**, 1732 (1962)].
18. J. J. M. Binsma, L. J. Giling, and J. Bloem, Phys. Status Solidi A **63**, 595 (1981).
19. I. V. Bodnar', B. V. Korzun, and A. P. Chernyakova, Phys. Status Solidi A **101**, 409 (1987).
20. I. N. Frantsevich, *Problems in Powder Metallurgy and Strength of Metals* (Naukova Dumka, Kiev, 1956).
21. B. M. Mogilevskiĭ and A. F. Chudnovskiĭ, *Thermal Conductivity in Semiconductors* (Nauka, Moscow, 1972).
22. R. E. Peierls, *Quantum Theory of Solids* (Clarendon Press, Oxford, 1955; Inostrannaya Literatura, Moscow, 1956).

Translated by V. Bukhanov

Semiconductors, Vol. 37, No. 11, 2003, pp. 1252–1256. Translated from Fizika i Tekhnika Poluprovodnikov, Vol. 37, No. 11, 2003, pp. 1290–1295.
Original Russian Text Copyright © 2003 by Sukach, Kidalov, Vlasenko, Potapenko.

Defect-Related Luminescence of GaN:Zn Films Thermally Treated in a Radio-Frequency Ammonia Plasma

G. A. Sukach*, V. V. Kidalov, A. I. Vlasenko*, and E. P. Potapenko***

**Institute of Semiconductor Physics, National Academy of Sciences of Ukraine, Kiev, 03028 Ukraine*
e-mail: sukach@isp.kiev.ua
***Berdyansk State Pedagogical Institute, Berdyansk, 71118 Ukraine*
Submitted December 15, 2002; accepted for publication February 4, 2003

Abstract—The effect of thermal annealing in nitrogen radicals obtained by the treatment of NH_3 in a radio-frequency discharge on the luminescence properties of GaN:Zn films grown by MOCVD/hydride epitaxy on sapphire (0001) substrates is investigated. As the thermal treatment temperature was increased, a steady weakening of the violet (2.88 eV) and near-edge (3.48 eV) photoluminescence bands was observed. As a result of the thermal treatment in nitrogen radicals at 500–750°C, new bands that peaked at 3.27 and 3.42 eV were detected; the intensities of these bands increased with increasing treatment temperature. The mechanism of formation and the origin of all the bands are analyzed comprehensively. It is found that the luminescence bands at 2.88, 3.42, and 3.27 eV are characteristic of the GaN films obtained by practically each technology and are associated with the simple structural defects. The participation of O in the formation of the band at 3.42 eV is proved experimentally. *© 2003 MAIK "Nauka/Interperiodica".*

1. INTRODUCTION

It is known that the electrical, and especially luminescence, properties of GaN films substantially depend not only on the technological growth conditions but also on the subsequent external treatments. The variation in technology parameters and, specifically, the postepitaxial external effects allows one to control the number and type of quasi-equilibrium defects in the films in a wide range.

Thus, Nakamura *et al.* [1] managed to obtain low-resistivity *p*-type GaN samples doped with Group II elements. The method for reducing to a minimum the effect of the self-compensation of acceptors by intrinsic donor-type defects, which form as the reaction of the material to the introduction of acceptors in the course of doping, was chosen. The problem was solved by using postepitaxial heating of semi-insulating GaN:Mn(Zn) samples in nitrogen at the temperature $T_a \approx 700$°C. In turn, the investigation of the photoluminescence (PL) allows one to establish the origin and mechanisms of formation of such defects. The rapid high-temperature thermal treatment of GaN in N_2 was considered by Zolper *et al.* [2]. However, such thermal treatment did not lead to the improvement of the structural and optical characteristics of the film because of the surface damage and evaporation of N from GaN. To increase the efficiency of the incorporation of N into GaN, an increase in the pressure of the more adsorptive and diffusion-active atomic N rather than molecular N, as well as a decrease in the thermal treatment temperature, is required. Georgobiani *et al.* [3] investigated the effect of thermal treatment in atomic N, which was obtained by the decomposition of N_2 into individual excited atoms (radicals) in the radio-frequency (rf) plasma, on the PL of high-resistivity (semi-insulating) *n*-GaN:Zn films with the electron density $n_0 = 5 \times 10^{14}$ cm^{-3}; these films were grown on sapphire (0001) substrates by molecular-beam epitaxy. It was found that the band at 2.88 eV initially slightly increases up to the thermal treatment temperature $T_a = 600$°C. Then, with increasing T_a, the intensity of the bands that peaked at $h\nu_m$ = 2.88 and 3.48 eV decreases, and a new band at $h\nu_m$ = 3.27 eV emerges. However, the kinetic efficiency of the nitrogen radicals formed was insufficiently high because of the low power of the rf discharge source.

It was interesting to investigate the spectral features of the defect-related PL and the processes of defect formation themselves after the thermal treatment in nitrogen radicals of low-resistivity *p*-GaN:Zn samples, which are widely used in technical applications; the majority-carrier density in these samples is close to their density in the materials used for the fabrication of commercially available emitters. Furthermore, in order to establish a general pattern, it is reasonable to investigate the formation of defects in the GaN films obtained by the most widespread technological method of MOCVD/hydride epitaxy (vapor-phase epitaxy from metalloorganic compounds). It was also interesting to use a more efficient method of obtaining the nitrogen radicals from NH_3, using a more powerful rf discharge source, rather than from N_2. This paper is devoted to these issues.

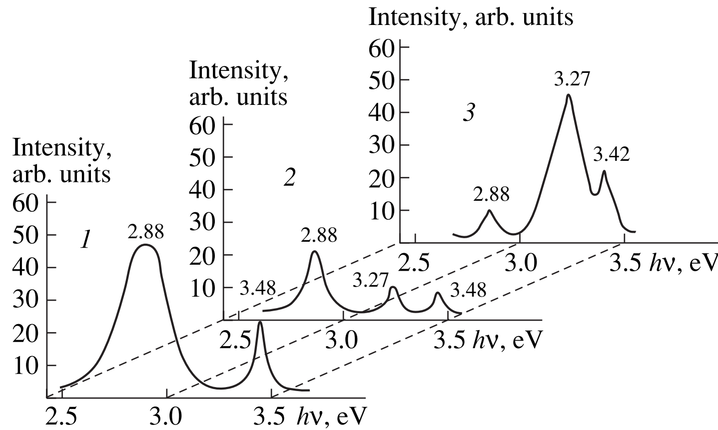

Fig. 1. Photoluminescence spectra of the GaN:Zn films prior to (*1*) and after thermal treatment in active nitrogen radicals obtained from rf NH_3 plasma with a pressure in the discharge chamber of 10^{-3} Torr and temperatures (*2*) 500 and (*3*) 750°C. The peak energies are given in eV.

2. EXPERIMENTAL

In this study, p-GaN:Zn films with the majority-carrier density $p_0 = 5 \times 10^{17}$ cm^{-3} were investigated. The films grown by MOCVD/hydride epitaxy on sapphire substrates (0001) (Nichia Chemical Industries Ltd.) were used. The films were thermally treated for 1–5 h at T_a = 500–750°C in active nitrogen radicals, which were obtained from NH_3, in a flow-through system similar to that described by Butkhuzi *et al.* [4]. As the activation source, the discharge of an rf oscillator with an operating frequency of 40 MHz, whose power was controlled within the range P = 1–2 kW, was used [5]. To prevent damage to the surface of GaN, the ion component was separated in a strong constant magnetic field. The concentration of atomic gases (N, O, etc.) was determined by the method of heating the catalytic samples, specifically, the platinum wire at which the excited atoms of gases recombine with the subsequent transformation of atoms into molecules. The highest concentration of active gases close to the sample surface determined in this way was 10^{18} cm^{-3}. The concentration of radicals of active gases in the discharge chamber was varied by varying the power of the rf oscillator. For example, at the pressure $p = 10^{-3}$ Torr, the flow of nitrogen radicals incident onto the sample surface varied within the range 10^{15}–10^{18} cm^{-2} s^{-1}. The yield of active nitrogen radicals under the conditions of our experiment exceeded that in the method using the plasma discharge in N_2 by an order of magnitude.

For the PL excitation, an LGI-21 pulse nitrogen laser with the wavelength λ = 337.1 nm and the pulse duration $t_i \leq 10$ ns was used. The excitation intensity L was varied using neutral gray filters in the range 10^{18}–5×10^{21} photon/cm^2 s, which provided low and moderate excitation levels ($\Delta n = \Delta p < (p_0 + n_0)$, where n_0, p_0, Δn, and Δp are the equilibrium and nonequilibrium electron and hole densities, respectively). The PL spectra were analyzed using a PC-controlled spectral complex based on an MDR monochromator [6]. The total systematic and random error in determining the wavelength with allowance made for the entire totality of noninformative and destabilizing factors was no larger than 0.052 nm. The PL spectra were measured using an optical cryostat at the temperature of liquid nitrogen.

The results of the investigation of the PL spectra on the scale of photon energies $h\nu$ of the p-GaN:Zn films treated in the activated gas medium are shown in Figs. 1 and 2 (thermal treatment in nitrogen radicals), as well as in the table (thermal treatment in nitrogen and oxygen radicals). The starting samples (Figs. 1, 2, curves *1*) feature a wide asymmetric band in the violet region of the spectrum with the peak emission energy $h\nu_m$ = 2.88 eV and a narrow near-edge emission band with the peak energy $h\nu_m$ = 3.48 eV. With increasing thermal-treatment temperature in high-efficiency nitrogen radicals, which were obtained from NH_3 (Fig. 1), as well as with increasing power of rf discharge (Fig. 2), the intensities of these bands decrease steadily. Note the

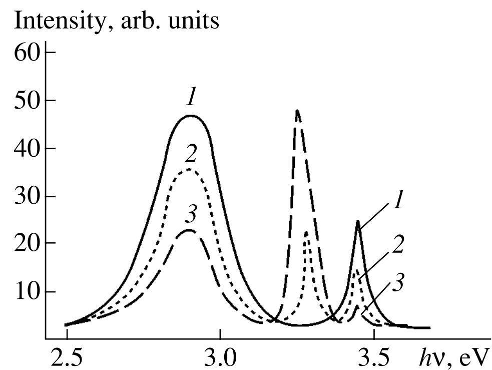

Fig. 2. Photoluminescence spectra of the GaN:Zn films prior to (*1*) and after thermal treatment in active nitrogen radicals obtained from rf NH_3 plasma with a pressure in the discharge chamber of 10^{-3} Torr, temperature 750°C, and power of rf discharge (*2*) 1120 and (*3*) 1800 W.

The effect of thermal-treatment conditions in nitrogen radicals and pure oxygen on the intensity of photoluminescence bands of the GaN : Zn samples

PL band energy, eV	Intensity of PL bands, arb. units			
	thermal treatment in NH_3 and residual oxygen			thermal treatment in pure oxygen
	25°C	500°C	750°C	750°C
2.88	48.8	21.1	9.3	8.6
3.27	0	8.6	46.6	42.7
3.42	0	0	15.1	73.6
3.48	24.6	6.6	0	0

practically in-phase decrease in the intensity of these starting PL bands with increasing T_a of the films, as well as with increasing rf discharge power. However, after these treatments, new bands peaked at $h\nu_m = 3.27$ and 3.42 eV emerge in the spectra. The intensity of the band at $h\nu_m = 3.27$ eV increases drastically as both the T_a and the intensity of the rf discharge increase (see Figs. 1, 2). For the band at $h\nu_m = 3.42$ eV, the intensity increases only with increasing T_a (see Fig. 1). After the thermal treatment of the films in active oxygen radicals, the intensity I of the band at $h\nu_m = 3.42$ eV increases draastically (table).

For all the PL bands investigated, the power-law dependence of intensity on the laser-excitation level was observed: $I \propto L^{\alpha}$. For the bands at $h\nu_m = 2.88$, 3.27, and 3.42 eV, the exponent α was close to unity ($\alpha = 1.0$–1.05), whereas for the near-edge PL band at $h\nu_m = 3.48$ eV, it was close to two ($\alpha = 1.8$).

3. DISCUSSION

The PL spectra are indicative of the variation in the defect composition of the GaN films during their thermal treatment in the rf discharge of the separated plasma, which was obtained from NH_3. Let us analyze the results obtained for all the PL bands.

3.1. The Violet Band at $h\nu_m = 2.88$ eV

This is a widely known PL band, which that characteristic of most epitaxial technologies and is related to the presence of nitrogen vacancies V_N in starting GaN. The presence of this band is indicative of the material nonstoichiometry and poor crystalline quality of the film grown. A band peaked at $h\nu_m = 2.88$ eV was observed in many studies [3, 7–9]. The generally accepted opinion in the literature is that this band is associated with the recombination of charge carriers inside the donor–acceptor pair [3, 7], in which the donor is the N vacancy and the acceptor is the substitutional impurity. Zn at the Ga site Zn_{Ca} (the majority acceptor) and other intrinsic defects dominating at temperatures $T > 40$ K are considered as the acceptors. As the growth temperature of the films increases, the concentration of the donors as a rule also increases. The diversity of the acceptor types in such donor–acceptor pairs and the different distances between the components of the donor–acceptor pairs (long-lived and short-lived donor–acceptor pairs) associated with this circumstance lead to an inhomogeneous broadening of the band with the formation of an overextended long-wavelength wing [1, 3, 9]. The same transitions with the emission of optical and acoustic phonons may also contribute to broadening. Note that the position of the band peak ($h\nu_m = 2.88$ eV) can be easily controlled by varying the partial Zn pressure in the course of growing (doping) the films. With changes in the thermal-treatment conditions, this band behaves in various ways variously. For example, after rapid thermal annealing of GaN films in N_2, its intensity increased drastically [2], and after annealing in nitrogen radicals the I magnitude initially increased up to $T_a = 600$°C and then dropped abruptly [3, 7].

A steady decrease in the intensity of the band at $h\nu_m = 2.88$ eV with increasing T_a, as well as the rf discharge power, in our case point to the fact that even insignificant external perturbations (variations of the temperature, pressure, and rf discharge frequency) lead to the decomposition of the donor–acceptor pair of the V_N–Zn_{Ca} type. This is caused by a decrease in the V_N concentration due to their replacement by activated N atoms from the N-containing medium surrounding the sample.

The results obtained demonstrated that the thermal annealing of low-resistivity p-GaN:Zn films in an activated N-containing medium, with NH_3 and a high-power rf discharge used as the source of radicals, exerts a stronger effect on the composition of point defects than does the same thermal annealing in vacuum, nitrogen vapors, or nitrogen radicals obtained using a less powerful source of rf discharge. Over the entire range of excitation levels investigated, the $I(L)$ dependence ($I \propto N_A^0 N_D^0 \propto N_D \Delta n$, where N_A^0 and N_D^0 are the concentrations of the neutral donors and acceptors and N_D is the total concentration of donors) for the band at $h\nu_m = 2.88$ eV was practically linear ($\alpha = 1.05$).

3.2. The Near-Edge Band at $h\nu_m = 3.48$ eV

Nekrasov *et al.* [10] attributed the peak with $h\nu_m = 3.48$ eV $\approx E_g$ (E_g is the band gap) to the band-to-band radiative recombination via two overlapping channels, namely, the radiative recombination of the electron bound by the shallow-level donor and the recombination of the electron and hole bound in the free-exciton radiative complex. In our case, it is necessary to consider both channels, as is indicated by the slope of the $I(L)$ dependence for this band ($\alpha \approx 1.8$) in the range $L = 10^{20}$–5×10^{21} photon/cm^2 s, which differs from the purely quadratic law ($\alpha = 2$). The latter is characteristic of the radiative recombination of free electrons and

holes. Note that the radiation, which is caused by various bound excitons, is quenched even at temperatures above 50 K; i.e., its contribution to the near-edge emission can be disregarded. A rapid temperature quenching of the PL band that peaked at $h\nu_m$ = 3.48 eV with increasing T_a and rf discharge power is apparently caused by the emergence of a more effective channel of the radiative (see below) and (or) nonradiative recombination with the involvement of the aforementioned shallow-level donor, as well as acceptors associated with the excess interstitial N atoms. These last intercept the recombination flux of the near-edge radiation.

Let us further discuss the behavior of the new PL bands that emerge after the rf thermal treatment.

3.3. The Ultraviolet Band at $h\nu_m$ = 3.27 eV

In many studies [11–15], this band was related to the recombination in donor–acceptor pairs. The absence of this band in the spectra of the initial samples, as well as a substantial increase in its intensity with increasing T_a and rf discharge power in the NH_3 plasma, are indicative of the activation or, most likely, the release of a particular component of the donor–acceptor pair from another complex. As the acceptor, the deep-level acceptor may be in this pair, and the shallow donor-type defect with the depth $E_d \approx$ 30 meV can serve as the other component of the pair [16]. In principle, this may be the same donor that was involved in the formation of the near-edge band at $h\nu_m$ = 3.48 eV prior to the treatment. An increase in $I = f(T_a, P)$ for the band at $h\nu_m$ = 3.27 eV is indicative of an abrupt increase in the concentration of the acceptor-type centers, which are most likely associated with the loss of the stoichiometry in the GaN films due to the excess of N formed during rf treatment in the NH_3 plasma. It is most likely that this is the interstitial N. On the one hand, the large halfwidth of the PL band suggests that the phonon replicas of its zero-phonon line contributes to the formation of the long-wavelength wing of this band [13]. On the other hand, the transitions between the conduction band and the Zn_{Ga} acceptor level (the ionization energy $E_a \approx$ 0.34 eV, see, for example, [17]) or, most likely, interstitial N contribute to the formation of the short-wavelength wing of this band. The latter assumption is supported by the insignificant shift (~0.025 eV) of the peak of the donor–acceptor pair band at $h\nu_m$ = 3.27 eV to shorter wavelengths with increasing rf discharge power, which leads to a superlinear growth of the concentration of acceptors of this type (see Fig. 2). The shape of this band differs from the shape inherent in the donor–acceptor pairs. However, the $I(L)$ dependence is linear ($\alpha \approx 1$) over the entire range of L investigated.

3.4. The Band at $h\nu_m$ = 3.42 eV

The origin of this peak, which is apparently a common feature of GaN films obtained by various methods except, as a rule, molecular-beam and MOCVD/hydride epitaxy, is the subject of active discussions.

Fischer *et al.* [18] attributed this band to the exciton bound by the structural defects along the crystallographic *c* axis in hexagonal GaN. However, the nature of these defects was not considered. Middleton *et al.* [19] and O'Donnell *et al.* [20] identified the position of this band with the exciton bound at the structural defects located at the interfaces between the cubic and wurtzite phases. Furthermore, it was assumed that the electron is located in the cubic phase, whereas the holes are located in the wurtzite phase [20]. Ren *et al.* [21] attributed the peak at $h\nu_m$ = 3.42 eV (at 100 K) to donor–acceptor pairs, in which the residual carbon ($E_a \approx$ 90 meV) or Ga vacancy served as the acceptor. This band may also be related to residual oxygen in the discharge chamber [22, 23]. Chung *et al.* [23] explained the emergence of the new band that peaked at $h\nu_m$ = 3.42 eV by the recombination of free holes with the electrons localized at the donor levels induced by oxygen, whose concentration increased with the deterioration of vacuum.

In order to establish the origin of the band at $h\nu_m$ = 3.42 eV unambiguously and to choose a specific mechanism of the formation of donor–acceptor pairs, two groups of experiments were carried out.

First, the dependence of the band intensity on the pressure of residual gases (p) in the discharge chamber during the thermal treatment of GaN films in nitrogen radicals, obtained from NH_3 plasma was investigated. As the pressure increased from 10^{-3} to 10^{-1} Torr, the intensity increased steadily by a factor of approximately 2.5; i.e., the relation between the random values of I and p could be represented by a regression equation in the form

$$I(p) = a_0 + a_1 p,$$

where a_0 and a_1 are the regression coefficients, which are determined by the least-squares method. The correlation index, which indicates how close the dependence between the measured I and p quantities is to the linear dependence, was close to unity, which allows one to conclude that the dependence $I(p)$ is practically functional and linear.

Since a deterioration of the vacuum at a practically constant concentration of nitrogen radicals in this range of quantity p is most likely associated with an increase in the concentration of residual oxygen in the reaction chamber, such behavior of quantity I can be supposedly associated with the presence of active oxygen radicals in the N-containing plasma.

Second, the components of all the gases of the surrounding atmosphere, as well as the components of the inner construction of the chamber, are also present in the discharge chamber rather than the components of NH_3 only. Therefore, to establish the physical nature of the band at $h\nu_m$ = 3.42 eV, the GaN:Zn samples, in which this band already existed after thermal treatment in the rf NH_3 plasma and residual oxygen radicals, were additionally thermally treated. This treatment was carried out at T_a = 750°C and $p = 10^{-3}$ Torr (see Fig. 1,

curve *3*) precisely in oxygen radicals that were obtained from a pure oxygen medium (compare the third and fourth columns of the table). The concentration of these radicals was by four to six orders of magnitude higher than the concentration of the radicals of residual oxygen in the chamber.

Analysis of the data given in the table indicates that the intensity of the band at $h\nu_m = 3.42$ eV after thermal treatment in oxygen radicals increases by a factor of approximately 5 compared with the intensity observed for the samples treated in radicals of residual oxygen. Consequently, the PL band at $h\nu_m = 3.42$ eV is caused by the recombination of free holes with electrons bound at the donor centers O_N (O at the N site). The linear run of the $I(L)$ dependence ($a \approx 1$), which is characteristic of the band-to-impurity transitions, confirms this fact. The results obtained by Grekov *et al.* [24] and Aleksandrov *et al.* [25] also indicate that O is an impurity that is easily introduced in GaN. Thus, the contribution of O to the formation of the band at $h\nu_m = 3.42$ eV can be considered as proved with a high degree of confidence.

A slight decrease in the intensities of the bands at $h\nu = 2.88$ and 3.27 eV after thermal treatment in oxygen radicals (see table) indicates that the donor properties of O are very complex. Oxygen and its associations with other defects may also generate centers of nonradiative recombination, which lead to a decrease in the effective lifetime of charge carriers. This in turn leads to a drop in the intensities of all PL bands without exception after destructuring treatments in O-containing media. Furthermore, an increase in the intensity of the PL band at $h\nu = 3.42$ eV against the background of the drop in I for all bands is associated with the generation (introduction) of additional centers of radiative recombination. These centers provide the prerequisites for the compensation of the drop in intensity caused by introducing the centers of nonradiative recombination.

4. CONCLUSION

Thus, our experimental investigations indicate that the luminescence bands at 2.88, 3.48, 3.27, and 3.42 eV are not a specific feature caused by a particular technology, but most likely a common property of GaN films that are fabricated using practically all epitaxial technologies, including the thermal treatment of GaN films in active nitrogen radicals obtained from rf NH_3 plasma. The origin of these bands is associated with simple defects of the GaN structure and their complexes, which are formed during the epitaxial growth and postepitaxial treatments and are common to all methods (residual oxygen, C, vacancies and interstitial atoms, etc.).

ACKNOWLEDGMENTS

This study was supported by the State Foundation for Fundamental Research of Ukraine (DFFD), project no. 04.07/256.

REFERENCES

1. S. Nakamura, M. Senoh, and T. Mukai, Jpn. J. Appl. Phys. **31**, L139 (1992).
2. J. C. Zolper, M. Hagerott, J. Grawtord, *et al.*, Appl. Phys. Lett. **68**, 200 (1996).
3. A. N. Georgobiani, A. N. Gruzintsev, U. A. Aminov, *et al.*, Fiz. Tekh. Poluprovodn. (St. Petersburg) **35**, 149 (2001) [Semiconductors **35**, 144 (2001)].
4. T. V. Butkhuzi, A. N. Georgobiani, E. Zade-Uly, *et al.*, Tr. Fiz. Inst. im. P.N. Lebedeva, Akad. Nauk SSSR **182**, 140 (1987).
5. G. A. Sukach, V. V. Kidalov, A. I. Vlasenko, *et al.*, Optoélektron. Poluprovod. Tekh. **37**, 91 (2002).
6. G. A. Sukach, N. I. Sypko, and V. M. Gladarevskiĭ, Optoélektron. Poluprovod. Tekh. **14**, 58 (1988).
7. U. Kaiser, A. N. Gruzintsev, I. I. Khodos, and W. Richter, Neorg. Mater. **6**, 458 (2000).
8. H. Amono, I. Akasaki, T. Kozawa, *et al.*, J. Lumin. **4**, 121 (1988).
9. S. V. Svechnikov, P. F. Oleksenko, G. O. Sukach, *et al.*, Ukr. Fiz. Zh. **43**, 1290 (1998).
10. V. Yu. Nekrasov, L. V. Belyakov, O. M. Sreseli, and N. N. Zinov'ev, Fiz. Tekh. Poluprovodn. (St. Petersburg) **33**, 1428 (1999) [Semiconductors **33**, 1284 (1999)].
11. C. H. Hong, D. Pavidis, and S. W. Brown, J. Appl. Phys. **77**, 1705 (1995).
12. G. Grimmeiss and B. Monemar, J. Appl. Phys. **41**, 4054 (1970).
13. R. Dingle and M. Ilegems, Solid State Commun. **9**, 175 (1971).
14. O. Langstrem and B. Monemar, J. Appl. Phys. **45**, 2266 (1974).
15. M. Ilegems and R. Dingle, J. Appl. Phys. **44**, 4234 (1973).
16. W. Gotz, N. M. Jonson, C. Chen, *et al.*, Appl. Phys. Lett. **68**, 2666 (1996).
17. S. Strite and H. Morkoc, J. Vac. Sci. Technol. B **10**, 1237 (1992).
18. S. Fischer, C. Wetzel, W. L. Hansen, and E. D. Bourret-Courchesns, Appl. Phys. Lett. **69**, 2716 (1996).
19. P. G. Middleton, K. P. O'Donnell, C. Trager-Cowan, *et al.*, Mater. Sci. Eng. B **59**, 133 (1999).
20. K. P. O'Donnell, M. Umlauf, M. Kraushaar, *et al.*, Mater. Sci. Eng. B **50**, 264 (1997).
21. G. B. Ren, D. J. Devsnip, D. E. Lacklison, *et al.*, Mater. Sci. Eng. B **43**, 242 (1997).
22. T. F. Huang, A. Marshall, S. Spruytte, and J. S. Harris, Jr., J. Cryst. Growth **200**, 362 (1999).
23. B. C. Chung and M. Gershenzon, J. Appl. Phys. **72**, 651 (1992).
24. F. F. Grekov, D. M. Demidov, and A. M. Zykov, Zh. Prikl. Khim. (Leningrad) **52**, 1394 (1979).
25. S. E. Aleksandrov, T. A. Gavrikova, and A. M. Zykov, Fiz. Tekh. Poluprovodn. (St. Petersburg) **34**, 297 (2000) [Semiconductors **34**, 291 (2000)].

Translated by N. Korovin

Semiconductors, Vol. 37, No. 11, 2003, pp. 1257–1258. Translated from Fizika i Tekhnika Poluprovodnikov, Vol. 37, No. 11, 2003, pp. 1296–1297.
Original Russian Text Copyright © 2003 by Nesmelova.

ELECTRONIC AND OPTICAL PROPERTIES OF SEMICONDUCTORS

Effective Electron Mass in a $Mn_xHg_{1-x}Te$ System

I. M. Nesmelova

State Institute of Applied Optics, Kazan, 420075 Tatarstan, Russia

e-mail: eugene@mi.ru

Submitted December 23, 2002; accepted for publication February 4, 2003

Abstract—The reflection spectra of n-$Mn_xHg_{1-x}Te$ single crystals and epitaxial layers were measured at 300 K. The effective electron mass was determined for the samples with $x = 0.06$–0.10 and an electron concentration $N > 6 \times 10^{16}$ cm^{-3}. The calculated values of effective electron mass are close to experimental values.
© 2003 MAIK "Nauka/Interperiodica".

$Mn_xHg_{1-x}Te$ mercury–manganese telluride (MMT) solid solutions exhibit stronger chemical bonds and, accordingly, a higher stability of electrical properties compared to those of mercury–cadmium telluride (MCT), which is the most widely used material in infrared optoelectronics [1]. However, some of the basic MMT parameters have been studied inadequately; in a number of cases, only calculated values of these parameters are available and have not been verified experimentally.

In this paper, we report the results of studying the reflection spectra of n-type MMT samples with the aim of determining the effective electron mass in relation to the electron concentration and the content of manganese telluride in the ternary compound.

The reflection spectra were measured at 300 K using an IKS-21 spectrometer in the spectral range 20–45 μm. The samples under investigation had a concentration of uncompensated donors $N = (6–60) \times 10^{16}$ cm^{-3} and were grown by recrystallization of a two-phase mixture with additional feeding and by liquid-phase epitaxy from the tellurium melt.

The reflection spectra of some of the samples are shown in the figure. Characteristic plasma minima in the spectra were observed for the samples with $N > 10^{17}$ cm^{-3}; the positions of these minima λ_{min} were used to calculate the effective electron masses using the formula

$$m_n/m_0 = (e^2 N\lambda_{min}^2)/(\pi c^2 \varepsilon_\infty m_0),$$

where the values of the relative optical permittivity $\varepsilon_\infty = n^2$ (n is the refractive index) were taken from [2].

Theoretical values of effective electron masses were calculated according to the Kane theory. If the condition $E_g \ll \Delta$ is satisfied (here, Δ is the spin–orbit coupling constant), the energy bands are spherically symmetrical, and the electron gas is degenerate, we obtain

$$m_n/m_0 = \{1 + (4/3P^2 m_0)/\hbar^2 \times [E_g^2 + 8/3P^2(3\pi^2 N)^{2/3}]^{-1/2}\}^{-1}.$$

This expression is identical to that derived previously [3]. The values of the band gap E_g and the Kane matrix element P in relation to x and temperature T were determined using empirical formulas [3]. The electrical parameters of the samples, whose reflection spectra are shown in the figure, and also the experimental and calculated values of effective electron masses are listed in the table. The experimental data are in satisfactory agreement with both the results of calculations and the theoretical values of effective masses obtained by Bodnaruk *et al.* [4].

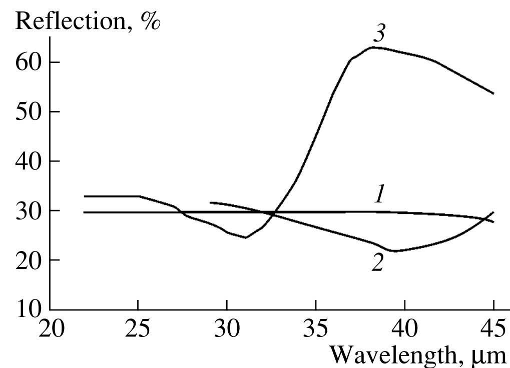

Reflection spectra of $Mn_xHg_{1-x}Te$ samples at $T = 300$ K; the electron concentration $N = (1)\ 6 \times 10^{16}$ cm^{-3}, $(2)\ 1.5 \times 10^{17}$ cm^{-3}, and $(3)\ 5.5 \times 10^{17}$ cm^{-3}; the mole fraction of MnTe $x = (1)$ 0.09, (2) 0.06, and (3) 0.10.

Characteristics of the samples at $T = 300$ K and effective masses of electrons in $Mn_xHg_{1-x}Te$ solid solutions

Mole fraction of $MnTe_x$	N, 10^{17} cm^{-3}	μ, 10^4 cm^2 V^{-1} s^{-1}	λ_{min}, µm	ε_∞	m_n/m_0	m_n/m_0
					Experiment	Theory
0.09	0.6	8.0	–	13.68	–	0.0194
0.06	1.5	5.0	40.5	13.68	0.0162	0.0190
0.10	5.5	1.3	31.0	13.10	0.0360	0.0345

Note: N is the electron concentration, μ is the mobility, and λ_{min} is the wavelength corresponding to the plasma minimum in the reflection spectrum.

It is noteworthy that the effective electron masses in an MMT solid solution are somewhat heavier than in an MCT compound (see, for example, [5]) for comparable values of N, x, and T. The differences increase with increasing N. This fact is indicative of a higher density of electronic states in the $Mn_xHg_{1-x}Te$ samples.

I thank L.N. Checherina for performing the galvanomagnetic measurements.

REFERENCES

1. A. Rogalski, Infrared Phys. **31** (2), 117 (1991).
2. I. M. Nesmelova, I. M. Lavrent'eva, N. S. Baryshev, and N. P. Tsitsina, Zh. Prikl. Spektrosk. **63**, 510 (1996).
3. A. Rogalski and K. Jozwikowski, Phys. Status Solidi A **122**, K39 (1990).
4. O. A. Bodnaruk, I. N. Gorbatyuk, S. É. Ostapov, and I. M. Rarenko, Fiz. Tekh. Poluprovodn. (St. Petersburg) **26** (3), 468 (1992) [Sov. Phys. Semicond. **26**, 264 (1992)].
5. I. M. Nesmelova, *Optical Properties of Narrow-Gap Semiconductors* (Nauka, Novosibirsk, 1992).

Translated by A. Spitsyn

Semiconductors, Vol. 37, No. 11, 2003, pp. 1259–1263. Translated from Fizika i Tekhnika Poluprovodnikov, Vol. 37, No. 11, 2003, pp. 1298–1302.
Original Russian Text Copyright © 2003 by Ushakov, Klevkov.

Effect of Grain Boundaries on the Properties of Cadmium Telluride Grown under Nonequilibrium Conditions

V. V. Ushakov* and Yu. V. Klevkov

Lebedev Physical Institute, Russian Academy of Sciences, Leninskiĭ pr. 53, Moscow, 119991 Russia

**e-mail: ushakov@mail1.lebedev.ru*

Submitted February 13, 2003; accepted for publication February 17, 2003

Abstract—Microphotoluminescence spectroscopy and imaging were used to study the effect of grain boundaries on the properties of textured CdTe polycrystals with a single-crystal grain size of 1–2 mm grown under nonequilibrium conditions. The technological procedure included low-temperature synthesis and purification of the material via congruent sublimation, with subsequent deposition under conditions of gas-dynamic vapor flow and high-rate low-temperature condensation. Microluminescence probing revealed that most of the grain boundaries are decorated with local centers emitting in the 1.4-eV band of donor–acceptor recombination involving shallow donors and *A*-center acceptors. The boundary regions are, to some extent, free of nonradiative recombination centers active at room temperature. Gettering activity of the grain boundaries could be detected at the distances up to 100 μm, which reflects the specific features of the nonequilibrium crystallization conditions of the material under study. © *2003 MAIK "Nauka/Interperiodica".*

1. INTRODUCTION

In the previous study, we used microphotoluminescence spectroscopy and imaging to examine the emission spectra of cadmium telluride grown by nonequilibrium techniques under conditions of congruent sublimation and gas-dynamic vapor flow in a reactor [1]. In addition to the identification of the radiative transitions, we established that, in this material, there is a tendency to aggregation of residual impurities and point defects with the formation of about 100-μm-size regions characterized by a high density of certain impurities. Grain boundaries play an important role in the structure of the samples investigated, which is textured with a single-crystal grain size of 1–2 mm. It is known that the grain boundaries in polycrystalline materials have a significant (and, in some cases, predominant) influence on their properties [2]. Due to high defect densities at the grain boundaries, they often feature high concentrations of efficient traps and charge-carrier recombination and scattering centers. The effect of the grain boundaries on the impurity segregation is also well known; this may result in the formation of heavily doped channels in the boundaries, which considerably affect the charge-carrier transport in experimental polycrystalline device structures. In this study, we used the microluminescence-probing technique to examine the effect of the grain boundaries on the properties of coarse-grained CdTe that crystallized under nonequilibrium conditions.

2. EXPERIMENTAL

The material under study was obtained using low-temperature synthesis and sublimation purification, yielding a compound of a composition corresponding to the minimum-pressure point [3]. To enhance the purification efficiency, in this study we used nonequilibrium technological processes taking place under conditions of congruent sublimation and gas-dynamic vapor flow in the reactor [4]. In combination with a deep prepurification of the source components (5–6*N*), this makes it possible to use the method of free growth to finally obtain polycrystalline ingots of CdTe (up to 70 mm in diameter) with the lowest possible deviation from the stoichiometry and a concentration of main residual impurities no higher than 10^{15} cm^{-3}. The rate of the vapor deposition, which took place at temperatures around 600°C, was an order of magnitude higher than the nearly equilibrium values typical of conventional technologies and was as high as ~500 μm/h. The samples under study were [111] textured with the single-crystal grain size of 1–2 mm. The sample surfaces (cut either parallel or perpendicular to the growth axis) were prepared by grinding, polishing, and etching in a bromomethanol solution. To reveal the grain boundaries and the crystal-structure defects inside the grains, the samples were treated with the selective etchant *E*-Ag-1. The main structural defects revealed by chemical etching were grain boundaries, twin boundaries, and dislocations, whose density inside a grain was lower than 10^3 cm^{-2} on average. At room temperature, according to the Hall measurements, the samples possess *p*-type conductivity and have a resistivity of 10^3–10^4 Ω cm.

After the measurements were carried out on as-grown samples, they were subjected to a 70-h annealing in an atmosphere of saturated Cd vapor at 700°C.

The measurements were carried out using an automated microphotoluminescence scanner, which makes

1063-7826/03/3711-1259$24.00 © 2003 MAIK "Nauka/Interperiodica"

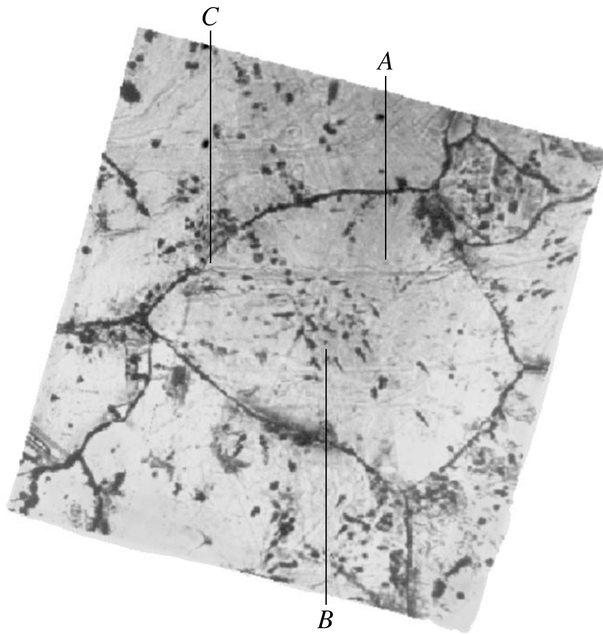

Fig. 1. The structure of a 1.0×0.8 mm single-crystal grain; the luminescence spectra presented in Fig. 2 were taken at the points indicated by letters.

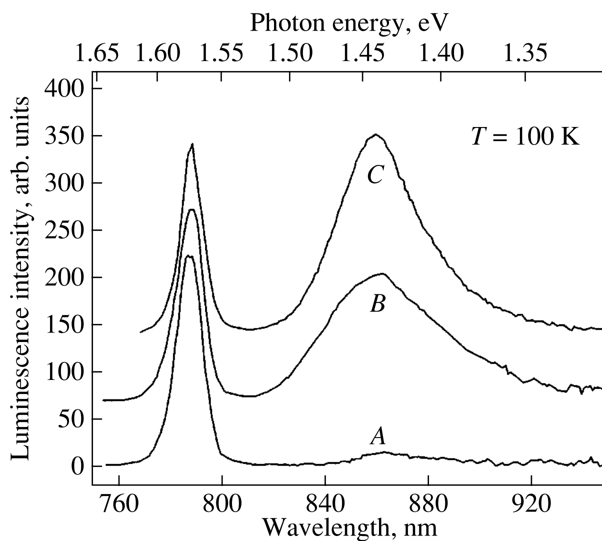

Fig. 2. A representative selection of the microphotoluminescence spectra of the material under study at 100 K, recorded at spots *A*, *B*, and *C* indicated in Fig. 1.

it possible to record both luminescence spectra at a given spot on the sample surface and luminescent images of the surface at a given wavelength. The samples were mounted on a cold finger in a cryostat, with the temperature variable from 100 to 300 K. The luminescence was excited by the radiation of a He–Ne laser (λ = 632.8 nm) using a focusing optical system. The power of excitation radiation on the sample surface was 2.5–3.0 mW, with the spot diameter of 8–10 μm (at a 0.1-maximum intensity level). The position of the excitation spot on the sample surface was visually monitored using a microscope-based "pointing system." The sample emission in the wavelength range up to 1 μm was spectrally analyzed by an MDR-12 wide-aperture grating monochromator and detected by a cooled FEU-83 photomultiplier; the PMT signal was recorded using the lock-in technique and processed on a computer. The cryostat was mounted on a special table whose motion was computer-controlled; scanning was performed by translating the table along two mutually perpendicular axes with respect to the laser beam, whose spatial position was kept fixed. The step size could be varied according to the requirements of the experiment at hand; in this study, the step was set at 25 μm. In the course of a spatial scan at a given wavelength, the data were output on the display using color representation of the luminescence intensity.

3. RESULTS AND DISCUSSION

The measurements were carried out in a region occupied by a typical single-crystal grain 1.0×0.8 mm in size, which is shown in Fig. 1. In addition to the grain boundaries, chemical etching revealed a certain cluster of extended structural defects (presumably, dislocations) at the center of the grain.

The results reported below were obtained for sample temperatures of 100 and 300 K; in this case, apart from intrinsic emission, radiative transitions involving relatively deep-level impurity and defect centers become important in the luminescence of CdTe.

Representative microphotoluminescence spectra, recorded at the spots of the crystal under study indicated in Fig. 1, are shown in Fig. 2. At 100 K, the edge-emission band (1.578 eV) and the "self-activation" impurity–defect band (1.48 eV) were predominant in the spectra. The origin of these bands had been identified previously [1]: the first band is related to the exciton, emission, and the second, to donor–acceptor pair recombination involving shallow donors and *A*-center acceptors ($V_{Cd}D$) [5–12]. As was shown in [1], the unusually high peak energy of the self-activation band is related to the fact that the excitation level is very high (10^{22} photons/(cm^2 s)) and the luminescence spectra are measured locally at the spots where the density of recombination centers increased considerably.

From the selection of locally probed spectra presented in Fig. 2, one can see that the intensity of the exciton band is nearly the same over different spots of the grain. At the same time, the intensity of the impurity–defect emission around 1.4 eV is high only in some regions of the sample. This conclusion is confirmed by the results of a detailed monochromatic mapping of the luminescence intensity carried out over a 1.25×1.25 mm area of the sample that includes the single-crystal grain shown in Fig. 1; the scan step was 25 μm. Figure 3 represents a luminescent image of the as-

grown (unannealed) sample at 100 K at a wavelength of 840 nm. It is evident that the intensity of 1.4-eV impurity and defect emission is high only in the regions adjacent to the grain boundaries and in the region of the defect cluster at the center of the grain; moreover, the intensity distribution along the grain boundary is not uniform and a part of the boundary (the lower portion of Fig. 3) is almost "invisible" at this wavelength. The intensity of intrinsic (excitonic) luminescence at 100 K is distributed relatively uniformly over the scanned area (the contrast, i.e., the ratio of the maximum to the minimum value of the intensity over the image, was about two). Thus, at this temperature, the variation in the lifetime of nonequilibrium charge carriers over the entire grain, including the boundary regions, is fairly modest—at least under conditions of the high level of excitation characteristic of this experiment. Consequently, notable variations in the intensity of luminescence of impurity and defect centers emitting in the self-activation band at 1.48 eV can be related to a sufficient degree of confidence in the variations in their local density. Then, we conclude from the data presented above that the density of impurity and defect centers responsible for the 1.4-eV emission increases notably within an area of 50–100 μm around the grain boundaries (the contrast of the luminescent image in Fig. 3 amounts to 37). Apparently, this decoration of the grain boundaries occurs due to gettering of residual impurities and defects caused by them, and to the diffusion of impurities over the boundaries in the course of the growth process (~600°C, 40–45 h) and the cooling of the material down to room temperature.

Similarly to previous results [1], the luminescence map in Fig. 3 contains some "bright" spots of sizes up to 100 μm, which cannot be related to any specific features of the crystal structure revealed by chemical etching. The detailed mechanism of their formation remains unclear. According to the previous data [1], neither single dislocations nor twin boundaries serve as their nucleation centers. It can be noticed only that, mainly, these bright spots are observed also in the relative vicinity of the grain boundaries.

Finally, we can see in Fig. 3 a region of increased density of "1.4-eV" centers, which stretches across the entire grain through its middle. Taking into account that these centers have a tendency to decorate extended structural defects, we are able to suggest that this indicates the presence of a pileup of dislocations in the middle of the grain, part of which are revealed by chemical etching (see Fig. 1). Investigation of other grains in this sample yielded similar results. Apparently, this means that the formation of subgrain boundaries in the middle region of single-crystal grains due to polygonization is an inevitable consequence of the kinetics of nonequilibrium crystallization in the technological processes employed.

To study the response of the impurity–defect ensemble of the as-grown crystals to the thermal treatment, the samples were annealed for 70 h in saturated Cd vapor at 700°C. After such a treatment, the intensity of both excitonic and impurity–defect spectral bands increased by 1.5–2 orders of magnitude at any spot of the sample surface, apparently owing to a significant decrease in the density of nonradiative recombination centers. This is evidence of a considerable deviation from equilibrium in the density (and, possibly, in the composition) of the residual defects in the as-grown crystals. In this respect, stoichiometry defects are the most probable candidates, despite the material being grown at low temperature under conditions of congruent sublimation. In addition, it is not improbable that, due to the difference in the condensation coefficients of the elements of the crystal matrix (Cd and Te_2), clusters of intrinsic and impurity-related point defects in the form of microprecipitates may appear around lattice irregularities under nonequilibrium crystallization conditions. It seems likely that, in general, the formation of crystal structures characterized by weak association of the residual defects is typical of the growth processes involving high crystallization rates under conditions of gas-dynamic vapor flow in the reactor [13].

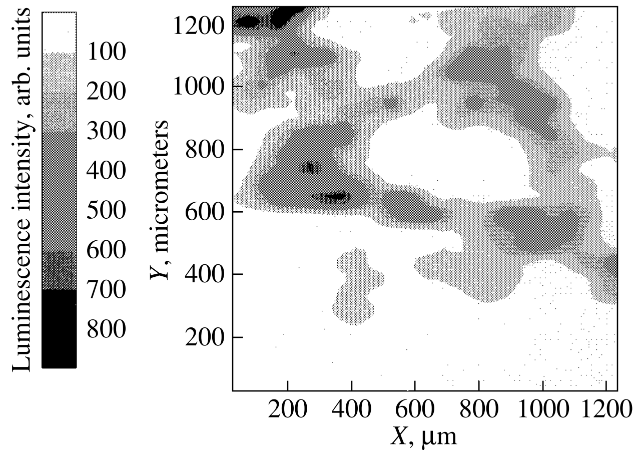

Fig. 3. Microphotoluminescence map of the as-grown (unannealed) sample at 100 K; a 1.25 × 1.25 mm^2 area including the single-crystal grain shown in Fig. 1 was scanned at the wavelength of impurity–defect emission (840 nm).

Annealing also leads to certain changes in the features of the luminescent image of the grain recorded at 840 nm, the wavelength of the impurity–defect emission (see Fig. 4). First, the image contrast is reduced down to five, and this takes place because of a relatively higher increase in the emission intensity inside the grain in comparison to the boundary regions. Second, all grain boundaries became clearly "visible" in the image upon annealing, including those poorly revealed by luminescent mapping of the as-grown material. Since the distribution of the excitonic-emission intensity over the surface of the sample at 100 K remained relatively uniform upon annealing, a buildup of the 1.4-eV luminescence along the lower (in terms of

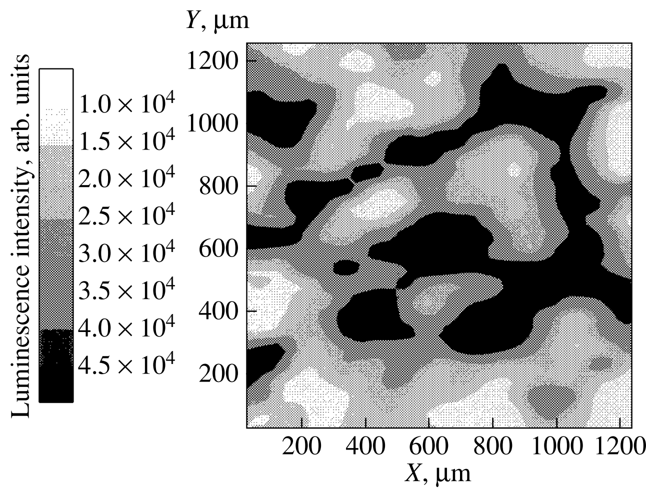

Fig. 4. Microphotoluminescence map of the sample annealed for 70 h at 700°C in saturated Cd vapor. The scan was taken at the wavelength of impurity–defect emission (840 nm) and covers the area including the single-crystal grain shown in Fig. 1; the sample temperature was 100 K.

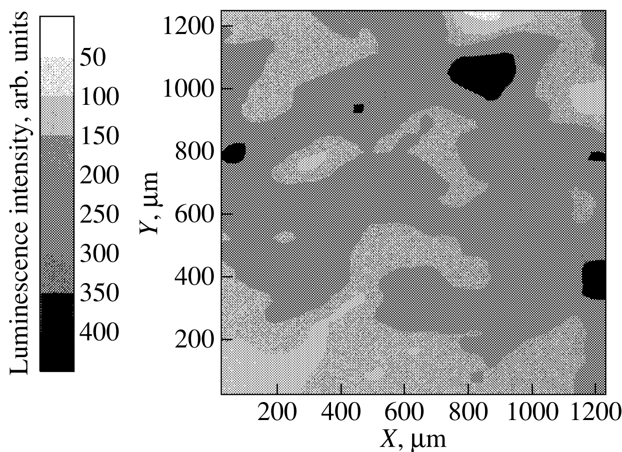

Fig. 5. Microphotoluminescence map of the annealed sample recorded at room temperature at the wavelength of intrinsic emission (821 nm); the scan covers the area including the single-crystal grain shown in Fig. 1.

Fig. 1) boundary of the grain should be also attributed to an increase in the density of the corresponding impurity–defect centers in this region. Most probably, this process occurs due to the diffusion of residual impurities gettered at the grain boundary during crystallization: the surrounding luminescence background in Fig. 4 is at a typical level, and the value of the diffusion coefficient needed ($\sim 10^{-10}$ cm^2 s^{-1} at 700°C) agrees fairly well with those for the main impurities in CdTe [14]. Another contribution may be related to the dissociation of microprecipitates containing residual impurities, taking place in the course of annealing [15]. Finally, it should be noted that the highest intensity of the "self-activation" band (and, thus, the highest density of the corresponding local centers) was observed in the boundary regions at the junction of several grains.

A reduction in the density of nonradiative recombination centers upon annealing enabled observation of the crystal luminescence at room temperature. It was possible to detect the edge-emission band that peaked at 1.502 eV (821 nm), comprising the band-to-band and exciton recombination radiation and its LO-phonon replicas [16]. It has already been mentioned that, at 100 K, the distribution of the intrinsic (exciton) luminescence intensity over the surface of the sample is rather uniform. However, from the map of the room-temperature luminescence at the intrinsic-emission wavelength (821 nm), shown in Fig. 5, it is evident that in this case, the boundary regions of the grain exhibit more intense emission than the inner regions. The difference between these two cases originates from the fact that activation mechanisms of nonradiative recombination, which are "frozen" at low temperatures, come into play at room temperature. Thus, the map image shown in Fig. 5 indicates that the regions adjacent to the grain boundaries, up to distances of 100 µm, are to some extent free of nonradiative recombination centers; apparently, this results from the gettering ability of the boundary. Probably, this also partially causes the above-mentioned decrease in the contrast of the impurity–defect map after annealing (Figs. 3, 4). It can be also seen from Fig. 5 that similar effect is observed in the vicinity of the subgrain boundary in the middle of the grain.

4. CONCLUSIONS

We showed in this study that microphotoluminescence may serve as an efficient tool for investigating the impurity–defect composition and the structure of CdTe grown by nonequilibrium technological processes that include low-temperature synthesis from deeply purified source components and subsequent purification of the compound under conditions of congruent sublimation, vapor flow in the gas-dynamic mode, and high-rate low-temperature condensation. As a result of these features of the crystallization process, the elements of both equilibrium and nonequilibrium arrangements of the impurity–defect structure are characteristic of the material thus obtained. A need for local analysis of the samples was essential in this study. Despite the relatively large grain size (1–2 mm), this material in general exhibits properties typical of both single crystals and polycrystals. The microluminescence probe revealed that the impurity–defect compositions of the boundary regions and the inner regions of single-crystal grains differ considerably. Most of the grain boundaries are decorated with impurity–defect centers emitting in the 1.4-eV band of donor–acceptor recombination involving shallow donors and *A*-center acceptors. In addition, due to segregation at the grain and subgrain boundaries, the boundary regions are, to some extent, free of nonradiative recombination centers that are active at room temperature. Gettering activity of the grain boundaries

could be detected at the distances up to 100 μm inside the grains.

ACKNOWLEDGMENTS

This study was supported by the Russian Foundation for Basic Research, project no. 01-02-16500.

REFERENCES

1. V. V. Ushakov and Yu. V. Klevkov, Fiz. Tekh. Poluprovodn. (St. Petersburg) **37**, 1067 (2003) [Semiconductors **37**, 1042 (2003)].
2. *Grain Boundaries in Semiconductors*, Ed. by H. J. Leamy, G. E. Pike, and C. H. Seager (North-Holland, New York, 1982).
3. A. V. Kvit, Yu. V. Klevkov, S. A. Medvedev, *et al.*, Fiz. Tekh. Poluprovodn. (St. Petersburg) **34**, 19 (2000) [Semiconductors **34**, 17 (2000)].
4. Y. Klevkov and S. Medvedieff, Brevet (France), No. 2782932.
5. K. Zanio, in *Semiconductors and Semimetals*, Ed. by R. K. Willardson and A. C. Beer (Academic, New York, 1978), Vol. 13.
6. T. Taguchi, J. Shirafuji, and Y. Inuishi, Jpn. J. Appl. Phys. **12**, 1558 (1973).
7. B. Furgolle, M. Hoclet, M. Vandevyver, *et al.*, Solid State Commun. **14**, 1237 (1974).
8. C. B. Norris and C. E. Barnes, Rev. Phys. Appl. **12**, 219 (1977).
9. C. E. Barnes and K. Zanio, J. Appl. Phys. **46**, 3959 (1975).
10. W. Stadler, D. M. Hofmann, H. C. Alt, *et al.*, Phys. Rev. B **51**, 10619 (1995).
11. G. Brunthaler, W. Jantsch, U. Kaufmann, and J. Schneider, J. Phys. C **1**, 1925 (1989).
12. D. M. Hofmann, P. Omling, H. G. Grimmeiss, *et al.*, Phys. Rev. B **45**, 6247 (1992).
13. K. Durose and G. J. Russell, J. Cryst. Growth **86**, 471 (1988).
14. D. Shaw, J. Cryst. Growth **86**, 778 (1988).
15. J. L. Pautrat, N. Magnea, and J. P. Faurie, J. Appl. Phys. **53**, 8668 (1982).
16. J. Lee, N. C. Giles, D. Rajavel, and C. J. Summers, Phys. Rev. B **49**, 1668 (1994).

Translated by M. Skorikov

Semiconductors, Vol. 37, No. 11, 2003, pp. 1264–1265. Translated from Fizika i Tekhnika Poluprovodnikov, Vol. 37, No. 11, 2003, pp. 1303–1304.
Original Russian Text Copyright © 2003 by Kidalov, Sukach, Revenko, Potapenko.

Ultraviolet Luminescence of Thin GaN Films Grown by Radical-Beam Gettering Epitaxy on Porous GaAs(111) Substrates

V. V. Kidalov*, G. A. Sukach, A. S. Revenko*, and E. P. Potapenko****

**Berdyansk State Pedagogical University, Berdyansk, 71100 Ukraine*
e-mail: kid@bdpu.org or kidalov32@rambler.ru
***Institute of Semiconductor Physics, National Academy of Sciences of Ukraine, Kiev, 01237 Ukraine*
Submitted February 5, 2003; accepted for publication February 25, 2003

Abstract—GaN films with a thickness of 0.1 μm were grown by radical-beam gettering epitaxy on porous GaAs(111) substrates. Excitonic luminescence bands are dominant in the photoluminescence spectra measured at 4.2 K. The energy positions of excitonic-band peaks are analyzed; as a result, it is concluded that there are stresses in the grown GaN films. *© 2003 MAIK "Nauka/Interperiodica".*

The ultraviolet (UV) spectral region is used in many optoelectronic devices [1]. The direct-gap semiconductor GaN, whose hexagonal modification has a band gap of 3.39 eV [2], is most promising as the material for light-emitting diodes (LEDs) that operate in this region of the spectrum. GaN UV emission is caused by recombination which involves the free and bound excitons [3]. In order to increase the efficiency of GaN LEDs, it is necessary to have GaN films of a high crystal quality. These films are grown on various substrates, including Si, GaAs, 3*C*-SiC, Al_2O_3, and 6*H*-SiC. The main problem is related to a reduction in the defect concentration at the film–substrate interface; these defects are caused by the lattice-constant mismatch between the film and the substrate.

Mamutin *et al.* [4] used for the first time a porous GaAs single crystal as a "soft" substrate for GaN films grown by molecular-beam epitaxy (MBE). In this study, we considered the possibility of forming GaN films on porous GaAs substrates with (111) orientation using radical-beam gettering epitaxy [5]. The main difference of this method from conventional epitaxy consists in the fact that one of the components (atomic nitrogen) is supplied from the gaseous phase, whereas the second component (gallium) is gettered from the bulk of the treated crystal. The second important special feature of radical-beam gettering epitaxy is related to the temperature distribution in the reactor. The treated crystal is positioned in a narrow high-temperature zone of the reactor; this zone occupies a small fraction of the total reactor volume, while the temperature of the remaining part of the reactor is lower. Such a temperature profile leads to the removal of impurities from the growth zone to the low-temperature part of the reactor, which ensures a high purity of the formed layers.

The *n*-GaAs(111) single crystals were treated in an aqueous solution of HF. Studies of porous GaAs by scanning electron microscopy showed that the pore diameter is on the order of 100 nm (for the specified conditions of the electrochemical treatment). The thickness of the porous GaAs layers is about 2 μm. An annealing of porous GaAs for 2 h in nitrogen plasma was performed in a setup for radical-beam gettering epitaxy, which was described in detail previously [6]. Extrapure ammonium was used as the nitrogen source. The distance between the plasma and the treated crystal was controlled using a magnetic field; the optimal distance was $d = 2$ cm. The etching of the crystal occurs at a smaller distance, whereas a drastic decrease in the atomic-nitrogen flux is observed for larger distances. The operating pressure in the atomic-nitrogen source was 10^{-3} Torr. Studies of optical emission spectra of high-frequency nitrogen discharge in the visible region of the spectrum revealed the presence of bands that corresponded to excited molecular and atomic nitrogen; a band that peaked at $\lambda = 747$ nm exhibited especially high intensity and was related to excited atomic nitrogen. The above features of the nitrogen gas discharge ensure the high efficiency of interaction of the gas phase with the GaAs substrate, which results in the formation of GaN.

In order to excite the photoluminescence (PL), we used an ILGI-503 nitrogen laser with an emission wavelength of 337.1 nm and a pulse duration of 10 ns. The PL spectra were analyzed using a computer-controlled MDR-12 monochromator. The samples were mounted in a liquid-helium cryostat at $T = 4.2$ K.

Low-temperature PL spectra of 0.1-μm-thick GaN films on porous GaAs substrates include a low-intensity yellow-region band and a band in the blue region of the spectrum; the latter band is related to radiative recombination within a donor–acceptor pair [7]. The most intense emission is observed in the spectral region that corresponds to free excitons (FE) (the peaks denoted by *A*, *B*, and *C*) and to bound excitons (BE) (see figure). The PL spectrum of a 0.3-μm-thick intrinsic GaN film

1063-7826/03/3711-1264$24.00 © 2003 MAIK "Nauka/Interperiodica"

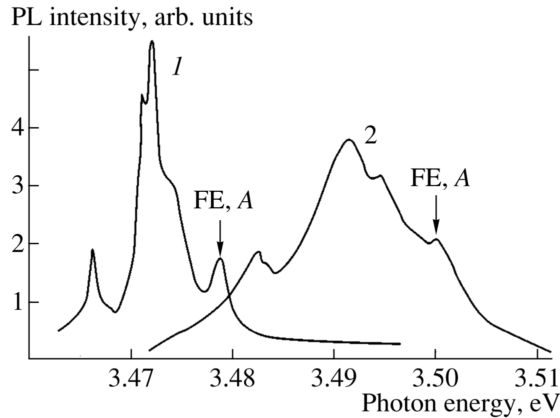

Photoluminescence spectra measured at 4.2 K for (*1*) an 0.3-μm-thick GaN film grown by molecular-beam epitaxy on bulk GaN crystals and (*2*) an 0.1-μm-thick GaN film grown by radical-beam gettering epitaxy on a porous GaAs substrate.

grown by MBE on bulk GaN single crystals is also shown in the figure [8, 9].

A comparison of spectra *1* and *2* in the figure shows that the peaks of excitonic bands of GaN films grown on porous GaAs substrates are shifted to higher energies by 0.02 eV. This shift of PL spectra is attributed to stresses in the films. Studies of angular dependence of X-ray diffraction in the angle range $2\theta = 25°–45°$ [10] revealed a diffraction peak at $2\theta = 34.6°$, which corresponded to reflection from the (0002) plane of the hexagonal GaN phase.

Thus, UV emission caused by recombination that involved the free and bound excitons in the hexagonal phase was observed in GaN films grown by gettering radical-beam epitaxy on porous GaAs(100) substrates; this emission suggests that the films are of high quality. An insignificant shift of excitonic bands to higher energies in the spectrum indicates that there are stresses in the GaN films; however, the magnitude of these stresses is much smaller than those in GaN films grown by radical-beam gettering epitaxy on single-crystal GaAs substrates, in which case excitonic emission was not observed [11].

REFERENCES

1. S. Nakamura, M. Senoh, and T. Mukai, Jpn. J. Appl. Phys. **31**, L139 (1992).
2. U. Kaufmann, M. Kunzer, and M. Maier, Appl. Phys. Lett. **72**, 1326 (1998).
3. B. Monemar, Phys. Rev. B **52**, R17028 (1974).
4. V. V. Mamutin, V. P. Ulin, V. V. Tret'yakov, *et al.*, Pis'ma Zh. Tekh. Fiz. **25** (1), 3 (1999) [Tech. Phys. Lett. **25**, 1 (1999)].
5. A. N. Georgobiani, M. B. Kotlyarevskiĭ, V. V. Kidalov, and L. S. Lepnev, Neorg. Mater. **37**, 1287 (2001).
6. T. V. Bumkhuzi, A. N. Georgobiani, E. Zade-Uly, *et al.*, Tr. Fiz. Inst. im. P.N. Lebedeva, Akad. Nauk SSSR **182**, 140 (1987).
7. A. N. Gruzintsev, U. Kaiser, I. I. Khodos, and W. Richter, Neorg. Mater. **37**, 704 (2001).
8. B. Monemar, W. M. Chen, P. P. Paskov, *et al.*, Phys. Status Solidi B **228**, 489 (2001).
9. H. Teisseyre, G. Nowak, M. Leszczynski, *et al.*, MRS Internet J. Nitride Semicond. Res. **1**, 13 (1996).
10. V. V. Kidalov, G. A. Sukach, A. O. Petukhov, *et al.*, in *Proceedings of International Conference on Luminescence and Optical Spectroscopy of Condensed Matter ICL'02, Budapest* (2002), p. 116.
11. M. B. Kotlyarevskiĭ, G. A. Sukach, V. V. Kidalov, and A. S. Revenko, Zh. Prikl. Spektrosk. **69** (2), 234 (2002).

Translated by A. Spitsyn

Semiconductors, Vol. 37, No. 11, 2003, pp. 1266–1274. Translated from Fizika i Tekhnika Poluprovodnikov, Vol. 37, No. 11, 2003, pp. 1305–1312.
Original Russian Text Copyright © 2003 by Pokrovskiĭ, Khval'kovskiĭ.

Hopping Polarization Photoconductivity of Silicon with the Involvement of Impurity Pairs of Groups III and V

Ya. E. Pokrovskiĭ* and N. A. Khval'kovskiĭ

Institute of Radio Engineering and Electronics, Russian Academy of Sciences, Mokhovaya ul. 11, Moscow, 103907 Russia

**e-mail: yaep@mail.cplire.ru*

Submitted February 11, 2003; accepted for publication March 3, 2003

Abstract—The long-wavelength bands of absorption by the impurity pairs and photoconductivity in the microwave (8 mm) electric field with the impurity pulse photoexcitation are investigated for Si doped by B, Al, Ga, In, P, As, and Sb in concentrations 10^{16}–10^{18} cm^{-3}. The correlation between the pair concentration and the emergence of a slow component of photoconductivity relaxation is ascertained. This component is associated with the polarization hopping photoconductivity that emerges due to the optical recharge of impurity states, namely, the ionization of isolated impurities, impurities in pairs, and dipoles (pairs of the majority and compensating impurity ions). The hopping transfer of ion charges during relaxation is analyzed. It is shown that the main contribution to the polarization photoconductivity at relatively low impurity concentrations is made by hopping transitions in impurity pairs; the contribution of hops with the involvement of isolated ions becomes dominant with increasing concentration. © *2003 MAIK "Nauka/Interperiodica".*

1. INTRODUCTION

It was found [1, 2] that in Si doped by a series of Group III and V impurities in concentrations $N > 10^{16}$ cm^{-3} and at a temperature $T < 20$ K, the slow component of the impurity photoresponse in an electric microwave (MCW) field (8 mm, 36–40 GHz) U_{MCW} manifested itself [3]. The relaxation time, which was estimated from the dependence of photoresponse U_{MCW} on the frequency of the periodic modulation of excitation radiation f (100 Hz–10 MHz) was about 10^{-5} s at 5 K. The relaxation time of the photoresponse in the constant electric field U_{DC} for B, In, and As impurities at 30 K did not exceed 10^{-7} s even for weakly compensated Si samples, and it decreased by two to three orders of magnitude with decreasing temperature and increasing degree of compensation. Identical relaxation times of the U_{MCW} photoresponse and dependences on the temperature and compensation were found for $f > 1$ MHz; i.e., in both cases the process was determined by the cascade trapping of free charge carriers by ionized impurity atoms [4]. At 5 K, the ratio of MCW responses for the quasi-steady ($f \approx 1000$ Hz) and radio-frequency ($f > 1$ MHz) excitation was almost as large as three orders of magnitude [2]. Thus, the slow relaxation of the impurity photoresponse prevailed only in the MCW electric field. Hence, it followed that this phenomenon was associated with the hopping photoconductivity. Here there is a complete analogy with [5], where the hopping conductivity of doped Si is investigated in the alternating electric field. The charge-carrier hops between the neutral and ionized impurities, which are induced by the alternating field, lead to variation in the distances between the ions of the majority and compensating impurity, i.e., to variation in the dipole moments. The conductivity itself is of polarization type and even at low frequencies (as low as 1.6×10^4 Hz) exceeds the percolation conductivity by several orders of magnitude. A similar situation also occurs for the MCW photoconductivity. It was also assumed that the slow relaxation of MCW photoconductivity is associated with the accumulation of charge carriers in long-lived excited 1*s* states of impurities with extended orbitals, optical transitions from which are forbidden in the dipole approximation. This was confirmed by the fact that, in Bi- and Ga-doped Si with $N < 3 \times 10^{16}$ cm^{-3}, the slow relaxation of U_{MCW} did not manifest itself [1, 2]. The Bi, Ga, and Al impurities have high excited states whose energies are close to the energies of optical phonons in Si [6]. Therefore, the captured charge carrier from these higher states can relax rapidly without the involvement of the excited 1*s* states.

A model of MCW polarization photoconductivity with the involvement of long-live excited states developed by Pokrovskii *et al.* [7] is consistent with a number of experimental results [8]. However, certain experiments fundamentally contradict the interpretation proposed. For example, a decrease in the excitation intensity leads to an increase in the relaxation time of U_{MCW} from 10 μs, which was measured in [1, 2], to 500 μs [8]. Such a profound effect of excitation conditions on the intracenter relaxation has not been explained. Further, it was found that the slow relaxation of U_{MCW} also manifested itself in Ga- and Al-doped Si if $N > 5 \times 10^{16}$ cm^{-3}. Finally, the estimations of probability of transitions with the emission of an acoustic phonon demonstrated that the lifetimes of excited 1*s* states in Si are no longer than 10^{-10} s. For these rea-

1063-7826/03/3711-1266$24.00 © 2003 MAIK "Nauka/Interperiodica"

sons, we suggest a new approach to the problem of hopping conduction in doped Si [9].

2. IMPURITY PAIRS

The approach is based on taking account of the role of impurity pairs in hopping transitions in the MCW field. In contrast to fast-diffusing impurities (Li, donors of Group VI) that form close pairs, the impurities of Groups III and V are distributed randomly at the sites of the crystal lattice. In the latter case, there is no clear distinction between the pairs and isolated impurities. However, it is possible to separate the group of impurities that might play the main role in the hopping polarization photoconductivity. Let us explain the situation, starting from the simplest analogue, specifically, the system of two protons and two electrons. This known pattern of single-electron terms of a hydrogen molecule is illustrated in Fig. 1 [10]. Here, the differences in energies between the dashed and solid lines correspond to a decrease in the energies of ionization and excitation of the electron to the 2s state compared with the energies of remote protons. It can be seen that the regions of a noticeable decrease in these energies correspond to relative distances between protons r/a = (2–5), where a is the Bohr radius. Furthermore, the energy of both neutral and ionized "molecules" is lower than that for an isolated atom and a hydrogen ion. This apparent paradox is associated with the fact that this system is not of single-electron type. A similar situation should also occur in the case of impurity pairs in crystals [11], but on different scales of distances and energies, which depend on the magnitude of the Bohr radii of impurities a.

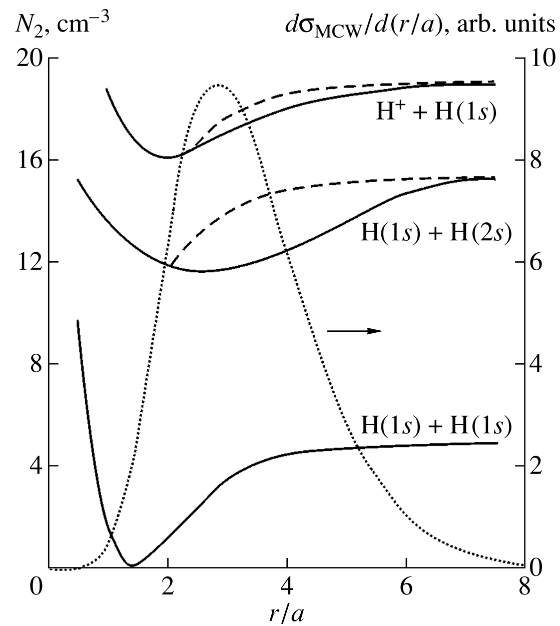

Fig. 1. Single-electron terms of the hydrogen molecule. The differences between the solid and dashed lines correspond to a decrease in energies of ionization and excitation E of single isolated atoms (r/a = 8). The dotted curve is the contribution of the electron transitions between the neutral and ionized atoms to the conductivity σ caused by the MCW electric field (λ = 8 mm) [5].

Figure 1 also shows the dependence of the contribution of charge carrier hops to the polarization conductivity $d\sigma_{MCW}/d(r/a)$ on r/a; this dependence was calculated for the MCW electric field (λ = 8 mm) with a random distribution of impurities [5]. In the calculation, the activation factors, which depend on $\Delta E/2kT$, are omitted. This should not affect the subsequent estimations, since large-scale potential fluctuations in doped Si could not cause significant variation in the ΔE energy for the hops over small distances in pairs. It can be seen that the main contribution to the hopping MCW conductivity is also made by impurity pairs that are localized in the region r/a = (2–5).

Let us estimate the concentration of such pairs. The probability that the impurity has no neighbors at a distance less than r_0 is $\exp(-r_0/r_{av})^3$, where $r_{av} = [(4/3)\pi N]^{-1/3}$ is the average distance between the impurities [12]. Hence, the concentration of impurities N_2, which have a single neighboring impurity at distances less than r_0, is

$$N_2 = N[1 - \exp(-r_0/r_{av})^3] = N[1 - \exp(-v_0 N)], \quad (1)$$

where $v_0 = (4/3)\pi r_0^3$. At $v_0 N \ll 1$, we have $N_2 \approx v_0 N^2$. Such quadratic dependences, which are characteristic of the concentration of pairs with a reduced ionization energy, were found in Si for an In impurity [13] from the temperature dependence of the Hall coefficient and for the P impurity [14] from the dependences of absorption coefficients k for the bands, which are shifted to lower energies relative to the narrow excitation peaks of isolated impurity atoms. Similar quadratic dependences of k on N were found for a number of other impurities of Groups III and V [15]. The broad adsorption spectra for these bands (Fig. 2) are the superposition of the contribution of pairs with different distances between impurities. The structure of such bands is different both for dissimilar impurities and for transitions to different excited states but is independent of the impurity concentration N.

To compare the data of Pokrovskii *et al.* [15] with expression (1), in the spectra in Fig. 2 the regions in which the integrated absorption corresponds to the concentrations N_2 of impurities localized at distances no larger than $r_0 = 5a$ are marked out by hatching. The Bohr radii of impurities a are assumed to be equal to $e^2/2\varepsilon E_i$, where ε = 12 is the relative permittivity and E_i is the ionization energy. The width of the regions is determined from the ratio of their areas to the areas under the narrow absorption peaks with transitions to similar excited states of the same impurities with known low ($N < 10^{15}$ cm^{-3}) concentrations. Such separation of the regions is associated with a certain arbitrariness due to the overlap of the bands during transitions to various excited states. However, this is insignif-

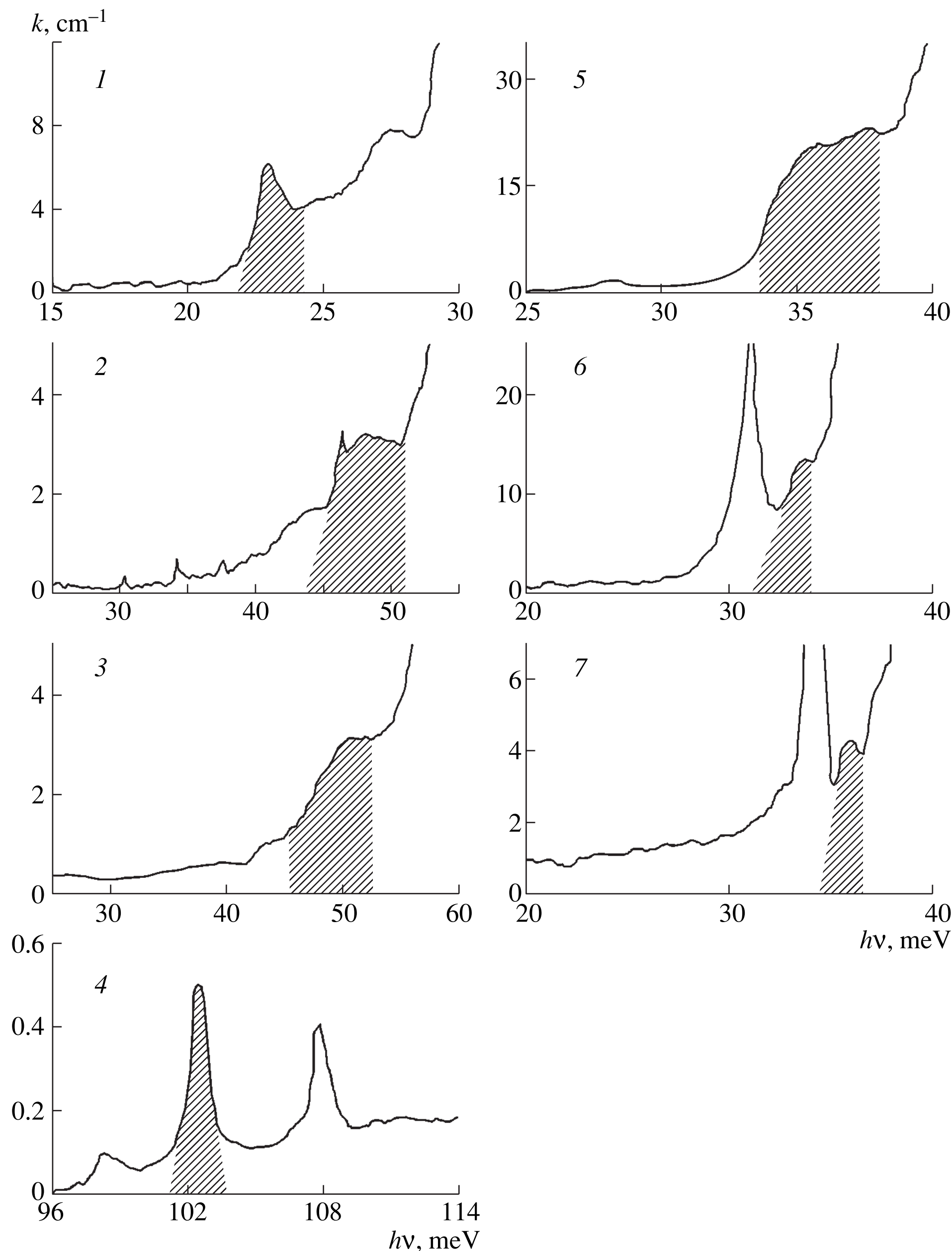

Fig. 2. Spectral dependences of absorption coefficients k for Si doped with impurities with concentrations N = (*1*) 7.6×10^{16} (B), (*2*) 15×10^{17} (Al), (*3*) 16×10^{17} (Ga), (*4*) 40×10^{17} In, [16]), (*5*) 18×10^{16} As), (*6*) 2.6×10^{16} (Sb), and (*7*) 1.5×10^{16} (P) cm^{-3}. The measurement temperature is 4.2 K.

icant for qualitative estimations. The dependences of impurity concentration in the pairs (N_2) on the concentration of the doping impurity (N), which were obtained based on expression (1) [15] and Fig. 2, are shown in Fig. 3. The N dependence of N_2 for an In impurity from [13] and N_2 values estimated from the photoconductivity spectrum [13] and from the absorption spectrum are also shown. It can be seen that the values of N_2, which are determined from various experiments, are consistent. The solid lines are calculated using expression (1) and correspond to the B (a = 1.3 nm) and In (a = 0.38 nm) impurities. Long-wavelength absorption starts to manifest itself at $N v_0 > 10^{-2}$. Thus, the stronger the carrier localization in the ground state of the impurity, the higher the concentrations at which the absorption by the impurity pairs is observed. Moreover, a slow relaxation of U_{MCW} is observed in the same regions of concentrations of different impurities. This is an important indication that impurity pairs are involved in the MCW photoconductivity. Note that in Fig. 3 the values of N_2 for two samples doped with Sb with a concentration of $N = 2.6 \times 10^{16}$ cm^{-3} coincide. These samples

have different concentrations of compensating impurities N_c (1.5×10^{15} and 10^{16} cm^{-3}). Hence, it follows that the compensation does not noticeably reduce the concentration of neutral pairs even if $N_2 < N_c$. This is in agreement with Fig. 1, since the interaction between the impurities leads to a decrease in the pair energy at any value of $r/a > 1$.

3. OPTICAL RECHARGE OF IMPURITY STATES AND THE EXCITATION RELAXATION

Let us consider the situation in n-Si in thermodynamic equilibrium at low temperatures.

When $N \gg N_c$, the pairs of doping impurity are mainly in a neutral state. Since the ions of the compensating impurity are also distributed randomly, their concentration "within" the pairs should be equal to

$$N_c N_2 v_0/2 \ll N_c, N_2,$$

if $N_c \ll N$ and $N_2 \ll N$. This is precisely the reason why the compensation only slightly affects the absorption by impurity pairs. However, the ions of the doping impurity are not distributed randomly. They are localized mainly at minimal distances from compensating ions and form pairs of another type, specifically, the dipoles with the N^{+-} concentration. Thus, under the conditions $T = 5$ K, $N = 10^{16}$ cm^{-3}, and $N_c = 10^{14}$ cm^{-3}, the concentration of ions N^+, which are not involved in the dipoles, does not exceed $0.1N_c$ and decreases with increasing N and N_c; i.e., $N^{+-} \approx N_c$ [4]. At low temperatures, the ions bound into dipoles cannot contribute to the MCW conductivity, since electron hops from more remote impurities to dipoles are possible only with energy absorption.

The excitation causes the random ionization of the majority impurity, whereas the capture of electrons causes optical recharge. These phenomena decrease the N^{+-} and increase the N^+ and N_2^+ concentrations. The electron hops between such ionized and neutral impurities contribute to the MCW photoconductivity. Let us consider the situation of Si excitation by radiation pulses with intensity I and duration Δt; the latter is much longer than the free-carrier lifetime τ_r, but much shorter than the relaxation time of the U_{MCW} photoresponse. In this case, for the time exceeding $\tau_r = 1/\alpha N_c$, the concentration of free carriers $n \approx ISN/\alpha N_c$ will be attained, where S is the cross section of photoionization and α is the trapping coefficient. In reality, the quantity n can change during excitation, since the coefficients of the carrier trapping by ions and dipoles are different [4]. However, this should not affect the subsequent qualitative conclusions, and the recharge process can be described by equations

$$dN^{+-}/dt = ISN - \alpha n N^{+-}, \quad N^{+-} = N_c - N^+ \ll N,$$
$$dN_2^+/dt = IS(N_2 - N_2^+) - \alpha n N_2^+; \tag{2}$$

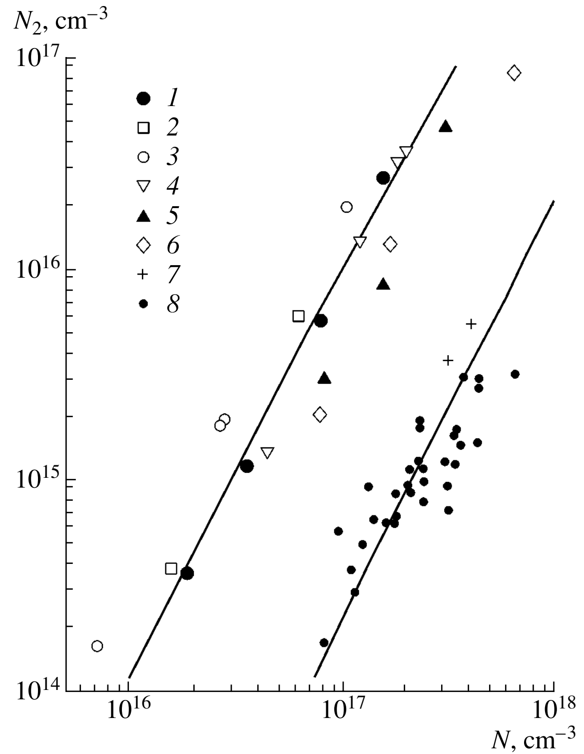

Fig. 3. Dependences of impurity concentrations in the pairs (N_2) on the concentration of the majority impurity (N) in Si doped with (*1*) B, (*2*) P, (*3*) Sb, (*4*) As, (*5*) Al, (*6*) Ga, and (*7*) In obtained from the absorption [16] and photoconductivity [13] measurements, and (*8*) In from the Hall effect [13].

it then follows that

$$N^+ = N/(1 + N/N_c)[1 - \exp(-IS(1 + N/N_c)t)],$$
$$N_2^+ = N_2/(1 + N/N_c)[1 - \exp(-IS(1 + N/N_c)t)], \tag{3}$$

when $N \gg N_c$, the amplitudes of U_{MCW}, which are controlled by the optical recharge of both isolated impurities and impurities in pairs, are proportional to N_c. It also follows from relationships (3) that if more than N_c ionization events occur for time t in the unit volume ($ISNt > N_c$), the limiting optical concentration of impurities is attained. Then, a nonequilibrium steady state will be established in the crystal; i.e.,

$$N^+ \approx N_c; \quad N^{+-} \approx N_c^2/N \ll N_c;$$
$$N_2^+ \approx N_2 N_c/N = v_0 N N_c \ll N_2, N^+. \tag{4}$$

A further increase in intensity should lead only to an increase in the free carrier density rather than to a noticeable variation in the ion concentrations. It can be seen from relationships (4) that only a small fraction of impurities in the pairs is ionized during recharge, and $N_2^+ \ll N^+$. Therefore, the contribution of electron hops involving isolated impurity ions to the U_{MCW} photoresponse should also be taken into account despite the

fact that the hop probability is substantially lower than in the pairs in this case.

Excitation relaxation is possible due to the hopping transitions of charge carriers between the neutral and ionized impurities. The ionized impurity in the pair can be neutralized due to a single hopping transition with energy release at each $r/a > 1$; the neutralization rate should not substantially depend on temperature. However, the probability of the presence of a third impurity at a small and even at a medium distance should decrease with decreasing r/a. Therefore, the charge-relaxation rate for "close" pairs should be substantially slower than for "extended" pairs, and the U_{MCW} relaxation should be nonexponential. A rough estimation of the relaxation rate for the B impurity in the samples investigated by us for the random impurity distribution can be obtained from formula (13a) by Pollak and Geballe [5]. For example, for the smallest possible distance to the nearest impurities $r/a = 5$, the relaxation rate is about 10^7 s^{-1}, whereas for $r/a = 10$ it is about 10 s^{-1}; i.e., the relaxation time can encompass a range of six orders of magnitude. However, the relaxation rate should vary proportionally to Na^3 and should weakly depend on N_2, since the impurities in the pair surroundings are mainly neutral.

The transitions of charge carriers with the involvement of isolated impurity ions with $r/a > 5$ can contribute to the hopping MCW photoconductivity (Fig. 1) until they are bound into dipoles. The localization occurs due to the hopping drift of the charge of isolated ions in the attraction electric field of point charges of the compensating impurity. At $N^+ \approx N^-$, the characteristic time of the charge drift from the average distance R to the nearest ion of the compensating impurity is $\tau_m = \varepsilon R^3/3e\mu = \varepsilon/4\pi e\mu N^+$, where μ is the hopping mobility of the charge. Note that the quantity τ_m is in effect the Maxwell relaxation time of the space charge $\tau_m = \varepsilon/4\pi\sigma$. This quantity is determined by the effective conductivity of the medium $e\mu N^+$. For the limiting optical recharge, the time dependence of the concentration N^+ can be described by the expression

$$N^+ = N_c \exp(-t/\tau_m). \tag{5}$$

The time τ_m itself depends on the concentration of isolated ions N^+. In order to compare with the experiment, it is convenient to transform expression (5) into the form

$$t = -(\varepsilon/4\pi e\mu N_c)(N_c/N^+)\ln(N^+/N_c). \tag{6}$$

The characteristic manifestation of this component of U_{MCW} should be an increase in the relaxation rate both with increasing N_c and with increasing N and T due to an increase in the hopping mobility μ. It should be expected that the hops with the involvement of the N^+ ions will manifest themselves at relatively high concentrations N. As for the lower concentrations, when the relaxation time of the space charge is longer than the period of the pulse excitation, a quasi-steady-state concentration N^+ will be established, and this variable component of U_{MCW} will be undetectable. Thus, the effect of the impurity concentration and temperature on the relaxation of the MCW photoconductivity with the involvement of the pairs and isolated impurities should be substantially different. This allows one to clarify the conditions under which each of these processes prevails.

To clarify this issue, the kinetics of the impurity photoresponse was investigated. The samples of doped Si were placed in the closed end of an 8-mm waveguide [3] and were excited by the radiation pulses of a CO_2 laser (10.6 μm, $h\nu = 117$ meV) with a repetition frequency of about 200 Hz. The photoresponses in the constant U_{DC} and microwave U_{MCW} electric fields were detected by a boxcar integrator with time windows of 0.5 and 5 μs. The pulse duration $\Delta t \approx 0.5$ μs was much longer than the free-carrier lifetime τ_r, but much shorter than the relaxation time of U_{MCW}. The pulse energy at $N_c \le 10^{14}$ cm^{-3} was usually no higher than 10^{-6} J and was sufficient for the saturation of the slow component of the MCW signal. A further increase in intensity caused a rise in the fast component of U_{MCW} only, which repeated the U_{DC} response and was caused by free charge carriers. The fast and slow components of U_{MCW} were of identical polarity, which corresponded to an increase in absorption of the MCW radiation due to increasing sample conductivity with the excitation of charge carriers. To achieve stability of the response and a satisfactory signal-to-noise ratio, it was necessary to tune the MCW system when replacing the samples. Furthermore, the excitation efficiency *ISN* depended on both the concentration and the type of impurities. For these reasons, the amplitudes of U_{MCW} responses for various samples were not compared quantitatively, and only the excitation relaxation was investigated.

In Fig. 4, the time dependences of the U_{MCW} photoresponse for Si doped with a number of Group III and V impurities are shown. It can be seen from Fig. 4 that the response relaxation for all impurities is nonexponential. In addition, the initial relaxation time corresponds to 10–50 μs and increases to 0.5–2.5 ms with increasing detection delay. It should be especially noted that the slow excitation relaxation in Si doped with Al and Ga manifested itself if the concentration of these impurities $N > 5 \times 10^{16}$ cm^{-3}. As was noted above, the Si samples with Ga and Bi in lower concentrations, at which the slow relaxation was not observed, were investigated previously [1, 2]. For In-doped Si, slow U_{MCW} relaxation also manifested itself with the excitation by a CO_2 laser. Photons with an energy of 117 meV can ionize only the impurity pairs with energies of interaction higher than 5 meV (the photoconductivity edge is 112 meV [13]). This confirms the contribution of the pairs of the majority impurity to the hopping pho-

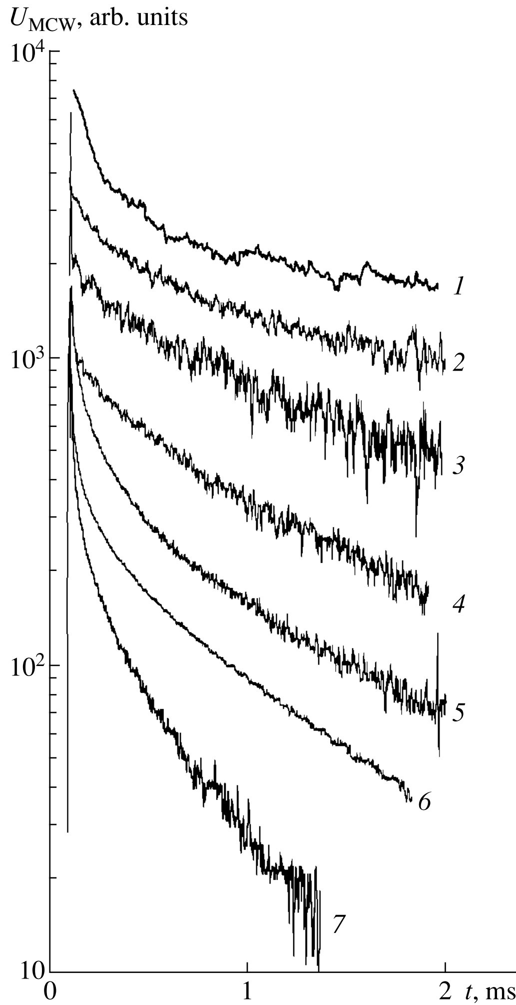

Fig. 4. Time dependences of the U_{MCW} photoresponse for Si doped with impurities with concentrations N = (*1*) 10 (In), (*2*) 2.6 (Sb), (*3*) 6 (Ga), (*4*) 2.4 (B), (*5*) 6 (Al), (*6*) 6 (P), and (*7*) 18 (As) (10^{16} cm^{-3}).

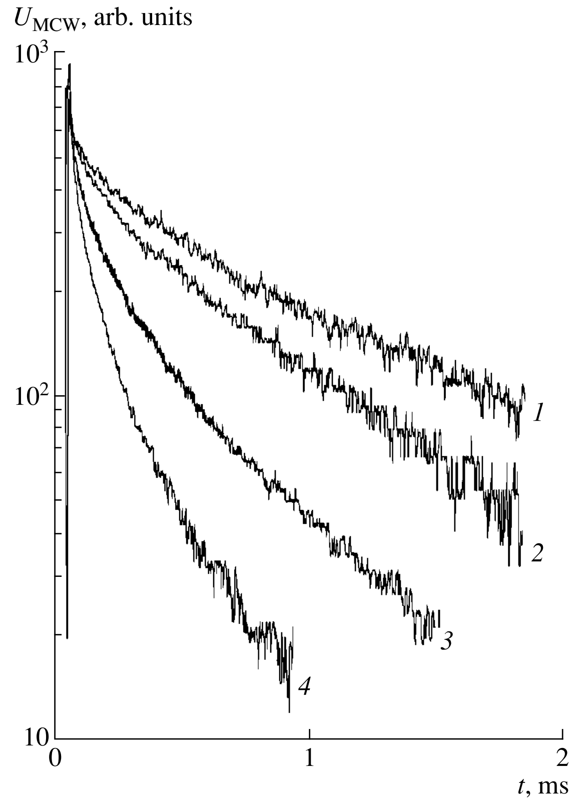

Fig. 5. Time dependences of the U_{MCW} photoresponse for B-doped Si. Concentrations N = (*1*) 1.8, (*2*) 2.4, (*3*) 3.3, and (*4*) 3.95 10^{16} cm^{-3}. $N_c = 10^{14}$ cm^{-3}.

toconductivity. However, the photoresponse with such excitation was too weak, and it could not be investigated reliably. Therefore, the time dependence of response with excitation by a CO_2 laser ($h\nu$ = 250 meV) is shown in Fig. 4 for In-doped Si. This dependence is the same as for other impurities at low concentrations. It can also be seen from Fig. 4 that the relaxation rate depends on the impurity type. For example, at $N = 6 \times 10^{16}$ cm^{-3}, the relaxation rate for Si doped with P, Al, and Ga decreases with increasing Bohr radii of these impurities.

The relaxation time of U_{MCW} also depends on the concentration of the majority impurity N. Figure 5 shows the time dependences of U_{MCW} for Si doped with B in relatively low concentrations. It can be seen that the initial relaxation time varies from 25 μs ($N = 1.8 \times 10^{16}$ cm^{-3}) to 10 μs ($N = 4 \times 10^{16}$ cm^{-3}), and with the detection delay of ~1 ms it varies from 1.2 to 0.5 ms, i.e., decreases approximately as $1/N$. However, at equal N values, the time dependences of U_{MCW} coincided even if the concentrations N_c in the samples differed severalfold. The photoresponse magnitude increases with increasing N_c. This is in agreement with the data in [2], where for a series of B-doped samples with $N = 3.3 \times 10^{16}$ cm^{-3}, which were compensated by P, it was found that at the modulation frequency of 800–1200 Hz of an intense (20–50 mW) excitation, $U_{MCW} \propto N_c$. In such conditions, the responses corresponded to the onset of relaxation, i.e., were approximately proportional to the signal amplitude.

Such simple dependences were observed only at B concentrations $N < 5 \times 10^{16}$ cm^{-3}. At higher concentrations, the slow relaxation component of U_{MCW} manifested itself again (Fig. 6). It can be seen from Fig. 6 that at 4.2 K the time dependences of U_{MCW} at $t >$ 0.5 ms are similar, although the N and N_c concentrations in the samples differ greatly. However, when the temperature was increased to 10.5 K, the relaxation rate at $N = 2.4 \times 10^{16}$ cm^{-3} did not change, whereas at $N = 5.5 \times 10^{16}$ cm^{-3} it increased appreciably. It follows then that, at relatively low B concentrations, the hopping transitions between the close pairs of the majority impurity make the main contribution to the polarization photoconductivity (Fig. 5), whereas the slow relaxation

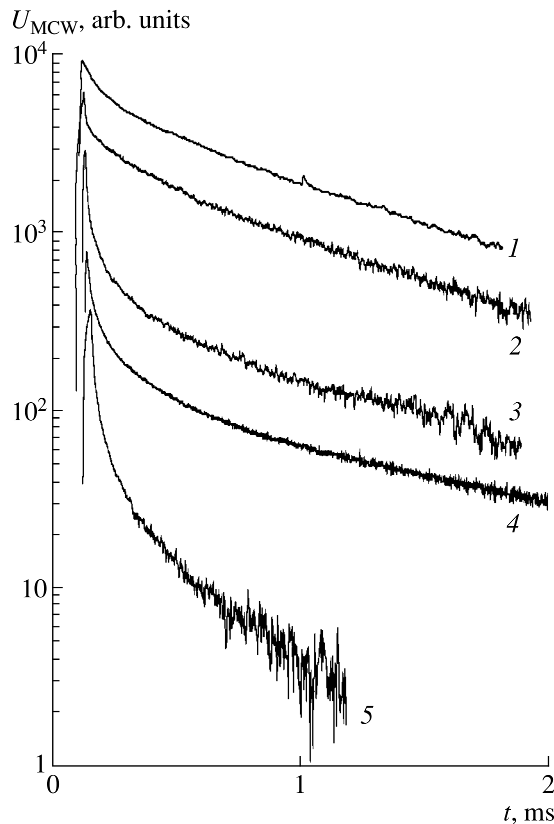

Fig. 6. Time dependences of the U_{MCW} photoresponse for B- and P-doped Si. Concentrations N = (*1*, *2*) 2.4, (*3*) 11.5 × 10^{16} cm^{-3}. N_c = (*1–3*) 0.1, (*4*), (*5*) 5 × 10^{15} cm^{-3}. T = (*1*, *3*, *4*) 4.2; (*2*, *5*) 10.5 K.

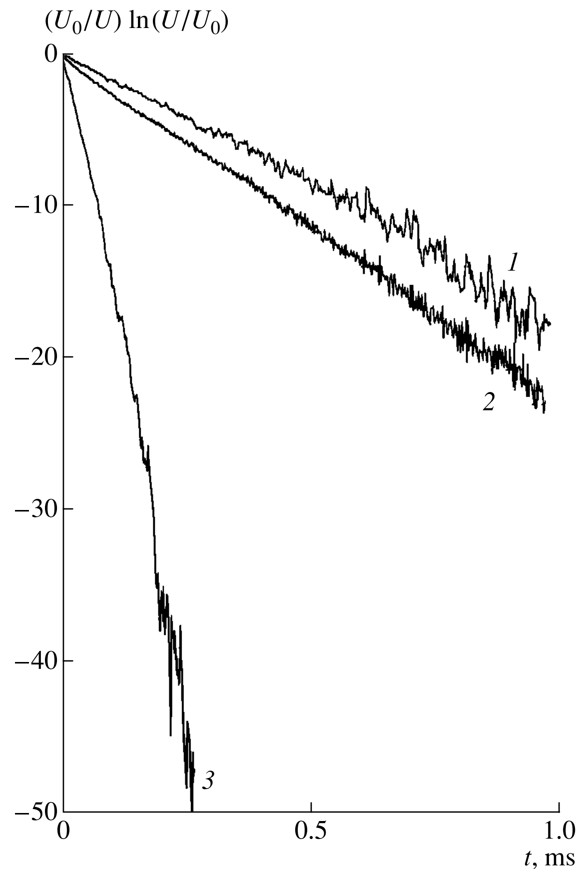

Fig. 7. Time dependences of the MCW photoresponse function $(U_0/U)\ln(U/U_0)$ for B- and P-doped Si. Concentrations N = (*1*) 11.5, (*2*) 5.5, and (*3*) 5.5 × 10^{16} cm^{-3}. N_c = (*1*) 0.1 and (*2*, *3*) 5 × 10^{15} cm^{-3}. T = (*1*, *2*) 4.2 and (*3*) 10.5 K.

of U_{MCW}, which is associated with the contribution of isolated ions to the photoconductivity, manifests itself with increasing N. In this case, the time dependence of $U_{MCW} \propto N^+$ should be described by Eq. (6).

Figure 7 shows the time dependences of U_{MCW} for two samples. According to expression (6), these dependences are given by

$$[U(0)/U(t)]\ln[U(t)/U(0)] = t. \qquad (7)$$

It can be seen that the experimental points fall well on the straight lines according to formula (7). Hence, it follows that the mobility μ is independent of time and has the usual physical meaning. The slope of the straight lines should correspond to the value of $\varepsilon/4\pi e\mu N_c$. It follows from Fig. 7 that, for the sample with concentrations $N = 5.5 \times 10^{16}$ and $N_c = 5 \times 10^{15}$ cm^{-3} at T = 4.2 K, $\sigma(0) = 2.4 \times 10^{-8}$ Ω^{-1} cm^{-1}, and $\sigma(0) = 2 \times 10^{-7}$ Ω^{-1} cm^{-1} at T = 10.5 K. Accordingly, hopping mobilities μ are equal to 3×10^{-5} and 2×10^{-4} cm^2/(V s). For the sample with $N = 1.15 \times 10^{17}$ and $N_c = 10^{14}$ cm^{-3} at 4.2 K, $\sigma(0) = 2 \times 10^{-8}$ Ω^{-1} cm^{-1} and $\mu = 1.25 \times 10^{-3}$ cm^2/(V s). These results confirm the contribution of hopping transitions of isolated N^+ ions to the polarization photoconductivity. However, the absolute values of hopping conductivity in a constant electric field estimated by us were several orders of magnitude larger than the typical values of doped Si in thermodynamic equilibrium. Furthermore, the conductivity of the sample with $N = 5.5 \times 10^{16}$ cm^{-3} increases with increasing temperature from 4.2 to 10.5 K only by an order of magnitude, whereas with the activation energy E_3 = 4.3 meV, which corresponds to this concentration, an increase in σ by a factor of approximately 250 should be expected (see [17, 18] and the references therein). Such a discrepancy is to be expected for two reasons. First, at low temperatures in the absence of excitation, most ions of the majority impurity are bound into dipoles [4], which do not contribute to the hopping conductivity. Second, a drift of the charge of the majority-impurity ions occurs due to several hops in the quantum well over the states of impurities with the energies decreasing as the ions of the compensating impurity are approached. Such a charge transfer is not of the activation type, and its rate might not depend on temperature at all. It is possible that the temperature dependence observed is associated with the thermal

ionization of dipoles at 10.5 K [4], which leads to an increase in both the equilibrium concentration N^+ and the relaxation rate. This behavior undoubtedly takes place for the heavily doped and lightly compensated sample ($N = 1.15 \times 10^{17}$, $N_c = 10^{14}$ cm^{-3}), for which only an initial fast decay of U_{MCW} manifested itself at 10.5 K and only a noise plateau was observed with increasing delay. Thus, the hopping conductivity in a constant electric field of the point charges, which determines the relaxation rate of microwave photoconductivity, fundamentally differs from the percolation hopping conductivity in an external electric field. For the magnitudes of conductivity determined from Fig. 7, the slow component of photoconductivity relaxation in a constant electric field can be easily detected even at 4.2 K. However, even at elevated temperatures and with a sufficiently sensitive method of detection (a signal-to-noise ratio of ~10^3), we failed to separate such a component of U_{DC}. A detailed discussion of the temperature and concentration dependences of polarization photoconductivity seems to be premature because of the lack of experimental data.

4. CONCLUSION

A new explanation of the physical nature of polarization hopping photoconductivity of doped Si in an MCW electric field is suggested. This explanation is based on consideration of the optical recharge of various states of Group III and V impurities, namely, isolated ions, pairs of the majority impurity atoms, and impurity dipoles (pairs of the majority and compensating impurities). From the spectra of absorption bands, the concentrations N_2 of the impurity pairs in Si doped with B, Al, Ga, In, P, As, and Sb in concentrations $N = 10^{16}$–10^{18} cm^{-3} are estimated. It is found that these bands manifest themselves if $N_2 > 10^{-2}N$. The smaller the Bohr radius a of the ground state of impurities, the higher the concentration at which the long-wavelength absorption manifests itself. It is shown that the slow relaxation of the MCW photoconductivity and the long-wavelength absorption by the impurity pairs emerge in the same concentration ranges. The kinetics of relaxation of MCW photoconductivity is investigated using short-pulse excitation. It is found that the relaxation is nonexponential, and its rate increases with increasing N and a but depends only slightly on temperature. For B impurity, it is shown that these trends are observed at $N < 5 \times 10^{16}$ cm^{-3}, whereas the slower relaxation of MCW photoconductivity emerges again at higher concentrations. The rate of this relaxation increases with increasing temperature. Simple equations that allow one to explain the main experimental results are suggested.

The photoexcitation of a semiconductor causes the random ionization of impurities, and the capture of the carriers causes the optical recharge of the impurity states. The concentration of dipoles N^{+-}, in which the ions of the majority and compensating impurity were bound prior to excitation, decreases, whereas the concentration of ionized impurities in the N_2 pairs and isolated ions N^+ increases. These ions are involved in hopping transport and contribute to the MCW photoconductivity. As the intensity of optical excitation increases, the maximum optical recharge is attained, at which the slow component of MCW photoconductivity is saturated. Recharge relaxation occurs due to the hopping transport of charge carriers. One hop is sufficient to neutralize the ionized pairs, and this fast relaxation of photoconductivity prevails at low N concentrations. The isolated ions are involved in photoconductivity until they are bound into the dipoles; the latter do not contribute to photoconductivity, due to the hopping charge drift in the attraction field of the ions of the compensating impurity. The process rate in this case is determined by the relaxation time of the charge, which depends heavily on the concentrations of the majority and compensating impurities. Thus, the MCW photoconductivity with the involvement of isolated ions manifests itself at high N and a considerable degree of compensation. Drift occurs in quantum wells that are generated by the ion of the compensating impurity and is not associated with the percolation. The magnitudes of conductivity that determine the drift velocity of ion charges are estimated. These magnitudes are larger by several orders of magnitude than those of the well-understood percolation conductivity in Si with almost the same impurity composition.

ACKNOWLEDGMENTS

This study was supported by the Russian Foundation for Basic Research, project no. 02-2-16272.

REFERENCES

1. Ya. E. Pokrovskiĭ and O. I. Smirnova, Pis'ma Zh. Éksp. Teor. Fiz. **51**, 377 (1990) [JETP Lett. **51**, 429 (1990)].
2. Ya. E. Pokrovskiĭ and O. I. Smirnova, Mater. Sci. Forum **65–67**, 271 (1990).
3. I. V. Altukhov, Ya. E. Pokrovskiĭ, O. I. Smirnova, *et al.*, Fiz. Tekh. Poluprovodn. (Leningrad) **24**, 1134 (1990) [Sov. Phys. Semicond. **24**, 717 (1990)].
4. V. N. Abakumov, V. I. Perel', and I. N. Yassievich, *Nonradiative Recombination in Semiconductors* (Peterb. Inst. Yad. Fiz. Ross. Akad. Nauk, St. Petersburg, 1997).
5. M. Pollak and T. M. Geballe, Phys. Rev. **122**, 1724 (1961).
6. A. K. Ramdas and S. Rodrigues, Rep. Prog. Phys. **44**, 1278 (1981).
7. Ya. E. Pokrovskiĭ and O. I. Smirnova, Zh. Éksp. Teor. Fiz. **103**, 1411 (1993) [JETP **76**, 690 (1993)].
8. Ya. E. Pokrovskiĭ and O. I. Smirnova, Zh. Éksp. Teor. Fiz. **102**, 660 (1992) [Sov. Phys. JETP **75**, 353 (1992)].

9. Ya. E. Pokrovskiĭ and N. A. Khvalkovskiĭ, Phys. Status Solidi C, No. 2, 707 (2003).
10. *Tables of Physical Data: Reference Book*, Ed. by I. K. Kikoin (Atomizdat, Moscow, 1976).
11. Sh. M. Kogan and A. F. Polupanov, Inst. Phys. Conf. Ser., No. 95, 527 (1988).
12. L. B. Lopatin and Ya. E. Pokrovskiĭ, Zh. Éksp. Teor. Fiz. **87**, 1381 (1984) [Sov. Phys. JETP **60**, 793 (1984)].
13. B. Baron, M. H. Young, J. K. Neeland, and O. J. Marsh, Appl. Phys. Lett. **30**, 694 (1977).
14. G. A. Thomas, M. Capizzi, F. DeRosa, *et al.*, Phys. Rev. B **23**, 5472 (1981).
15. Ya. E. Pokrovskiĭ, O. I. Smirnova, and N. F. Khval'kovskiĭ, Zh. Éksp. Teor. Fiz. **122**, 97 (2002) [JETP **95**, 83 (2002)].
16. W. Scott, Appl. Phys. Lett. **32**, 540 (1978).
17. B. I. Shklovskiĭ and A. L. Éfros, *Electronic Properties of Doped Semiconductors* (Nauka, Moscow, 1979; Springer, New York, 1984).
18. R. K. Ray and H. Y. Fan, Phys. Rev. **121**, 768 (1961).

Translated by N. Korovin

Semiconductors, Vol. 37, No. 11, 2003, pp. 1275–1277. Translated from Fizika i Tekhnika Poluprovodnikov, Vol. 37, No. 11, 2003, pp. 1313–1315.
Original Russian Text Copyright © 2003 by Yakovyna, Zayachuk, Berchenko.

Defect Formation in PbTe under the Action of a Laser Shock Wave

V. S. Yakovyna*, D. M. Zayachuk*, and N. N. Berchenko**

**Lviv Polytechnical National University, Lviv, 79013 Ukraine*
e-mail: yakovyna@polynet.lviv.ua
***Rzeszow University, Rzeszow, 35310 Poland*
Submitted November 18, 2002; accepted for publication March 7, 2003

Abstract—Mechanisms of the defect formation in PbTe thin films on BaF_2 substrates under shock-wave action are studied, and the kinetics of the annealing of the resulting nonequilibrium crystal defects at room temperature is analyzed. The respective roles of the first- and second-order annealing reactions in settling of the equilibrium state of the defects are estimated. The contributions of Frenkel pair annihilation in both sublattices and migration of interstitials to sinks to a change in the total concentration of nonequilibrium defects at different stages of annealing are considered. © *2003 MAIK "Nauka/Interperiodica".*

INTRODUCTION

The interaction of laser radiation with semiconductor materials has aroused considerable interest due to the opening of possibilities for the laser modification and, in sight of this, laser control of the properties of both monoatomic and more complex systems. One effect induced in a solid subjected to pulsed laser radiation is the generation of an intense compression pulse, i.e., an acoustic wave, which may turn into a shock wave under certain conditions [1, 2].

The influence of laser-induced shock waves (LSWs) on the properties of different materials have been widely investigated during the past two decades [2–8]. These studies are motivated by high technological efficiency and convenience of handling LSWs and the possibility of wide-range variation of their parameters by changing the characteristics of pulsed laser radiation.

By the example of HgCdTe solid solutions, we have previously shown that the efficiency of the defect formation under the action of LSWs grows with an increase in the concentration of defects in the initial sample [8]. The residual changes in the electrical properties of semiconductors turned out to be fairly small. This fact may be attributed to either the low stability of the LSW-induced primary defects or the low efficiency of their production. In order to clarify this point, we have carried out similar experiments with a binary IV–VI compound PbTe in this study. Smaller self-diffusion coefficients of host atoms in IV–VI compounds as compared to those in II–VI materials allow us to trace the dynamics of the LSW-induced defect formation [9] and to reveal the general aspects of LSW action on different types of semiconductors with a high concentration of intrinsic point defects.

EXPERIMENTAL

We used both *n*- and *p*-type PbTe samples grown by flash evaporation and deposition on freshly cleaved BaF_2 (111) surfaces. The samples of *n*-type BaF_2 were grown from an undoped charge; the *p*-type samples were obtained from a thallium-doped charge. The free-carrier concentration at room temperature in *n*- and *p*-type samples was about 7×10^{16} and 3.5×10^{17} cm^{-3}, respectively; their mobility was about 1×10^3 and 150 cm^2 V^{-1} s^{-1}, respectively.

The electrical properties of samples before and after exposure to shock-wave action, as well as after the annealing at room temperature, were estimated from the measurements of the electric conductivity and the Hall effect with the magnetic field varying in the range 0.1–1.6 T.

LSWs were produced at room temperature by a GOS-1001 pulsed neodymium-glass laser with a LiF Q-switch (1.06 μm wavelength and 30 ns pulse width). To avoid the direct action of radiation on a semiconductor sample, we covered it with 100-μm-thick copper foil. The treatment was performed in such a way as to provide for the generation of a LSW in the foil and to avoid its attenuation at the interfaces by matching the shock impedances of the media according to the technique described in detail in [10]. A typical value of pressure at the LSW front was 0.6 GPa.

RESULTS AND DISCUSSION

LSW treatment of both the *n*- and *p*-type film samples of PbTe changes the concentration of charge carriers by the same value of $\sim 2 \times 10^{16}$ cm^{-3}. For *n*-type films, the carrier concentration increases; i.e., the nonstoichiometry of the film composition grows. In contrast, the carrier concentration in *p*-type films decreases

1063-7826/03/3711-1275$24.00 © 2003 MAIK "Nauka/Interperiodica"

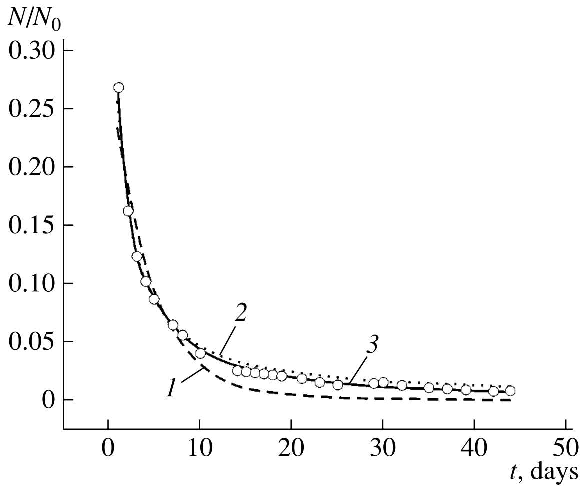

Fig. 1. Time dependence of the nonequilibrium electron concentration in an *n*-PbTe sample annealed in air at 300 K. Circles show the experimental data; curves are calculated in terms of (*1*) the first- and (*2*) the second-order annealing reactions and (*3*) the linear combination of both reactions.

by the value specified above and the film composition comes closer to stoichiometry.

The oppositely directed changes in the carrier concentration in *n*- and *p*-type PbTe films and the resulting different character of changes in their composition lead also to differences in the subsequent annealing of LSW-induced crystal defects, which are responsible for the presence of free carriers. As the *n*-type samples are held in air at room temperature, the electron concentration decreases with time *t* towards the initial value but does not reach it. This relaxation process is illustrated by Fig. 1. However, in the *p*-type samples exposed to an LSW, no relaxation of free carrier concentration is observed. Note that the mobility of charge carriers in both the *n*- and the *p*-type samples remained nearly constant throughout the shock treatment.

It would appear reasonable to attribute the observed variations in the free-carrier concentration with the changes in the concentration of intrinsic point defects in the crystal lattice of films subjected to the action of an LSW. According to the modern concepts, vacancies in the metal and halcogen sublattices are doubly charged acceptors and doubly ionized donors, respectively. Interstitial lead ions are singly or doubly charged donors. Interstitial tellurium is, most likely, electrically neutral [11]. Therefore, generation of Frenkel pairs consisting of lead ions and vacancies must either cause no change in the free-carrier concentration in PbTe or increase the hole concentration, which was not observed experimentally. In contrast, the appearance of Frenkel pairs involving tellurium must increase the free-electron concentration in PbTe, which correlates with the observed changes in the carrier concentration for both the *n*- and the *p*-type samples subjected to the action of an LSW.

In the general form, the kinetic equation for the annealing of nonequilibrium defects can be written as [12]

$$\frac{dN}{dt} = -KN^{\alpha}, \quad (1)$$

where N is the concentration of nonequilibrium defects, t is time, K is a constant, and the parameter α is the so-called order of reaction. The first-order annealing reaction ($\alpha = 1$) corresponds to capture of defects by different traps, while the second-order reaction ($\alpha = 2$) describes the direct recombination of different randomly distributed defects. In these two cases, the solution to Eq. (1) has the form

$$N(t) = N_0 \exp(-K_1 t) \quad (2)$$

and

$$N(t) = \frac{N_0}{1 + N_0 K_2 t}, \quad (3)$$

respectively, where $N_0 \equiv N(0)$.

Figure 1 shows the curves calculated by the least-squares method to describe the kinetics of the first- and the second-order annealing. It can be seen that neither of the reactions taken separately describes adequately the actual relaxation of nonequilibrium defects. Agreement between the calculated and experimental dependences $N(t)$ can be significantly improved by using a linear combination of the kinetic expressions for the first- and the second-order annealing reactions:

$$\frac{N}{N_0} = A_1 \exp(-K_1 t) + \frac{A_2}{1 + K_2 t}. \quad (4)$$

For the case shown in Fig. 1, the closest correlation between the calculated and the experimental data is obtained for the following values: $A_1 = 0.058$, $A_2 = 1.02$, $K_1 = 0.127$ day^{-1}, and $K_2 = 3.7$ day^{-1} (Fig. 2, curve *3*). Curves *1* and *2* in Fig. 2 illustrate the partial contributions of the first- and the second-order reactions to the total annealing with the above parameters.

As is evident from Fig. 2, the initial stages of annealing are governed mainly by the exponential component (Fig. 2, curve *1*), which is related to the migration of interstitials to sinks. In particular, the film surface or the film–substrate interface may serve as such sinks. In the following stages, the role of the second-order reaction increases: the mutual recombination of point defects be comes noticeable.

In view of the above discussion, the recombination of Frenkel pairs involving lead ions most likely has no effect on the resulting concentration of free carriers; otherwise, free-electron concentration should increase, which lacks experimental support. Unlike this behavior, the recombination of tellurium-containing pairs decreases the donor concentration and, consequently, the concentration of free electrons.

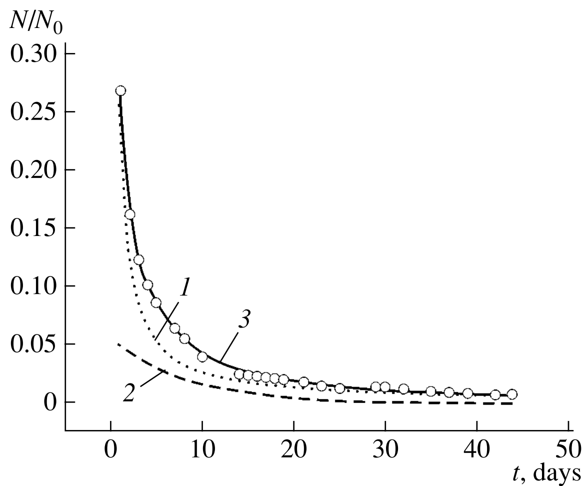

Fig. 2. Partial contributions of (*1*) the first- and (*2*) the second-order reactions to the total annealing (curve (*3*)) of an *n*-PbTe sample at 300 K Circles show the experimental data.

Apparently, changes in the free-carrier concentration in the latest annealing stages results from the fact that the interstitial lead emerges at the film surface, which is equivalent to a decrease in the concentration of donor centers in the bulk. Undoubtedly, the interstitial tellurium also migrates to the surface; however, this process does not change the concentration of electrically active centers in the film bulk. Furthermore, the coefficient of self-diffusion of tellurium is lower by several orders of magnitude than that of lead (8×10^{-19} cm^2/s against 2×10^{-15} cm^2/s at room temperature [9]), which makes the migration of defects in the tellurium sublattice unlikely.

CONCLUSION

As a result of the action of a laser-induced shock wave on lead telluride, the generation of Frenkel pairs occurs in both the metal and the halcogen sublattices. Due to the specific features of the electrical activity of point defects in PbTe, the concentration of free carriers increases in *n*-type films and drops in *p*-type films.

The decrease in the excess concentration of free electrons with time is controlled by the annihilation of Frenkel pairs containing tellurium ions (this process predominates in the initial stage of the annealing of nonequilibrium defects at room temperature) and by the migration of interstitial lead to the sinks (which prevails in the later stage of annealing).

REFERENCES

1. V. A. Yanushkevich, Fiz. Khim. Obrab. Mater., No. 5, 9 (1975).
2. L. I. Ivanov, N. A. Litvinova, and V. A. Yanushkevich, Kvantovaya Élektron. (Moscow) **4**, 204 (1977).
3. P. Peyre, P. Merrien, H. P. Lieurade, and R. Fabbro, Surf. Eng. **11**, 47 (1995).
4. M. V. Sil'nikov, A. I. Mikhaĭlin, A. V. Petrov, *et al.*, Pis'ma Zh. Tekh. Fiz. **26** (16), 77 (2000) [Tech. Phys. Lett. **26**, 734 (2000)].
5. Y. K. Zhang, C. L. Hu, L. Cai, *et al.*, Appl. Phys. A **72**, 113 (2001).
6. V. A. Gnatyuk, A. I. Vlasenko, P. O. Mozol', and O. S. Gorodnychenko, Semicond. Sci. Technol. **13**, 1298 (1998).
7. A. Baĭdullaeva, A. I. Vlasenko, B. L. Gorkovenko, *et al.*, Fiz. Tekh. Poluprovodn. (St. Petersburg) **34**, 443 (2000) [Semiconductors **34**, 429 (2000)].
8. N. N. Berchenko, V. S. Yakovyna, Yu. N. Nikiforov, and I. S. Virt, Proc. SPIE **4355**, 200 (2001).
9. Yu. I. Ravich, B. A. Efimova, and I. A. Smirnov, *Semiconducting Lead Chalcogenides* (Nauka, Moscow, 1968; Plenum, New York, 1970).
10. Y. Nikiforov, V. Yakovyna, and N. Berchenko, Mater. Sci. Eng. A **288**, 173 (2000).
11. D. M. Zayachuk and V. A. Shenderovs'kiĭ, Ukr. Fiz. Zh. **36**, 1692 (1991).
12. J. Bourgoin and M. Lannoo, *Point Defects in Semiconductors* (Springer, New York, 1983; Mir, Moscow, 1985).

Translated by A. Sidorova

Semiconductors, Vol. 37, No. 11, 2003, pp. 1278–1282. Translated from Fizika i Tekhnika Poluprovodnikov, Vol. 37, No. 11, 2003, pp. 1316–1320.
Original Russian Text Copyright © 2003 by Kar'kin, Shchennikov, Danilov, Arbuzov, Goshchitskiĭ.

ELECTRONIC AND OPTICAL PROPERTIES OF SEMICONDUCTORS

Galvanomagnetic Effects in Atomic-Disordered $HgSe_{1-x}S_x$ Compounds

A. E. Kar'kin, V. V. Shchennikov, S. E. Danilov, V. A. Arbuzov, and B. N. Goshchitskiĭ*

Institute of Metal Physics, Ural Division, Russian Academy of Sciences, Yekaterinburg, 620219 Russia

**e-mail: bng@imp.uran.ru*

Submitted December 16, 2002; accepted for publication February 25, 2003

Abstract—In HgSe and $HgSe_{1-x}S_x$ single crystals irradiated with electrons of 5 MeV energy at 270 K, resistivity and the Hall effect have been studied in the temperature range 1.7–370 K in magnetic field up to 13.6 T. Changes in the carrier density and mobility upon generation of radiation-induced defects and subsequent isochronous annealings have been determined. The irradiation made it possible to reduce the electron density to a greater extent than do conventional methods, as well as to restore the initial value by annealing. © *2003 MAIK "Nauka/Interperiodica".*

1. INTRODUCTION

The introduction of atomic-size radiation-induced defects into ordered crystals (radiation disordering) represents one of the methods of studying the fundamental properties of the solid state [1]. The study of the crystal response to this impact, in which the stoichiometric composition is retained, opens ways of revealing specific features of the electron and phonon subsystems defining the crystal properties, including those in the initial ordered state [2–4]. An indubitable virtue of the method is the possibility of introducing defects of different kinds, dependending on the irradiation type and temperature, with smooth variation of the defect concentration. The annealing of irradiated samples provides complete reversibility of the process; i.e., it allows multiple restoration of any intermediate state or the initial state in one and the same sample.

The role of atomic disordering in the formation of electron states in narrow-gap semiconductors was investigated in [4, 5]. It has been shown that radiation defects, which arise under irradiation with electrons having an energy of 1–5 MeV, can induce the conduction conversion from *n*- to *p*-type. Irradiation with high-energy particles usually results in the formation of deep levels in the semiconductor energy gap or in the allowed bands [4, 5]. The presence of these levels accounts for the observed changes in the carrier density and mobility, Hall sign reversal upon irradiation of semiconductors with different doses [4] or annealing at fixed dose [5], and semiconductor–metal transitions occurring in these cases [4, 5].

Mercury selenide and HgSeS substitutional solid solutions are semimetals (zero-gap semiconductors), in which the high density of electrons is due to the overlapping of the conduction and valence bands [6–9]. However, the origin of the band responsible for "impurity" electrons in HgSe, as well as in other mercury chalcogenides with sphalerite structure (HgTe, HgS), still has no unambiguous explanation [7]. In fact, in the majority of models, the overlapping of electron bands is somehow associated with the crystal structure defects. In ternary compounds, the content of the third component is an additional parameter for the variation of the semiconductor properties. In a HgSe–S system, the substitution of S for Se enhances the semimetallic properties, since the band overlapping is enhanced [9].

Due to overlapping, conventional methods allow only limited variation of the electron density. For example, the annealing in mercury vapor for 500 h at 300°C temperature raises the electron density to 3×10^{18} cm^{-3}, and annealing in Se vapor for 500 h at 220°C reduces it to 4×10^{17} cm^{-3} [10]. However, attempts to reduce the electron density below the minimum value of ~10^{17} cm^{-3} and obtain, e.g., *p*-HgSe by deviation from the stoichiometry or even by doping, have failed [9, 10]. The electron density in cubic HgSe is never lower than ~10^{18} cm^{-3}, either [9]. Since irradiation by high-energy particles is the most efficient method of direct impact on the defect structure in semiconductor crystals, the present study is devoted to the effect of electron irradiation on the electrical properties of ternary HgSeS crystals, with the goal of investigating the possibility of efficiently controlling the carrier parameters. Substitutions in the anion and cation sublattices, hydrostatic pressure, and electron irradiation are complementary methods for modifying the electronic structure.

2. SAMPLES AND EXPERIMENTAL METHODS

On the whole, the measurement procedure was the same as in [5]. Galvanomagnetic effects in $HgSe_{1-x}S_x$ single crystals ($x = 0$, 0.104, and 0.508) were measured in the temperature range 1.7–380 K in a static magnetic field up to 13.6 T. The composition of samples was determined by X-ray fluorescence microanalysis on a

1063-7826/03/3711-1278$24.00 © 2003 MAIK "Nauka/Interperiodica"

Superprobe-JCXA-733 instrument. Electrical contacts no more than ~50×50 μm^2 in size were fabricated by ultrasonic soldering with an In–Ga eutectic. The Hall factor was measured on samples ~$1 \times 2 \times 0.2$ mm^3 in size with four symmetrical contacts in the Montgomery configuration [5]. The measurements were performed on an Oxford Instruments device [5]. The samples were irradiated in the accelerator channel with 5 MeV electrons, under cooling with purified He gas to a temperature below 270 K. After irradiation, the samples were transferred to the measurement chamber without warming to above 290 K. Isochronous annealing of samples for 20 min at temperatures up to 390 K was performed in a helium atmosphere, to avoid mercury loss. The irradiation and annealing modes were chosen in the same way as in similar studies of the narrow-gap Bi_2Te_3 semiconductor [5].

3. RESULTS

Figures 1 and 2 show temperature dependences of the Hall factor R_H and resistivity ρ of the studied samples in the initial state after the irradiation and after subsequent annealings. Before irradiation, only a weak temperature dependence of R_H measured in a magnetic field of 12 T was observed for $HgSe_{1-x}S_x$ samples of all the compositions. The temperature dependence of resistivity was fairly well described by a second-order polynomial. At a fixed temperature of $T = 4.2$ K, the $R_H(B)$ curves for the initial samples exhibited weak dependence on magnetic field B (Figs. 3 and 4), which indicates the predominant contribution to the conduction made by electrons of a single band. Earlier [11], the Shubnikov–de Haas oscillations were studied in the same HgSeS crystals, and the density and mobility of the conduction electrons were determined in terms of a single-band model.

The irradiation of HgSe crystal with electrons raised the resistivity (especially in the low-temperature range, Fig. 1b), and a strong dependence on magnetic field B appeared in the Hall factor (Fig. 3). In weak fields B at $T = 4.2$ K, the Hall factor increased in magnitude; on the contrary, in high fields, it decreased by nearly a factor of 2 (Fig. 3). The irradiation of $HgSe_{0.9}S_{0.1}$ sample with the same dose gave opposite results: a decrease in resistivity and increase in the magnitude of the Hall factor, both in weak and strong fields (Figs. 2b, 4). Usually, a strong dependence of R_H on magnetic filed indicates a contribution from the second type of carriers to conduction. In the case in question, these carriers can be called "heavy electrons," since their mobility μ is considerably lower than the electron mobility in the initial crystals, as shown below. Weak dependences of R_H on magnetic field were observed in the $HgSe_{0.5}S_{0.5}$ sample (not shown in the figure).

In annealings of an irradiated HgSe crystal, the high-field Hall factor, which is defined by the total electron density, grows in magnitude with increasing annealing temperature T_{ann} and approaches its value in the initial sample (Fig. 1a). The resistivity increases after annealing, as occurs under irradiation, and it decreases only after annealing at a maximum temperature of $T_{ann} = 390$ K (Fig. 1b). For the intermediate annealing temperature, the Hall factor in weak magnetic field strongly increases in magnitude, which usually indicates the two-band conduction mode (Fig. 3).

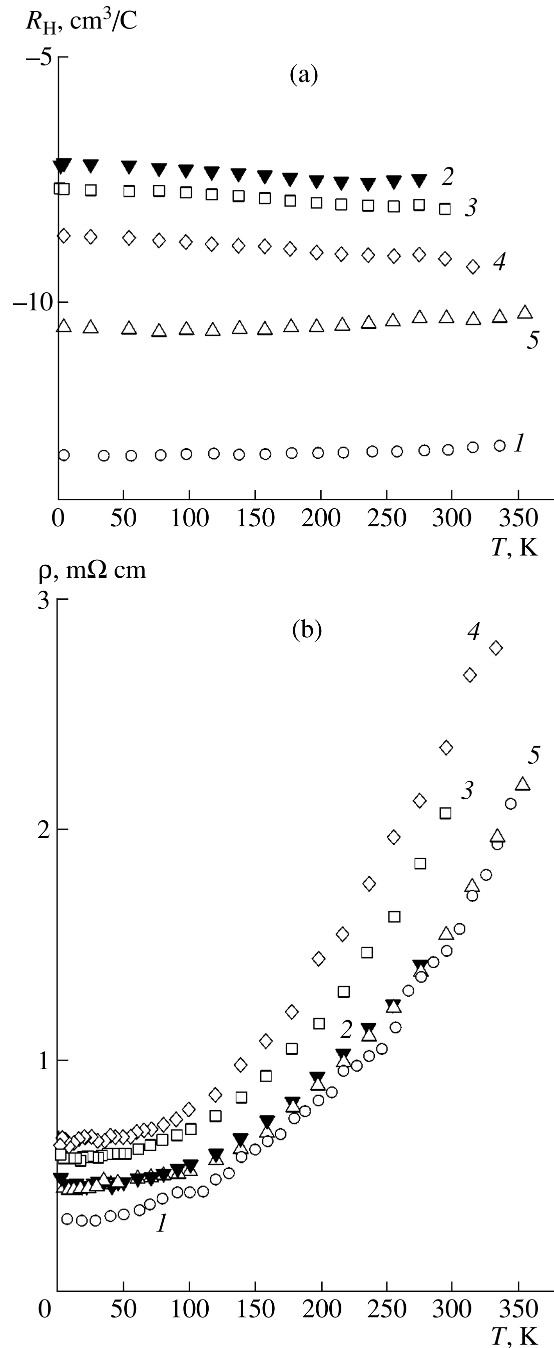

Fig. 1. Temperature dependences of (a) the Hall factor R_H and (b) resistivity ρ for HgSe samples: (*1*) initial; (*2*) irradiated with electrons with fluence of 10^{19} cm^{-2}, and further annealed at the temperature T_{ann}: (*3*) 330, (*4*) 360, and (*5*) 390 K.

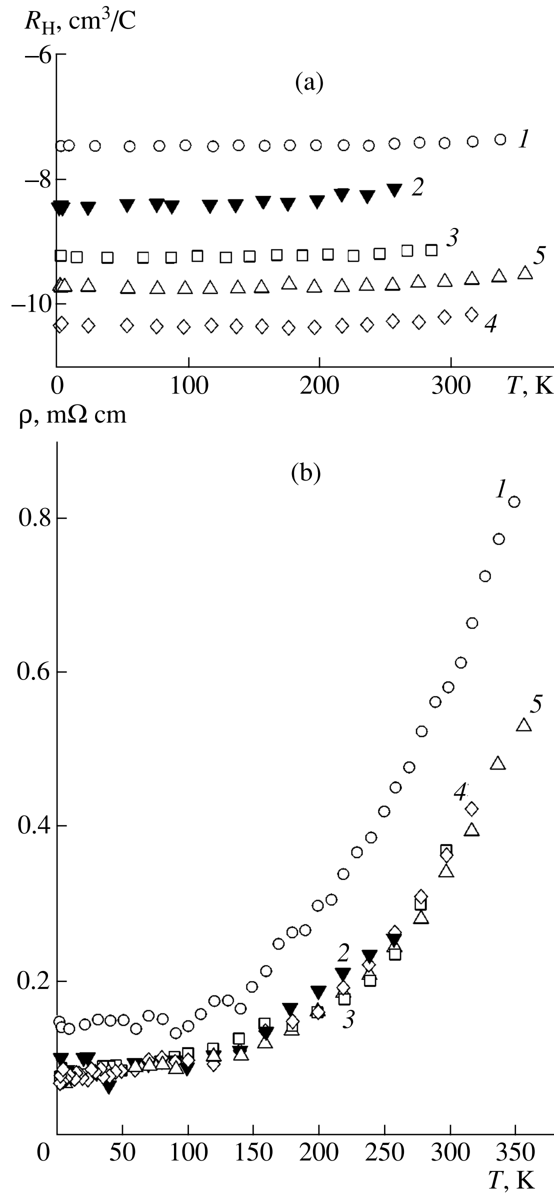

Fig. 2. Temperature dependences of (a) the Hall factor R_H and (b) resistivity ρ for $HgSe_{0.9}S_{0.1}$ samples. Curve designations as in Fig. 1.

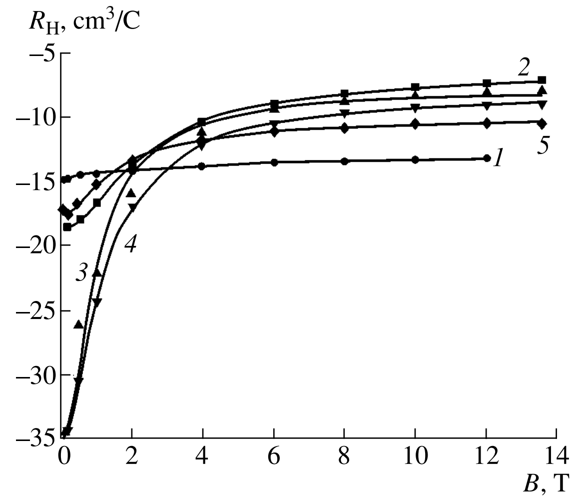

Fig. 3. The Hall factor R_H for HgSe samples vs the magnetic induction B at $T = 4.2$ K. Curve designations as in Fig. 1. Solid lines, calculation by relations (1)–(3).

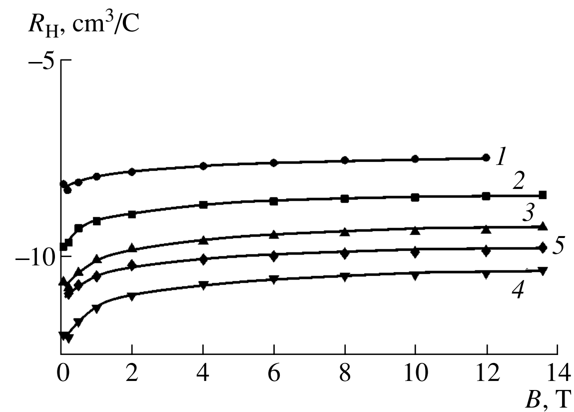

Fig. 4. The Hall factor R_H for $HgSe_{0.9}S_{0.1}$ samples vs the magnetic induction B at $T = 4.2$ K. Curve designations as in Fig. 1. Solid lines, calculation by relations (1)–(3).

For a $HgSe_{0.9}S_{0.1}$ crystal, the value and temperature dependence of resistivity remain virtually unchanged after annealing, and the Hall factor shows the same behavior in weak and strong magnetic fields: with increasing T_{ann}, it first grows in magnitude and then, at the maximum temperature $T_{ann} = 390$ K, decreases, but remains higher than the initial value (Figs. 2, 4). It may be concluded that the contribution of heavy carriers to conduction is not too large and irradiation only reduces the electron density. In the $HgSe_{0.5}S_{0.5}$ sample, the changes in similar temperature and field dependences after irradiation and annealings were even smaller (not shown in the figure). The irradiation slightly raised the resistivity and electron density and reduced the electron mobility. Annealing restored the initial properties. The Hall factor corresponded to an electron density of $n = 4 \times 10^{18}$ cm^{-3} and was nearly independent of magnetic field.

4. DISCUSSION

The obtained dependences of the Hall factor on magnetic field (Figs. 3, 4) are adequately described in terms of a two-band model. The carrier densities and mobilities served as fitting parameters, and their values are listed in Tables 1 and 2. The Hall factor for an isotropic semiconductor can be presented in the following form [12]:

$$R_H = \frac{\langle R_H\sigma^2\rangle}{\langle\sigma\rangle^2 + (\langle R_H\sigma^2\rangle B)^2}, \quad (1)$$

Table 1. Fitting parameters for $R_H(B)$ dependences for HgSe at $T = 4.2$ K

Fluence, 10^{19} cm^{-2}	Annealing temperature, °C	n_1, 10^{17} cm^{-3}	μ_1, 10^4 cm^2 V^{-1} s^{-1}	n_2, 10^{17} cm^{-3}	μ_2, 10^4 cm^2 V^{-1} s^{-1}
0	–	4.7	4.8	–	–
1	–	3.4	4.0	5.5	0.03
1	330	1.7	6.0	6.5	0.03
1	360	1.8	5.2	5.5	0.03
1	390	3.5	4.3	2.5	0.03

Table 2. Fitting parameters for $R_H(B)$ dependences for $HgSe_{0.9}S_{0.1}$ at $T = 4.2$ K

Fluence, 10^{19} cm^{-2}	Annealing temperature, °C	n_1, 10^{17} cm^{-3}	μ_1, 10^4 cm^2 V^{-1} s^{-1}	n_2, 10^{17} cm^{-3}	μ_2, 10^4 cm^2 V^{-1} s^{-1}
0	–	8.3	5.0	–	–
1	–	6.5	8.8	1.1	0.03
1	330	5.7	12	1.3	0.03
1	360	5.2	5–10	0.6	0.03
1	390	5.6	10	0.7	0.02

where quantities in the angle brackets are defined by

$$\langle\sigma\rangle = \frac{\sum_i \sigma_i}{1+(R_i\sigma_i B)^2}, \quad \langle R\sigma^2\rangle = \frac{\sum_i R_i(\sigma_i)^2}{1+(R_i\sigma_i B)^2}. \quad (2)$$

Here, $\sigma_i = 1/\rho_i$ and R_i are the conductivities and Hall factors for individual bands [12]. For the case of two-band conduction, relations (1), (2) are reduced to the standard form discussed in [13]. The field dependence of single-band parameters was taken into account by using simple interpolation formulas describing the transition from weak to strong magnetic fields:

$$R_i(B) = \frac{R_i(\infty)[a_R + b(\mu_i B)^2]}{1+b(\mu_i B)^2}, \quad (3)$$

where μ_i is the mobility; $R_i(0)$ and $R_i(\infty)$ are, respectively, the Hall factors in the limits of small and high magnetic fields [12]; $a_R = R_i(0)/R_i(\infty)$; and b is a fitting parameter.

Analysis of the experimental data has shown that irradiation with 5-MeV electrons reduces the conduction of electrons in a HgSe crystal by reducing their density (see Table 1). At the same time, the contribution to conduction from heavy electrons, which is negligible in the initial sample, increases. The minimum density of electrons is obtained at annealing temperatures of 330–360 K; in this range they have the highest mobility. The density of heavy electrons is at a maximum at these annealing temperatures (see Table 1). The mobility of heavy carriers, determined with low precision, was assumed to remain unchanged upon irradiation and annealing, which was confirmed also with calculations by relations (1)–(3), where this parameter was a variable.

In the $HgSe_{0.9}S_{0.1}$ sample, irradiation reduces the density of electrons, but raises their mobility. No manifestations of heavy carriers are actually observed (Table 2). Annealings also reduce the density of electrons, with their mobility remaining high. As a result, the conductivity of the $HgSe_{0.9}S_{0.1}$ sample remains nearly twice the initial value, in contrast to HgSe, where it decreased irreversibly by a factor of 1.5. It is noteworthy that even upon subjecting HgSeS samples to a high pressure of 0.4–0.7 GPa, which causes a reversible phase transition with a large volume effect of ~10%, the formed defects did not change the behavior of the temperature and magnetic-field dependences of resistivity, but only raised the values of ρ and reduced μ [11, 14]. This fact demonstrates the decisive role of intrinsic defects, which define the electrical properties of such crystals.

Obviously, deep levels related to radiation defects lie within the continuous energy spectrum of zero-gap semiconductors HgSe and HgSeS. Relatively low electron density in the HgSe sample (Table 1) suggests a high content of interstitial Se and Hg vacancies, whereas in ternary compounds, in which the electron density is higher (Table 2), the most probable defects are interstitial Hg atoms [10]. Presumably, the different natures of intrinsic defects is one of the reasons for the different behaviors of crystals under irradiation and annealing. According to calculations [15], the energy of the Hg vacancy formation in HgSe, HgS, and HgSeS is considerably lower than the energy for Se or S vacancy formation. Therefore, the most probable radiation defects are cation vacancies or associated complexes, which, indeed, must reduce the electron density in HgSe [10].

Electron irradiation raises the density of states in defect-related electron bands lying below the Fermi level. The transition of electrons to the defect band raises the density of heavy carriers in this band at the expense of the conduction band filling, i.e., via a decrease in the Fermi level. The behavior of the mobility in irradiation and annealing of samples (Tables 1, 2) is adequately explained by the dependence of the effective electron mass in the conduction band on the electron density:

$$m^*(n) = m_n^*[1 + n^{2/3}2(3\pi^2)^{2/3}\hbar^2/\varepsilon_g m_n^*]^{1/2}.$$

This dependence is typical of degenerate semiconductors with a nonquadratic dispersion law [6–8]. Here, m_n^* is the effective mass at the bottom of the band, and ε_g is the energy gap. At the same time, a strong change in the defect concentration can also modify the mobility, since relaxation time τ is inversely proportional to the electron density for the mechanisms of scattering when there are charged and neutral impurities [12]. In particular, the increase in mobility in the $HgSe_{0.9}S_{0.1}$ sample after irradiation can be related to the decrease in total concentration of charged centers, i.e., vacancies and interstitial atoms.

5. CONCLUSION

The irradiation made possible deeper reduction of the electron density than is usually obtained by conventional long-term high-temperature annealing in a Se atmosphere [10]. Heavy carriers in the band of defect states were revealed. In ternary compounds the density is also reduced; however, since in these crystals, under the electron energy of 5 MeV used, the concentration of intrinsic defects is higher than that of radiation-induced ones, the effect of irradiation is smaller.

ACKNOWLEDGMENTS

This study was supported by the program of the Ministry of Industry, Science, and Technology of the Russian Federation (state contract nos. 40.012.1.1.1150 and 40.020.1.1.1166, project no. 10/02), the program of the Russian Academy of Sciences "Quantum Macrophysics" (project no. 25/02), "Scientific School" program (grant no. 00-15-96581), and the Russian Foundation for Basic Research (project no. 01-02-16877).

REFERENCES

1. B. N. Goshchitskiĭ, V. E. Arkhipov, and Yu. G. Chukalkin, Sov. Sci. Rev., Sect. A **8**, 519 (1987).
2. B. A. Aleksashin, V. I. Voronin, S. V. Verkhovskiĭ, *et al.*, Zh. Éksp. Teor. Fiz. **95**, 678 (1989) [Sov. Phys. JETP **68**, 382 (1989)].
3. A. E. Kar'kin, S. A. Davydov, A. V. Mirmel'shteĭn, and B. N. Goshitskiĭ, Sverkhprovodimost: Fiz., Khim., Tekh. **5**, 2215 (1992).
4. N. B. Brandt and E. P. Skipetrov, Fiz. Nizk. Temp. **22**, 870 (1996) [Low Temp. Phys. **22**, 665 (1996)].
5. A. E. Kar'kin, V. V. Shchennikov, B. N. Goshchitskiĭ, *et al.*, Zh. Éksp. Teor. Fiz. **113**, 1787 (1998) [JETP **86**, 976 (1998)].
6. I. M. Tsidil'kovskiĭ, *Electrons and Holes in Semiconductors* (Nauka, Moscow, 1972).
7. B. L. Gel'mont, V. I. Ivanov-Omskiĭ, and I. M. Tsidil'kovskiĭ, Usp. Fiz. Nauk **120**, 337 (1976) [Sov. Phys. Usp. **19**, 879 (1976)].
8. I. M. Tsidil'kovskiĭ, *Zero-Gap Semiconductors as a New Class of Substances* (Nauka, Moscow, 1986).
9. N. N. Berchenko, V. E. Krevs, and V. G. Sredin, *Semiconductor II–VI Solid Solutions and Their Applications: Reference Book* (Voenizdat, Moscow, 1982).
10. P. I. Baranskiĭ, V. P. Klochkov, and I. V. Potykevich, *Semiconductor Electronics* (Naukova Dumka, Kiev, 1975).
11. V. V. Shchennikov, A. E. Kar'kin, I. P. Gavaleshko, and V. M. Frasunyak, Fiz. Tverd. Tela (St. Petersburg) **39**, 1717 (1997) [Phys. Solid State **39**, 1528 (1997)].
12. P. S. Kireev, *Physics of Semiconductors* (Vysshaya Shkola, Moscow, 1969).
13. C. C. Y. Kwan, J. Basinski, and J. C. Woolley, Phys. Status Solidi B **48**, 699 (1971).
14. V. V. Shchennikov, N. P. Gavaleshko, V. M. Frasunyak, and V. I. Osotov, Fiz. Tverd. Tela (St. Petersburg) **37**, 2398 (1995) [Phys. Solid State **37**, 1311 (1995)].
15. M. A. Berding, A. Sher, and A.-B. Chen, J. Appl. Phys. **68**, 5064 (1990).

Translated by D. Mashovets

Semiconductors, Vol. 37, No. 11, 2003, pp. 1283–1290. Translated from Fizika i Tekhnika Poluprovodnikov, Vol. 37, No. 11, 2003, pp. 1321–1328.
Original Russian Text Copyright © 2003 by V. Rud', Yu. Rud', Vaĭpolin, Bodnar', Fernelius.

Photosensitive Structure on $CdGa_2S_4$ Single Crystals

V. Yu. Rud'*^, Yu. V. Rud', A. A. Vaĭpolin**, I. V. Bodnar'***, and N. Fernelius******

**St. Petersburg State Technical University, Politekhnicheskaya ul. 29, St. Petersburg, 195251 Russia*
^e-mail: rudvas@spbstu.ru
***Ioffe Physicotechnical Institute, Russian Academy of Sciences, Politekhnicheskaya ul. 26, St. Petersburg, 194021 Russia*
****Belarussian State University of Informatics and Radioelectronics Engineering, ul. Brovki 17, Minsk, 220027 Belarus*
*****Air Force Wright Lab., Wright Patterson AFB, OH, USA*
Submitted January 8, 2003; accepted for publication January 10, 2003

Abstract—Single crystals of the $CdGa_2S_4$ ternary compound were grown either from melt or by chemical-vapor deposition. The crystal-lattice parameters and some physical properties of homogeneous crystals having defect chalcopyrite structure with the point symmetry group $I\bar{4}$ (S_4^2) are determined. A number of photosensitive structures—Schottky barriers, heterostructures, photoelectrochemical cells, and natural-protein–$CdGa_2S_4$ barriers—were formed for the first time on the basis of the single crystals under investigation. The photoelectric properties of the structures obtained were studied using natural and linearly polarized light at $T = 300$ K. The main parameters of these structures are determined, and it is concluded that they can be used in photodetectors.
© 2003 MAIK "Nauka/Interperiodica".

1. INTRODUCTION

Cadmium thiogallate $CdGa_2S_4$ belongs to a wide class of $A^{II}B_2^{III}C_4^{VI}$ semiconductors (where A^{II} = Zn, Cd, Hg; B^{III} = Al, Ga, In; C^{VI} = S, Se, Te), which includes a large group of direct-gap materials with wide band gap (up to ~4.0 eV). In principle, these semiconductors make it possible to significantly expand the range of materials used in optoelectronics in the highly popular short-wavelength spectral range (the number of these materials is far from sufficient) [1, 2]. Urgent demands for semiconductor optoelectronics to advance into the short-wavelength region imply, in particular, expansion of technological and research studies of new wide-gap semiconductors, including $CdGa_2S_4$ crystals. This study, undertaken within this promising line, is devoted to solving the problems of fabrication and investigation of photosensitive structures of different types based on $CdGa_2S_4$ single crystals.

2. $CdGa_2S_4$ SINGLE CRYSTALS

The photosensitive structures were formed using $CdGa_2S_4$ single crystals grown both from melt and by chemical-vapor deposition. In the former case, single crystals were grown by the Bridgman–Stockbarger method from previously synthesized single-phase polycrystalline ingots of this compound. Synthesis was performed from binary components CdS and Ga_2S_3, which were loaded into conical crucibles made of pyrolitic boron nitride with an inner diameter of 16 mm and a length of 90 mm. Then, the crucibles loaded with starting components were placed into quartz cells. Each cell was equipped with a quartz rod to be installed on a mechanical vibrator. An evacuated and sealed cell was placed in a single-zone vertical furnace and heated at a rate of 100 K/h to 1020–1050°C. The cell was kept at this temperature for 3 h with continuous vibrational mixing, after which the melt was cooled at a rate of 100 K/h to room temperature.

After synthesis, the cell was transferred into a vertical two-zone furnace, in which single crystals were grown. The temperatures of the melting and annealing zones were set at ~1030°C and ~830°C, respectively. The melt was kept under these conditions for 24 h, after which the cell with the melt was lowered through the crystallization zone at a rate of ~0.26 mm/h with a temperature gradient of ~40°C/cm. After melt crystallization, the crystals grown were generally subjected to homogenizing annealing for 72 h. The single-crystal ingots obtained by this method (16 mm in diameter, 40 mm long) were sufficiently transparent in transmitted white light and had a uniform light-yellow color.

Along with crystallization from melt, the method of gas-transport reactions in a closed volume, using iodine as a carrier, was also employed. This made it possible to obtain $CdGa_2S_4$ single crystals with a natural faceting typical of ternary compounds of this type [3]. The average size of prisms was as high as $10 \times 3 \times 0.5$ mm. The (112) face was most developed, whereas the $(\bar{1}\bar{1}\bar{2})$ face was uneven. The faces of the [110] zone, including the (001) face, were distinct, but poorly developed and imperfect. In the pair $(\bar{1}\bar{1}2)/(11\bar{2})$, the $(\bar{1}\bar{1}2)$ face is also of higher quality, whereas the (001) face is out-

Photoelectric properties of structures formed on $CdGa_2S_4$ single crystals, measured at $T = 300$ K

Structure	$\hbar\omega^m$, eV	δ, eV	S_u^m, V/W	P_η^m, %
In–$CdGa_2S_4$	2.70, 3.67	0.4	50	–
GaSe–$CdGa_2S_4$	2.8, 2.9	0.35–0.46	50	–90
H_2O–$CdGa_2S_4$	3.67	0.2–0.3	300	50
Protein–$CdGa_2S_4$	~3.7	–	~5	–

lined in the form of a fine line. The (100) face also turned out to be rather developed.

On the basis of X-ray investigations, we found the unit-cell parameters of the $CdGa_2S_4$ single crystals: $a = 5.546 \pm 0.001$ Å and $c = 10.165 \pm 0.001$ Å for the crystals grown from melt and $a = 5.5465 \pm 0.0002$ Å and $c = 10.1646 \pm 0.0005$ Å for the crystals grown by chemical-vapor deposition. The high quality of the single crystals obtained allowed us to determine the unit-cell parameters more accurately compared to the data of [2, 4]. As can be seen, the $CdGa_2S_4$ crystals obtained by different methods have similar values of a and c. However, with regard to the data of [2, 4], we should mention a certain spread of the parameters noted, which may be caused by their possible dependence on the crystallization conditions. With regard to this circumstance, we assign $CdGa_2S_4$ to phases of variable composition [5]. In order to clarify this issue, detailed investigation of the interrelation between the composition and properties of $CdGa_2S_4$ crystals should be performed.

It is also noteworthy that rough estimation of the intensities of a number of X-ray reflections reveals an expected and repeatable difference between $F^2(hkl)$ and $F^2(khl)$ for odd l. This difference manifests itself in the fact that the nonequivalence of the hkl and khl reflections is typical of the $I\bar{4}\,(S_4^2)$ symmetry group (to which the imperfect chalcopyrite structure belongs) and is absent in the case of the $I42m(D_{2d}^{11})$ symmetry characteristic of the thiogallate structure. The crystals grown by chemical-vapor deposition and the crystals grown from melt had similar colors.

Nominally undoped $CdGa_2S_4$ single crystals obtained by both of the above methods had n-type conductivity and a resistivity of $\rho \approx 10^8$–10^{10} Ω cm at 300 K; notably, the crystals with the highest resistivity were grown by chemical-vapor deposition. The concentration and the electron Hall mobility evaluated for the $CdGa_2S_4$ single crystals from the Hall measurements are, respectively, $n \approx 10^8$–10^9 cm^{-3} and $\mu_n \approx 1$–10 cm^2/(V s) at 300 K.

3. GaSe–$CdGa_2S_4$ HETEROSTRUCTURES

Since $CdGa_2S_4$ single crystals can be grown only with n-type conductivity, we used the method of bringing different semiconductors into optical contact with each other [6, 7] to fabricate heterostructures. The surface of a $CdGa_2S_4$ single crystal, polished mechanically and chemically, polished was brought into contact with the surface of a fresh natural cleavage of a layered semiconductor GaSe with a hole density of $\approx 10^{14}$ cm^{-3} and a Hall mobility of ≈ 40 cm^2/(V s) at $T = 300$ K. The measurements of the steady-state current–voltage (I–V) characteristics showed that such a contact demonstrates distinct rectification characterized by the rectification factor $K \simeq 10$–15 at voltages $U \simeq 100$ V. A positive bias at the p-GaSe wafer generally corresponds to the conducting direction in such heterostructures. Illumination of the heterostructures gives rise to the photovoltaic effect. Generally, the photosensitivity is higher when the structures are exposed to light from the $CdGa_2S_4$ side. Irrespective of the photon energy and the geometrical conditions of illumination, a $CdGa_2S_4$ crystal is charged negatively, which corresponds to the rectification polarity. The highest photovoltaic sensitivity of the best heterostructures is $S_u^m \simeq 50$ V/W at 300 K (see table).

Figure 1 (curves *1*, *2*) shows the typical spectral dependences of the relative quantum efficiency of photoconversion $\eta(\hbar\omega)$ of the p-GaSe–n-$CdGa_2S_4$ heterostructures for the case of illumination by natural radiation either on the $CdGa_2S_4$ or from the GaSe sides. When light is incident on the $CdGa_2S_4$ side, the photosensitivity spectrum, observed in a wide range from 1.0 to 4.0 eV, is characterized by the full width at half-maximum $\delta \approx 0.4$ eV (see table). Notably, the photosensitivity is highest in the short-wavelength region, being peaked at $\hbar\omega \simeq 2.75$–2.90 eV for different heterostructures. The long-wavelength edge of photosensitivity is controlled by the interband absorption in GaSe. When the heterostructures are illuminated from the GaSe side, an abrupt short-wavelength falloff appears in the spectral dependence of η (Fig. 1, curve *2*) at the energy close to the width of the GaSe band gap ($E_g \approx 2.0$ eV [3, 8]). This phenomenon is caused by the fact that absorption occurs mainly near the GaSe surface when the active region in the structures is shifted at distances exceeding the diffusion length of photoelectrons in GaSe. As can be seen from Fig. 1 (curve *1*), when the GaSe–$CdGa_2S_4$ heterostructures are exposed to radiation with the photon energy exceeding the band gap of gallium selenide ($\hbar\omega > E_g$), an increase in the photosen-

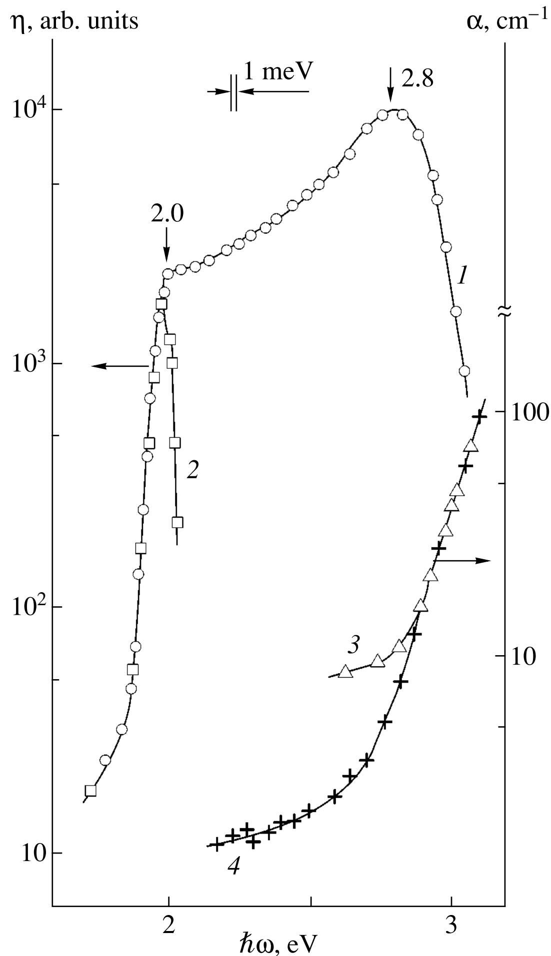

Fig. 1. Spectral dependences of the relative quantum efficiency of photoconversion of the *p*-GaSe–*n*-$CdGa_2S_4$ heterostructures (sample 7; illumination (*1*) on the $CdGa_2S_4$ side and (*2*) on the GaSe side; the thicknesses of the $CdGa_2S_4$ and CdSe wafers d = 0.5 and 0.18 mm, respectively) and the coefficient of optical absorption of $CdGa_2S_4$ (sample 11*K*, d = (*3*) 0.15 and (*4*) 0.5 mm) at T = 300 K for unpolarized radiation.

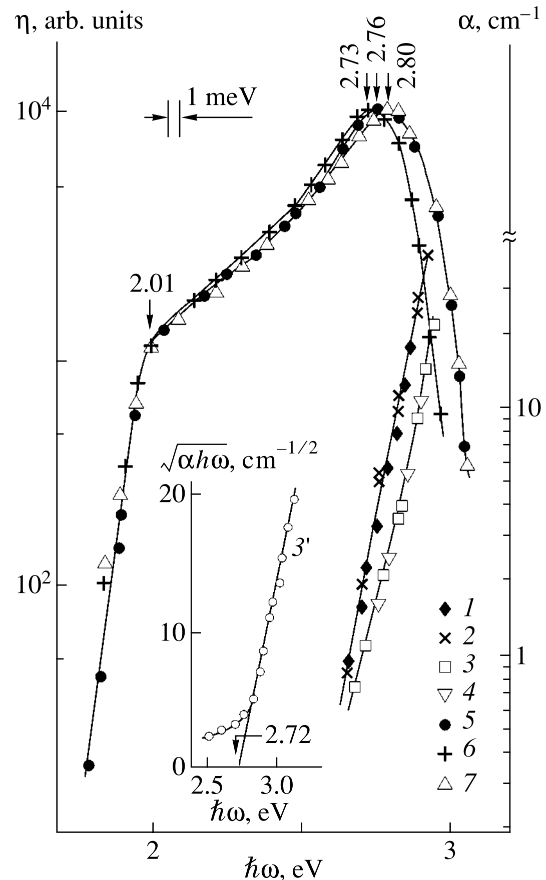

Fig. 2. Spectral dependences of the coefficient of optical absorption of $CdGa_2S_4$ single crystals ((*1*, *3*, *3*') sample 10*K*; sample 7*B* with the (100)-oriented wafers; the wafer thickness d = (*1*, *3*) 0.13 and (*2*, *4*) 0.15 mm; the radiation polarization (*1*, *2*) **E** ∥ **c** and (*3*, *4*) **E** ⊥ **c**) and the relative quantum efficiency of photoconversion for a *p*-GaSe–*n*-$CdGa_2S_4$ heterostructure (sample 8, (*5*) unpolarized radiation and radiation with polarizations (*6*) **E** ∥ **c** and (*7*) **E** ⊥ **c**) at T = 300 K.

sitivity is observed. This increase can be characterized by the ratio of the photosensitivity at $\hbar\omega^m$ to the photosensitivity at the photon energy close to E_g. For the heterostructures fabricated, this ratio changes in a fairly wide range: 5–100, which is related to changes in the electrical properties of the phases in contact. The maximum of photosensitivity of the heterostructures is located in the region $\hbar\omega^m \gg E_g$ because the resistivity of $CdGa_2S_4$ significantly exceeds that of GaSe, due to which the active region in the heterostructures is located mainly in $CdGa_2S_4$.

The optical absorption spectra $\alpha(\hbar\omega)$ of the $CdGa_2S_4$ single crystals on which heterostructures were formed are shown in Fig. 1 (curves *3*, *4*). Comparison of the spectra $\eta(\hbar\omega)$ and $\alpha(\hbar\omega)$ shows that the short-wavelength falloff of the photosensitivity of the heterostructures corresponds to the abrupt increase in the optical absorption of $CdGa_2S_4$. This circumstance suggests that the short-wavelength falloff of η in the spectra of the heterostructures, being controlled by the effect of radiation absorption deep in the $CdGa_2S_4$ wafers, becomes for this reason weaker with decreasing thickness of these wafers. At the same time, the fact that the heterostructures obtained exhibit high photosensitivity in the range between the gallium selenide band gap and the energy at which the optical absorption in $CdGa_2S_4$ begins to increase suggests that the method of bringing semiconductors with different parameters and lattice types into direct optical contact [3, 7] opens for the first time the possibility of fabricating real structures with broadband spectral characteristic $\eta(\hbar\omega)$ on the new semiconductor [2].

It can also be seen from Fig. 2 (curve *3*') that, in the $(\alpha\hbar\omega)^{1/2}$–$\hbar\omega$ coordinates, the optical absorption spectra contain a straight-line portion, which makes it pos-

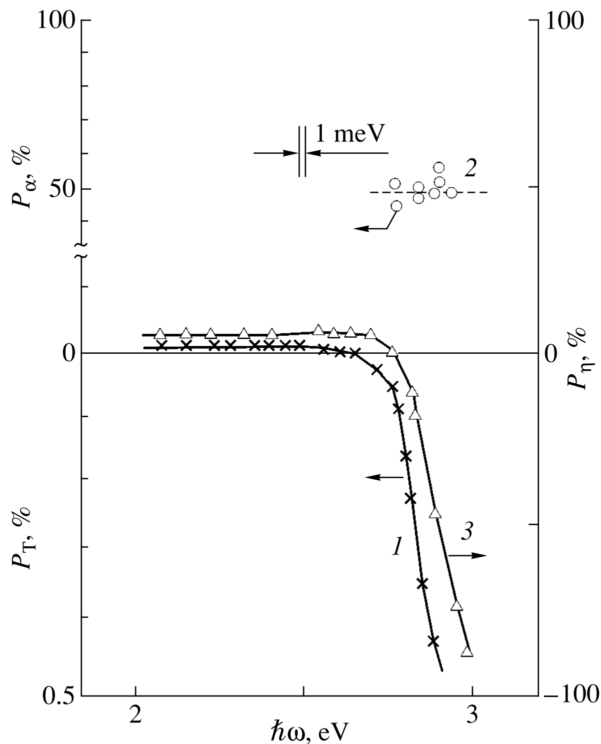

Fig. 3. Spectral dependences of the coefficients of the (*1*) optical-transmittance pleochroism (curve *1*, sample *6K*, $d = 0.25$ mm) and (*2*) absorption pleochroism (curve *2*, sample *7B*, $d = 0.15$ mm) of single-crystal $CdGa_2S_4(100)$ wafers and the spectral dependences of the coefficients of natural photopleochroism of a *p*-GaSe–*n*-$CdGa_2S_4$ heterostructure (curve *3*, sample 8, $CdGa_2S_4$-wafer thickness $d = 0.15$ mm, illumination on the $CdGa_2S_4$ side) at $T = 300$ K.

sible (according to [9]) to relate the absorption observed with indirect interband transitions in $CdGa_2S_4$ crystals and to evaluate (using the extrapolation $(\alpha\hbar\omega)^{1/2} \longrightarrow 0$) the indirect energy gap in the electronic spectrum of this compound: $E_g \approx 2.72$ eV at 300 K.

In order to study the polarization photosensitivity, heterostructures were fabricated on *n*-$CdGa_2S_4$ single crystals oriented in the (100) and (001) planes. The main result of these investigations is that the heterostructures formed on (001) wafers, being illuminated at a normal to the surface of the $CdGa_2S_4$ crystal, did not show any dependence of the photosensitivity on the direction of the electric-field vector **E** of light wave, whereas in the structures formed on $CdGa_2S_4(100)$ wafers coplanar with the tetragonal *c* axis, a periodic dependence of η on the spatial orientation of **E** is observed [10]. This observation, being consistent with the symmetry of the $CdGa_2S_4$ crystal [2, 3], makes it possible to relate the polarization dependence of η to the anisotropy of photoactive absorption in $CdGa_2S_4$.

The typical spectral dependences $\alpha(\hbar\omega)$ for $CdGa_2S_4$ crystals and $\eta(\hbar\omega)$ for the heterostructures formed on these crystals, measured using linearly polarized radiation (LPR), are shown in Fig. 2. It can be seen that the coefficient of optical absorption in the LPR spectrum is split in such a way that $\alpha^{\parallel} > \alpha^{\perp}$, due to which the spectrum shifts parallel to the abscissa axis to shorter wavelengths by ~80 meV when the polarization changes from $\mathbf{E} \parallel \mathbf{c}$ to $\mathbf{E} \perp \mathbf{c}$. This means that indirect interband transitions are allowed mainly for the polarization $\mathbf{E} \parallel \mathbf{c}$, as in the case of uniaxial $A^{II}B^{IV}C_2^V$ crystals [11, 12]. The polarization photosensitivity arises only in the heterostructures formed on $CdGa_2S_4(100)$ wafers. The long-wavelength edge of the photosensitivity of heterostructures, governed by the interband absorption in GaSe (when the latter is exposed to radiation propagating along the isotropic direction), as one should expect [10], is insensitive to the radiation polarization. The polarization photosensitivity, which arises only when the photon energy exceeds the band gap of gallium selenide, may be related to the anisotropy of photoactive absorption in $CdGa_2S_4$ crystals. This anisotropy turns out to be rather specific. When the radiation is polarized, the spectrum $\eta(\hbar\omega)$ is split by ~80 meV (Fig. 2, curves *6*, *7*), as well as the spectrum $\alpha(\hbar\omega)$ of the wafer that the heterostructure is formed on. In this case, a photoisotropic point ($\hbar\omega_i \approx 2.76$ eV) is revealed in the spectrum $\eta(\hbar\omega)$, at which $\eta^{\parallel} = \eta^{\perp}$; notably, below and above $\hbar\omega_i$, $\eta^{\parallel} > \eta^{\perp}$ and $\eta^{\parallel} < \eta^{\perp}$, respectively. Hence, the photosensitivity anisotropy is consistent with the anisotropy of the optical-absorption coefficient only in the long-wavelength region ($\hbar\omega < \hbar\omega_i$) (Fig. 2), whereas at $\hbar\omega > \hbar\omega_i$, the sign of the photosensitivity anisotropy ($\eta^{\perp} > \eta^{\parallel}$) becomes opposite to that of the dichroism of optical absorption ($\alpha^{\parallel} > \alpha^{\perp}$). This difference may be due to the following. In the spectral region $\hbar\omega > \hbar\omega_i$, the photosensitivity of the GaSe–$CdGa_2S_4$ heterostructures begins to be controlled by the optical transmittance of the $CdGa_2S_4$ wafer since the radiation with polarization $\mathbf{E} \perp \mathbf{c}$, being weakly absorbed in $CdGa_2S_4$, still contributes to the photosensitivity of the heterostructure, whereas the absorption depth of the radiation with polarization $\mathbf{E} \parallel \mathbf{c}$ in $CdGa_2S_4$ turns out to be smaller then the diffusion length of photoholes in this compound.

Let us analyze the anisotropy of the optical properties of $CdGa_2S_4$ crystals and the polarization photosensitivity of heterostructures based on them using generally accepted quantitative characteristics [10]. Figure 3 shows the spectra of the coefficients of transmittance and absorption pleochroism (curves *1*, *2*) of $CdGa_2S_4$ single crystals, and of the coefficient of natural photopleochroism (curve *3*) of the GaSe–$CdGa_2S_4$ heterostructure. The coefficient of optical-transmittance pleochroism is determined by the expression

$$P_T = [(T^{\parallel} - T^{\perp})/(T^{\parallel} + T^{\perp})] \times 100\%, \quad (1)$$

where $T^{\parallel}$ and $T^{\perp}$ are the optical transmittances for the polarizations $\mathbf{E} \parallel \mathbf{c}$ and $\mathbf{E} \perp \mathbf{c}$, respectively. The coefficient of the optical-transmittance pleochroism for $CdGa_2S_4$(100) wafers exhibits a noticeable increase in amplitude and a negative sign at $\hbar\omega > 2.7$ eV, tending to the limiting value (–100%) in the vicinity of $\hbar\omega \simeq 2.9$ eV.

The coefficient of absorption pleochroism is determined by the ratio

$$P_{\alpha} = [(\alpha^{\parallel} - \alpha^{\perp})/(\alpha^{\parallel} + \alpha^{\perp})] \times 100\%, \qquad (2)$$

where $\alpha^{\parallel}$ and $\alpha^{\perp}$ are the absorption coefficients for the corresponding polarizations of radiation with respect to the tetragonal **c** axis of the crystal. It can be seen from Fig. 3 that the coefficient of absorption pleochroism of $CdGa_2S_4$ is positive and fairly high (~50%) in the spectral region under study. In this region, the coefficient of natural photopleochroism is determined by the expression

$$P_{\eta} = [(\eta^{\parallel} - \eta^{\perp})/(\eta^{\parallel} + \eta^{\perp})] \times 100\%, \qquad (3)$$

where $\eta^{\parallel}$ and $\eta^{\perp}$ are the quantum photoconversion efficiencies for the given polarizations. It can be seen from Fig. 3 that the spectral behavior of natural photopleochroism of the heterostructures under study is similar to that of $P_T(\hbar\omega)$. This circumstance is due to the features of the heterostructure photosensitivity. Obviously, in order to ensure correspondence between P_{α} and P_{η}, we should exclude the absorption of radiation in the region of $CdGa_2S_4$ adjacent to the active region of the heterostructures.

4. In–$CdGa_2S_4$ STRUCTURES

Preliminary investigations of the contacts of some metals with the surface of $CdGa_2S_4$ showed rectifying properties of the contact formed by a layer of pure indium and a $CdGa_2S_4$ single crystal. The rectification direction for the ln–$CdGa_2S_4$ structures obtained by vacuum thermal evaporation of indium generally corresponds to the positive bias on indium layers; the rectification factor $K \approx 5$ at $U \approx 10$ V. The photosensitivity of the best structures was found to be highest in the case of illumination from the side of the In layer and comparable to that typical of other structures fabricated by us (see table). Under illumination, the indium layers are charged positively, which is consistent with the rectification direction for these structures.

The spectra $\eta(\hbar\omega)$, typical of the surface-barrier ln–$CdGa_2S_4$ structures, are shown in Fig. 4. The photosensitivity of these structures manifests itself in a wide spectral range (1–4 eV); its spectrum is shifted to shorter wavelengths ($\hbar\omega > 2.7$ eV) with respect to the heterostructures (Fig. 1). The photosensitivity spectra of the barrier structures are rather complex and contain a large number of broad bands. The energy positions of the band peaks and the value of η vary drastically from sample to sample. The spectra of many barrier structures formed on the $CdGa_2S_4$ single crystals grown from melt contain a peak at $\hbar\omega^m = 3.67$ eV in the short-wavelength region, which corresponds to direct interband transitions in $CdGa_2S_4$ [2, 13, 14]. It should be noted that some of the peaks and inflections present in the long-wavelength part of the spectra $\eta(\hbar\omega)$ of the ln–$CdGa_2S_4$ structures (indicated by arrows in Fig. 4) were also observed in other studies [15–17], where the local states of $CdGa_2S_4$ were considered. The origin of these features has not been ascertained yet and requires finding the relation of the spectra $\eta(\hbar\omega)$ with the specific conditions of growth and subsequent thermal treatment of $CdGa_2S_4$ single crystals. The variety of the spectra $\eta(\hbar\omega)$ revealed (Fig. 4) suggests that investigation of the spectra $\eta(\hbar\omega)$ of surface-barrier structures is highly efficient in studying the energy spectrum and the structural quality of $CdGa_2S_4$ crystals. For example, as can be seen from Fig. 4 (curve 5), the surface-barrier structures formed on $CdGa_2S_4$ single crystals grown by

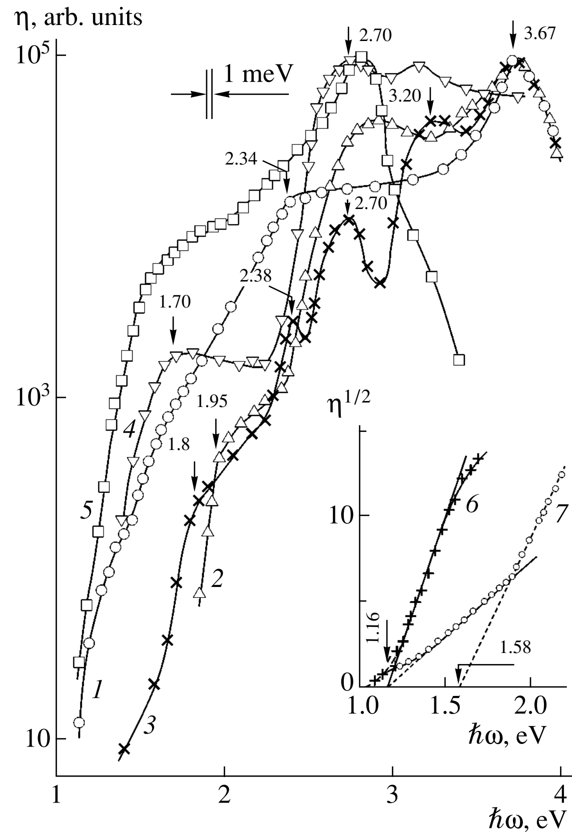

Fig. 4. Spectral dependences of the relative quantum efficiency of photoconversion of the surface-barrier In–*n*-$CdGa_2S_4$ structures, formed on $CdGa_2S_4$ single crystals grown (*1–4*, *6*, *7*) from melt and (*5*) by vapor-phase deposition, exposed to natural light at $T = 300$ K (illumination on the barrier side; samples (*1*, *7*) 17*K*, (*2*) 19*B*, (*3*) 21*SP*, (*4*) 34*SP*, (*5*, *6*) 3*SP*). The dependences $\eta^{1/2} - \hbar\omega$ are shown in the inset.

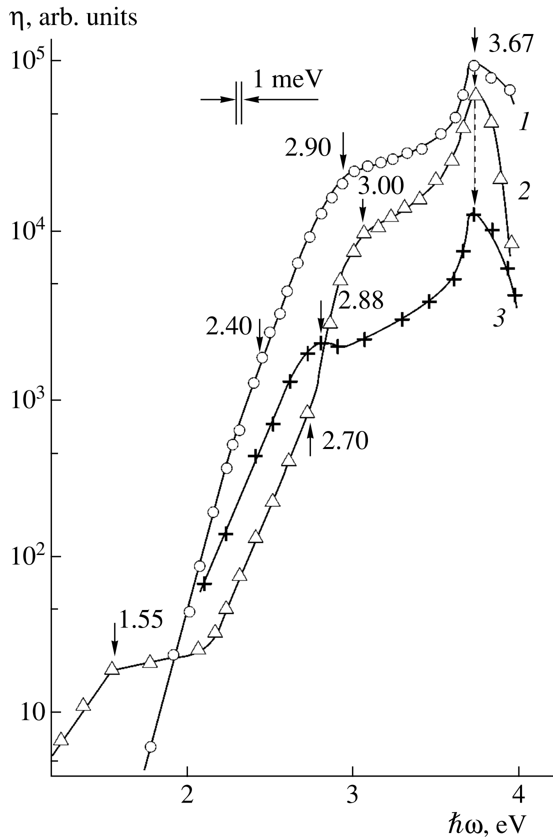

Fig. 5. Spectral dependences of the relative quantum efficiency of photoconversion of (*1*, *2*) photoelectrochemical cells H_2O–*n*-$CdGa_2S_4$ and (*3*) In–*n*-$CdGa_2S_4$ structure at $T = 300$ K for unpolarized light (illumination on the side of H_2O and In layers; samples (*1*) 18*K*, (*2*) 35*K*, (*3*) 16*K*).

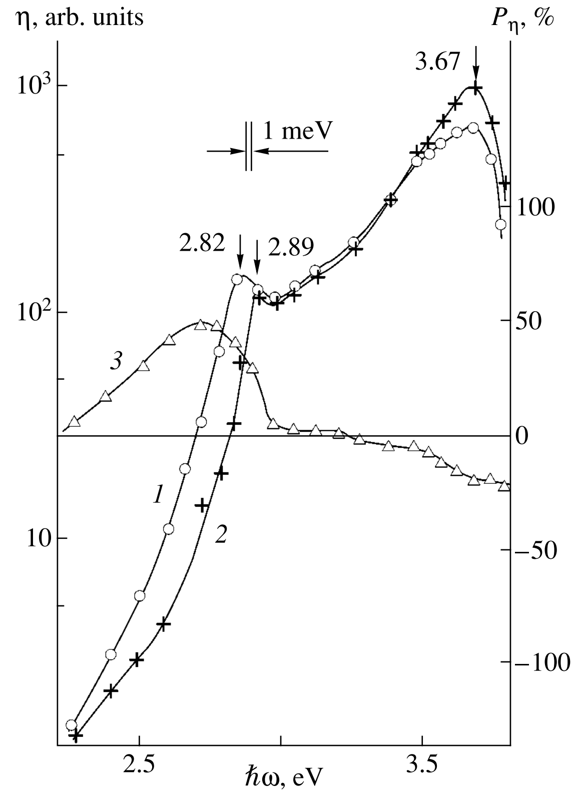

Fig. 6. Spectral dependences of the relative quantum efficiency of photoconversion ((*1*) **E** || **c**, (*2*) **E** ⊥ **c**) and (*3*) the coefficient of natural photopleochroism of a photoelectrochemical cell H_2O–*n*-$CdGa_2S_4$ at $T = 300$ K (illumination on the electrolyte side, sample 39*SP*).

chemical-vapor deposition exhibit an abrupt short-wavelength falloff of η at $\hbar\omega > 2.8$ eV, which makes impossible to record a photoresponse in the region of direct interband transitions. Along with this circumstance, the relative contribution of photoactive absorption to photosensitivity in the impurity region for the structures formed on crystals grown by chemical-vapor deposition was found to be significantly larger than for the single crystals grown from melt.

The long-wavelength part of the spectra $\eta(\hbar\omega)$ of the ln–$CdGa_2S_4$ structures is described by the Fowler relationship (Fig. 4, curves *6*, *7*), which allows us to relate this part to the photoemission of electrons into the semiconductor. Hence, extrapolation of the long-wavelength part of the photosensitivity spectra $\eta^{1/2} \longrightarrow 0$ yields the estimate for the energy-barrier height: $\varphi_B \simeq$ 1.2 eV.

5. PHOTOELECTROCHEMICAL CELLS

Investigations of photoelectrochemical cells (PECs) are widely used in the fabrication of photosensitive structures based on various ternary compounds [18, 19]. Thus, along with the structures considered above, we also attempted to fabricate such cells on the basis of $CdGa_2S_4$ single crystals. As a result, it was shown that H_2O–$CdGa_2S_4$ structures, as well as solid-state structures, exhibit rectification and photovoltaic effect. The rectification factor of the H_2O–$CdGa_2S_4$ structures is as high as $K \simeq 10^2$ at $U \simeq 10$ V. Illumination of these structures gives rise to a photovoltage. Among the structures fabricated by us, the H_2O–$CdGa_2S_4$ cells exhibited the highest photosensitivity (see table). Notably, the photoelectrode always has a negative potential, which is consistent with the rectification direction.

The typical spectral dependences $\eta(\hbar\omega)$ for the PECs and surface-barrier structures are shown in Fig. 5. In both types of structures, photosensitivity is highest in the region of direct interband transitions in $CdGa_2S_4$, being peaked at $\hbar\omega^m \simeq 3.67$ eV at $T = 300$ K under illumination from the barrier side. The long-wavelength part of the spectra $\eta(\hbar\omega)$ of the PECs obtained is similar to that of the In–$CdGa_2S_4$ structures (Fig. 4). The reason is that the long-wavelength part of the spectra is due to the impurity and fundamental transitions in $CdGa_2S_4$ crystals.

It was ascertained [10, 12, 19] that PECs formed on $CdGa_2S_4$(100) wafers are characterized by polarization photosensitivity, which is typical of anisotropic semiconductors. The main results of this series of studies (see Fig. 6) consist of the following. When a PEC is illuminated on the electrolyte side normally to the (100) plane of the photoelectrode, the long-wavelength edge of photosensitivity in the region of indirect optical transitions exhibits the same polarization dependence as the coefficient of optical absorption of $CdGa_2S_4$ (Fig. 2, curves *1–4*). This dependence manifests itself as a shift of the long-wavelength part of the spectra $\eta(\hbar\omega)$ to shorter wavelengths with polarization changing from $\mathbf{E} \parallel \mathbf{c}$ to $\mathbf{E} \perp \mathbf{c}$. The shift is due to the fact that the inequality $\eta^{\parallel} > \eta^{\perp}$ has now been satisfied. In the case of GaSe–$CdGa_2S_4$ heterostructures, the short-wavelength falloff of photosensitivity caused by the optical absorption in $CdGa_2S_4$ was found to be of opposite direction as compared to what could be expected from the inequality $\alpha^{\parallel} > \alpha^{\perp}$. Only for PECs, where the effect of absorption in $CdGa_2S_4$ on the photoconversion was excluded, did we find the correspondence between the anisotropies of α and η. In the case of correspondence between the processes of absorption and photoconversion in PECs, the inequality $\eta^{\parallel} > \eta^{\perp}$ is satisfied. The shift of the spectra $\eta(\hbar\omega)$ by ≈70–80 meV with radiation polarization changing from $\mathbf{E} \parallel \mathbf{c}$ to $\mathbf{E} \perp \mathbf{c}$ (Fig. 6, curves *1*, *2*) may be caused by the lift of degeneracy of the empty band and its splitting due to the natural tetragonal compression in $CdGa_2S_4$ crystals.

The coefficient of natural photopleochroism P_η was found to be positive in the region of indirect interband transitions in $CdGa_2S_4$. The largest value of P_η is ~50% at a photon energy of ~2.7 eV (Fig. 6, curve *3*), which is close to the energy of indirect interband transitions in $CdGa_2S_4$. With an increase in $\hbar\omega$ above 2.9 eV (Fig. 6, curve *3*), the coefficient of natural photopleochroism remains small ($P_\eta \simeq 0$) up to 3.4 eV, which may be due to the competition between the optical transitions with opposite selection rules. The amplitude of the negative photopleochroism coefficient increases to ~20% only when the photon energy approaches the energy of direct optical transitions This circumstance means that direct interband transitions in $CdGa_2S_4$ are allowed mainly for the polarization $\mathbf{E} \perp \mathbf{c}$. Unfortunately, detailed theoretical calculations of the band structure of $CdGa_2S_4$ crystals are lacking to date [2, 20–22]. Hence, the results we obtained cannot be compared with theory.

6. NATURAL-PROTEIN–$CdGa_2S_4$ STRUCTURES

The structures formed by bringing into contact a natural protein with the surface of $CdGa_2S_4$ wafers were prepared in the same way as in [23]. Measurements of such systems revealed broadband photosensitivity with spectral features similar to those considered above for PECs. The table lists the values of the highest photovoltaic sensitivity of the protein–$CdGa_2S_4$ structures illuminated on the protein side. The photosensitivity spectra of the structures under investigation also have a peak at $\hbar\omega^m$ ~ 3.7 eV. The result obtained suggests that a natural protein serves as an electrolyte in such structures.

7. CONCLUSION

Thus, photosensitive structures of several types were fabricated for the first time on the basis of single crystals of the $CdGa_2S_4$ ternary compound. These are heterostructures, surface-barrier structures, photoelectrochemical cells, and natural-protein–semiconductor heterocontacts. The photoelectric properties of the structures formed on $CdGa_2S_4$ single crystals were studied using natural and linearly polarized light. It is shown that the structures fabricated can be used as photoconverters of natural and linearly polarized light.

ACKNOWLEDGMENTS

This study was supported by the International Science and Technology Center, grant no. 2008.

REFERENCES

1. N. A. Goryunova, *Compound Diamond-Like Semiconductors* (Sovetskoe Radio, Moscow, 1968).
2. A. N. Georgobiani, S. I. Radautsan, and I. M. Tiginyanu, Fiz. Tekh. Poluprovodn. (Leningrad) **19**, 193 (1985) [Sov. Phys. Semicond. **19**, 121 (1985)].
3. A. A. Vaĭpolin, N. A. Goryunova, É. O. Osmanov, *et al.*, Dokl. Akad. Nauk SSSR **154**, 1116 (1964).
4. *Physicochemical Properties of Semiconductor Materials: A Handbook* (Nauka, Moscow, 1978).
5. F. A. Kröger, *The Chemistry of Imperfect Crystals* (Wiley, New York, 1964; Mir, Moscow, 1969).
6. I. V. Bodnar', V. Yu. Rud', and Yu. V. Rud', Fiz. Tekh. Poluprovodn. (St. Petersburg) **28**, 2137 (1994) [Semiconductors **28**, 1175 (1994)].
7. I. V. Bodnar, V. Yu. Rud', and Yu. V. Rud', Cryst. Res. Technol. **31S**, 261 (1996).
8. N. M. Makhtiev, Yu. V. Rud', and É. Yu. Salaev, Fiz. Tekh. Poluprovodn. (Leningrad) **12**, 1566 (1978) [Sov. Phys. Semicond. **12**, 924 (1978)].
9. Yu. A. Ukhanov, *Optical Properties of Semiconductors* (Nauka, Moscow, 1977).
10. Yu. V. Rud', Izv. Vyssh. Uchebn. Zaved. Fiz. **29** (8), 68 (1986).
11. V. D. Prochukhan and Yu. V. Rud', Fiz. Tekh. Poluprovodn. (Leningrad) **12**, 209 (1978) [Sov. Phys. Semicond. **12**, 121 (1978)].
12. F. P. Kesamanly, V. Yu. Rud', and Yu. V. Rud', Fiz. Tekh. Poluprovodn. (St. Petersburg) **30**, 1921 (1996) [Semiconductors **30**, 1001 (1996)].
13. A. G. Areshkin, V. F. Zhitar', S. I. Radautsan, *et al.*, Fiz. Tekh. Poluprovodn. (Leningrad) **13**, 337 (1979) [Sov. Phys. Semicond. **13**, 194 (1979)].

14. A. N. Georgobiani, Yu. V. Ozerov, S. I. Radautsan, and I. M. Tiginyanu, Fiz. Tverd. Tela (Leningrad) **23**, 2094 (1989) [Sov. Phys. Solid State **23**, 1221 (1989)].
15. P. Kivits, V. Wijnakker, J. Glassen, and J. Ceerts, J. Phys. C: Solid State Phys. **11**, 2361 (1978).
16. A. N. Georgobiani, A. N. Gruzintsev, and I. M. Tiginyanu, Kratk. Soobshch. Fiz., No. 2, 3 (1981).
17. A. N. Georgobiani, S. I. Radautsan, and I. M. Tiginyanu, Phys. Status Solidi A **69**, 513 (1982).
18. Yu. V. Rud' and M. A. Tairov, Fiz. Tekh. Poluprovodn. (Leningrad) **21**, 615 (1987) [Sov. Phys. Semicond. **21**, 377 (1987)].
19. V. Yu. Rud', Yu. V. Rud', and M. Serginov, Phys. Status Solidi A **121**, K171 (1990).
20. D. A. Guseĭnova, T. G. Kerimova, and R. Kh. Nani, Fiz. Tekh. Poluprovodn. (Leningrad) **11**, 1135 (1977) [Sov. Phys. Semicond. **11**, 670 (1977)].
21. A. N. Georgobiani and I. M. Tiginyanu, Kratk. Soobshch. Fiz., No. 2, 8 (1981).
22. V. N. Panyutin, B. É. Ponedel'nikov, A. É. Rozenson, and V. I. Chizhikov, Izv. Vyssh. Uchebn. Zaved. Fiz. **23** (8), 57 (1979).
23. V. Yu. Rud', Yu. V. Rud', and V. Kh. Shpunt, Zh. Tekh. Fiz. **70**, 114 (2000) [Tech. Phys. **45**, 255 (2000)].

Translated by Yu. Sin'kov

Semiconductors, Vol. 37, No. 11, 2003, pp. 1291–1295. Translated from Fizika i Tekhnika Poluprovodnikov, Vol. 37, No. 11, 2003, pp. 1329–1333.
Original Russian Text Copyright © 2003 by Nikitin, Nikolaev, Polushina, V. Rud', Yu. Rud', Terukov.

Photoelectric Phenomena in ZnO:Al–*p*-Si Heterostructures

S. E. Nikitin*, Yu. A. Nikolaev*, I. K. Polushina*, V. Yu. Rud', Yu. V. Rud'*, and E. I. Terukov***

**Ioffe Physicotechnical Institute, Russian Academy of Sciences, Politekhnicheskaya ul. 26, St. Petersburg, 194021 Russia*

e-mail: yuryrud@mail.ioffe.ru

***St. Petersburg State Polytechnical University, St. Petersburg, 195251 Russia*

Submitted January 20, 2003; accepted for publication January 21, 2003

Abstract—Al-doped zinc-oxide (ZnO:Al) films are obtained by magnetron sputtering. Based on an investigation of electrical properties of the films, it is shown that the electron density in these films is as high as 5×10^{20} cm^{-3} and is practically constant in the temperature range 77–300 K, which indicates high efficiency of doping ZnO with an Al impurity. It is found that the deposition of thin films ($d \approx 1$ μm) on the *p*-Si(111) surface leads to the formation of heterostructures with the highest photosensitivity of ~400 V/W at $T = 300$ K, which oscillates in the spectral range 1.3–3.5 eV. With the oblique incidence of linearly polarized radiation, induced pleochroism emerges in such heterostructures. The magnitude of pleochroism oscillates in the range 5–40% ($\theta \approx 75°$), which is associated with the interference phenomena in the ZnO films. The prospects of using the heterostructures obtained as highly selective photosensors of natural and linearly polarized radiation are considered. *© 2003 MAIK "Nauka/Interperiodica".*

High-conductivity transparent oxide films are finding increasingly wide application in optoelectronics. A substantial increase in the quantum efficiency of photoconversion of solar energy is attained by introducing an antireflection coating into a heterophotoconverter [1, 2]. Among such oxides, Al-doped ZnO films (ZnO:Al) occupy an important place [3–5]. This study belongs to this promising area of research and is devoted to the investigation of photoelectric processes in ZnO:Al heterostructures exposed to natural and linearly polarized radiation. With the fabrication of such structures, the effect of doping ZnO:Al films with an Er impurity on their electrical and photoelectric properties was also analyzed.

The heterostructures were obtained by the deposition of ZnO:Al films on the surface of polished wafers of single-crystal Si(100) of KDB-10 grade (*p*-Si:B with a resistivity of 10 Ω cm) with a thickness $d \approx 0.3$ mm. The ZnO:Al films were obtained by dc magnetron sputtering in Ar. In order to provide the necessary doping level, a sintered target of ZnO powder with an Al content of ~2.4 at % was used. According to the published data [3–5], the above process ensures the stoichiometric composition of the film. The Ar pressure during deposition was kept at $P = 0.5$ Pa, whereas the temperature of the substrate with the growing film was 40–50°C. The ZnO:Al films were deposited both on the Si substrates and on the polished substrates from fused quartz, whereas the ZnO:(Al, Er)–*p*-Si heterostructures were obtained by introducing a thin film of pure Er in the sputtering zone. The films obtained adhered quite well to the surfaces of Si and fused quartz. The process of doping depending on the modes of deposition of the ZnO:Al films was investigated by measuring the temperature dependences of the Hall coefficient $R(T)$ and conductivity $\sigma(T)$ by a dc compensation method in weak electric and magnetic fields in the temperature range 77–300 K. In order to measure the kinetic coefficients, ZnO:Al films ~1 μm thick were deposited on plates of fused quartz through a cross-shaped mask. The ohmic contacts to the ZnO:Al films were formed by soldering with pure In or by depositing Ag paste on the corresponding areas of the film. The typical dependence $R(T)$ for one of the films, which was obtained in the presence of Er, is shown in Fig. 1 (curve *1*). The

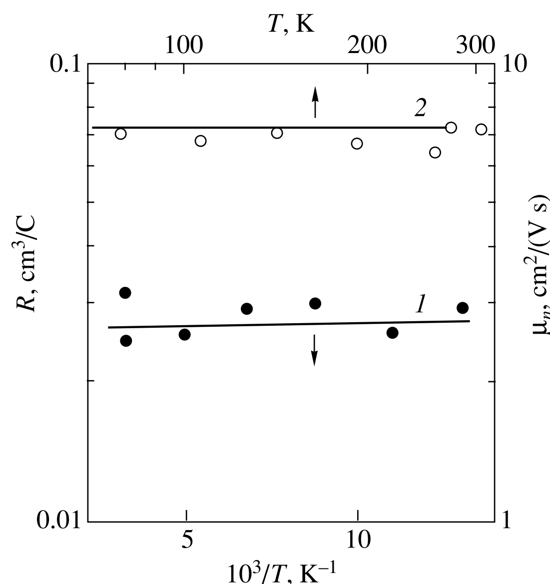

Fig. 1. Temperature dependences of (*1*) the Hall coefficient and (*2*) the electron Hall mobility in the ZnO:(Al, Er) layer (sample *1n*).

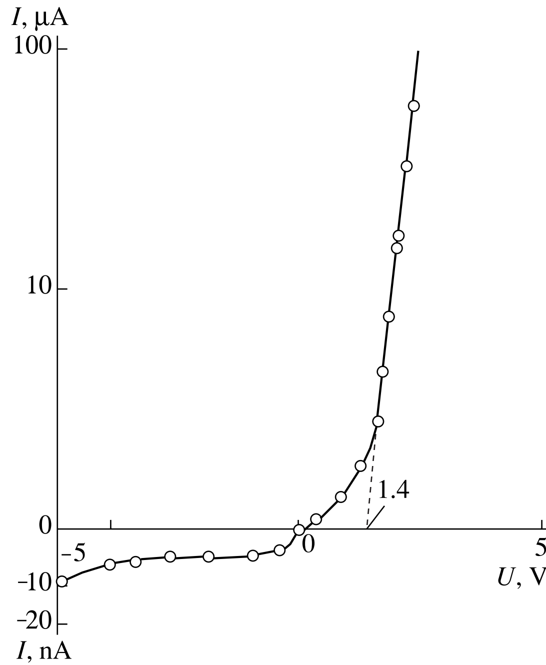

Fig. 2. Steady-state current–voltage characteristic of the ZnO:Al–*p*-Si heterostructure at $T = 300$ K. The conducting direction corresponds to the negative polarity of the external bias at the ZnO layer.

Hall coefficient and the calculated electron density in the range 77–300 K are practically independent of temperature; the electron density in the ZnO:Al films usually is in the range ((2.5–5) $\times 10^{20}$ cm^{-3} at $T = 300$ K and is insensitive to the presence of Er in the sputtering zone. The conductivity of the ZnO:Al films in the range 77–300 K does not depend on temperature and is equal to 230–250 Ω^{-1} cm^{-1} for various samples. The Hall electron mobility in such samples is $\mu \approx 5$–6 cm^2/(V s), which is characteristic of heavily doped ZnO. The results of measurements of kinetic coefficients for the ZnO:Al films suggest that a high doping level is attained, which is necessary for their application in developing various facilities and devices of semiconductor electronics. In addition, we may assume that the high film conductivity is determined mainly by the Al impurity, whereas the presence of Er in the reaction zone has practically no effect on the electrical properties of the ZnO:Al films obtained.

The measurements of the steady-state current–voltage (*I–V*) characteristics of the ZnO:Al–*p*-Si heterostructures obtained showed that the process used ensures the attainment of high degree of rectification, which may be characterized by the factor $K \approx 10^3$–10^4. This factor is defined as the ratio of the forward current to the reverse current at the bias voltages $U \leq 5$ V. The conducting direction for the heterostructures obtained corresponds to the negative polarity of the external bias at the ZnO:Al layer. The typical steady-state *I–V* characteristic for one of the heterostructures obtained is shown in Fig. 2. At voltages $U \geq 2$ V, the forward portion of the *I–V* characteristic follows the relationship

$$I = (U - U_0)/R_0, \quad (1)$$

where the residual resistance $R_0 \cong (4–8) \times 10^4\ \Omega$ and the cutoff voltage $U_0 \cong 0.6$–1.4 V for various structures (see table). It should be noted that the lowest R_0 values were characteristic of the heterostructures obtained by the deposition of ZnO:Al films in the presence of Er. For voltages $U < 0.1$ V, the forward current in the heterostructures obtained grew exponentially according to the relationship

$$I = I_0[\exp(eU/\beta kT) - 1], \quad (2)$$

where the diode factor $\beta > 10$. The largest β values are usually inherent in the heterostructures obtained by deposition of the ZnO:Al films in the presence of Er. Large values of β reflect the effect of high series resistance on the charge transport in such structures, which does not allow one to draw an definitive conclusion about the nature of the forward current.

A photovoltaic effect in the ZnO:Al–*p*-Si structures prevails when they are illuminated on the wide-gap ZnO:Al oxide side. The highest voltaic photosensitivity $S \approx 400$ V/W at $T = 300$ K is usually found for the heterostructures containing ZnO:Al films that were deposited without introducing Er into the reaction zone (see table). The typical spectral dependences of the relative quantum efficiency of photoconversion η in the presence of Er (curve *1*) and in its absence in the reaction zone (curve *2*) are shown in Fig. 3. It can be seen that the η spectra for the heterostructures obtained are similar, and their specific features amount to the following. The photosensitivity of the heterostructures obtained is of the broad-band type and is observed in the range 1.1–3.5 eV. The long-wavelength boundary of η is determined by the band-to-band absorption in the Si substrate. Therefore, a sharp rise in the photosensitivity is observed for the photon energies $h\omega > 1.1$ eV. The full half-width of the photosensitivity spectra $\delta \approx 1.7$–

Photoelectric properties of ZnO–*p*-Si heterostructures at 300 K. The illumination is from the side of the ZnO films using nonpolarized radiation

Heterostructures	R_0, Ω	U_0, V	δ, eV	S_u^m, V/W	S_I^m, mA/W	$\hbar\omega^m$, eV
ZnO:Al–*p*-Si	2.5×10^4	1.4	1.68	400	10	1.3, 1.62, 2.04, 2.55, 2.82, 3.15, 3.55
ZnO:Al, Er–*p*-Si	7×10^4	0.6	1.71	35	2	1.41, 1.85, 2.35, 2.76, 3.15

1.8 eV (see table). In addition, distinct and practically equidistant maxima and minima of η in the region of highest photosensitivity of these heterostructures are observed. It is reasonable to relate the existence of these specific features to the interference of the incident radiation in the ZnO:Al films. The ratio of the peak efficiency of photoconversion Δ (η^{max}) to the lowest efficiency (η^{min}) for the structures investigated is $\Delta = \eta^{max}/\eta^{min} \approx 1.5$–$1.6$. This rather large value of Δ characterizes the ZnO:Al layers obtained in the technological process developed as rather homogeneous and of high quality. It can be seen from the table and Fig. 3 (curves *1* and *2*) that the spectral positions of the maxima and minima in the $\eta(\hbar\omega)$ dependences for two different structures are different. This circumstance may be caused by differences in the thickness d of the ZnO:Al films deposited. From the spectral dependences $\eta(\hbar\omega)$, according to the formula for the refractive index n [6]

$$n = \lambda_m \lambda_{m-1}/2d(\lambda_m - \lambda_{m-1}), \qquad (3)$$

where λ_m is the wavelength at η^{max} and m is the peak number, using the n value known for ZnO:Al [7], the film thickness was estimated to be $d \approx 0.7$–0.9 µm. These values are in satisfactory agreement with the data obtained by measuring the thickness of the ZnO:Al films.

The short-wavelength decay of η for the heterostructures obtained becomes substantial in the region of photon energies $\hbar\omega > 3.2$ eV, which corresponds to the onset of band-to-band absorption in ZnO:Al [7]. The very fact that heterostructures with a pronounced interference pattern in the spectra of η are obtained may be used in developing natural radiation sensors, whose parameters are controlled by the deposition conditions of the ZnO:Al films.

The investigations of the photosensitivity of heterostructures obtained in linearly polarized radiation demonstrated that the polarization photosensitivity emerges only under conditions of the oblique radiation incidence on the outer mirror plane of the ZnO:Al film. This, in turn, allows one to relate it to the induced photopleochroism [8]. At incidence angles $\Theta > 0$, the short-circuit photocurrent begins to follow the periodic law [8] depending on the azimuth angle φ between the vector of the electric wave **E** and the plane of incident radiation(PIR):

$$i = i^p \cos^2\varphi + i^s \sin^2\varphi. \qquad (4)$$

Here, i^p and i^s are the photocurrents of the heterostructure for *p*-polarized and *s*-polarized incident radiation, i.e., for **E** ∥ PIR and **E** ⊥ PIR, respectively. Typical spectra of η for the region of high photosensitivity of the ZnO:Al–Si heterostructures at $\Theta \approx 75°$ are shown in Fig. 3 (curves *3*, *4* and *5*, *6*). A comparison of these spectra clearly shows that the photosensitivity η^p relative to η^s varies in the antiphase. Moreover, the η^p maximum corresponds to the η^s minimum, and vice versa. As a result, it is possible to distinguish the photon energies at which the values of η^p and η^s diverge to the greatest extent and then converge until they “touch”. With increasing photon energy, these specific features alternate in accordance with the photosensitivity oscillations associated with the interference-controlled photoactive radiation absorption in the active region of the heterostructures and the subsequent separation of photogenerated carriers in the electric field. The ratio Δ in the photosensitivity spectra is larger for the *s* wave, which is in agreement with the behavior of the induced pleochroism established for other heterostructures [8].

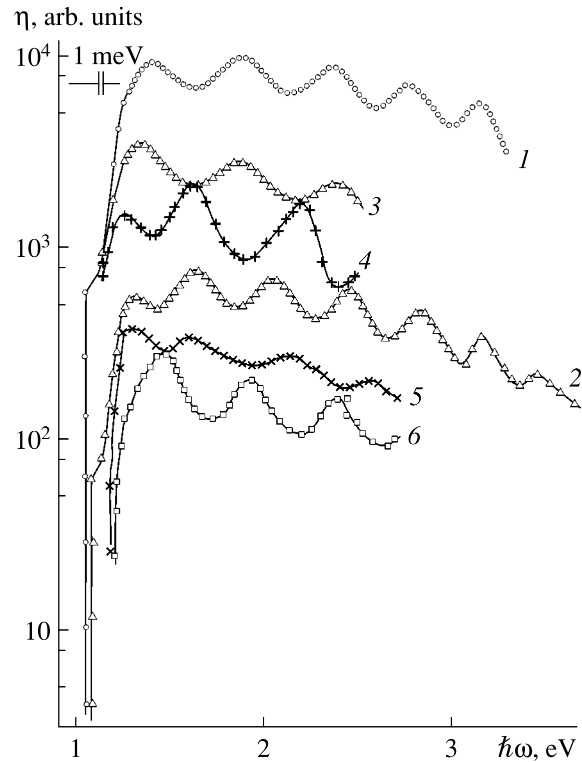

Fig. 3. Spectral dependences of the relative quantum efficiency of photoconversion for the ZnO–*p*-Si heterostructures (*1*, *3*, and *4* correspond to the ZnO:(Al, Er) layer; *2*, *5*, and *6* correspond to the ZnO:Al layer; $\theta = 0$) exposed to natural and linearly polarized radiation (*3* and *5* correspond to *p*-polarization; *4* and *6* correspond to *s*-polarization; $\theta = 75°$). *1* and *2* are normalized to the absolute maximum, and *3–6* are normalized to the maximum of η in the *p*-polarization. To exclude overlapping, the η spectra are shifted in parallel to each other along the ordinate.

Figure 4 shows examples of typical dependences of photocurrents i^p and i^s, as well as of the coefficient of the induced photopleochroism P_I, on the angle of incidence Θ for two characteristic photon energies, which correspond to the largest divergence (curves *1–3*) and convergence (curves *4–6*) in the η^p and η^s spectra for one of the heterostructures. From the point of view of angular dependences of photocurrents, which are shown in Fig. 4, these situations are basically different.

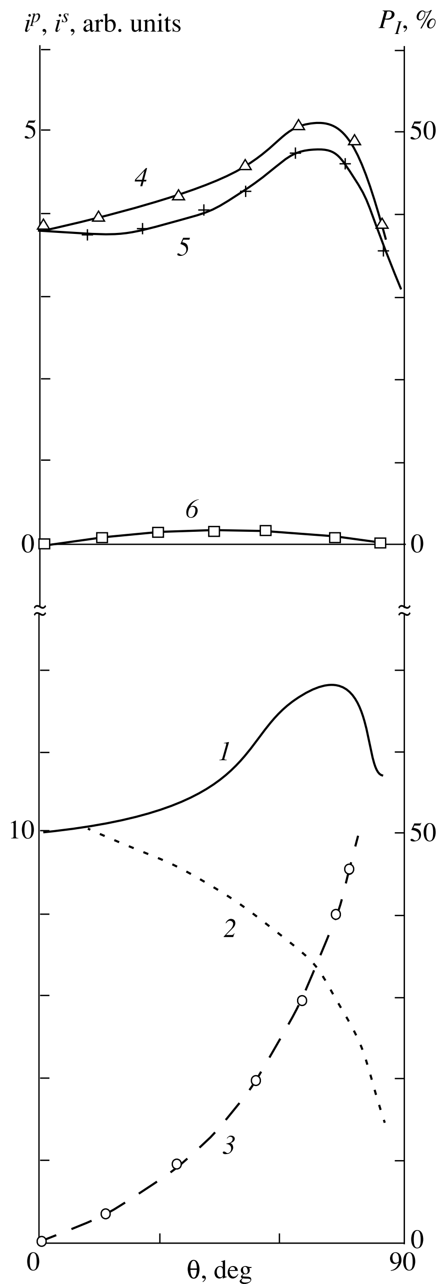

Fig. 4. Photocurrents and the coefficient of induced pleochroism in relation to the angle of incidence of linearly polarized radiation on the receiving ZnO:(Al, Er) plane of the ZnO:Al, Er–p-Si heterostructure at T = 300 K ($\hbar\omega$ = (*1–3*) 1.24 eV; (*4–6*) 1.36 eV; radiation polarization: *1* and *4* correspond to p polarization; *2* and *5* correspond to s polarization).

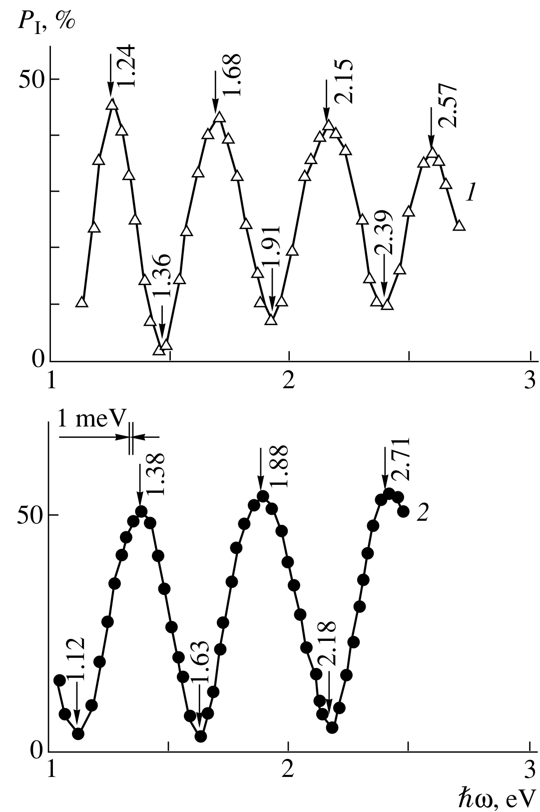

Fig. 5. Spectral dependences of the induced-photopleochroism coefficient for the ZnO–p-Si heterostructures with an oblique incidence of linearly polarized radiation on the ZnO side at T = 300 K (*1* corresponds to the n-ZnO:Al layer, θ = 75°; *2* corresponds to the ZnO:(Al, Er) layer, θ = 80°).

In one of them, the angular dependences of photocurrents are conventional (Fig. 4, curves *1–3*). In fact, due to a reduction of the losses for the reflection of the wave at $\Theta > 0$, the photocurrent i^p initially increases, passes through the maximum, and finally decreases. At the same time, the photocurrent i^s decreases steadily with increasing Θ over the entire Θ range investigated, whereas the coefficient of the induced photopleochroism follows the parabolic law [8]

$$P_I \propto \Theta^2 \quad (5)$$

and, for example, for $\Theta = 70°$ attains the value P_I = 40%. This value of P_I is in accordance with the theoretical estimation [8], in which the refractive index for ZnO:Al [7] was taken into account. For the region of the closest convergence of the η^p and η^s spectra, the angular dependences of photocurrents become similar (Fig. 4, curves *4*, *5*). As a result, the P_I magnitude drops abruptly relative to the theoretical estimate for ZnO:Al, which was made disregarding the interference (Fig. 4, curve *6*). The shape of the angular dependences for i^p and i^s (Fig. 4, curves *4*, *5*) allows one to assume that a decrease in the reflection losses due to the interference blooming of the receiving plane of the heterostructure by the ZnO:Al film occurs both for the p wave and for the s wave. The typical spectra of the induced-photopleochroism coefficient P_I for the heterostructures, which include the ZnO:Al films obtained in various technological processes and Si substrates, are shown in Fig. 5. These spectra are similar, and from the point of view of previous studies [8–11], there are grounds to believe

that they result from interference of the linearly polarized radiation in the ZnO:Al films. The distinctions observed in the values of Δ and the energy positions of extrema in the $\eta(\hbar\omega)$ spectra may be a consequence of the effect of fabrication conditions on the deposition of ZnO:Al films.

The common specific feature of the induced photopleochroism is the existence of oscillations of the P_I coefficient in the range from the highest to the lowest value, when the induced photopleochroism practically vanishes due to the convergence of η^p and η^s. Both of these cases are of apparent practical interest. The induced photopleochroism, which is close to the theoretical estimate, allows one, on the one hand, to use the structures obtained as selective photoanalyzers of linearly polarized radiation. On the other hand, the fact that the induced photopleochroism vanishes can be used in monitoring the blooming of prepared photoconverters, specifically, the spectral range and the detailed structure of the spectra of the induced photopleochroism.

Thus, heavily doped ZnO:Al layers are obtained by magnetron sputtering. Their deposition on the surface of single-crystal Si allows one to obtain ZnO:Al–*p*-Si heterostructures with the highest photosensitivity in the range of 1.3–3.4 eV. It is found that the induced photopleochroism can be used in the development of selective semiconductor sensors of linearly polarized radiation.

REFERENCES

1. N. Mardeesich, in *Proceedings of 15th IEEE Photovoltaic Specialists Conference, Kissimee* (IEEE, 1981), No. 4, p. 446.
2. M. M. Koltun, *Optics and Metrology of Solar Radiation* (Nauka, Moscow, 1985).
3. T. Minami, T. Yamamoto, and T. Miata, Thin Solid Films **366**, 63 (2000).
4. J. Hu and R. C. Gordon, J. Appl. Phys. **71**, 880 (1992).
5. H. Fujiwara and M. Okuda, Jpn. J. Appl. Phys. **35L**, 5457 (1996).
6. G. S. Landsberg, *Optics* (Nauka, Moscow, 1976).
7. *Physicochemical Properties of Semiconductors: Handbook* (Nauka, Moscow, 1978).
8. F. P. Kesamanly, V. Yu. Rud', and Yu. V. Rud', Fiz. Tekh. Poluprovodn. (St. Petersburg) **33**, 513 (1999) [Semiconductors **33**, 483 (1999)].
9. V. M. Botnaryuk, A. V. Koval', V. Yu. Rud', *et al.*, Fiz. Tekh. Poluprovodn. (St. Petersburg) **31**, 800 (1997) [Semiconductors **31**, 677 (1997)].
10. V. Yu. Rud', Yu. V. Rud', and H. W. Schock, Fiz. Tekh. Poluprovodn. (St. Petersburg) **33**, 484 (1999) [Semiconductors **33**, 463 (1999)].
11. Yu. A. Nikolaev, V. Yu. Rud', Yu. V. Rud', *et al.*, Fiz. Tekh. Poluprovodn. (St. Petersburg) **36**, 1128 (2002) [Semiconductors **36**, 1048 (2002)].

Translated by N. Korovin

Semiconductors, Vol. 37, No. 11, 2003, pp. 1296–1298. Translated from Fizika i Tekhnika Poluprovodnikov, Vol. 37, No. 11, 2003, pp. 1334–1336.
Original Russian Text Copyright © 2003 by Gadzhialiev, Pirmagomedov.

SEMICONDUCTOR STRUCTURES, INTERFACES, AND SURFACES

The Thermoelectric Power of a Semiconductor *p–n* Heterojunction

M. M. Gadzhialiev* and Z. Sh. Pirmagomedov
Amirkhanov Institute of Physics, Dagestan Scientific Center, Russian Academy of Sciences, ul. 26 Bakinskikh Komissarov, Makhachkala, 367003 Russia
**e-mail: Kamilov@datacom.ru*
Submitted February 20, 2003; accepted for publication March 4, 2003

Abstract—Extended Ge–GaAs *p–n* heterojunctions were fabricated and studied. The thermoelectric power of the heterojunction was measured as a function of the temperature difference at the structure ends, which was varied from 10 to 180 K, while the average temperature was maintained constant at 300 K. It is found that experimental data obtained at a large temperature gradient are consistent with theoretical predictions that take into account the emergence of minority charge carriers due to thermal emission. *© 2003 MAIK "Nauka/Interperiodica".*

The thermoelectric properties of *p–n* junctions and heterojunctions have been studied previously [1–6]. It was found that the thermoelectric power of heterostructures is contributed by the bulk thermoelectric power, the Benedix voltage for the *p*- and *n*-type regions, and the barrier thermoelectric power at the heteroboundary α_b itself. It was ascertained that at a small temperature difference (such that $E_g\Delta T \ll kT_0^2$, where E_g is the band gap of a narrow-gap semiconductor, ΔT is the temperature difference at the structure ends, T_0 is the heterojunction (HJ) temperature, and k is the Boltzmann constant), the calculated values of the HJ's effective thermoelectric power α_{eff} were consistent with experimental data.

In this paper, we report the results of studying thermoelectric power in a situation where the inequality $E_g\Delta T > kT_0^2$ is satisfied, i.e., where there is a large temperature gradient.

In order to perform the experiment, we fabricated extended Ge–GaAs *p–n* heterostructures in which the sizes of the base regions $(-A)(-d_1)$ and (d_2B) were much larger than the width of the space-charge regions $(-d_10)$ and $(0d_2)$; i.e., we had $(-A)(-d_1) \gg (-d_10)$ and $(d_2B) \gg (0d_2)$ (see Fig. 1).

Heterojunctions were formed using the method suggested by Anderson [7]. Rectangular platelets with dimensions of $0.1 \times 1 \times 3$ mm^3 were cut from *n*-GaAs and *p*-Ge. After grinding and polishing, the platelets of *n*-GaAs and *p*-Ge were superimposed on one another so that the total length was 4 mm. The samples were then transferred to a vacuum chamber; in the region of superposition of platelets on one another, a large temperature gradient was formed in an atmosphere of flowing helium. As a result, the material with a higher melting point (gallium arsenide) was found to be on the high-temperature side. As the temperature gradient increased and the germanium plane adjacent to gallium arsenide began to melt, the heating was switched off immediately; the molten layer then recrystallized and the heterojunction was formed. X-ray diffraction analysis showed that the recrystallized interfacial region between germanium and gallium arsenide is single-crystalline and interfacial planes of gallium arsenide and germanium are rotated by no more than 3° with respect to each other.

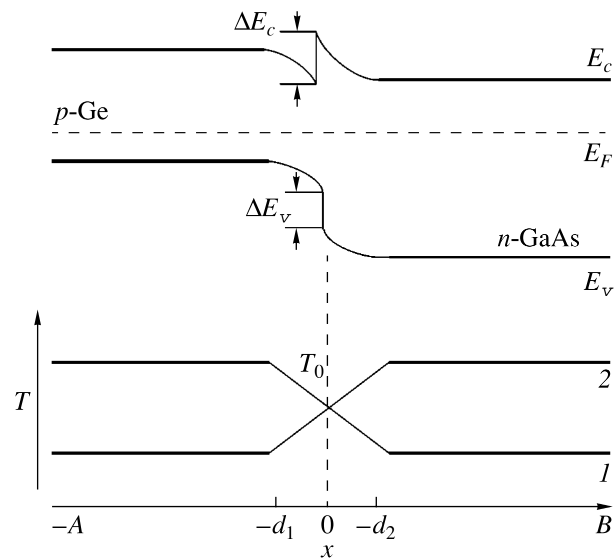

Fig. 1. The energy-band diagram of a Ge–GaAs *p–n* heterojunction in the absence of the temperature gradient and two variants of the temperature distribution along the *x* axis: E_c and E_v are the conduction- and valence-band edges, ΔE_c and ΔE_v are the corresponding band offsets at the heteroboundary, and E_F is the Fermi level; curve *1* corresponds to the thermal-flux direction (+) and curve *2* corresponds to the direction (–).

1063-7826/03/3711-1296$24.00 © 2003 MAIK "Nauka/Interperiodica"

The current–voltage (*I–V*) characteristic of the above-described Ge–GaAs heterojunctions (Fig. 2) is similar to that obtained by Anderson [7] at a heterojunction formed by epitaxy of germanium onto the gallium arsenide surface [7]; this similarity indicates that the heterojunctions are of high quality.

The heterojunctions formed by the above-described method were transferred to a setup for measuring the thermoelectric power at a large temperature gradient [8].

We measured the dependence of thermoelectric power generated by the Ge–GaAs heterojunction on the temperature gradient at the same average heterojunction temperature if the thermal flux is directed either (i) from germanium to gallium arsenide or (ii) from gallium arsenide to germanium.

It was shown by Balmush *et al.* [4] that, in contrast to the barrier-layer photovoltage, the barrier thermoelectric power α_b can exhibit not only the conducting (forward) direction (with the sign "+" at the *p*-type region and a minus sign at the *n*-type region) but also the blocking (reverse) direction, which depends on the sign of the temperature gradients and on the physical parameters of the *p–n* structure. In what follows, the direction of the thermal flux from germanium to gallium arsenide is denoted by sign "+" and the reverse direction of this flux is denoted by "–".

In Fig. 3, we show dependences of thermoelectric power on the magnitude of the difference between temperatures of the hot and cold ends of the HJ at the same average temperature equal to 300 K. Curve *3* was obtained at a thermal-flux direction (+), and curve *4* was obtained at a thermal-flux direction (–). Curve *1* represents the ΔT dependence of $\alpha_{\text{eff}}^{\text{av}}$ averaged over two thermal-flux directions.

The values of effective thermoelectric power calculated using the formula derived by Lidorenko *et al.* [3] are also shown in Fig. 3 (curve *2*); this formula is written as

$$\alpha_{\text{eff}} = \frac{K}{e}\frac{T_0}{\Delta T}\ln\left\{1+\left(1+\frac{d_1}{L_n}\right)\times\left[\left(1+\frac{3\Delta T}{T_0}\right)e^{E_{g1}\Delta T/kT_0^2}-1\right]\right\}, \quad (1)$$

where T_0 is the average temperature of an HJ, ΔT is the temperature difference between the hot and cold HJ ends, E_{g1} is the band gap of the narrow-gap semiconductor in the heteropair (E_{g1} = 0.74 eV for germanium), d_1 is the width of the space-charge region in the narrow-gap semiconductor, and L_n is the diffusion length of the minority charge carriers.

Formula (1) is valid only if ΔT is large, in which case the minority charge carriers are thermally generated in the semiconductor bulk. As mentioned above, the temperature differences are recognized as large if the inequality $E_g\Delta T > kT_0^2$ is satisfied. In the case under consideration, this inequality is satisfied if $\Delta T > 80$ K. Therefore, the values of α_{eff} calculated using formula (1) are shown in Fig. 3 only for $\Delta T \geq 80$ K. As can be seen from Fig. 3, the calculated values of α_{eff} are close to experimental data in the region where $\Delta T > 80$ K. This fact indicates that the situation where the determining role in the HJ thermoelectric power is played by the thermoelectric power of minority charge carriers gener-

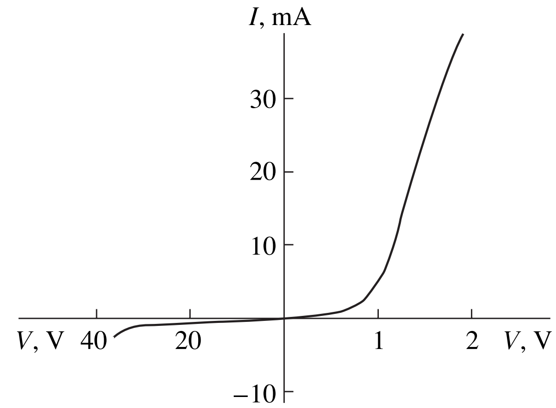

Fig. 2. The current–voltage $I(V)$ characteristic of a Ge–GaAs *p–n* heterostructure at 300 K.

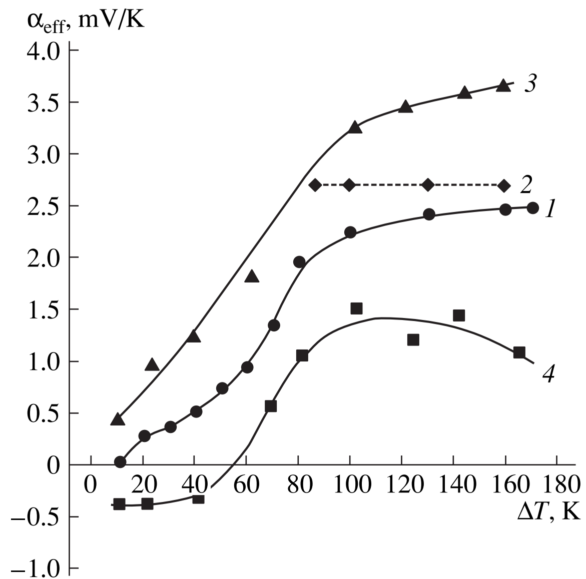

Fig. 3. Dependences of thermoelectric power for a Ge–GaAs *p–n* heterojunction on the temperature difference ΔT at the heterostructure ends at an average temperature of 300 K: (*1*) average values of thermoelectric power $\alpha_{\text{eff}}^{\text{av}}$; (*2*) the results of calculation of $\alpha_{\text{eff}}^{\text{av}}$ based on formula (1) for large temperature gradients; (*3*) α_{eff} at the thermal flux (+); and (*4*) α_{eff} at the thermal flux (–).

ated by the temperature gradient is realized only if this gradient is large.

In the case of the aforementioned procedure for processing the experimental data, the effective thermoelectric power α_{eff}^{av} primarily includes only the barrier thermoelectric power α_b, since all the other components (the bulk thermoelectric powers of the base regions and the Benedix thermoelectric power for the *p*- and *n*-type regions) cancel each other out in the course of averaging as a consequence of the sign reversal of the above components when the thermal-flux direction is reversed. The sign of the barrier thermoelectric power is also reversed. However, the values of α_b differ for the thermal fluxes (+) and (–) as a consequence of the fact that the concentrations of the minority charge carriers coming from *p*-Ge to *n*-GaAs and vice versa are dissimilar for opposite directions of thermal fluxes; as a result, the barrier thermoelectric powers α_b, which are different in magnitude and opposite in sign, appear in both cases, so that we obtain nonzero average values α_g of α_{eff}^{av}.

On the basis of the results obtained, we may state that the values of α_{eff} calculated using formula (1) are consistent with experimental data for α_{eff}^{av} at large values of ΔT.

REFERENCES

1. B. L. Sharma and R. K. Purohit, *Semiconductor Heterojunctions* (Pergamon Press, Oxford, 1974; Sovetskoe Radio, Moscow, 1979).
2. J. Tauc, *Photo- and Thermoelectric Effects in Semiconductors* (Pergamon Press, Oxford, 1962; Inostrannaya Literatura, Moscow, 1962).
3. N. S. Lidorenko, I. I. Balmush, Z. M. Dashevskiĭ, *et al.*, Dokl. Akad. Nauk SSSR **272**, 855 (1983) [Sov. Phys. Dokl. **28**, 888 (1983)].
4. I. I. Balmush, Z. M. Dashevskiĭ, and A. I. Kasiyan, Fiz. Tekh. Poluprovodn. (St. Petersburg) **29**, 1796 (1995) [Semiconductors **29**, 937 (1995)].
5. I. I. Balmush, Z. M. Dashevskiĭ, and A. I. Kasiyan, *Thermoelectric Effects in Multilayered Semiconductors* (Shtiintsa, Kishinev, 1992).
6. R. H. Rediker, S. Stopek, and J. H. R. Ward, Solid-State Electron. **7**, 621 (1964).
7. R. L. Anderson, Solid-State Electron. **5**, 341 (1962).
8. M. M. Gadzhialiev and V. A. Elizarov, Fiz. Tekh. Poluprovodn. (St. Petersburg) **32**, 1313 (1998) [Semiconductors **32**, 1168 (1998)].

Translated by A. Spitsyn

Semiconductors, Vol. 37, No. 11, 2003, pp. 1299–1302. Translated from Fizika i Tekhnika Poluprovodnikov, Vol. 37, No. 11, 2003, pp. 1337–1340.
Original Russian Text Copyright © 2003 by Oleĭnich-Lysyuk, Beshley, Fodchuk.

On the Influence of a Si Single-Crystal Real Surface on the Low-Frequency Internal Friction and the Behavior of an Effective Shear Modulus

A. V. Oleĭnich-Lysyuk, N. P. Beshley, and I. M. Fodchuk

Chernovtsy National University, Chernovtsy, 58012 Ukraine

Submitted February 11, 2003; accepted for publication March 4, 2003

Abstract—The spectra of low-frequency internal friction and the behavior of the effective shear modulus $G_{eff}(T)$ in a Czochralski grown silicon single crystal were investigated after mechanical and chemical–mechanical treatment of the surface and after natural aging at room temperature over a long period of time. The mechanical treatment of the Si surface was shown to initiate unusual structural phase transitions accompanied by an inverse hysteresis in the $G_{eff}(T)$ dependence. Such a behavior of $G_{eff}(T)$ is assumed to be associated with the formation of incommensurate phases. It was also found that aging at room temperature for more than 10000 h leads to the onset of decomposition of the supersaturated solid solution of oxygen in silicon and to the generation of substantial stresses that initiate structural phase transitions in the samples. *© 2003 MAIK "Nauka/Interperiodica".*

It is well known that fabrication of the majority of semiconductor devices on the basis of single-crystal silicon is, one way or another, associated with the treatment of its surface. The result of this treatment (mechanical, chemical, thermal, etc.) is far from always predictable and unambiguous. Many studies [1–4] were concerned with investigating this complicated problem. However, today many questions remain open to discussion, in particular, regarding the state and structure of a thin oxide layer that forms on the real silicon surface in the course of technological operations [1–3], how this treatment affects the structure of the regions adjoining the surface, and many others [4].

In this study, we attempt to investigate the influence of the state of a Si single-crystal real surface obtained as a result of certain technological operations (polishing, chemical–mechanical polishing, oxidation in air at room temperature T_{room}, etc.) on the low-frequency internal friction (LFIF) and the behavior of an effective shear modulus G_{eff}.

The internal friction (IF) was investigated using a semiautomatic relaxometer of the inverse-torsion-pendulum type at frequencies on the order of 1–3 Hz in a pressure of ~10^3 Pa and for amplitudes of external strains $\gamma = (2.5–3) \times 10^{-5}$. Simultaneously with the investigation of elastic-energy absorption, we measured the squared frequency of natural torsion vibrations (f^2), which is known to be proportional to the effective shear modulus G_{eff}.

We selected a Czochralski ⟨111⟩ silicon single crystal as the object of study. The samples were cut in the shape of $1.5 \times 1.5 \times (80–90)$-$mm^3$ parallelepipeds from highly perfect silicon single crystals in the direction perpendicular to the growth direction so that the faces parallel to the (111) plane lay along the long axis of the sample. The single crystal was grown and all the technological operations associated with the fabrication of the samples, apart from artificial oxidation at 200°C, were performed under production conditions using conventional technologies. In parallel with measuring the IF, the aged samples–witnesses were used to study their microhardness (H_μ). The microhardness H_μ was measured using a PMT-3 microhardness meter at room temperature according to the conventional procedure with an indenter load $P = 100$ g. The results of measurements were averaged over 10 runs (10–15 measurements in various areas of the sample). The relative errors were less than 1% in measuring the internal friction Q^{-1} and less than 0.1% for f^2.

Three groups of samples were investigated (three samples in each group) after various types of treatment of the silicon surface:

the first group included the samples after mechanical treatment with an ASM-1/0 diamond paste when fabricating "silicon straw," i.e., parallelepipeds of $1.5 \times 1.5 \times (80–90)$ mm^3;

the second group included the samples after a complete series of chemical–mechanical treatment under the production conditions; and

the third group included the samples prepared in the same way as the second group but after natural aging in air at temperatures of T_{room} for more than 10000 h.

The typical temperature dependences of the internal friction and the squared frequency f^2 are shown in Figs. 1 and 2 for the first-group samples.

As can be seen, the mechanical treatment of the single-crystal silicon in the course of fabricating the sam-

1063-7826/03/3711-1299$24.00 © 2003 MAIK "Nauka/Interperiodica"

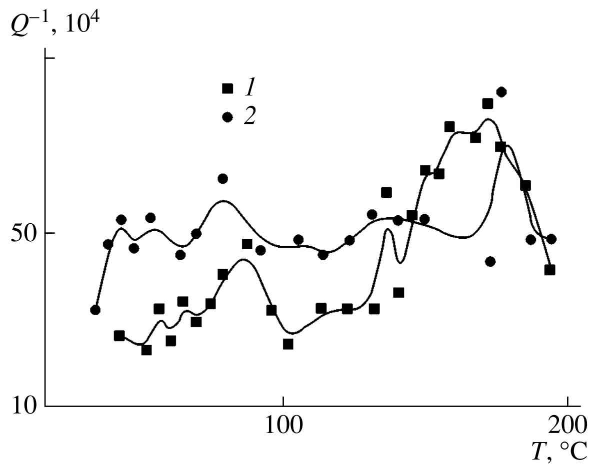

Fig. 1. Temperature dependences of a low-frequency internal friction for the first-group samples measured during (*1*) heating and (*2*) cooling.

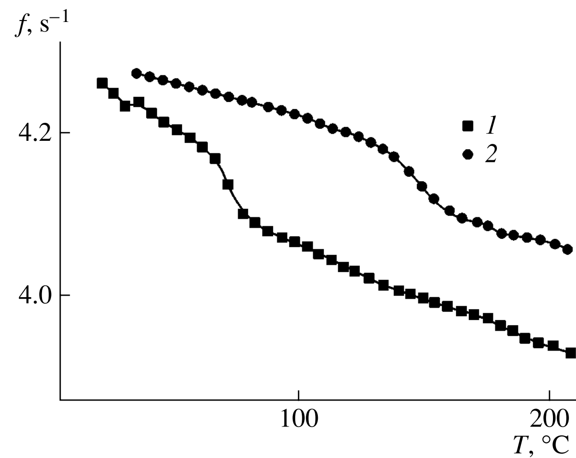

Fig. 2. Temperature dependences of the squared frequency f^2 of natural torsional vibrations for the first-group samples measured during (*1*) heating and (*2*) cooling.

ples leads to the initiation of an anomalous, nonrelaxational, IF within 20–200°C accompanied by a stepwise modification of the $G_{\rm eff}(T)$ temperature dependence and by an "inverse" temperature hysteresis of the modulus, which is unusual for structural phase transformations (SPTs): the curves of heating pass much lower and to the left of the curves of cooling. This behavior of the modulus is almost completely reversible. However, each subsequent cycle of heating in the range 20–200°C leads to a certain reduction in the absorption level and to a narrowing of the $G_{\rm eff}(T)$ loop. For example, the degree of loop unclosure $(\Delta f^2/f^2)_T$ after two to three cycles decreases almost by half. It should be noted that such temperature behavior of the modulus is characteristic of polytype transformations with the involvement of incommensurate structures [5, 6]; this behavior is also affected by the relaxation of stresses and the relaxation processes induced by defects. These defects are generated as a result of the mechanical treatment of the silicon surface, since the general level of IF decreases during the thermocycling and certain peaks disappear from the spectra of elastic-energy absorption. However, the SPTs themselves remain and do not disappear even after removing the strained layer at a depth from 40 to 70 μm. In this case, the IF level decreases by almost an order of magnitude, and the absorption character is somewhat modified. The series of peaks in the range 20–200°C transforms into a single poorly discernible peak in the region of 20–150°C. In this case, the dependence $G_{\rm eff}(T)$ is modified to a much lesser extent. The inverse hysteresis of the modulus is retained when the loop is opened to a somewhat lesser degree $(\Delta f^2/f^2)_T$ as compared with the initial one (Fig. 3, curves *1*, *2*).

The aging of silicon in air at $T_{\rm room}$ for a long time leads to an abrupt increase in the absorption level (by almost a factor of 100) and to the appearance of a region of two-lobe hysteresis at the $G_{\rm eff}(T)$ curves: below 150°C, the hysteresis is conventional and characteristic of the first-order phase transition; above 150°C, the hysteresis is inverse. The $G_{\rm eff}(T)$ behavior is virtually completely reversible in this case.

Such an anomalous increase in IF and the modifications in the shear-modulus behavior may be a consequence of the initiation of substantial stresses arising either in the samples during the aging at $T_{\rm room}$, or as a result of the decomposition of a supersaturated solid solution (SSS) of oxygen in silicon, or due to oxidation of the sample surface [1]. In order to clarify the possible origin of these stresses, the third-group samples were annealed at 400°C (over various periods of time) to promote the processes of oxygen release from the SSS. After such a treatment, the LFIF of the samples abruptly decreases (by more than a factor of 100), the absorption peak is located in the region of 150°C, and the two-lobe feature of the $G_{\rm eff}(T)$ curves is retained with the only difference that the degree of loop opening decreases by almost an order of magnitude, while the shape of the $G_{\rm eff}(T)$ dependences becomes stepwise (Fig. 3, curves *3*, *4*). It is likely that the aging at $T_{\rm room}$ for a long time (more than 10000 h) initiated the oxygen release from the supersaturated solid solution in the third-group samples; we fixed the earliest stages of this process (probably, the stage of formation of the Guinier–Preston bands), which are known to be accompanied by the initiation of appreciable stresses in the crystal [7]. The measurements of microhardness for the control samples subjected to the treatment at 400°C show that, if the treatment time increases, the value of H_μ first slightly rises from 1150 ± 33 kg/mm^2 to 1250 ± 35 kg/mm^2 and, then, decreases down to (1000 ± 32) kg/mm^2; this behavior agrees well with the data for LFIF and corroborates our assumptions about the origin of the generated stresses. In fact, the treatment at 400°C, as follows from the data of [4], leads to the isolation of SiO_x intermediate phases, which are better

known as quenched-in donors as thermodonors (TD-1), thus decreasing the stresses associated with this process. In our opinion, of more interest are the results of the effect of the decomposition of the SSS of oxygen on the SPTs, which apparently proceed both on the Si surface and in its surface layers. In fact, Shmyt'ko *et al.* [8] found that new Si modifications with a relatively high stability were formed on the Si surface during the deformation, which were attributed to polytype modifications. The mechanism of formation of polytypes in the diamond structure of silicon during the plastic deformation is believed to be based [8] on a correlated motion of partial dislocations along the ⟨112⟩ direction in the slip plane {111}. It is well known that this process requires a sufficient quantity of dislocations; therefore, in a dislocation-free sample, the dislocations are generated only at the surface, which leads to the appearance of new phases only at the surface. However, one of the dislocation sources that provide polytype reconstructions may be the scratches that form on the surface during a mechanical polishing or the dislocation loops that appear in the Si structure in the course of decomposition of a supersaturated solid solution of oxygen. It should be recalled that the faceting of Si crystals investigated previously [8] and the crystals investigated in this study is virtually coincided and favored the initiation of the slip predominantly in the {111} planes. Therefore, the periodic shear deformation of the crystal that took place in the LFIF experiments might well be the cause of the correlated motion of the partial dislocations in these planes and the formation of polytype modifications. It should be noted that the formation of polytypes proceeds more intensely in samples subjected to the mechanical treatment; it proceeds less intensely in polished samples. The inverse hysteresis in the $G_{eff}(T)$ dependence points to the fact that the transition apparently involves incommensurate phases because such behavior of elastic characteristics was observed only in investigations of incommensurate phases [5, 6]. Moreover, the temperature hysteresis in the elastic characteristics observed previously [5, 6] was also completely reversible and was also accompanied by a "jump" in the characteristic values if heating was changed to cooling, as in our case.

At the same time, the authors of [2] observed multiple SPTs in the spectra of exoemission from a Si single crystal and attributed these transformations to the structural transitions in a thin oxide layer (i.e., on the real silicon surface itself). Therefore, we decided to clarify the role of the oxide layer in the processes of elastic-energy absorption and the behavior of the effective shear modulus. For this purpose, the third-group samples were subjected to additional low-temperature oxidation.

The additional oxidation of samples at 200°C for 2 h with restricted access of air (in the device with a residual air pressure of ~0.1 Pa) drastically suppressed the general level of absorption (all the observed peaks of absorption virtually disappeared) and transformed the two-lobe hysteresis of the modulus into a hysteresis of

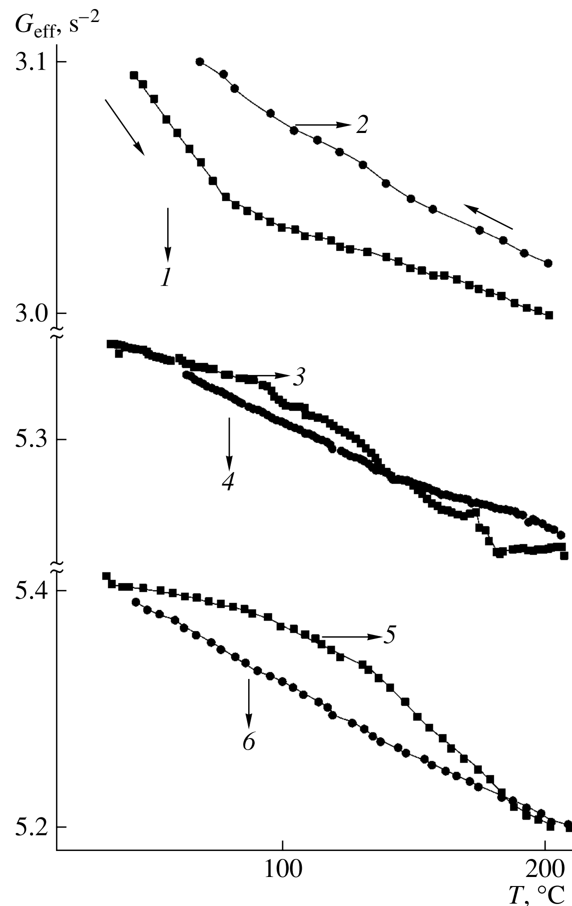

Fig. 3. Temperature dependences of effective shear modulus for a Si single crystal after various treatments of the surface: (*1*, *2*) after chemical–mechanical polishing; (*3*, *4*) after additional aging at 400°C for 5 h; and (*5*, *6*) after oxidation at 200°C for 2 h. The curves with odd numbers correspond to the processes of heating, and the curves with even numbers correspond to cooling.

the type characteristic of the first-order phase transition (Fig. 3, curves *5*, *6*). In this case, the loop in the temperature dependence of the shear modulus was again totally closed, which is indicative of the complete reversibility of the processes that occur in the sample. The measurements of the microhardness showed that values of H_μ for the samples after such a treatment were virtually twice as small than those in the samples after annealing at 400°C.

Thus, the features of the variations in LFIF behavior and in the effective shear modulus after the additional oxidation suggest that the incommensurate phases, which induce the inverse temperature hysteresis of the modulus, do arise in the surface layers of silicon itself. It is possible that these phases appear as a result of the previous mechanical treatment of the surface, whose effect can be made more profound by additional stresses on the interface between Si and SiO_2 or by the stresses arising during the decomposition of SSS of oxygen in silicon at room temperature. It is likely that

we succeeded in detecting experimentally also the structural phase transitions that proceed in the thin oxide layer, as indicated by the complicated two-lobe shape of the $G_{eff}(T)$ curves and the temperature position of certain observed anomalies in the elastic-energy absorption (for example, the peaks at ~50 and 105°C). However, in order to clarify this question and also to separate the contributions from the structural transitions in the thin oxide layer and in surface layers, special (structural) investigations are required.

Thus, the main results of this study are as follows.

(i) The mechanical treatment of a surface of single-crystal silicon was shown to initiate unusual polytype transitions accompanied by an anomalous (reversible) hysteresis in the temperature dependence $G_{eff}(T)$ of the shear modulus.

(ii) The aging of a Si single crystal at room temperature for a long time was found to lead to the onset of decomposition of the supersaturated solid solution of oxygen in silicon. The decomposition of the solution is accompanied by an insignificant (~10%) increase in the microhardness, a drastic (by two orders of magnitude) increase in elastic-energy absorption, and the emergence of two-lobe hysteresis in the $G_{eff}(T)$ dependence.

REFERENCES

1. V. S. Vavilov, V. F. Kiselev, and B. N. Mukashev, *Defects in the Bulk and at the Surface of Silicon* (Nauka, Moscow, 1990).
2. I. V. Krylova and A. G. Petrukhin, Fiz. Tekh. Poluprovodn. (St. Petersburg) **30**, 415 (1996) [Semiconductors **30**, 231 (1996)].
3. M. V. Zamoryanskaya and V. I. Sokolov, Fiz. Tverd. Tela (St. Petersburg) **40**, 1984 (1998) [Phys. Solid State **40**, 1797 (1998)].
4. V. M. Babich, N. I. Bletskan, and E. F. Venger, *Oxygen in Crystals of Silicon* (Interpres, Kiev, 1997).
5. B. F. Borisov, T. Kraevskiĭ, A. K. Radzhabov, and E. V. Charnaya, Fiz. Tverd. Tela (St. Petersburg) **35**, 241 (1993) [Phys. Solid State **35**, 127 (1993)].
6. O. G. Vlokh, A. V. Kityk, O. M. Mokryĭ, and V. G. Gribik, Fiz. Tverd. Tela (Leningrad) **33**, 312 (1991) [Sov. Phys. Solid State **33**, 181 (1991)].
7. K. V. Chuistov, Metallofiz. Noveishie Tekhnol. **17**, 7 (1995).
8. I. M. Shmyt'ko, A. N. Izotov, N. S. Afonikova, *et al.*, Fiz. Tverd. Tela (St. Petersburg) **40**, 746 (1998) [Phys. Solid State **40**, 687 (1998)].

Translated by V. Bukhanov

Semiconductors, Vol. 37, No. 11, 2003, pp. 1303–1307. Translated from Fizika i Tekhnika Poluprovodnikov, Vol. 37, No. 11, 2003, pp. 1341–1345.
Original Russian Text Copyright © 2003 by Antonova, Stuchinskiĭ, Naumova, Nikolaev, Popov.

SEMICONDUCTOR STRUCTURES, INTERFACES, AND SURFACES

Charge Fluctuations at the Bonding Interface in the Silicon-on-Insulator Structures

I. V. Antonova, V. A. Stuchinskiĭ, O. V. Naumova, D. V. Nikolaev, and V. P. Popov

Institute of Semiconductor Physics, Siberian Division, Russian Academy of Sciences, pr. Akademika Lavrent'eva 13, Novosibirsk, 630090 Russia

Submitted February 10, 2003; accepted for publication March 6, 2003

Abstract—Starting from the data of deep-level transient spectroscopy, the charge fluctuations at the interface between the top Si layer and buried insulator in Si-on-insulator structures are evaluated. The interface was prepared by bonding Si with the thermally oxidized substrate. The magnitude of fluctuations at the interface is found to be equal or exceed $(1.5–2.0) \times 10^{11}$ cm^{-2} against the charge background of $\sim 5 \times 10^{11}$ cm^{-2} at this interface. It is shown that the fluctuations are most likely associated with the negative charge at the surface states rather than with the fluctuations of the fixed positive charge within oxide. © *2003 MAIK "Nauka/Interperiodica"*.

1. INTRODUCTION

It is known that the two main parameters that characterize the Si/SiO_2 interface are the charge within the insulator and the density of states at the interface [1]. As a rule, the positive charge is present in the thermally grown oxide, whereas the sign of the charge captured at the interface states is governed by the conductivity type of Si. It is evident that the values of both parameters mentioned can somewhat fluctuate over the Si/SiO_2 interface. As a rule, these fluctuations are not very significant and practically do not manifest themselves in the investigation of interfaces or device structures. According to the data in [2, 3], the standard deviation of the potential distribution at the thermal Si/SiO_2 interface and at the interface between grains in polysilicon does not exceed 0.05 eV. At present, a nontraditional technique of formation of the Si/SiO_2 boundaries has appeared, specifically, bonding technology [4], which is widely used for the fabrication of silicon-on-insulator (SOI) structures [5, 6]. The Si/SiO_2 interface formed in such a manner substantially differs from the interface formed by the thermal oxidation [7–9]. Specifically, on the investigation of the mechanisms of the current flow over a thin (8–11 nm) Si layer in an SOI structure, where the bonding interface in the structures under investigation was located between the top Si layer and the buried insulator, oscillations of the current were found at room temperature. These oscillations are apparently associated with considerable fluctuations of the fixed charge within the oxide or the charge at the interface states [10].

The purpose of this study is to estimate the fluctuations of the charge, namely, the fixed charge within the oxide or the charge at the interface states, at the Si/SiO_2 interface prepared by the bonding technique in an SOI structure.

2. EXPERIMENTAL

The electron densities in the top Si layer and in the substrate of the SOI structures, which were determined from the capacitance–voltage (C–V) characteristics, were $(3–10) \times 10^{15}$ and 1.5×10^{15} cm^{-3}, respectively. The top Si layer in the structures was 0.5 μm thick, whereas the buried insulator was 0.4 μm thick. In the structures investigated, the interface between the top Si layer and the buried oxide is the bonding interface, whereas the interface between the substrate and the buried oxide is the interface between Si and the oxide thermally grown on it.

In the study, we used the data obtained from the measurements of the *C–V* characteristics at a frequency of 1 MHz and by the method of deep-level transient spectroscopy (DLTS) [8, 9]. From the available variations of the DLTS technique, the so-called charge DLTS (*Q*-DLTS) [11] was used. This version of the DLTS technique provides wider possibilities for the investigation of interfaces in insulator–semiconductor structures. All the measurements were carried using the mesa structures. The contacts were formed by the deposition of Al. The area of the mesa structures varied within the range 0.5–1 mm^2.

3. RESULTS AND DISCUSSION

The capacitance of the mesastructure without application of a voltage is governed mainly by the capacitance of the buried insulator. A decrease in the capacitance in the voltage range of 10–16 V (see inset to Fig. 1) corresponds to the formation of the space-charge region (SCR) in the top Si layer. In this mode, the substrate is enriched with charge carriers. For a voltage higher than 16 V, an inversion layer is formed in the top layer, the thickness of the SCR ceases to increase, and the capacitance ceases to decrease. A sim-

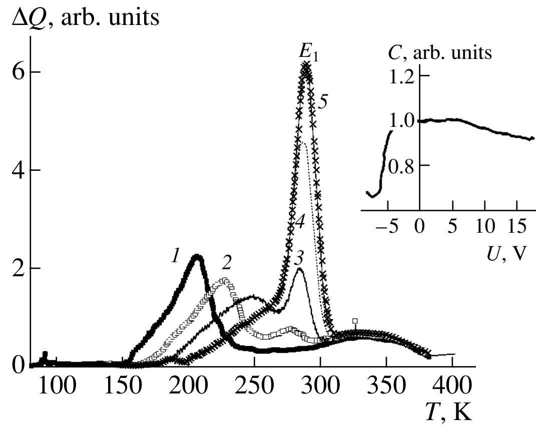

Fig. 1. DLTS data obtained for the SOI mesa structure and measured in the mode of the depleted top Si layer and the enriched substrate. The amplitude of the filling pulse U_1 = –2 V; the bias applied to the structure during measurements U_2 = (*1*) 8, (*2*) 10, (*3*) 12, (*4*) 14, and (*5*) 16 V. E_1 is the deep level in the top Si layer [9]. The capacitance–voltage characteristic of the structure is shown in the inset.

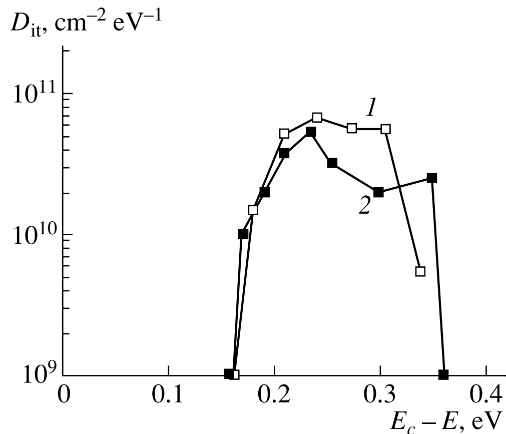

Fig. 2. Energy distributions of states at the interface between the top Si layer and the buried insulator layer of the SOI structure obtained by method (i) (curve *1*) and method (ii) (curve *2*).

ilar region of capacitance modulation, which is associated with the formation of the SCR in the substrate, is observed for the negative biases at the structure.

The DLTS data [9] for the SOI mesa structure that are measured at the voltages when the top Si layer is in a state of depletion, while the substrate is enriched with carriers, are shown in Fig. 1. In this case, the recharge of states at the interface between the top Si layer and the oxide is observed. The E_1 peak in the spectra corresponds to a deep-level center in the top Si layer [9]. The other part of the spectrum is associated with the recharge of the states at the interface between the top Si layer and the insulator.

The distribution of states in energy at the Si/SiO_2 interface, according to DLTS data, can be calculated by three different methods.

(i) For the buildup of the distributions by the first method, the method suggested by Hofmann and Schulz [12] was used. The energy of the centers, which give the main contribution to the DLTS signal at a given temperature and in the time window, is determined by the expression $E_c - E = kT\ln(\sigma v N_c \tau)$, where E is the level energy, σ is the capture cross section at the level, N_c is the density of states in the conduction band, and τ is the magnitude of the time window in which the DLTS measurements were carried out. This method calls for knowledge of the capture cross section at the level, which can be estimated from the DLTS data measured at the relatively low amplitude of the filling pulse, when the traps are recharged within a relatively narrow energy range. The peaks obtained in such a manner can be described approximately by the expressions for the recharge of the centers with fixed energies and cross sections. The estimations of the capture cross section for the traps at the bonding interface yielded a value of 10^{-18} cm^2 for the entire spectrum of the traps. We calculated the distribution of the states in energy using the capture cross section for the levels and the DLTS data obtained for the voltage across the structure U_2, at which the lowest capacitance is reached, and for the amplitude of the pumping pulse, which is equal to the width of the transition region in the *C*–*V* characteristic. The density of states was determined as the product of the bulk concentration of the center by the width of the region probed. The results of the calculation are shows in Fig. 2 (curve *1*).

(ii) Figure 2 also shows the distribution of states in energy, which is obtained from the approximation of each spectrum, measured at the relatively low amplitude of the filling pulse by the expressions for the recharge of the centers with fixed energies and capture cross sections.

(iii) The third method of the calculation of the distribution of states in energy is as follows. For each voltage and amplitude of the filling pulse used, it is possible to calculate the magnitude of the band bending at the bonding interface and to determine the range of energies of the traps, which should recharge under these conditions.

Figure 3 illustrates the band bending for the top layer of the SOI structures for the case when the top Si layer is in a state of depletion, while the substrate is enriched with carriers. Such an approach is conventional for the calculation of the distribution of the traps at the Si/SiO_2 interface in metal–insulator–semiconductor structures [13] and at the interface formed by the thermal oxidation in the SOI structures [10] for the case of a continuous spectrum of states. The band bending for Si at the interface between the top Si layer and the oxide ϕ_{s1} was calculated as follows. In the case of a grounded substrate, the voltage V applied to the structure can be written as [13]

$$V = -\phi_{s1} + \phi_{s2} + V_{ox} + W_{12}, \quad (1)$$

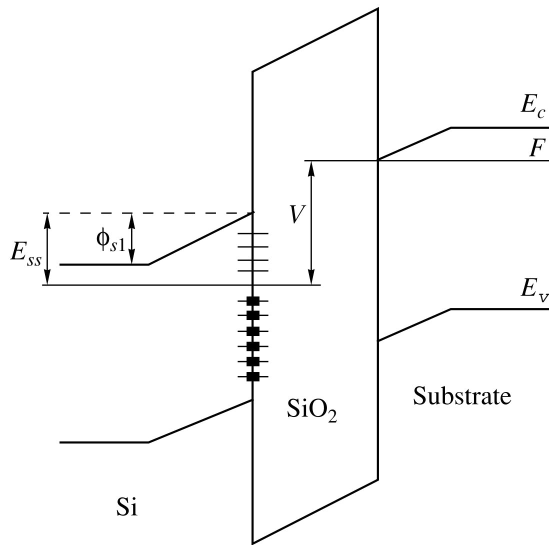

Fig. 3. Schematic representation of the band bending in the top Si layer of SOI structures for the case when the top Si layer is in a state of depletion and the substrate is enriched with carriers.

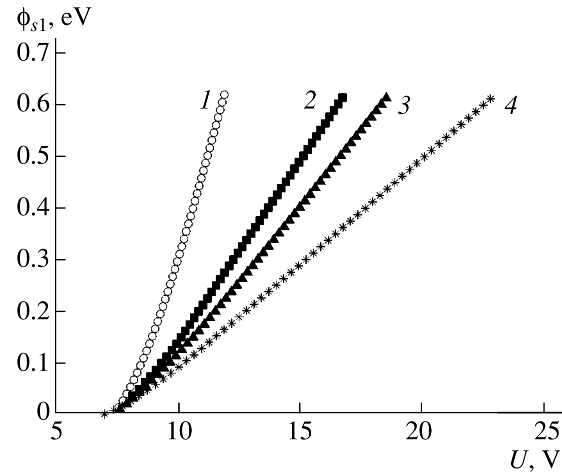

Fig. 4. Calculation of the band bending ϕ_{s1} in Si at the substrate/oxide interface for the same structure as that for which the data are given in Fig. 1, while the parameter N_{ss}, 10^{11} is varied: (*1*) 1, (*2*) 5, (*3*) 6.5, and (*4*) 10 cm^{-2}. The parameters V_{FB} = 7 V and $Q_f = 3.6 \times 10^{11}$ cm^{-2} were unchanged during the calculations.

where V_{ox} is the voltage drop across the insulator; ϕ_{s1} and ϕ_{s2} are the surface potentials at the interfaces between the top Si layer and SiO_2 and between the substrate and SiO_2, respectively; and W_{12} is the contact potential difference between the film and the substrate. If the substrate is enriched with carriers, we may disregard the ϕ_{s2} quantity compared with the ϕ_{s1} quantity; in addition, $V_{ox} = Q/C_{ox}$, where C_{ox} is the oxide capacitance, and the charge Q can be expressed as

$$Q = Q_{s1} + Q_{t1} + Q_{f1}. \quad (2)$$

Here indices 1 are related to the top Si layer, Q_s is the charge in the depletion region of the semiconductor, Q_f is the fixed charge in the oxide, and Q_t is the charge captured by the traps at the interface.

We have

$$Q_f = -(V_{FB} - W_{12})C_{ox},$$

where V_{FB} is the flat-band voltage,

$$Q_t = qN_{ss}\phi_s,$$

where N_{ss} is the density of states at the Si/SiO_2 interface, and

$$Q_s = \sqrt{2\varepsilon_a q N_D(\varphi_s - kT/q)}.$$

For the calculations, the V_{FB}, N_{ss}, and Q_f quantities, which were obtained from the results of the *C–V* measurements under the assumption that the traps are uniformly distributed in energy, were used. For example, for the structure for which the DLTS data are shown in Fig. 1, the following parameters were determined: V_{FB} = 7 V, $N_{ss} = 5 \times 10^{11}$ cm^{-2} eV^{-1}, and $Q_f = 3.6 \times 10^{11}$ cm^{-2}. The $\phi_{s1}(U)$ dependence calculated from these data is shown in Fig. 4 (curve *2*). Using the $\phi_s(U)$ dependence, the range of the ϕ_{s1} values, which corresponds to the bias U applied to the structure and the bias during the filling pulse $U_2 + U_1$, was determined for each spectrum in Fig. 1. Thus, the obtained band bending ϕ_{s1} and the ranges of trap energies E_{ss}^{th}, which should be recharged during each measurement in the context of a laterally uniform model, are given in the table (see also Fig. 2).

The band bending for the semiconductor can be obtained also by another simpler method, which does not require knowledge of such parameters as the fixed

Calculated (ϕ_{s1}, E_{ss}^{th}) and experimental (E_{ss}^{exp}) parameters of the structures investigated

$U_1 + U_2$, V	ϕ_{s1}, eV	E_{ss}^{th}, eV	E_{ss}^{exp}, eV
16–14	0.58–0.43	0.80–0.65	0.3–0.35
14–12	0.43–0.28	0.65–0.48	0.26
12–10	0.28–0.14	0.48–0.36	0.21–0.24
10–8	0.14–0.04	0.36–0.2	0.2–0.23
8–6	0.04–0	0.2–0.15	0.17–0.21

Note: ϕ_{s1} is the band bending at the interface between the top Si layer and the buried insulator and corresponds to the voltages at which the spectra shown in Fig. 1 were recorded; E_{ss}^{th} is the calculated range of energy levels of the traps, which should be observed experimentally on the basis of the ϕ_{s1} magnitude; and E_{ss}^{exp} are the energy levels of the traps, which are really recharged under these experimental conditions.

charge in the oxide and the density of states at the interface. The capacitance of the structure under the conditions of a substrate enriched with carriers is determined by two series-connected capacitances, namely, the capacitance of the buried insulator and the capacitance of the space-charge region of Si. This circumstance allows one, knowing the insulator thickness and the structure capacitance for the specific voltage, to calculate the space-charge region thickness. Further, using the known Schottky formula, we calculated the band bending ϕ_{s1} at the Si/SiO_2 interface. These data coincided with the results of calculation of the voltage drop across the structure and served as the criterion of correctness of determining the parameters of the structure, specifically N_{ss}.

The energy levels of traps $E_{ss}^{\exp}$, which are actually recharged in the structures under investigation, are listed in the table. These energies were determined by method (ii) from the experimental data shown in Fig. 1. It can be seen that despite an increase in the band bending ϕ_{s1}, which was calculated in the laterally uniform model of the structure, a recharge of the levels with relatively low energies is observed in the spectra as before. Thus, a discrepancy is found between the band bendings at the interface with the oxide, which are calculated within the framework of the laterally uniform model, and the energies of the traps, which recharge during the DLTS measurements. It should be noted that for the second Si/SiO_2 interface (the interface with the substrate), which is formed by thermal oxidation, all three methods yield the distribution of states in energy, which are in good agreement with each other.

What may cause such a discrepancy between the band bendings at the interface with the oxide and the energies of the traps recharged? During the DLTS measurements, the process of carrier emission from the surface states is fixed. In the case of quite large band bending and a relatively narrow energy range of the states recharged, the trap recharge can be the result of fluctuations of the surface potential. The data of the table permit one to estimate the fluctuations of the surface potential $\Delta\phi_{s1} = 0.30–0.35$ eV for the various structures measured; these fluctuations are necessary to bring into coincidence the calculation and the experimental data.

The existence of fluctuations may be associated with fluctuations in the built-in charge within the oxide, with the charge at the surface states, and with the inhomogeneous impurity distribution. In the last case, a lower surface potential can be obtained in local regions, where the impurity concentration exceeds the average concentration obtained from the $C–V$ measurements. The estimations demonstrated that such fluctuations of the impurity concentration at local places should be no less than three orders of magnitude larger than the average value. The existence of such high concentration fluctuations is unlikely.

It is known that at the traditional Si/SiO_2 interface, which is prepared by thermal oxidation, insignificant fluctuations of the charge (the fixed charge and the charge of the surface states) $\Delta\phi_s \le 0.05$ eV occur. The existence of substantial charge fluctuations at the bonding interface in certain regions of the mesa structure may provide conditions for the recharge of relatively shallow-lying states despite the relatively high average surface potential. In this case, the fluctuating charge should reduce the band bending in a semiconductor. If the positive charge in the semiconductor fluctuates, it should decrease substantially in certain local regions. If the negative charge fluctuates, the centers giving rise to this charge should form agglomerates at the Si/SiO_2 interface. Only the positive fixed charge is found in the buried insulator of SOI structures, whereas the surface states at the Si/SiO_2 interface with n-type silicon are charged negatively. In our opinion, the existence of significant fluctuations of the positive charge in an insulator seems to be unlikely, since this is oxide formed by the thermal oxidation. Most likely, considerable fluctuations of the charge at the surface states exist precisely at the bonding interface. The dependences of ϕ_{s1} on the voltage applied for various densities of states at the Si/SiO_2 interface, which are obtained in the approximation of the laterally uniform model, are shown in Fig. 4. According to the calculations of $\Delta\phi_{s1}$ using N_{ss} as the parameter, potential fluctuations $\Delta\phi_{s1} = 0.30–0.35$ eV correspond to the fluctuations of the surface charge $\Delta N_{ss} = (1.5–2.2) \times 10^{11}$ cm^{-2}.

We mentioned above the data for one of the SOI structures investigated. Similar calculations carried out for other structures yield similar results. The spread of the $\Delta\phi_{s1}$ and ΔN_{ss} values is given with allowance made for the data obtained for all the structures investigated. It should be noted that the estimations yield the minimal fluctuations of the density of states at the interface, which are necessary to explain the experimental results. The actual amplitude of fluctuations may be larger.

The question arises as to the possible reasons for such strong fluctuations of the density of states at the bonding interface. It is known that the traps at the Si/SiO_2 interface formed by the thermal oxidation, as a rule, are determined by the transition SiO_x layer. At the Si/SiO_2 interface, which is prepared by bonding, such a transition layer is practically absent [10]. However, the Si and SiO_2 lattices are significantly mismatched. Due to the bonding of these materials, misfit dislocations can emerge at the interface. However, electron microscopy reveals no dislocations in the SOI structures [14]. We assume that extended defects are formed in the plane of the Si/SiO_2 interface during bonding without the transition layer. For example, these defects may appear in regions where there is no close bonding. It is possible that these are the defects that are responsible for a certain patchiness of the top Si layer, which is revealed by high-resolution X-ray diffraction [15]. These defects can be also responsible for the relatively narrow spectrum of the states observed at the bonding

interface, which is close to the spectrum of the traps at dislocations [16], and for other specific features of these states, specifically, for their unusual behavior during thermal treatment in hydrogen [17].

4. CONCLUSION

The existence of charge fluctuations is found at the Si/SiO_2 interface, which is obtained by bonding technology. These fluctuations lead to fluctuations of the surface potential at the interface between the buried insulator and the top Si layer; the latter fluctuations have a magnitude of 0.30–0.35 eV. It is shown that the fluctuations are most likely associated with the negative charge of the surface states rather than with the fluctuations of the positive charge within the oxide. These fluctuations are, at least, according to the lower estimate, $(1.5–2.2) \times 10^{11}$ cm^{-2} against the charge background of $\sim 5 \times 10^{11}$ cm^{-2}.

ACKNOWLEDGMENTS

This study was supported by the Russian Foundation for Basic Research, project no. 01-02-16986.

REFERENCES

1. S. Sze, *Physics of Semiconductor Devices*, 2nd ed. (Wiley, New York, 1981; Mir, Moscow, 1984).
2. E. H. Nicollian and A. Goetzberger, Bell Syst. Tech. J. **46**, 1055 (1967).
3. *Polycrystalline Semiconductors: Physical Properties and Applications*, Ed. by G. Harbeke (Springer, Berlin, 1985; Mir, Moscow, 1989).
4. M. K. Weldon, Y. J. Chabal, D. R. Hamann, *et al.*, J. Vac. Sci. Technol. B **14**, 3095 (1996).
5. M. Bruel, Electron. Lett. **31**, 1201 (1995).
6. K. Sakaguchi, N. Sato, K. Yamagata, *et al.*, IEICE Trans. Electron. **80-C**, 378 (1997).
7. I. V. Antonova, J. Stano, D. V. Nikolaev, *et al.*, Fiz. Tekh. Poluprovodn. (St. Petersburg) **36**, 65 (2002) [Semiconductors **36**, 60 (2002)].
8. I. V. Antonova, O. V. Naumova, J. Stano, *et al.*, Appl. Phys. Lett. **79**, 4539 (2001).
9. I. V. Antonova, J. Stano, O. Naumova, *et al.*, in *Proceedings of International Conference on Ion Implantation Technology* (2000), p. 273.
10. O. V. Naumova, I. V. Antonova, V. P. Popov, *et al.*, Microelectron. Eng. (in press).
11. J. W. Farmer, C. D. Lamp, and J. M. Meese, Appl. Phys. Lett. **41**, 1063 (1982).
12. K. Hofmann and M. Schulz, J. Electrochem. Soc. **132**, 2201 (1985).
13. S. Cristoloveanu and S. S. Li, *Electrical Characterization of Silicon-on-Insulator Materials and Devices* (Kluwer Academic, Boston, 1995).
14. V. P. Popov, I. V. Antonova, V. F. Stas, *et al.*, Mater. Sci. Eng. B **73**, 82 (2000).
15. I. V. Antonova, V. P. Popov, J. Bak-Misiuk, and J. Z. Domagala, J. Electrochem. Soc. **149**, G490 (2002).
16. W. Schröter, V. Kveder, and H. Hedemann, Solid State Phenom. **82–84**, 213 (2002).
17. I. V. Antonova, O. V. Naumova, V. P. Popov, *et al.*, J. Appl. Phys. **93**, 426 (2003).

Translated by N. Korovin

Semiconductors, Vol. 37, No. 11, 2003, pp. 1308–1310. Translated from Fizika i Tekhnika Poluprovodnikov, Vol. 37, No. 11, 2003, pp. 1346–1348.
Original Russian Text Copyright © 2003 by Bodnar', Polubok, V. Rud', Yu. Rud'.

SEMICONDUCTOR STRUCTURES, INTERFACES, AND SURFACES

Photosensitive Structures Based on In_2S_3 Crystals

I. V. Bodnar'*, V. A. Polubok*, V. Yu. Rud', and Yu. V. Rud'*****

**Belarussian State University of Informatics and Radiolectronics, ul. Brovki 17, Minsk, 220072 Belarus*
e-mail: chemzav@gw.bsuir.unibel.by
***St. Petersburg State Polytechnical University, Politekhnicheskaya ul. 29, St. Petersburg, 195021 Russia*
****Ioffe Physicotechnical Institute, Russian Academy of Sciences, Politekhnicheskaya ul. 26, St. Petersburg, 194021 Russia*
Submitted March 5, 2003; accepted for publication March 7, 2003

Abstract—Crystals of the compound In_2S_3 were grown by planar crystallization of the melt. The composition, structure, and electrical characteristics of the crystals obtained were determined. Photosensitive structures based on the grown In_2S_3 crystals were fabricated for the first time; spectral dependences of photoconversion quantum efficiency for H_2O/In_2S_3 cells were measured. The features of the band-to-band absorption are discussed; energies of the direct and indirect optical transitions for In_2S_3 crystals are estimated. It is stated that In_2S_3 crystals can be used in wide-range (1.5–3.5 eV) photoconverters of nonpolarized radiation (in particular, in solar cells). *© 2003 MAIK "Nauka/Interperiodica".*

1. INTRODUCTION

Complex semiconducting phases formed at the interfaces between the I_2–VI and III_2–VI_3 compounds are becoming the subject of rapidly expanding research owing to the possibility of using these phases in semiconductor optoelectronics and photoelectronics [1, 2]. Theoretical studies of interactions in such systems suggest that the latter can involve a number of stability regions with formed positionally ordered phases, which contain stoichiometric vacancies [3, 4]. The data on III_2–VI_3 binary phases appearing in the quasi-binary (I_2–VI)–(III_2–VI_3) section are very scarce so far [2, 5, 6]. The expansion of investigation into the aforementioned phases is becoming increasingly relevant because of the need to analyze the interactions in the systems under consideration.

In this paper, we report the results of studying the physical properties of one of the aforementioned compounds (In_2S_3); we were also concerned with the fabrication of photosensitive structures based on In_2S_3 crystals.

2. EXPERIMENT, RESULTS, AND DISCUSSION

Crystals of the binary compound In_2S_3 were grown by planar crystallization of the melt (the horizontal Bridgman–Stockbarger method). Metallic indium of 99.9999% purity (in a quartz boat) and sulfur of 99.99999% purity were loaded into different parts of an evacuated quartz cell. The amount of sulfur was in excess with respect to stoichiometry; this excess was necessary to ensure a sulfur vapor pressure of 1.5–2.0 atm above the formed melt. The cell was placed in a two-zone horizontal furnace with independently controlled temperatures in the zones. The temperature of the zone with indium was kept within 1380–1400 K; the temperature of the zone with sulfur was first increased to 700 K with a rate of 50 K/h and was then maintained at 700 K for 2 h for the chemical reaction between indium and sulfur to proceed. In order to ensure that this reaction is close to completion, we increased the temperature of the zone with sulfur to ~780 K with a rate of 50 K/h and then kept the temperature at 780 K for 1 h. Thereafter, we carried out the planar crystallization by lowering the melt temperature to 1050 K with a rate of ~5 K/h; the substance formed was then subjected to homogenizing annealing for 100 h at 1050 K. The crystals obtained had a large-block structure, with the dimensions of separate blocks being $(20–25) \times 10 \times 5$ mm^3. The composition of as-grown crystals was determined from the results of a chemical analysis using the methods suggested previously [7, 8]. The content of elements in the as-grown crystals, [In] : [S] = 39.75 : 60.25 at %, was consistent with the specified composition of the charge in the growth cell, [In] : [S] = 40.00 : 60.00 at %. According to the data obtained, the composition of as-grown crystals corresponded to the formula In_2S_3, i.e., [In] : [S] = 2 : 3.

The structural state of equilibrium of as-grown crystals was determined from X-ray diffraction analysis using a DRON-3M diffractometer equipped with a Ni filter; CuK_α radiation was employed. The analysis showed that the In_2S_3 crystals obtained had a cubic spinel-type structure with the unit-cell parameter $a = 10.774 \pm 0.005$ Å at room temperature, which was consistent with the data on the lattice constant reported previously [9, 10].

According to the thermoelectric-power sign, the In_2S_3 crystals had the n-type conductivity; the resistivity was $\rho \approx 10^3$–10^5 Ω cm at $T = 300$ K for the samples cut from different parts of the ingot. In transmitted light, the In_2S_3 wafers 2–4 mm thick were uniformly dark-cherry-colored.

1063-7826/03/3711-1308$24.00 © 2003 MAIK "Nauka/Interperiodica"

Photoelectrochemical cells were fabricated on the basis of In_2S_3 crystals; the structure of these cells is shown schematically in the inset to Fig. 1. An In_2S_3 wafer with a thickness of ~(1–2) mm and an area of ~2×4 mm^2 was provided with an ohmic contact *1*, which was formed by depositing the silver paste on one of the sample faces. The ohmic contact with the corresponding wire was covered with an insulating lacquer ($\rho \approx 10^{10}$ Ω cm) in order to eliminate direct contact with liquid electrolyte *2*; the photoelectrode was then placed in a quartz dish *3* filled with electrolyte *2*. Counterelectrode *4* was immersed opposite the photoelectrode; this counterelectrode was made of platinum wire with a diameter of ~0.05 mm. Distilled water was commonly used as the electrolyte in the aforementioned cell.

Studies of the steady-state current–voltage (*I–V*) characteristics showed that the fabricated photoelectrochemical cells feature a rectifying characteristic; the rectification factor for the *I–V* characteristic was typically as large as ~10^2 at a bias voltage of ~10 V. The conducting direction for the cells under consideration is always attained at the negative polarity of external bias applied to the *n*-In_2S_3 photoelectrode.

When the photoelectrochemical cells are illuminated on the counterelectrode side, a photovoltaic effect arises; the sign of this effect is independent of either the energy of incident photons or the location of the optical beam (with a diameter of about 0.2–0.4 mm) on the photodetecting surface of the cells. This fact suggests that the photovoltaic effect is caused by separation of photogenerated electron–hole pairs in a single active region which is formed at the contact of liquid electrolyte with the free surface of the In_2S_3 wafer. It is also noteworthy that an In_2S_3 crystal is always charged negatively in the illuminated cells under consideration, which correlates with the rectification direction. The highest voltage photosensitivity in the photoelectrochemical cells amounts to $S_u^m \approx$ 3000–3500 V/W at 300 K and is well reproduced at photoelectrodes formed of the In_2S_3 wafers cut from various parts of the ingot. This circumstance is indicative of the adequate homogeneity of In_2S_3 crystals. No degradation effects were observed for the photoelectrochemical cells. It is also worth noting that, according to the results of preliminary studies, the solid-state structures obtained by vacuum-evaporation deposition of thin indium layers (with a thickness of ~0.1 μm) and by chemical deposition of copper and gold on the cleaved surface of In_2S_3 crystals also exhibit a photosensitivity; however, the values of S_u^m in these structures are, as a rule, two to three orders of magnitude smaller than in the case of H_2O/In_2S_3 photoelectrochemical cells.

In Fig. 1, we show the spectral dependence of relative quantum efficiency $\eta(h\nu)$ for photoconversion in an H_2O/In_2S_3 cell in the photodetection geometry illustrated in the inset to Fig. 1. It can be seen that a broad-band photosensitivity is characteristic of these cells. An exponential increase in the photosensitivity with photon energy $\eta(h\nu)$ is observed for $h\nu$ ranging from ≈ 1.2 to ≈ 1.5 eV. The increase in η is characterized by a fairly steep slope $S = \delta\ln(\eta)/\delta h\nu \approx$ 18–20 eV^{-1}. In the photon-energy region of $h\nu > 1.6$ eV, the photosensitivity continues to increase up to a photon energy of ~3.5 eV. Figure 2 shows the results of analyzing the photosensitivity spectrum on the basis of the theory of the band-to-band absorption in semiconductors [11]. It can be seen that the long-wavelength portion of the photosensitivity spectrum (curve *1*) is linearized in the coordinates $(\eta h\nu)^{1/2} = f(h\nu)$. This circumstance makes it possible to relate this portion of the spectrum to indirect band-to-band transitions. The band gap for indirect band-to-band transitions, which is obtained by extrapolation $(\eta h\nu)^{1/2} \longrightarrow 0$, can be estimated at $E_g^{in} \approx 1.40$ eV at 300 K. It also follows from Fig. 2 that the short-wavelength portion of the photosensitivity spectrum can be linearized in the coordinates $(\eta h\nu)^2 = f(h\nu)$; we can then use the extrapolation $(\eta h\nu)^2 \longrightarrow 0$ to estimate the band gap of In_2S_3 for direct band-to-band transitions at $E_g^{dir} \approx 2.54$ eV at 300 K. It is noteworthy that our data are not consistent with those reported in [2, 5, 6], which

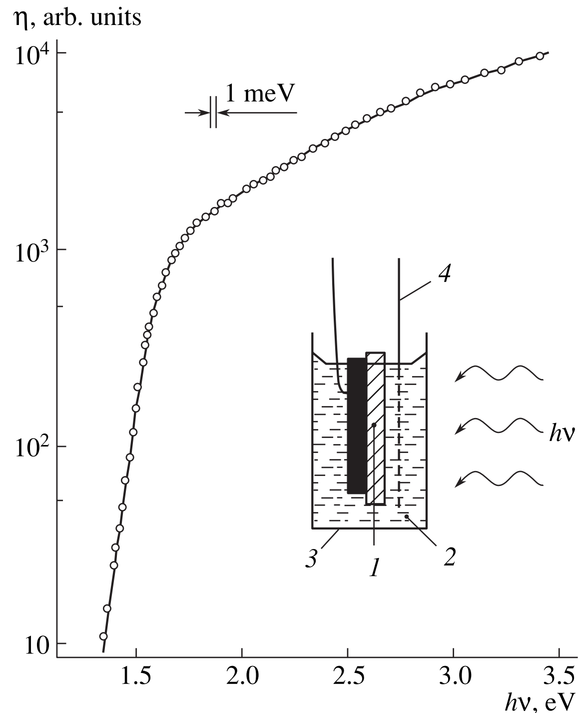

Fig. 1. Spectral dependence of relative quantum efficiency of photoconversion for an In_2S_3 structure at $T = 300$ K. The structure was exposed to nonpolarized light. The inset illustrates the geometry of photodetection and the cell structure: *1* indicates the photoelectrode with an ohmic contact and corresponding coating of insulating lacquer; *2*, the electrolyte; *3*, the quartz cell; and *4*, the counterelectrode in the form of a platinum grid. The modulation frequency was ~24 Hz.

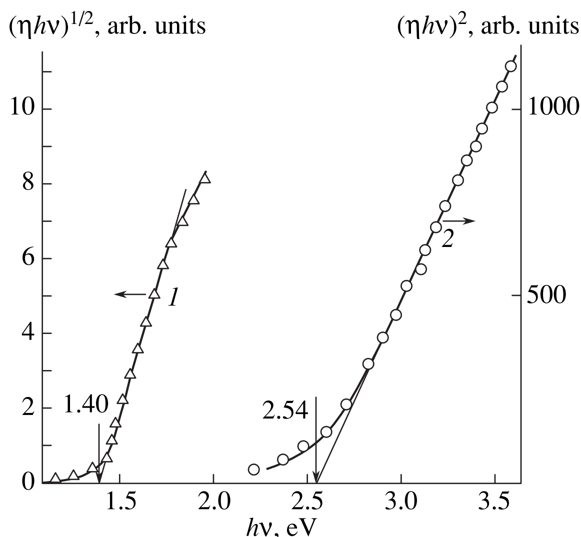

Fig. 2. The data of Fig. 1 represented as the dependences (*1*) $(\eta h\nu)^{1/2} = f(h\nu)$ and (*2*) $(\eta h\nu)^2 = f(h\nu)$.

calls for additional research. It cannot be excluded that the binary In_2S_3 compound belongs to the phases with variable composition; consequently, a divergence in the results of determining the value of E_g may be related with precisely the nonstoichiometry of the phases obtained.

3. CONCLUSION

We used planar crystallization of the melt to grow crystals of the binary compound In_2S_3. We fabricated for the first time photoelectrochemical cells based on these crystals. The features of the band-to-band transitions for In_2S_3 are discussed, and the energies of the indirect and direct band-to-band transitions are estimated. The structures obtained are of interest in relation to using them in solar cells and broad-band photoelectric converters of natural radiation.

REFERENCES

1. N. A. Goryunova, *Compound Diamond-Like Semiconductors* (Sovetskoe Radio, Moscow, 1968).
2. *Physicochemical Properties of Semiconductor Materials: Handbook*, Ed. by A. V. Novoselova and V. B. Lazarev (Nauka, Moscow, 1979).
3. S. B. Tsang, S. H. Wei, A. Zunger, and H. Katayama-Yoshida, Phys. Rev. B **57**, 9642 (1998).
4. S. H. Wei, S. B. Tsang, and A. Zumger, Appl. Phys. Lett. **72**, 3199 (1998).
5. E. Kauer and A. Rabenau, Z. Naturforsch. A **13**, 531 (1958).
6. W. Rehwald and G. Herbeke, J. Phys. Chem. Solids **26**, 1309 (1965).
7. L. G. Starobinets, N. N. Ishchenko, and L. I. Ganago, Izv. Akad. Nauk BSSR, Ser. Khim. Nauk **1**, 111 (1988).
8. P. P. Kish and S. T. Orlovskiĭ, Zh. Anal. Khim. **17**, 1057 (1962).
9. F. G. Donika, S. I. Radautsan, S. A. Semiletov, and I. G. Mustya, *Crystalline Structures of Inorganic Compounds* (Shtiintsa, Kishinev, 1974).
10. N. Kh. Abrikosov, V. F. Bankina, L. V. Poretskaya, E. V. Skudnova, and S. N. Chizhevskaya, *Semiconductor Chalcogenides and Chalcogenide-Based Alloys* (Nauka, Moscow, 1975).
11. J. I. Pankove, *Optical Processes in Semiconductors* (Prentice Hall, Englewood Cliffs, N.J., 1971; Mir, Moscow, 1973).

Translated by A. Spitsyn

Semiconductors, Vol. 37, No. 11, 2003, pp. 1311–1314. Translated from Fizika i Tekhnika Poluprovodnikov, Vol. 37, No. 11, 2003, pp. 1349–1351.
Original Russian Text Copyright © 2003 by Antyushin, Budanov, Kukharenko, Palishkin.

Kinetics of the Initial Stage in Chalcogenide Passivation of III–V Semiconductors

V. F. Antyushin, A. V. Budanov, D. S. Kukharenko, and D. A. Palishkin

Voronezh State Technological Academy, pr. Revolyutsii 19, Voronezh, 394017 Russia

Submitted March 3, 2003; accepted for publication March 31, 2003

Abstract—A mathematical model of thermally stimulated heterovalent substitution of anions in the III–V surface region in the course of chalcogenide passivation from the gaseous phase is substantiated and formulated. This model is represented in the form of a nonlinear system of differential equations. It is shown that the initial state of the surface (the initial surface concentration of anionic vacancies) profoundly affects the relevant kinetics.
© 2003 MAIK "Nauka/Interperiodica".

Chalcogen-containing layers on III–V crystals are used to passivate the surface and reduce the surface-state density [1], to improve the surface morphology, and, ultimately, to fabricate high-quality devices on III–V substrates. In order to form thin layers of indium and gallium sulfides or selenides, treatment in solutions containing sulfur, selenium, their salts, and other compounds is used or passivation from a gaseous chalcogen-containing phase is carried out [1]. Obviously, the thermally stimulated interaction of the surface with sulfur or selenium vapors according to the technology described in [2–6] eliminates the effect of collateral substances while retaining the purposeful controlled effect of Group-VI elements on a III–V surface.

An oxide layer with a thickness of several nanometers is removed from the surface during the formation of the passivating coating; this layer incorporates a mixture of various phases of semiconductor-component oxides. The surface becomes oxide-free and interacts with the adsorbed layer, which is enriched with sulfur. If the GaAs surface is sulfurized using either various solutions or a sulfur-containing gaseous phase at temperatures close to 295 K, As–S bonds are preferentially formed. However, at higher temperatures (280–450°C), arsenic atoms are removed from the surface, the As–S bonds are completely destroyed, and the total amount of sulfur on the surface remains virtually constant up to temperatures $T > 580°C$. Only the Ga–S bonds remain at the surface. In this situation, two sulfide components can be recognized; one of these is related to the sulfur that is incorporated into the near-surface GaAs bulk and substitutes arsenic atoms, and the other is related to the sulfur adsorbed on the surface. Ga–Se bonds are stronger than Ga–S bonds; however, a transfer of selenium from arsenic to gallium occurs at higher temperatures of passivation in selenium-containing media ($T > 550°C$) [1].

Antyushin *et al.* [7] reported the results of studying experimentally nucleation in the early stages of formation of (III_2–VI_3)–(III–V) heterosystems in an situation where the III–V surface was heat-treated in an atmosphere of selenium vapors; however, only a semiempirical phenomenological equation was suggested for a mathematical description of the nucleation process. Therefore, in this study, we substantiated a detailed model for the initial stage of thermally stimulated reaction of heterovalent replacement of anions with Group-VI chalcogenides and analyzed this model.

In previous experimental studies [2–6], (III_2–VI_3)–(III–V) heterostructures were formed by isothermal annealing of crystalline III–V substrates in chalcogen vapors in a quasi-closed graphite reactor at a vapor pressure of 0.133–1.33 Pa and at substrate temperatures of 550–620°C for the GaAs substrate and at a pressure of 10^{-2}–10^2 Pa for the InAs substrate heated to 150–350°C. For example, this method was used to obtain Ga_2Se_3–GaAs [2], In_2S_3–InAs [3, 4], In_2Se_3–InAs [5, 6], and other structures. Electron diffraction studies [2–6] showed that the crystal lattices of III–V substrates and single-crystal chalcogenide layers are isotype, with possible pseudomorphism of the surface layer. Depending on the specific technological conditions, a continuous layer of chalcogenides with the structural–stoichiometric formula $III_2[\ ]VI_3$ is formed on the surface of a III–V crystal in a time $t_0 = 3$–30 min. This inference is confirmed by the Auger (Fig. 1) and X-ray spectral measurements [3–7]. After the formation of the covalence bonds and the relaxation of the coordination surroundings, the stoichiometrically excess cation is found at the stoichiometric vacancy in the cationic sublattice of chalcogenide. Due to the saturation of bonds in the coordination environment of this cation, the latter is bonded weakly to the crystal lattice. The release of the cation as a result of the formation of a structural and chemical chalcogenide unit (Ga_2Se_3,

1063-7826/03/3711-1311$24.00 © 2003 MAIK "Nauka/Interperiodica"

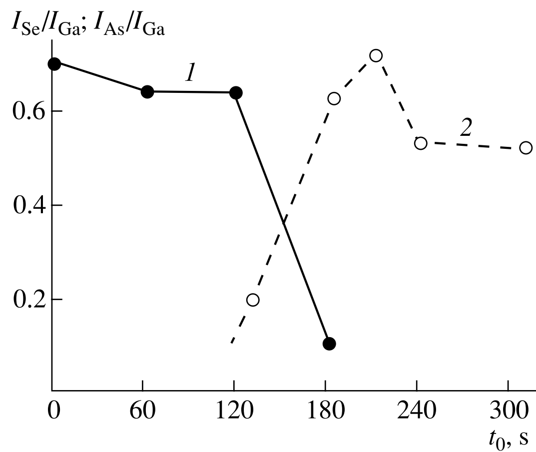

Fig. 1. Dependences of relative intensities I of main lines in the Auger spectra of gallium, arsenic, and selenium on time t_0 in a Ga_2Se_3–GaAs heterostructure: line *1* corresponds to I_{Se}/I_{Ga} and line *2* corresponds to I_{As}/I_{Ga}.

Ga_2S_3, In_2S_3, In_2Se_3, and others) gives rise to the second mechanism of the end-product synthesis as a result of interaction with adsorbed chalcogen.

We may assume that the microscopic substitution mechanism amounts to the adsorption of chalcogen on the substrate surface, chalcogen dissociation, the thermally stimulated destruction of low-energy bonds in the substrate material with the resulting formation of anionic vacancies after the anion evaporates into the reaction volume, and the formation of energetically more stable bonds between a III-Group element and a chalcogen (S, Se) when vacancies are filled with atomic chalcogen.

It is clear from the above reasoning that a physicochemical (and, correspondingly, mathematical) model of thermally stimulated heterovalent substitution should include a description of the kinetics for the generation of anionic vacancies on the crystal surface, the kinetics of the supply of chalcogen to the surface, and the kinetics of the heterovalent-substitution reaction itself.

Disregarding the times needed for the formation of valence bonds and the relaxation of coordination surroundings after an anionic vacancy is filled with atomic chalcogen, we can describe the kinetics of synthesis of the surface chalcogenide layer by the following equation:

$$\frac{dU_s}{dt} = \frac{3}{2}V_sS_s. \quad (1)$$

Here, U_s, V_s, and S_s are the surface concentrations of the structural–chemical units of chalcogenide, the anionic vacancies in the III–V crystal lattice, and the atomic chalcogen in the adsorbed layer, respectively (all these concentrations are expressed in units of U_{s0}, the surface concentration of structural–chemical units of chalcogenide in a situation where there is a continuous chalcogenide film on the surface); and t is the time expressed in units of $1/U_{s0}\alpha$, where α is the reaction-rate constant with the dimension of [m^2/s].

The generation kinetics for anionic vacancies can be described by the following equation:

$$\frac{dV_s}{dt} = \delta(1 - U_s - V_s) - \frac{dU_s}{dt}. \quad (2)$$

Here, δ is a dimensionless constant accounting for the evaporation of anions from the III–V surface into the volume of the reaction chamber. The quantity $(1 - U_s - V_s)$ represents the dimensionless surface concentration of stoichiometric structural–chemical III–V units on the crystal surface. The second term on the right-hand side of Eq. (2) accounts for the recombination of anionic vacancies and chalcogen.

The adsorption coefficients may differ for the III–V and $III_2[\ ]VI_3$ surfaces (the same may be true of the reaction-rate constant for dissociation, which gives rise to atomic chalcogen). Therefore, assuming that a quasi-equilibrium is established and using the linear approximation in U_s, we can express the surface concentration of atomic chalcogen (in the same units as all the other surface concentrations) as

$$S_s = S_{s0}\left(1 + \frac{S_s^0 - S_{s0}}{S_{s0}}U_s\right), \quad (3)$$

where S_{s0} and S_s^0 are the concentrations of atomic chalcogen on the III–V and $III_2[\ ]VI_3$ surfaces, respectively; these concentrations are in equilibrium with the atmosphere in a quasi-closed volume in the reaction chamber.

Equations (1)–(3) form a system of equations that describe the synthesis kinetics for $III_2[\ ]VI_3$ chalcogenide on a III–V crystal surface.

The quantities δ, S_s^0, and S_{s0} are technology-dependent; the same is true for the time scale. The initial conditions of the process

$$U_s|_{t=0} = 0, \quad V_s|_{t=0} = V_s^0 \quad (4)$$

and the asymptotic behavior

$$U_s|_{t\to\infty} = 1, \quad V_s|_{t\to\infty} = 0 \quad (5)$$

uniquely define the kinetics of increase in the surface concentration of structural–chemical units for the compound $III_2[\ ]VI_3$ on the crystal surface.

Variations in V_s^0 may account for changes in the initial state of the III–V crystal surface before switching on the chalcogen-vapor source.

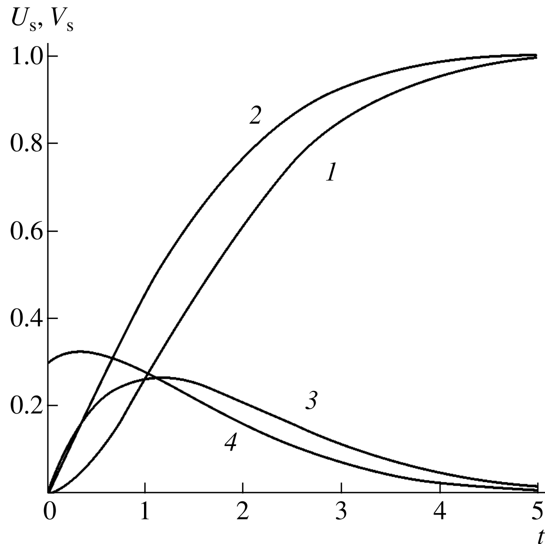

Fig. 2. Dependences (*1*, *2*) $U_s(t)$ and (*3*, *4*) $V_s(t)$. Curves (*1*, *3*) correspond to $V_s^0 = 0$ and curves (*2*, *4*) correspond to $V_s^0 = 0.3$. $S_{s0} = S_s^0 = 1$ and $\delta = 0.6$.

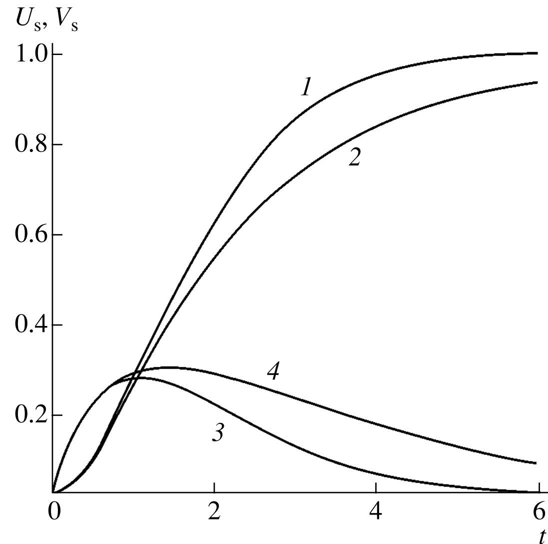

Fig. 3. Illustration of a manifestation of nonlinearity in the system of equations under consideration in the final stage of heterovalent substitution. Curves (*1*, *2*) correspond to $U_s(t)$ and curves (*3*, *4*) correspond to $V_s(t)$. $S_{s0} = S_s^0 = 1$ for curves *1* and *3*; $S_{s0} = 1$ and $S_s^0 = 0.25$ for curves *2* and *4*. $V_s^0 = 0$ and $\delta = 0.6$.

The nonlinearity of the system of equations under consideration is related to Eqs. (1) and (3) and is insignificant in the early stages of the process (when $U_s \longrightarrow 0$) and also if $(S_s^0 - S_{s0})/S_{s0} \longrightarrow 0$. Solutions to the linear system are given by

$$U_s = 1 - \frac{2\delta - 2V_s^0 S_{s0}}{2\delta - 3S_{s0}} \exp\left(-\frac{3}{2}S_{s0}t\right) - \frac{3S_{s0} - 2V_s^0 S_{s0}}{2\delta - 3S_{s0}} \exp(-\delta t) \quad (6)$$

and are shown in Fig. 2. The characteristic time delay of the onset of the process and the profound effect of the initial surface concentration of anionic vacancies can be clearly recognized. Figure 3 illustrates a manifestation of nonlinearity in the system of equations at the final stages of the process.

Since the equations under analysis fail to account for the spatial redistribution of the reactants and the reaction products over the crystal surface, these equations can be used to describe objects whose distribution over the surface is only slightly nonuniform. For example, if there are large-scale fluctuations in the surface concentration of anionic vacancies before the onset of the heterovalent-substitution process, the kinetics of the chalcogenide formation at the fluctuation center will differ from that at the periphery of the fluctuation (Fig. 2). It is also clear that the surface is decorated with a chalcogenide layer in the early stage of the process; this layer reproduces the profile of the areas with increased initial concentration of anionic vacancies. After the time delay has elapsed, the chalcogenide concentration becomes close to unity at the periphery of fluctuations in the arsenic vacancies; as a result, the surface is found to be covered with a continuous $III_2[\ ]VI_3$ layer. This circumstance manifests itself in the reflection spectra of Ga_2Se_3–GaAs heterostructures [7]. In the initial stage of heterovalent substitution, the reflection spectrum is of the Rayleigh type (light is scattered by the microinhomogeneities of the surface). As time passes, the reflection becomes specular.

In our opinion, the mathematical model we developed makes it possible to gain an insight into the kinetics of the initial stage of interaction of chalcogen with a III–V surface, to the point when a continuous chalcogenide layer forms on the surface. We ascertained that the surface concentration of vacancies of Group-V elements profoundly affects the kinetics of heterovalent substitution, which, in turn, affects the crystal quality of the layers formed.

The reasoning used in this study can be generalized later on to the kinetics of planar growth of III_2–VI_3 layers on III–V substrates.

REFERENCES

1. V. N. Bessolov and M. V. Lebedev, Fiz. Tekh. Poluprovodn. (St. Petersburg) **32**, 1281 (1998) [Semiconductors **32**, 1141 (1998)].

2. B. I. Sysoev, V. F. Antyushin, V. D. Strygin, and V. N. Morgunov, Zh. Tekh. Fiz. **56**, 913 (1986) [Sov. Phys. Tech. Phys. **31**, 554 (1986)].
3. B. I. Sysoev, B. L. Agapov, N. N. Bezryadin, *et al.*, Fiz. Tekh. Poluprovodn. (Leningrad) **25**, 699 (1991) [Sov. Phys. Semicond. **25**, 421 (1991)].
4. N. N. Bezryadin, E. A. Tatokhin, I. N. Arsent'ev, *et al.*, Fiz. Tekh. Poluprovodn. (St. Petersburg) **33**, 1447 (1999) [Semiconductors **33**, 1301 (1999)].
5. N. N. Bezryadin, A. V. Budanov, E. A. Tatokhin, *et al.*, Neorg. Mater. **36**, 1037 (2000).
6. N. N. Bezryadin, Ya. A. Boldyreva, A. V. Budanov, and E. A. Tatokhin, in *Proceedings of XII International Symposium on Thin Films in Electronics* (Kharkov, 2001), p. 169.
7. V. F. Antyushin, A. V. Budanov, E. A. Tatokhin, and Ya. A. Boldyreva, Pis'ma Zh. Tekh. Fiz. **28** (7), 68 (2002) [Tech. Phys. Lett. **28**, 295 (2002)].

Translated by A. Spitsyn

Semiconductors, Vol. 37, No. 11, 2003, pp. 1315–1320. Translated from Fizika i Tekhnika Poluprovodnikov, Vol. 37, No. 11, 2003, pp. 1352–1357.
Original Russian Text Copyright © 2003 by Volodin, Gatskevich, Dvurechenskiĭ, Efremov, Ivlev, Nikiforov, Orekhov, Yakimov.

LOW-DIMENSIONAL SYSTEMS

Pulsed-Laser Modification of Germanium Nanoclusters in Silicon

V. A. Volodin*, E. I. Gatskevich, A. V. Dvurechenskiĭ*, M. D. Efremov*, G. D. Ivlev**, A. I. Nikiforov*, D. A. Orekhov***, and A. I. Yakimov***

**Institute of Semiconductor Physics, Siberian Division, Russian Academy of Sciences, pr. Akademika Lavrent'eva 13, Novosibirsk, 630090 Russia*

e-mail: volodin@isp.nsc.ru

***Institute of Electronics, Belarussian Academy of Sciences, Minsk, 220090 Belarus*

****Novosibirsk State University, ul. Pirogova 2, Novosibirsk, 630090 Russia*

Submitted January 27, 2003; accepted for publication February 10, 2003

Abstract—The effect of pulsed ruby laser radiation on Ge nanoclusters grown on a (100)-oriented Si substrate is studied. The energy density of radiation corresponds to the melting threshold of the Si surface. Changes in the structure of nanoclusters are analyzed by comparing the experimental Raman spectra to those calculated in terms of Born–von Karman and Vol'kenstein models. It is established that the action of one pulse changes the cluster size and partly relieves the compression. Still greater changes take place in a sample subjected to ten pulses. The Ge nanoclusters transform into clusters of Ge_xSi_{1-x} solid solution, presumably due to the stress- and vacancy-aided diffusion. Laser-induced thermal processes in germanium nanoclusters in silicon are numerically simulated. © *2003 MAIK "Nauka/Interperiodica".*

INTRODUCTION

Silicon is the basic material of microelectronics; however, because of the indirect band gap and the resulting low probability of radiative transitions, its application in optoelectronics is very limited. One possibility of enhancing the probability of radiative transitions is to make use of the effective "convolution" of a wave vector in silicon-based nanometer-sized structures. The interest in the self-organization of Ge quantum dots (QDs) in Si also stems from the promise offered by such structures for fabrication of optoelectronic devices operating by the optical transitions between the energy levels of dimensional quantization for holes [1]. An important point for obtaining a structure with the given properties is the opportunity to control the size and the density of germanium QDs. A wide variety of methods to directly modify the size of Ge nanoclusters during the crystal growth is presented in [2]. These methods consist in are varying the growth temperature and rate, changing the value of mechanical stress at a heterojunction with the help of the buffer layers, introducing impurities that serve as nucleation centers for Ge islands, ion-beam stimulation of the island growth [3], and oxidizing the ultrathin silicon layer prior to germanium deposition [4, 5]. The aim of this study is to find out whether it is possible to modify the size, composition, and stresses in germanium QDs by means of pulsed laser irradiation. The structural state of Ge QDs was detected by a rapid, nondestructive, and informative method of Raman spectroscopy with the subsequent comparison of simulation results with experimental spectra. The latter procedure implies that, similar to an electron spectrum, the phonon spectrum of a QD as an artificial molecule is determined by the size, shape, and composition of a nanocluster, as well as by the properties of the surrounding material and the stresses [6].

EXPERIMENTAL

A set of three initial experimental samples was fabricated by molecular-beam epitaxy (MBE) on a (100)-oriented Si substrate. At first, a 150-nm-thick buffer silicon layer was grown on a KÉF-5 (n-Si:P, ρ = 5 Ω cm) substrate at 600°C. Then, the Ge layer with an effective thickness of four, eight, and ten monolayers (MLs) was grown at 300°C. The Ge nanoclusters were covered with a 150-nm-thick silicon layer at a temperature of 500°C. As the radiation source, we used a ruby laser with a wavelength of λ = 694 nm and a pulse duration of τ_p = 80 ns. The optical scheme ensured a highly uniform beam: energy variations within a spot 6 mm in diameter were no greater than ±5%. The energy density W in a pulse was close to 1 J/cm^2; i.e., it corresponded to the melting threshold of single-crystal Si [7]. The samples were subjected to one or ten pulses. The resulting structural changes in Ge nanoclusters were analyzed on the basis of the Raman spectra (RS) obtained before and after the exposure of samples. The spectra were measured at room temperature using a computer-controlled setup based on a DFS-52 spectrometer (LOMO, St. Petersburg); an Ar laser (λ = 514.5 nm) was used as the pump for the Raman pro-

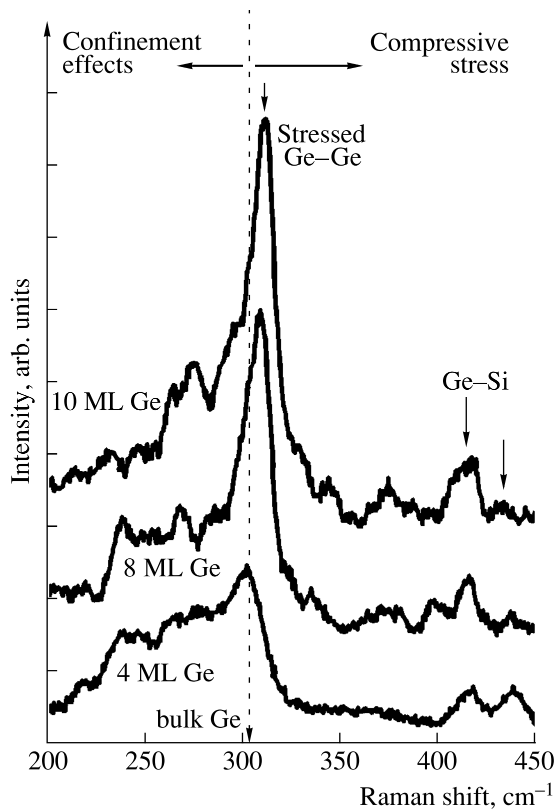

Fig. 1. Raman spectra of the initial samples containing Ge nanoclusters.

cess. We used the quasi-backscattering geometry, the incident radiation was polarized along ⟨001⟩ crystallographic direction, and the scattered light was detected in ⟨010⟩ polarization. The chosen configuration is allowed for the scattering by longitudinal optical (LO) phonons in germanium and silicon and forbidden for the two-phonon scattering by transverse acoustical (TA) phonons in the silicon substrate. This circumstance enabled us to avoid complexities encountered when interpreting Raman spectra [8]. In order to investigate the structural properties of Ge nanoislands, we numerically calculated the eigenfrequencies and eigenvectors of oscillations in the Born–von Karman approximation with five coordination shells being taken into consideration; then, the Raman spectra were calculated in terms of the Vol'kenstein model of additive bond polarizability [9] and compared to the experimental data.

RESULTS AND DISCUSSION

Figure 1 shows the RS of the initial samples. A peak observed in a range from 300 to 312 cm^{-1} (depending on the effective thickness of germanium) corresponds to the scattering by the optical vibrations of Ge–Ge bonds. In bulk germanium (in the absence of stresses), the peak of scattering by longitudinal and transverse optical phonons (LO and TO) falls at the Brillouin zone center, at 302 cm^{-1}. Due to the effect of optical phonon localization, a decrease in the size of Ge QDs shifts the peak to lower frequencies, whereas compressive stresses shift it to the higher frequencies. All of the peaks feature a low-frequency wing, which arises from the contribution of higher order localized modes, whose frequencies are lower because of the dispersion of optical phonons. Another possible contribution to the wings stems from fluctuations of the Ge layer thickness, especially in the case of samples with eight and ten Ge monolayers, where both the QDs and the wetting layer contribute to the scattering process. Samples with four Ge monolayers seem to contain no dots higher than 1 nm; otherwise, the existing stresses would shift the peak to the range from 310 to 318 cm^{-1}, which is indeed observed for samples with a thicker germanium layer. Because of the compression stresses, the RS peak in these samples is shifted to higher frequencies from its position in bulk germanium. This shift considerably exceeds the red shift arising from the optical phonon localization. Thus, the Raman spectroscopy data obtained provide evidence of the formation of stressed germanium QDs in the samples where the germanium layer has an effective thickness of eight and ten monolayers. Peaks observed in the range from 350 to 450 cm^{-1} correspond to Raman scattering by optical vibrations of Ge–Si bonds. A similar doublet structure of the Ge–Si peak was also observed previously [10, 11]. The positions of peaks depend on the stresses and stoichiometry. Since the peaks related to Ge–Si have a low intensity, one may consider the heteroboundary to be fairly abrupt (as it must be if low-temperature epitaxy is used), without intermediate layer of germanium–silicon solid solution.

In order to estimate the Raman shift as a function of the germanium layer thickness, the spectra were numerically simulated. The eigenfrequencies and eigenvectors of vibrations were calculated in terms of the Born-von Karman model. The fitting procedure for the force constants implied that the dispersions of the phonon modes in bulk germanium and silicon could be approximated by dependences derived from the analysis of slow neutron scattering [12]. The force constants for germanium and silicon differ by scale factor only, which allowed us to construct a unit cell of a Ge–Si heterostructure on the basis of the mass-replacement principle. With the values of eigenfrequencies and eigenvectors determined, we calculated the Raman spectra in terms of the Vol'kenstein model of the additive polarizability of bonds [9]. Some aspects of the calculation are presented in [13, 14]. In view of the fact that the unit-cell volume estimated for a typical Ge nanocluster size includes more than ten of thousands of atoms, we used a one-dimensional model with periodic boundary conditions in order to save computing time. The effect of stresses was disregarded in the calculation; however, one can take this effect into consideration by shifting each frequency by a value proportional to the stress.

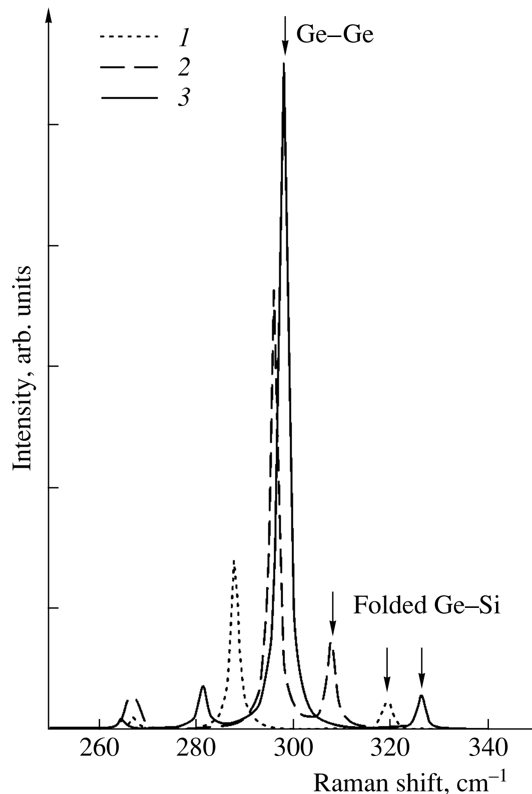

Fig. 2. Calculated Raman spectra of samples containing planar Ge layers with a thickness of (*1*) 4, (*2*) 8, and (*3*) 10 ML.

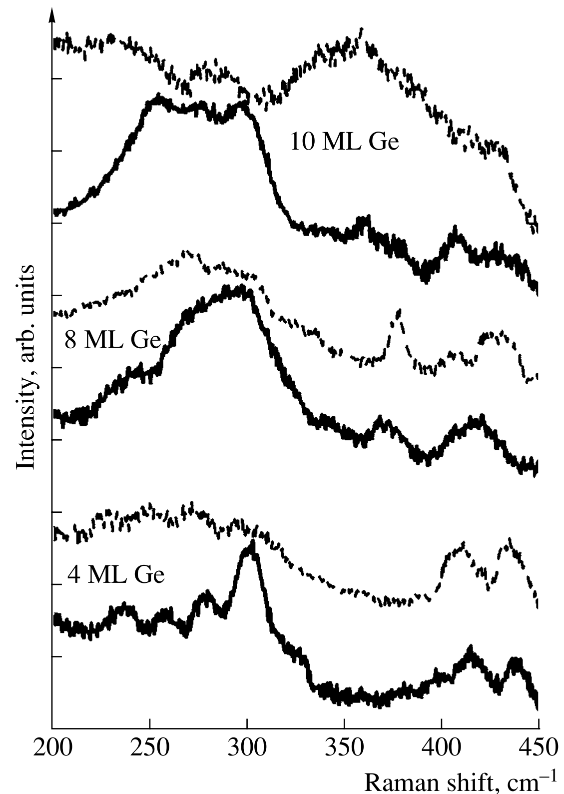

Fig. 3. Raman spectra of samples modified by (*1*) one and (*2*) ten laser pulses.

The results of the calculation (Fig. 2) are indicative of a blue shift of the RS peak corresponding to Ge–Ge bonds with a decrease in the germanium thickness (the aforementioned effect of optical phonon localization). The analysis of eigenvectors suggests that LO vibrations in germanium (LO_{Ge}) interact with the longitudinal acoustic vibrations in silicon (LA_{Si}). As a consequence of the periodic boundary conditions, this interaction gives rise to the folded modes LO_{Ge}–LA_{Si}. However, since only a single germanium layer was present in the studied samples, no experimental evidence of such modes can be obtained. The phonon frequency in the main Ge–Ge mode in a sample with ten monolayers is only by 4 cm^{-1} lower than the phonon frequency in bulk germanium. In Ge QDs, the effective germanium thickness is still larger and the quantum-dimensional shift is accordingly smaller. Therefore, the blue shift due to stresses in the studied samples (Fig. 1) does not exceed 12 cm^{-1}, which indicates partial relaxation of the initial stress. For comparison, the shift in completely strained structures is 17 cm^{-1} [15].

From comparison of the RS in the initial and the laser-modified samples (Fig. 3), we may conclude that the action of even a single pulse radically changes the structure of germanium QDs; this change is especially pronounced in samples with eight and ten germanium monolayers. The RS peak corresponding to the vibrations of Ge–Ge bond broadens and shifts to lower frequencies. These changes are indicative of a decrease in the size of pure germanium clusters (due to the formation of boundary Ge–Si layer) and an increase in their size spread, and, likely, they suggest some relaxation of compressive stress in them. Still more drastic changes are observed in the samples exposed to ten laser pulses. In this case, the RS analysis indicates that a Ge–Si solid solution is formed in all of the samples. An increase in the intensity and broadening of RS peaks corresponding to the vibrations of Ge–Si bonds are observed; the special features appearing in the range from 220 to 300 cm^{-1} are attributed to the scattering by local optical vibrations of Ge–Ge bonds in the solid solution [10, 11]. The Raman spectroscopy data considered are indicative of the laser-induced modification of both the size and the composition of germanium QDs, as well as of the stresses in the heterostructure; the extent of this modification depends on the conditions of the laser irradiation.

The analysis of the temperature conditions of QD treatment was aided by numerical simulation. Because of the low volume content, the germanium nanoclusters produce only a slight effect on the thermal properties of the structures; this fact enabled us to disregard the presence of QDs and to consider only the interaction of laser radiation with single-crystal Si. We also disregarded the contribution of nanoclusters to the absorp-

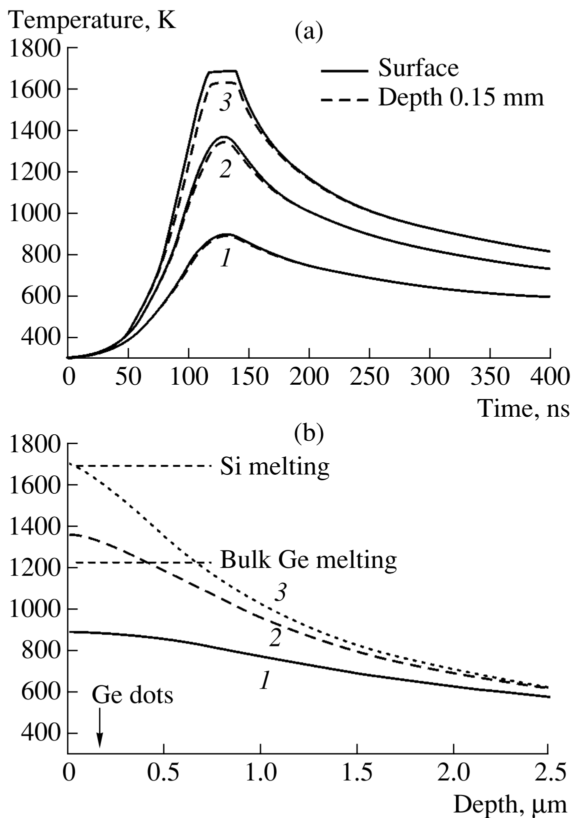

Fig. 4. Calculated (a) time and (b) depth distributions of temperature for the energy density of (*1*) 0.6 (131 ns), (*2*) 0.8 (128 ns), and (*3*) 0.9 (130 ns) J/cm^2.

tion of radiation. In the given experimental conditions, the calculation may be restricted to the one-dimensional case since the intensity of radiation is uniform over the irradiated region and the spot size is considerably larger than the thermal diffusion length even for a time that exceeds the duration of the pulsed heating by an order of magnitude. The one-dimensional nonlinear heat conduction equation with the Stefan condition at the phase interface was written as

$$\rho(x, T)[c(x, T) + L\delta(T - T_m)]\frac{\partial T}{\partial t} = \frac{\partial}{\partial x}\left[k(x, T)\frac{\partial T}{\partial x}\right] + Q(x, t),$$

$$\left.\frac{\partial T}{\partial x}\right|_{x=0} = 0,$$

$$T|_{x=D} = T|_{t=0} = T_0,$$

where T is the temperature, $T_0 = 300$ K, t is the time, coordinate x is directed inward the sample, ρ is the density, c is the specific heat, k is the thermal conductivity, L is the latent heat of melting, T_m is the melting point, and $\delta(T)$ is the Dirac δ function. Function $Q(x, t)$ describes the amount of heat released during the absorption of laser radiation; i.e.,

$$Q(x, t) = \alpha(T)(1-R)q(t)\exp\left\{-\int_0^x \alpha[T(x')]dx'\right\},$$

where α is the absorption coefficient, R is the reflection coefficient, $q(t)$ is the pulse shape, and $q(t) = W/\tau_p \sin^2(\pi t/2\tau_p)$.

Our calculation involved the dependences of optical and thermal parameters on the phase state and temperature [16]. The heat conduction equation was solved in terms of finite differences using the sweep method. An implicit difference scheme was used. The problem was actually solved for below-threshold conditions, and the term containing the δ function was required only to determine the onset of melting in single-crystal silicon. From numerical simulation, we derived the time dependences of the temperature on the surface and at a depth of QDs (~0.15 μm) for different energy densities in the laser pulse (Fig. 4a), as well as the depth distribution of temperature at its maximum (Fig. 4b). For the energy densities above 0.9 J/cm^2, the surface temperature becomes as high as the melting threshold ($T_{m\mathrm{Si}}$), although the temperature at the position of nanoclusters is lower. At $W \approx 0.8$ J/cm^2, Si remains crystalline and Ge inclusions heat up nearly to the melting point of bulk Ge ($T_{m\mathrm{Ge}}$). Thus, the most interesting conditions are those with energy densities ranging from 0.7 to 1 J/cm^2.

From the data calculated, we also derive the nanocluster liquid-phase lifetime as a function of the pulse energy density (Fig. 5). Assume that the melting point of a nanocluster (T_{mN}) is lower than that of the bulk germanium ($T_{m\mathrm{Ge}}$). Let the values of T_{mN} be equal to 1000, 1100, or 1200 K. Let the melting point coincide with the solidification point, which is not generally true since, due to the interdiffusion and the formation of QDs from Ge–Si solid solution, the solidification point of a nanocluster, may be higher than the melting point; as a result, the nanoclusters liquid-phase lifetimeis reduced. As the energy density increases from 0.7 to 0.9 J/cm^2, the nanocluster liquid-phase lifetime grows from 50 to 170 ns under the assumption that T_{mN} = 1000 K. Naturally, this time decreases when a higher melting point is assumed. The results of calculation suggest that, under the given experimental conditions, nanoclusters remain melted for approximately 100 ns.

Assuming that the interdiffusion of Ge and Si takes place in a solid phase and using the diffusion coefficients of germanium in bulk silicon (D_{Si}[cm^2/s] = 2 × 10^{3}exp(–5 [eV]/kT)) and silicon in bulk germanium (D_{Ge}[cm^2/s] = 20exp(–3 [eV]/kT)) (see [17] and references therein), we estimate the mean free path at ~1 Å. For example, at 1600 K, the depths of penetration of Ge into Si and Si into Ge achieved in 100 ns are 0.06 and 3 Å, respectively. As can be seen from the experimental data (Fig. 3), a noticeable modification of QD compo-

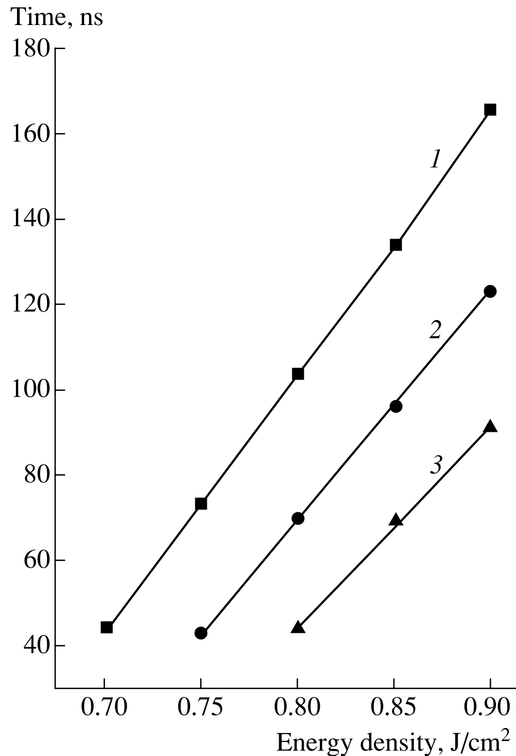

Fig. 5. Ge nanocluster liquid-phase lifetime calculated as a function of the pulse energy density with the melting point of nanoclusters T_{mN} set at (*1*) 1000, (*2*) 1100, and (*3*) 1200 K.

sition occurs even in the samples exposed to one laser pulse. This fact suggests that the mechanism of interdiffusion differs from that in the "classical" case. Melting of Ge QDs takes place, and the diffusion coefficient increases by several orders of magnitude [18]. The dependence of the melting point of semiconductor nanoclusters on their size, on the material of the environment, and on the stresses is not completely understood. From both theoretical analysis [19] and the experimental data [20], it is known that the melting point of semiconductor free-boundary nanoclusters decreases with a decrease in their sizes. The melting point of germanium decreases in the case of extension and increases in the case of compression, which may explain the lowering of the melting point for free-boundary nanoclusters. However, the melting point of nanoclusters embedded in a host matrix may be higher or lower than that of the bulk material depending on the material of the environment (see [19] and references therein). For example, while remaining crystalline, the silicon matrix may "keep" the embedded germanium nanoclusters from melting. The smaller the germanium cluster, the smaller the probability of a critical liquid-phase nucleus appearing in it since the surrounding silicon remains crystalline. Our experiments show that a sample incorporating a Ge layer with a thickness of four monolayers (Fig. 3) is less liable to undergo laser-assisted diffusion; in contrast, the Ge QDs are likely to melt in samples with eight and ten monolayers. In situ measurements of QD optical properties by means of ellipsometry with high time resolution during pulsed heating [21] revealed no abrupt phase transition at a certain temperature. It seems likely that the melting point of QD depends on its size, which can be used for the modification of QD sizes with the aim of reducing both their size and the size spread. At the cooling stage a strain-induced [22] or a defect-induced diffusion [23] is possible. According to the data of the spectroscopy of proton annihilation in epitaxial silicon layers grown at a low temperature, the concentration of vacancy-containing defect complexes may be as high as 10^{18} cm^{-3} [24]. Vacancy-defect-stimulated diffusion of germanium into the layers of low-temperature-epitaxy silicon results in the transformation of Ge nanoclusters into the clusters of Ge_xSi_{1-x} solid solution, which we actually observed after the ten-pulse irradiation (Fig. 3). Moreover, the expansion of the melting material raises the internal pressure, which increases the energy of germanium atoms. This circumstance may facilitate the transfer of germanium atom into the surrounding silicon matrix, where vacancy-accelerated diffusion is realized.

CONCLUSION

It has been established that the action of even one laser pulse changes the QD properties, modifies their size and composition, and partially reduces the stresses. Still more pronounced changes are observed in samples subjected to ten laser pulses. In particular, the Ge clusters transform into clusters of Ge_xSi_{1-x} solid solution, presumably due to the diffusion mixing of the interface during the melting of clusters and vacancy-aided diffusion.

ACKNOWLEDGMENTS

This study was supported by the Russian Academy of Sciences Commission on Training Young Scientists, project no. 60 of the 6th Competition-Appraisal of Young-Scientist Projects.

REFERENCES

1. A. I. Yakimov, A. V. Dvurechenskiĭ, N. P. Stepina, *et al.*, Zh. Éksp. Teor. Fiz. **119**, 574 (2001) [JETP **92**, 500 (2001)].
2. O. P. Pchelyakov, Yu. B. Bolkhovityanov, A. V. Dvurechenskiĭ, *et al.*, Fiz. Tekh. Poluprovodn. (St. Petersburg) **34**, 1281 (2000) [Semiconductors **34**, 1229 (2000)].
3. A. V. Dvurechenskiĭ, V. A. Zinov'ev, and Zh. V. Smagina, Pis'ma Zh. Éksp. Teor. Fiz. **74**, 296 (2001) [JETP Lett. **74**, 267 (2001)].
4. A. V. Kolobov, A. A. Shklyaev, H. Oyanagy, *et al.*, Appl. Phys. Lett. **78**, 2563 (2001).
5. V. A. Volodin, M. D. Efremov, A. I. Nikiforov, *et al.*, Fiz. Tekh. Poluprovodn. (St. Petersburg) **37**, 1220 (2003) [Semiconductors **37**, 1190 (2003)].

6. *Light Scattering in Solids*, No. 5: *Superlattices and Other Microstructures*, Ed. by M. Cardona and G. Güntherodt (Springer, Berlin, 1989).
7. G. D. Ivlev, E. I. Gatskevich, and D. N. Sharaev, Proc. SPIE **4157**, 78 (2001).
8. A. V. Kolobov, J. Appl. Phys. **87**, 2926 (2000).
9. M. Vol'kenshteĭn, Dokl. Akad. Nauk SSSR **32**, 185 (1941).
10. J. C. Tsang, P. M. Mooney, F. Dacol, and J. O. Chu, J. Appl. Phys. **75**, 8098 (1994).
11. M. I. Alonso and K. Winer, Phys. Rev. B **39**, 10056 (1989).
12. G. Nelin and G. Nilsson, Phys. Rev. B **5**, 3151 (1972).
13. M. D. Efremov, V. A. Volodin, V. A. Sachkov, *et al.*, Pis'ma Zh. Éksp. Teor. Fiz. **70**, 73 (1999) [JETP Lett. **70**, 75 (1999)].
14. V. A. Sachkov, V. V. Bolotov, V. A. Volodin, and M. D. Efremov, Preprint No. 2000-01, IMSÉ SO RAN (Inst. of Sensor Microelectronics, Siberian Division, Russian Academy of Sciences, Novosibirsk, 2000).
15. J. L. Liu, J. Wan, Z. M. Jiang, *et al.*, J. Appl. Phys. **92**, 6804 (2002).
16. C. P. Zhvavyĭ, Zh. Tekh. Fiz. **70**, 58 (2000) [Tech. Phys. **45**, 1014 (2000)].
17. K. Dettmer, W. Freiman, M. Levy, *et al.*, Appl. Phys. Lett. **66**, 2376 (1995).
18. V. A. Volodin, E. I. Gatskevich, A. V. Dvurechenskiĭ, *et al.*, in *Proceedings of Meeting on Silicon-2000* (Novosibirsk, 2002), p. 43.
19. Z. Zhang, J. C. Li, and Q. Jiang, J. Phys. D **33**, 2653 (2000).
20. A. N. Goldstein, Appl. Phys. A **62**, 33 (1996).
21. V. A. Shvets, S. I. Chikichev, A. S. Mardezhov, *et al.*, in *Proceedings of Meeting on Silicon-2000* (Novosibirsk, 2002), p. 186.
22. N. E. B. Cowern, P. C. Zalm, P. van der Sluis, *et al.*, Phys. Rev. Lett. **72**, 2585 (1994).
23. *Problems of Radiation Technology of Semiconductors*, Ed. by L. S. Smirnov (Nauka, Novosibirsk, 1980).
24. T. Ueno, T. Irisawa, Y. Shiraki, *et al.*, J. Cryst. Growth **227–228**, 761 (2001).

Translated by A. Sidorova

Semiconductors, Vol. 37, No. 11, 2003, pp. 1321–1325. Translated from Fizika i Tekhnika Poluprovodnikov, Vol. 37, No. 11, 2003, pp. 1358–1362.
Original Russian Text Copyright © 2003 by Bagaev, Zhuravlev, Sveshnikova, Badmaeva, Repinskiĭ, Voelskow.

LOW-DIMENSIONAL SYSTEMS

Photoluminescence from Cadmium Sulfide Nanoclusters Formed in the Matrix of a Langmuir–Blodgett Film

E. A. Bagaev*, K. S. Zhuravlev*^, L. L. Sveshnikova*, I. A. Badmaeva*, S. M. Repinskiĭ*, and M. Voelskow**

**Institute of Semiconductor Physics, Siberian Division, Russian Academy of Sciences, Novosibirsk,630090 Russia*

^e-mail: zhur@thermo.isp.nsc.ru

***Institute of Ion Beam Physics and Materials Research, Research Center Rossendorf, 01314 Dresden, Germany*

Submitted February 13, 2003; accepted for publication February 17, 2003

Abstract—Photoluminescence (PL) from CdS nanoclusters formed in the matrix of a Langmuir–Blodgett film and from the same clusters with the matrix removed has been studied. The PL spectrum of clusters in the matrix has the form of a broad band (full width at half-maximum (FWHM) ~ 0.6 eV) peaked at 2.4 eV. After removing the matrix with hexane, the PL spectrum consists of a high-energy band at 2.9 eV (FWHM ~ 0.2 eV) and two low-energy bands at 2.4 and 2.0 eV (FWHM ~ 0.5 eV). The high-energy band is attributed to exciton recombination in the nanoclusters, and the bands at 2.4 and 2.0 eV, to recombination via levels related to defects in the bulk of the matrix and at the nanocluster–matrix interface, respectively. © *2003 MAIK "Nauka/Interperiodica"*.

1. INTRODUCTION

Semiconducting materials in the form of clusters distributed in an organic or silicate matrix have aroused keen interest of researchers working in the fields of chemistry and physics of low-dimension systems and nonlinear optics [1, 2]. Materials of this kind exhibit unusual, as compared to bulk materials, optical and electronic properties [3, 4]. Specific features of these materials are determined both by individual properties of nanoclusters and by their interaction with one another and with the matrix. Nanosize semiconducting materials are commonly obtained by a number of methods, such as molecular-beam epitaxy [5], sol-gel technology [6], and the Langmuir–Blodgett (LB) technique [7–9]. Nanoclusters are synthesized in solutions [10], glasses [11], and polymers [12]. The LB method is a simple and inexpensive technique for obtaining multimolecular layered systems, which can be transformed by modification into a system of nanoclusters distributed in a solid multimolecular matrix.

It is known that the state of the surface of nanoclusters formed in glass and polymer matrices largely determines their optical and electronic properties [13]. The present study is concerned with photoluminescence (PL) from cadmium sulfide nanoclusters embedded in the matrix of an LB film and those after removal of the matrix.

2. SAMPLES AND EXPERIMENTAL PROCEDURE

Cadmium behenate films were obtained using the LB method by transferring of monolayers from the surface of a liquid subphase onto a solid substrate. Cadmium chloride solution with a concentration of 3×10^{-4} M and pH 6.0 served as the subphase. The monolayers were transferred under a surface pressure of 30 mN/m and a temperature of 22–23°C. As substrates, polished single-crystal silicon wafers were used. Films with 20–80 monolayers (MLs) (60–240 nm) were studied. Cadmium behenate films were sulfided at an H_2S vapor pressure of 100 Torr at 22°C; the time of sulfidation was 1–3 h. The chemical reaction

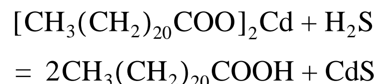

$$[CH_3(CH_2)_{20}COO]_2Cd + H_2S = 2CH_3(CH_2)_{20}COOH + CdS$$

yielded cadmium sulfide nanoclusters distributed in a behenic acid matrix. The formation of CdS and completeness of cadmium behenate conversion into behenic acid were monitored by IR spectroscopy. The preparation procedure and kinetics of sulfidation of cadmium behenate films were described in detail in [14]. The behenic acid matrix was removed in two ways: by treating a film containing nanoclusters with hexane or by thermal desorption of behenic acid in a vacuum at 200°C over the course of 2 h. The samples obtained were studied by the Rutherford backscattering technique, UV spectroscopy, and the PL method. Rutherford backscattering spectra were recorded using a beam of 1.2 MeV He^{2+} ions. The beam diameter was about 1 mm, and the beam current, 20 nA. Absorption spectra in the UV and visible spectral ranges were recorded with a Shimatzu spectrometer at wavelengths of 200–700 nm. PL was excited with a pulsed nitrogen laser (wavelength 337.1 nm, pulse duration 7 ns, average excitation density 0.04 kW/cm^2). PL spectra were mea-

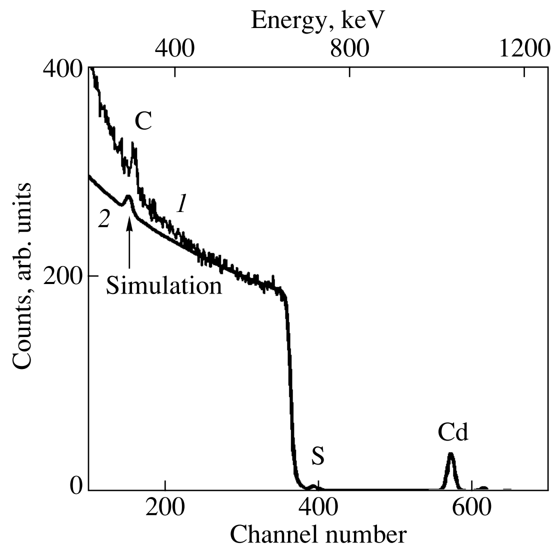

Fig. 1. Rutherford backscattering spectrum of a cadmium behenate film (40 MLs) on asilicon substrate after treatment with hydrogen sulfide. (*1*) Experimental spectrum and (*2*) approximation of the spectrum with a theoretical curve simulated by RUMP spectrum-processing software.

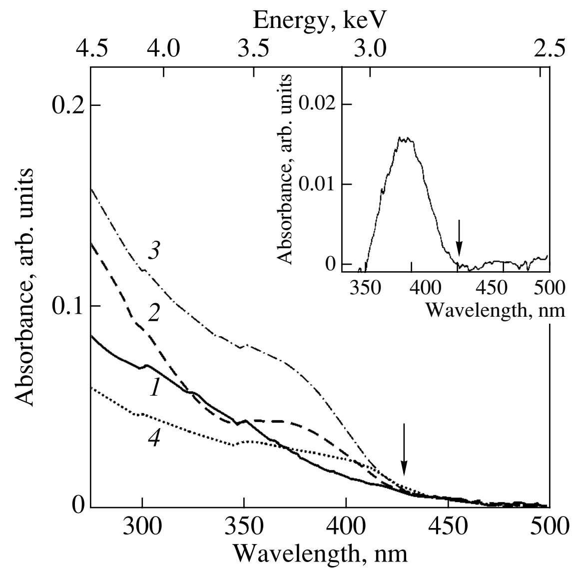

Fig. 2. Optical absorption spectra of LB films of cadmium behenate on a quartz substrate before and after treatment with hydrogen sulfide. Initial film thickness 80 MLs. (*1*) Before treatment and (*2*) after treatment; after removal of the matrix: (*3*) with hexane and (*4*) by annealing in vacuum at 200°C for 2 h. Insert: difference optical absorption spectrum of an LB film with CdS nanoclusters, obtained by subtraction of the spectrum of a quartz substrate from that of a film with nanoclusters. Arrows in the figures show the absorption edge associated with nanoclusters.

sured with a spectrometer based on an SDL-1 double monochromator equipped with a cooled FEU-79 photomultiplier operating in the single photon counting mode.

3. EXPERIMENTAL RESULTS

Figure 1 shows a Rutherford backscattering spectrum of a film consisting of 40 MLs of cadmium behenate on a silicon substrate after treatment with hydrogen sulfide. The spectrum contains in its high-energy part peaks corresponding to scattering of helium ions on cadmium and sulfur atoms in the surface layer of the film, which is about 10 nm thick. The low-energy part of the spectrum shows a pronounced shoulder corresponding to scattering on silicon atoms. A peak related to carbon atoms is seen on the background of the shoulder. The relative contents of cadmium, sulfur, and carbon were determined by processing the spectrum with RUMP standard software. For cadmium and sulfur, the relative contents are the same and equal to about 3%. This indicates that cadmium sulfide is formed in a stoichiometric ratio.

Figure 2 shows optical absorption spectra of LB films of cadmium behenate on quartz substrates before and after treatment with hydrogen sulfide. The initial film thickness was 80 MLs. It can be seen from the figure that the optical absorption of cadmium behenate grows steadily with photon energy increasing from 2.5 to 4.5 eV. Sulfidation gives rise to a broad absorption band at photon energies of 3.0 to 3.5 eV, which is due to absorption in CdS. The optical absorption threshold, found from the peak position in the second derivative of the absorption spectrum, lies at 2.9 eV. The shift of the absorption threshold with respect to the bulk energy gap of CdS (2.5 eV) is associated with quantum confinement of excitons in CdS nanoclusters. After treatment of the initial film with hexane, the position of the absorption threshold remains unchanged. At the same time, annealing of the initial film shifts the absorption threshold to lower energies, to 2.8 eV. The steady rise in the optical absorption of the films with increasing photon energy is probably due to absorption in the quartz substrate. To resolve the absorption associated with nanoclusters, the optical absorption spectrum of a quartz substrate was subtracted from the spectrum of a film with nanoclusters. The resulting difference optical absorption spectrum is shown in the insert to Fig. 2. The spectrum has the form of a band well approximated by a Gaussian function with maximum at 3.2 eV and fFWHM of 0.3 eV.

The size of nanoclusters is commonly found from optical absorption data by approximating experimental optical absorption spectra with theoretical functions taking into account the absorption spectrum of a single nanocluster and the influence of the cluster size variance [15, 16]. In this case, the width of the absorption band of a separate nanocluster is a function of its size. The nanocluster sizes were evaluated using the difference optical absorption spectrum in terms of a simplified model on the assumption that the width of the

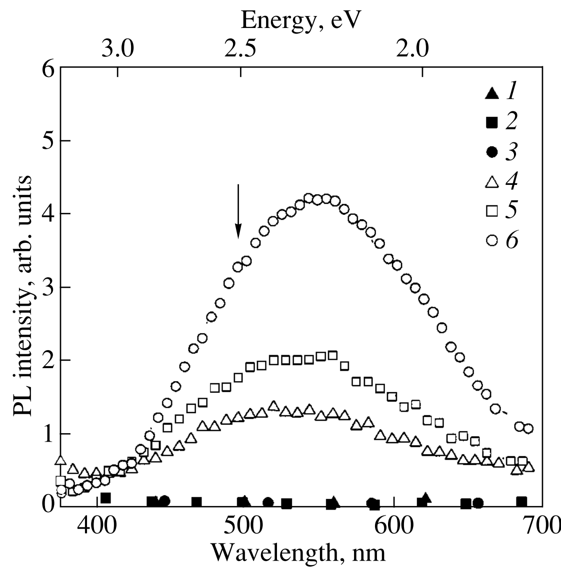

Fig. 3. PL spectra of the following samples: (*1*) silicon substrate; (*2*) film composed of 40 MLs of behenic acid; (*3*) film composed of 40 MLs of cadmium behenate before treatment with hydrogen sulfide; (*4–6*) cadmium behenate films composed of, respectively, 30, 40, and 80 MLs after treatment with hydrogen sulfide. The arrow shows the energy gap of bulk CdS.

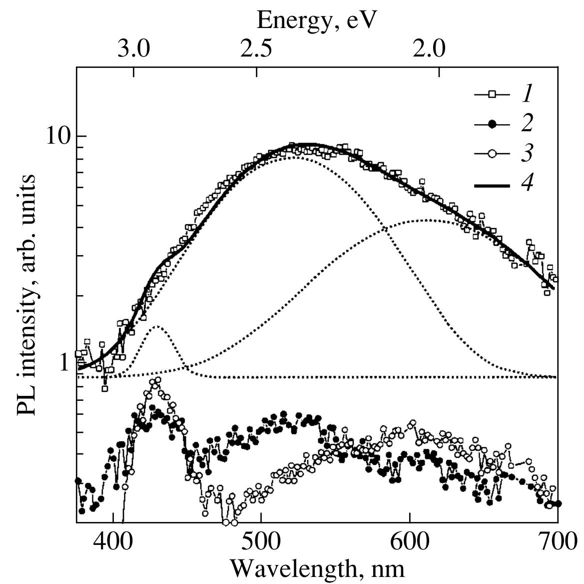

Fig. 4. PL spectra of cadmium sulfide nanoclusters in a behenic acid matrix and after its removal: (*1*) nanoclusters in a behenic acid matrix, (*2*) nanoclusters after removal of the matrix with hexane, and (*3*) nanoclusters after removal of the matrix by annealing at 200°C; (*4*) curve approximating the spectrum of nanoclusters in a matrix with three Gaussian curves. The Gaussian curves are shown by dashed lines.

absorption band of a separate nanocluster is independent of its size and the size distribution of nanoclusters is described by a Gaussian function. In this case, the peak position of the absorption band determines the average nanocluster size, and the FWHM of the band characterizes the nanocluster size variance. With the use of the dependence of the exciton energy on nanocluster size from [17], the average size and size variance of nanoclusters were found to be 1.5 and 0.1 nm, respectively.

Figure 3 shows PL spectra of LB films on silicon with a varied number of monolayers. A broad (FWHM 0.6 eV) asymmetric band appears in the PL spectrum of a film with nanoclusters in the behenic acid matrix. The peak position of this band corresponds to a photon energy of $\hbar\omega = 2.4$ eV, which is lower than the energy gap of bulk cadmium sulfide, equal to 2.5 eV. With an increasing number of layers, the PL intensity grows, but the shape of the spectrum is not significantly changed. The same figure shows PL spectra of silicon, behenic acid, and cadmium behenate. It can be seen that no PL is recorded from these substances.

Figure 4 compares a PL spectrum of cadmium sulfide nanoclusters in a behenic acid matrix to that measured after removal of the matrix. The integral intensity of PL from nanoclusters decreases by more than an order of magnitude after removal of the matrix. The PL spectrum of a sample treated with a hexane solution comprises a high-energy band peaked at 2.9 eV and bands at about 2.4 and 2.0 eV. The FWHM of the bands is 0.2 eV for the high-energy band and 0.5 eV for the other two. After annealing a sample at $T = 200$°C, the PL spectrum consists of a band that peaked at 2.9 eV (FWHM 0.2 eV) and that at 2.1 eV. The latter is well approximated with two bands at 2.4 and 2.0 eV (both with a FWHM of 0.5 eV). The dashed lines show Gaussian curves with peaks at 2.9, 2.4, and 2.0 eV and a FWHM of, respectively, 0.2, 0.5, and 0.5 eV, which approximate the PL spectrum of nanoclusters in a matrix.

Figure 5 shows PL spectra of a sample onto which 40 MLs of behenic acid were deposited after the sample was treated with hexane. It can be seen that, after deposition of the matrix, a new band that peaked at 2.1 eV (FWHM 0.6 eV) appears in the spectrum and the high-energy band at 2.9 eV disappears. The band at 2.1 eV is approximated with a sum of two bands with different intensities, which peaked at 2.4 and 2.0 eV (for both bands, the FWHM is 0.5 eV).

4. DISCUSSION

It can be assumed that the PL band that peaked at 2.9 eV, which is present in the sample spectra after removal of the matrix, is related to exciton recombination in CdS nanoclusters. The width of this band is in good agreement with that of the optical absorption band characterizing the nanocluster size variance. The peak position of the emission associated with exciton recombination in nanoclusters of various sizes must be deter-

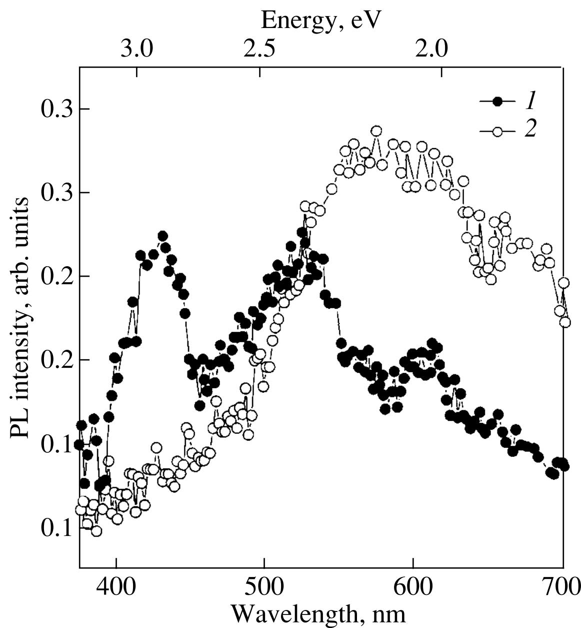

Fig. 5. PL spectra of (*1*) a sample containing cadmium sulfide nanoclusters after removal of the matrix with hexane and (*2*) the same sample after deposition of 40 MLs of behenic acid.

mined by the average size of nanoclusters (on the assumption that the recombination probability is size-independent). The peak position calculated on the basis of the average size corresponds to a photon energy of 3.2 eV. The observed peak of the high-energy band is shifted from the calculated value to lower energies, to 2.9 eV. The possible reason for the Stokes shift of the peak is related to capture of excitons into surface states of the nanoclusters.

The PL band peaked at 2.4 eV, which is observed after sample treatment with hexane, is probably associated with recombination via levels related to defects within the matrix bulk. This assumption is in agreement with the fact that the PL intensity decreases after removal of the matrix and that this band has an even lower intensity after annealing of the sample, which leads to more complete removal of the matrix.

The band that peaked at 2.0 eV, observed after removal of the matrix, is probably associated with PL via states situated at the nanocluster–matrix interface [18, 19]. Possibly, the states at the nanocluster–matrix interface are due, in the case under consideration, to the presence of the matrix. The increase in the intensity of the band that peaked at 2.0 eV and the decrease in the intensity of the band at 2.9 eV after deposition of a matrix onto the nanoclusters are due to an increase in the density of these states and to capture of nonequilibrium carriers, or excitons formed in the nanoclusters, by these states.

The above analysis suggests that the broad asymmetric PL band that peaked at 2.4 eV, observed for samples containing nanoclusters in a matrix, is a superposition of three bands: the band of exciton recombination in nanoclusters, the band associated with recombination via defect levels in the matrix, and the band related to states at the nanocluster–matrix interface. As seen from Fig. 4, the PL spectrum of nanoclusters in a matrix is indeed well approximated with three bands with peak positions and an FWHM corresponding to the respective values for the bands observed after matrix removal.

5. CONCLUSION

The paper reports on a study of PL from cadmium sulfide nanoclusters formed in the matrix of an LB film and after its removal. The data obtained by the methods of Rutherford backscattering and optical absorption confirm the formation of cadmium sulfide nanoclusters in the matrix of an LB film of behenic acid in the interaction of the cadmium behenate film with hydrogen sulfide gas. A study of PL from CdS nanoclusters revealed that the broad asymmetric band (at 2.4 eV) of PL from nanoclusters in the matrix is associated with recombination via levels related to defects in the matrix bulk and traps at the nanocluster–matrix interface, as well as with exciton recombination in nanoclusters. The emission associated with defects in the matrix bulk predominates, and that associated with exciton recombination in nanoclusters can be clearly seen only after removal of the matrix.

ACKNOWLEDGMENTS

This study was supported by the Russian Foundation for Basic Research (project no. 01-03-32796), the Program of the Ministry of Industry, Science and Technology, and the U.S. Civilian Research and Development Foundation, program rec. 008.

REFERENCES

1. E. S. Snow, P. M. Campbell, R. W. Rendel, *et al.*, Semicond. Sci. Technol. **13**, A75 (1998).
2. H. Weller, Angew. Chem. Int. Ed. Engl. **37**, 1658 (1998).
3. S. P. Beaumont and C. N. Sotomayor-Torres, *Science and Engineering of One- and Zero-Dimensional Semiconductors* (Plenum, New York, 1990), Vol. 214.
4. A. G. Milekhin, L. L. Sveshnikova, S. M. Repinskiĭ, *et al.*, Fiz. Tverd. Tela (St. Petersburg) **44**, 1884 (2002) [Phys. Solid State **44**, 1976 (2002)].
5. D. Leonard, M. K. Krishnamurthy, C. M. Reeves, *et al.*, Appl. Phys. Lett. **63**, 3203 (1993).
6. P. V. Kamat and D. Meisel, *Semiconductor Nanoclusters* (Elsevier, New York, 1996), Vol. 103.
7. N. A. Kotov, F. C. Meldrum, C. Wu, and J. H. Fendler, J. Phys. Chem. **98**, 2735 (1994).

8. J. Xu, H. Mao, and Y. Du, J. Vac. Sci. Tecnol. B **15**, 1465 (1997).
9. A. V. Nabok, A. K. Ray, and A. K. Hassan, J. Appl. Phys. **88**, 3 (2000).
10. J. H. Fendler and F. C. Meldrum, Adv. Mater. **7**, 607 (1995).
11. P. Nemec and P. Maly, J. Appl. Phys. **87**, 3342 (2000).
12. Xiying Ma, Gongxuan Lu, and Baojun Yang, Appl. Surf. Sci. **187**, 235 (2002).
13. U. Woggon, *Optical Properties of Semiconductor Quantum Dots* (Springer, Berlin, 1996).
14. C. M. Repinskiĭ, L. L. Sveshnikova, and Yu. I. Khapov, Zh. Fiz. Khim. **72**, 825 (1999).
15. B. G. Potter, J. H. Simmons, P. Kumar, and C. J. Stanton, J. Appl. Phys. **75**, 8039 (1994).
16. H. Matheu, T. Richard, J. Allegre, *et al.*, J. Appl. Phys. **77**, 287 (1995).
17. Y. Wang and N. Herron, Phys. Rev. B **42**, 7253 (1990).
18. X. Ma, G. Lu, and B. Yang, Appl. Surf. Sci. **187**, 235 (2002).
19. A. Hasselbarth, A. Eychmuller, H. Weller, *et al.*, Semicond. Sci. Technol. **13**, A75 (1998).

Translated by M. Tagirdzhanov

Semiconductors, Vol. 37, No. 11, 2003, pp. 1326–1330. Translated from Fizika i Tekhnika Poluprovodnikov, Vol. 37, No. 11, 2003, pp. 1363–1368.
Original Russian Text Copyright © 2003 by Kryzhanovskaya, Gladyshev, Kovsh, Soshnikov, Tsatsul'nikov, Kirmse, Neumann, Chi, Wang, Wei, Ledentsov, Ustinov.

LOW-DIMENSIONAL SYSTEMS

Optical Properties of MBE-Grown Ultrathin GaAsN Insertions in GaAs Matrix

N. V. Kryzhanovskaya[1]*, A. G. Gladyshev[1], A. R. Kovsh[1, 2], I. P. Soshnikov[1], A. F. Tsatsul'nikov[1], H. Kirmse[3], W. Neumann[3], J. Y. Chi[2], J. S. Wang[2], L. Wei[2], N. N. Ledentsov[1], and V. M. Ustinov[1]

[1]*Ioffe Physicotechnical Institute, Russian Academy of Sciences, St. Petersburg, 194021 Russia*
**e-mail: kryj@pop.ioffe.rssi.ru*
[2]*Industrial Technology Research Institute, Hsinchu 310, Taiwan, R.O.C.*
[3]*Institute für Physik, Humboldt Universität, 10115 Berlin, Germany*
Submitted February 25, 2003; accepted for publication March 4, 2003

Abstract—Optical properties of MBE-grown ultrathin GaAsN insertions in a GaAs matrix have been studied, with the goal of deriving methods for the intentional formation of carrier localization regions in GaAsN layers. In the case of a short-period GaAs/GaAsN superlattice, an additional long-wavelength line is observed in the photoluminescence spectrum. Comparison of the optical data with the transmission electron microscopy data shows that this line is related to the emission from the formed regions enriched with nitrogen (up to 8.5%). The characteristic size of these nitrogen-enriched regions in upper layers of the superlattice is larger than in lower ones, and it increases with the number of the deposited layers increasing. © *2003 MAIK "Nauka/Interperiodica".*

1. INTRODUCTION

Since the first GaAsN layers were obtained in 1992 [1], considerable attention is paid to this material, owing to extraordinary strong reduction of the energy gap with increasing nitrogen content. This property makes it possible to fabricate InGaAsN structures with emission in the IR-range covering the optical fiber spectral windows of 1.3 and 1.55 μm, thus opening prospects for the design of light emitters and detectors for optical fiber communication lines. As compared to currently widely used InGaAsP/InP heterostructures, the main advantage of InGaAsN structures on GaAs substrates are (i) higher temperature stability of the laser characteristics, related to enhanced energy of the carrier localization in the active region, and (ii) the possibility of fabricating surface-emitting lasers with monolithic AlGaAs/GaAs Bragg reflectors.

Up to the present, GaAsN properties have been studied for the case of low nitrogen content (<10%) [2]. It was shown that the recombination of excitons localized on the fluctuations of the energy gap width is the predominant mechanism of radiative recombination at low temperatures. The observed potential of localization arises due to inhomogeneous distribution of nitrogen atoms in the layer, the electronegativity of these atoms strongly differing from that of arsenic. With increasing nitrogen content, the photoluminescence (PL) intensity I_{PL} strongly decreases, owing to the formation of nonradiative recombination channels. The point is that rather low growth temperatures are commonly used upon deposition of InGaAsN by MBE, which raises the impurity concentration in the growing layers. Therefore, optical properties of structures are strongly dependent on the cleanliness of the working volume of the growth chamber and the purity of the starting materials. Further, the low growth temperature favors the formation of defects, such as interstitial Ga atoms, incorporation of Ga atoms into the sublattice of Group V elements, etc., which serve as nonradiative recombination centers. It was shown that the annealing of structures improves their structural quality and raises the PL intensity [3].

In the present study, we have investigated the possibility of intentional creation of localization centers in GaAsN-based structures by means of formation of ultrathin GaAsN layers in GaAs matrix. As it was shown previously [4, 5] for the InGaAs/GaAs system, the deposition of ultrathin InGaAs layers in GaAs matrix results in the formation of indium-enriched regions (quantum dots, QDs), which enables a considerable red shift of the emission line as compared with InGaAs quantum wells (QWs). The present study shows that this approach is applicable for the GaAsN system. When GaAsN solid solution is replaced by a GaAsN/GaAs superlattice with the same average composition, an additional line appears in the PL spectrum, with its peak considerably shifted to lower photon energies. Comparison of the optical data with the results of transmission electron microscopy (TEM) shows that this line corresponds to the emission from nitrogen-enriched nanoclusters formed in thin GaAsN layers.

2. EXPERIMENTAL

We have studied GaAsN layers in a GaAs matrix, deposited by different methods. The structures were MBE-grown on [001] n^+-GaAs substrates, under conditions of As enrichment. An RF plasma source was used to obtain atomic nitrogen. After the initial annealing, a GaAs buffer layer was deposited onto the substrate; all the structures had a 30-nm-thick GaAs capping layer. In the reference sample (structure I), a $GaAsN_{0.013}$ layer 0.1 μm thick was introduced into GaAs matrix. Structure II was produced by a 70-fold repetition of cycles comprising the deposition of five GaAs monolayers (MLs) with subsequent exposure of the surface to a flow of atomic nitrogen during the time necessary for growing one GaAs ML. Structure III was a 70-period superlattice composed of $GaAs/GaAsN_{0.05}$ layers of 4ML/1ML thickness. Thus, the thickness of nitrogen-containing layers in structures II and III was 0.1 μm also. The growth temperature was 520°C for GaAsN layers and 600°C for GaAs.

The structure characterization was performed by TEM and *X*-ray diffraction (XRD) analysis. The PL was excited with Ar^+ laser (incident power density up to $W = 5$ kW cm^{-2}). The PL excitation and transmission spectra were recorded using an incandescent halogen lamp. The PL was detected with a cooled Ge diode. A closed-cycle helium cryostat was used for studies at different temperatures.

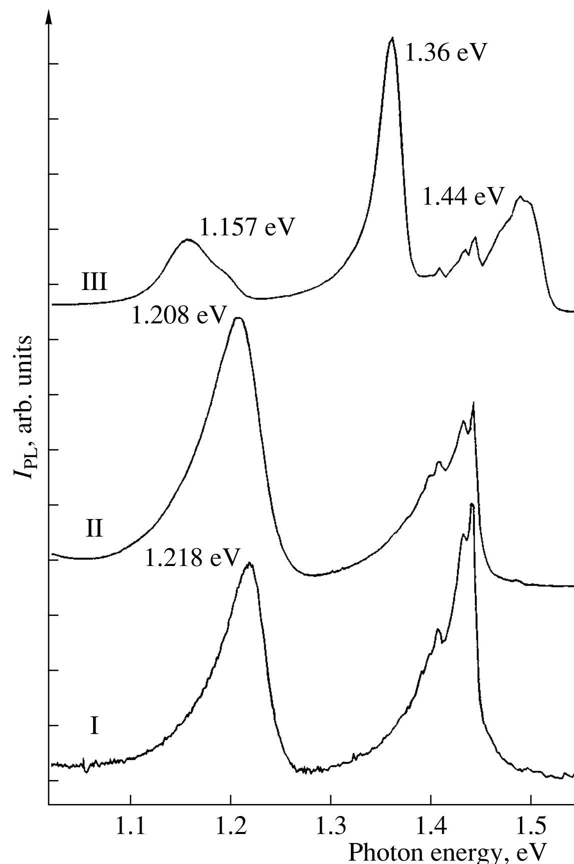

Fig. 1. PL spectra of GaAsN/GaAs structures at 20 K. I, II, and III are the numbers of the structures.

3. RESULTS AND DISCUSSION

The average nitrogen content in the grown structures was determined from the XRD data recorded with a double-crystal diffractometer, using Vegard's law for the case of an elastically strained layer. The maximum nitrogen content (1.58%) was found in structure III, grown using the layer-by-layer technique. For structure I, the N content in the layer was 1.36%. The lowest N content, 1.18%, was found in structure II fabricated with nitrogen introduced using the substitution scheme.

Figure 1 shows the PL spectra of the structures under study, recorded at a temperature of $T = 20$ K. The spectra of all the samples studied demonstrate—along with the emission band peaked at about 1.44 eV, which are attributed to the recombination in the transition layer (formed when the nitrogen source is turned on during GaAs growth)—emission lines related to recombination in the GaAsN region. The positions of these lines for samples I and II virtually coincide (1.218 and 1.208 eV), and the spectrum of structure III exhibits, instead of one emission line, two bands peaked at 1.157 and 1.36 eV. At the same time, the integral intensity of emission from sample III is considerably lower. These results suggest that sample III is characterized by the highest inhomogeneity of nitrogen incorporation into GaAs.

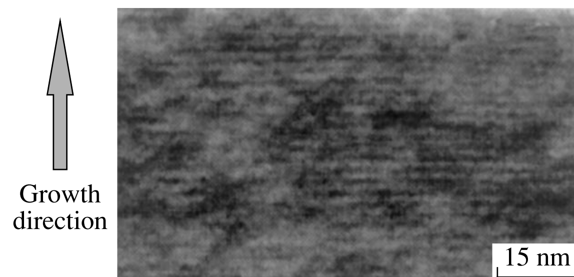

Fig. 2. Bright-field (110) cross-sectional (004) TEM image of structure III.

Cross-sectional TEM studies showed that the GaAsN/GaAs superlattice is formed only in the case of layer-by-layer deposition (structure III). Figure 2 shows the TEM data for this structure. At the same time, a nitrogen-containing layer, without any pronounced specific features, is formed in structure II, similarly to structure I. The quantitative analysis of the cross-sectional image of structure III, recorded by means of high-resolution electron microscopy, shows that the distribution of nitrogen in this sample is very inhomogeneous. The formation of regions strongly enriched with nitrogen (up to 8.5%) is observed in each

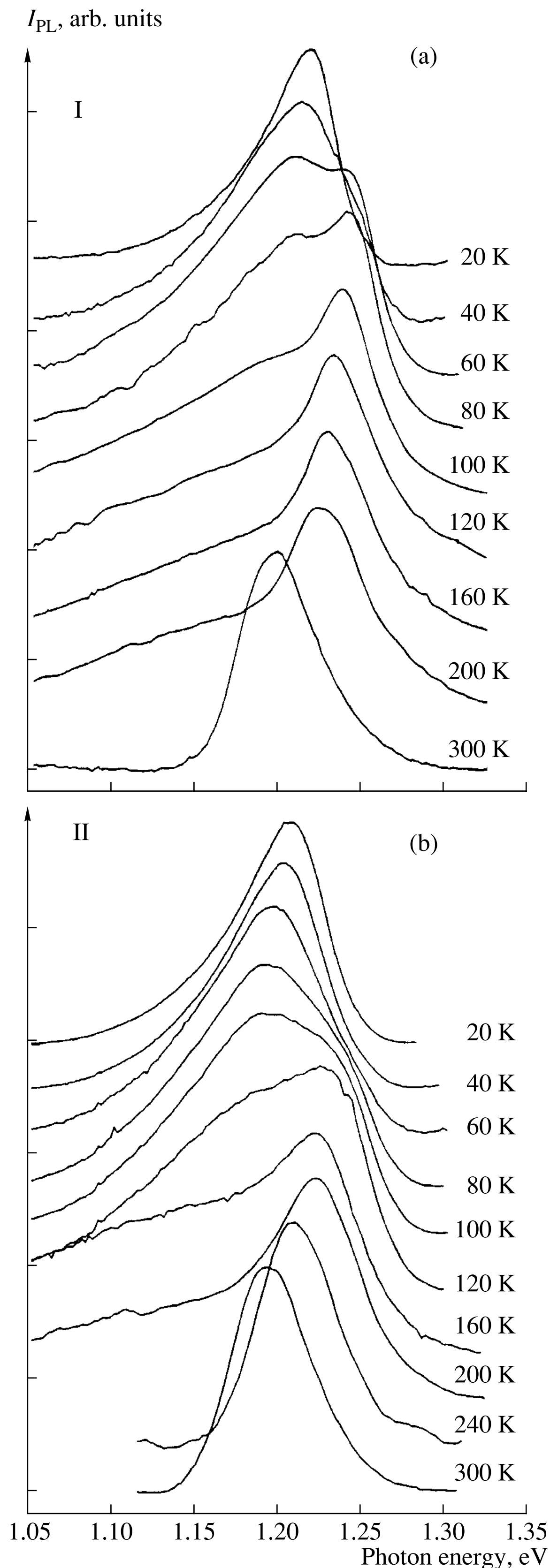

Fig. 3. PL spectra of structures (a) I, (b) II at different temperatures.

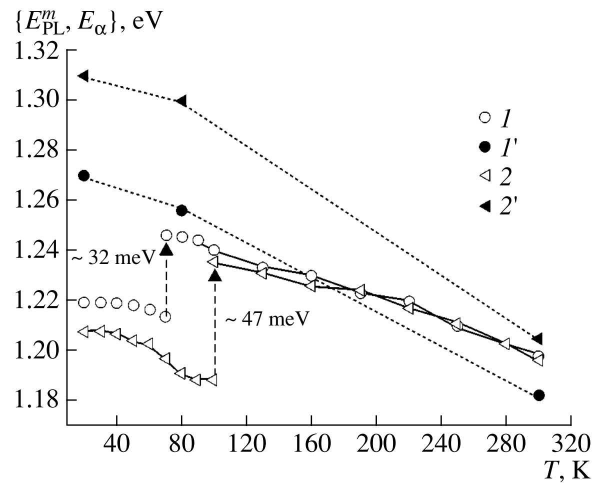

Fig. 4. Temperature dependences of energies of (*1*, *2*) PL peak E^m_{PL} and (*1*', *2*') absorption edge E_α for the structures: (*1*, *1*') I, and (*2*, *2*') II.

GaAsN layer. The typical lateral size of these regions is 5–10 nm.

Comparison of TEM data with the results of the optical study leads to the conclusion that the long-wavelength PL line is related to the recombination in the regions of GaAsN/GaAs superlattice with high nitrogen content, while the short-wavelength line is attributed to the recombination in the regions where the nitrogen content is low.

To study the effect of the GaAsN layer deposition technique on the optical properties and to better understand the details of the recombination processes, we have investigated the PL temperature dependences. Figure 3 shows PL spectra of samples I and II, recorded at different temperatures. With rising temperature, the behavior of the PL peak, which is typical of the system of materials under study, is observed [6]. At low temperatures, the radiative processes in the GaAsN layer are governed by the recombination of excitons in the formed centers of the carrier localization. With rising temperature, thermal emission of carriers to shallow centers becomes possible (in the temperature range 80–140 K), which accounts for the blue shift of the peak. A further increase in temperature leads to a red shift resulting from the energy gap decreasing.

To determine the absorption edge in the layers, the transmission spectra were recorded and the absorption spectra were calculated from these data. The reflection from the sample was disregarded in the calculations. The obtained absorption edge energies in structures I and II (Fig. 4) are in good agreement with the literature data on the GaAsN layer energy gap [7]. In this context, the following fact is noteworthy. The energy spacing between the emission-line peak (E^m_{PL}) and the absorption edge in structure II is larger, in spite of the lower nitrogen content in this structure than in sample I. In

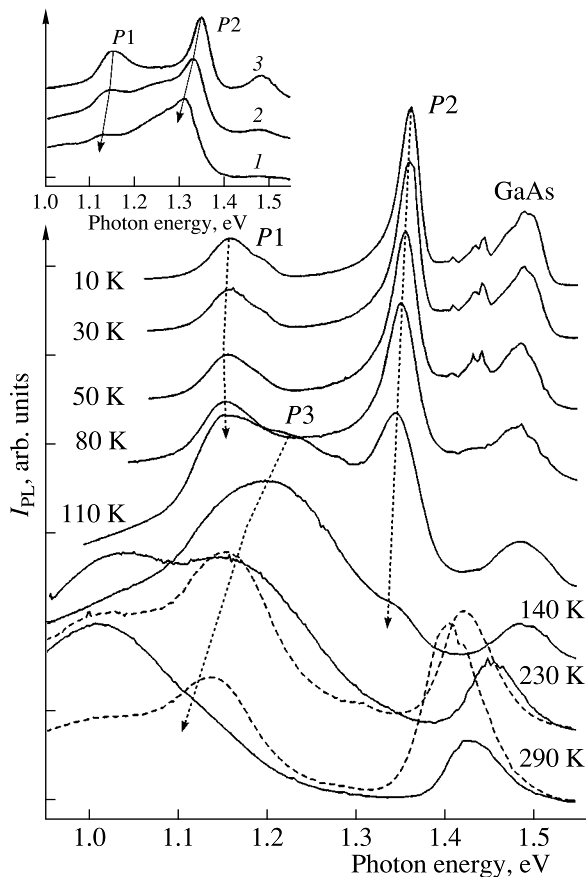

Fig. 5. PL spectra of structure III at different temperatures at pumping densities of (solid lines) 500 W cm^{-2} and (dashed lines) 5 kW cm^{-2}. Inset: PL spectra at 80 K temperature at excitation densities of (*1*) 5, (*2*) 50, and (*3*) 500 W cm^{-2}.

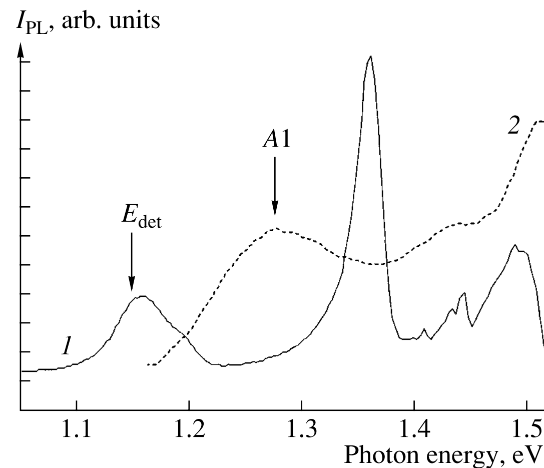

Fig. 6. (*1*) PL spectrum and (*2*) PL excitation spectrum for structure III at 7 K. E_{det} is the energy of the excitation spectrum recording.

addition a rise in the temperature at which the short-wavelength peak begins to predominate is observed. These facts suggest that localization centers resulting from inhomogeneous incorporation of nitrogen atoms into GaAs are formed more effectively in structure II, fabricated with the nitration technique applied for the production of GaAsN layers.

In structure III, the PL temperature behavior (Fig. 5) is different from that in samples I and II. As mentioned above, at low temperatures the PL spectra of structure III show two peaks, *P*1 and *P*2. The observed shoulder of the *P*1 peak is attributed to the splitting of light and heavy hole levels (the splitting energy is ~40 meV) in strained GaAsN [8]. The intensity of *P*1 and *P*2 peaks decreases with increasing temperature, and an additional line *P*3 appears in the spectrum, which predominates at high temperatures and high pumping levels (the long-wavelength peak near 1 eV corresponds to defect-related emission from GaAs substrate).

The obtained temperature dependences can be explained on the basis of the TEM data, which indicate a strong inhomogeneity of the nitrogen distribution in the formed ultrathin layers. This is also indicative, taking into account the fact that the bowing coefficient of the dependence of the energy gap on nitrogen content in GaAsN is 0.18 eV/%, of a strong variation in the energy gap upon insignificant variations of the average nitrogen content. In this case, the energy spectrum of the structure is represented by a quasi-continuous set of states distributed by a certain law. As follows from the TEM data, the density of nitrogen-enriched regions is high in sample III. Therefore, the transitions of carriers between localized states corresponding to separate islands are possible. The optical data indicate that some features are observed in the energy spectrum of carriers localized in the GaAsN layer at energies corresponding to *P*1 and *P*2 optical transitions. With rising temperature, the population of less localized states becomes possible owing to thermal emission of carriers, which is manifested in the appearance of the *P*3 peak. In this situation, the thermal emission of carriers from the states giving rise to the *P*2 PL line leads to "quenching" of this emission line. The spectra obtained at a low pumping density at 80 K (see the inset to Fig. 5) exhibit a considerable broadening of the emission spectrum, which confirms the conclusion that a broad spectrum of energy states is formed.

These results are supported by the data on the PL excitation spectra (Fig. 6), which demonstrate a peak, denoted as *A*1, slightly shifted to a shorter wavelength with respect to the *P*3 line of PL. This behavior is typical of the absorption by localized states, and it confirms the conclusion that an additional peak exists in the density-of-states spectrum. One should note that the position of this peak corresponds to the energy gap of GaAsN solid solution with 1.5% nitrogen content, which agrees with the XRD data.

To investigate processes of the formation of nitrogen-enriched regions in the growing of a multilayer GaAsN/GaAs structure, we applied gradient etching

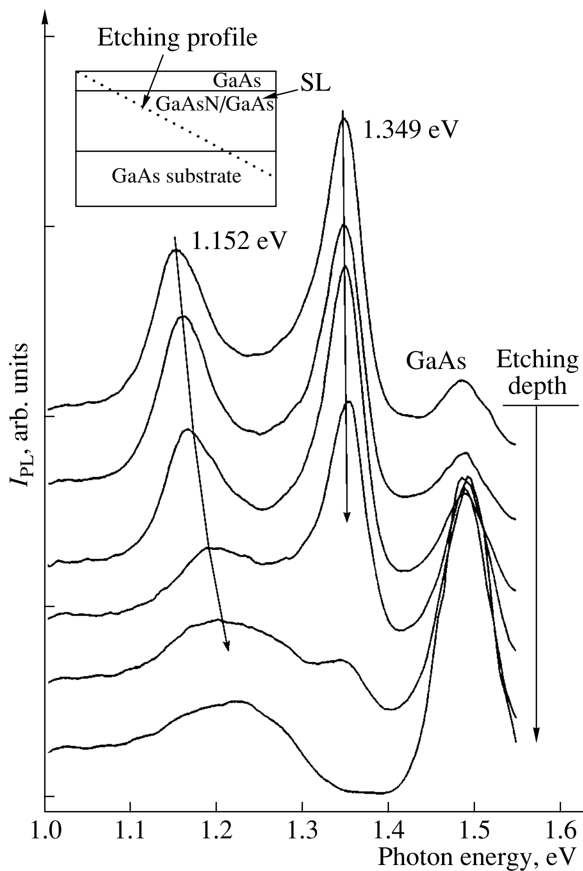

Fig. 7. PL spectra of structure III recorded at 77 K from different points of the sample after the gradient etching.

and studied the PL spectra from different points of the sample (Fig. 7). Blue shift of *P*1 line is observed with increasing etching depth, whereas the position of *P*2 band remains virtually unchanged. Such a shift of the *P*1 line indicates that either the size of islands or the nitrogen content in them increases with an increasing number of GaAsN deposition cycles. We believe that this fact is related to the effect of elastic stress induced in the structure by islands of the preceding layers. Similar enlargement of the lateral size was observed in the case of InAs QDs in GaAs [9], which resulted in a considerable red shift of the emission line. At maximum etching depth, the PL spectrum demonstrates only the peaks related to emission from the GaAs substrate.

4. CONCLUSION

Optical properties of GaAsN/GaAs heterostructures grown in different deposition techniques have been studied. The layer-by-layer growth mode ensures a considerable increase in the emission wavelength as compared with the emission from the layer of the same average composition, since the recombination proceeds in the formed nitrogen-enriched regions. The application of the nitration technique to obtain GaAsN layers enhances the formation of the carrier localization centers resulting from inhomogeneous incorporation of nitrogen atoms into GaAs.

ACKNOWLEDGMENTS

This study was supported by the Russian Foundation for Basic Research (project no. 02-02-17677) and by the ITRI–Ioffe Joint Scientific Program.

We are grateful to E.V. Nikitina, I. Hannert, and I. Hausler for assistance.

REFERENCES

1. M. Weyers and M. Sato, Jpn. J. Appl. Phys. **31**, L853 (1992).
2. I. A. Buyanova, W. M. Chen, and B. Monemar, MRS Internet J. Nitride Semicond. Res. **6**, 2 (2001).
3. T. Kitatani, K. Nakahara, M. Kondow, *et al.*, J. Cryst. Growth **209**, 345 (2000).
4. V. Bressler-Hill, A. Lorke, S. Varma, *et al.*, Phys. Rev. B **50**, 8479 (1994).
5. P. D. Wang, N. N. Ledentsov, C. M. Sotomayor Torres, *et al.*, Appl. Phys. Lett. **64**, 1526 (1994).
6. I. A. Buyanova, W. M. Chen, G. Pozina, *et al.*, Appl. Phys. Lett. **75**, 501 (1999).
7. M. Kondow, K. Uomi, K. Hosomi, and T. Mozume, Jpn. J. Appl. Phys. **33**, L1056 (1994).
8. Y. Zhang, A. Mascarenhas, H. P. Xin, and C. W. Tu, Phys. Rev. B **61**, 4433 (2000).
9. B. V. Volovik, D. S. Sizov, A. F. Tsatsul'nikov, *et al.*, Fiz. Tekh. Poluprovodn. (St. Petersburg) **34**, 1368 (2000) [Semiconductors **34**, 1316 (2000)].

Translated by D. Mashovets

Semiconductors, Vol. 37, No. 11, 2003, pp. 1331–1335. Translated from Fizika i Tekhnika Poluprovodnikov, Vol. 37, No. 11, 2003, pp. 1369–1373.
Original Russian Text Copyright © 2003 by Bakhtin, Varavin, Dvoretskiĭ, Kravchenko, Latyshev, Mikchaĭlov, Sabinina, Sidorov, Yakushev.

LOW-DIMENSIONAL SYSTEMS

Spontaneous Formation of the Periodic Composition-Modulated Nanostructure in $Cd_xHg_{1-x}Te$ Films

P. A. Bakhtin, V. S. Varavin*, S. A. Dvoretskiĭ, A. F. Kravchenko, A. V. Latyshev, N. N. Mikchaĭlov, I. V. Sabinina, Yu. G. Sidorov, and M. V. Yakushev**

Institute of Semiconductor Physics, Siberian Division, Russian Academy of Sciences, Novosibirsk, 630090 Russia

**e-mail: varavin@isp.nsc.ru*

***e-mail: krav@thermo.isp.nsc.ru*

Submitted January 27, 2003; accepted for publication March 7, 2003

Abstract—Anomalous electrical properties have been observed in $Cd_xHg_{1-x}Te$ films grown on GaAs substrates by MBE at elevated temperature. The anomalies are manifested in the conductivity anisotropy, modifications of the transmission and photoconductivity spectra upon low-temperature annealing, and the existence of a periodic undulatory surface microprofile. The temperature dependence of conductivity along and across the microprofile waves has been studied. It is suggested that a $Cd_xHg_{1-x}Te$ film with anomalous electrical properties is a spontaneously formed periodic structure in the form of vertical nanowalls of different compositions. Possible mechanisms for the formation of such a structure are discussed. © *2003 MAIK "Nauka/Interperiodica"*.

1. INTRODUCTION

Semiconductor solid solutions based on $Cd_xHg_{1-x}Te$ (mercury cadmium telluride, MCT) represent the leading material in the production of IR photodetectors sensitive in 1-20-μm wavelength range.

Electrical properties of MCT are strongly dependent not only on electrically active point defects, but on the composition and conduction microinhomogeneities, which give rise to anomalous temperature and field dependences [1]. In turn, the homogeneity and imperfection of a material are defined, to a great extent, by the method of fabrication.

The method best suited for growing of large-area MCT films is molecular beam epitaxy (MBE), which allows the use of alternative substrates, such as GaAs or Si. The growth temperature (180–200°C) in MBE is lower than in other methods, and the formation of structural defects and the microprofile of the growing surface depend intricately on the growth conditions, such as the growth temperature and rate, Hg vapor pressure, orientation and material of the substrate. The emergence of a microprofile at early growth stages can give rise to the formation of structural and conductivity inhomogeneities in the bulk, which will strongly affect the parameters of the structures grown.

Structural and conductivity inhomogeneities may arise from the instability of the solid solution and from elastic strains. As known from the literature, an undulatory surface and the composition modulation in the film bulk have been observed in a large number of epitaxial structures based on semiconductor solid solutions [2–7]. These phenomena may be linked to the fact that, in some ranges of temperature and composition, homogeneous semiconductor solid solutions become unstable and dissociate into periodic structures with alternating compositions. The first experimental studies related to this subject were casual, since the main goal was to obtain a stable homogeneous solid solution. The latest studies of the instability in solid solutions suggest that this phenomenon can be used to obtain nanoheterostructures [2]. To describe the instability of multicomponent solid solutions, the theory of spinodal decomposition, derived for metallic alloys, is frequently used [2–4]. For example, a characteristic photoluminescence (PL) spectrum with two peaks has been observed [2] in films of InGaAsP solid solution obtained in the instability region on InP and GaAs substrates. The presence of two peaks in PL spectra led to the suggestion that the epitaxial layer (epilayer) was heterogeneous, consisting of two solid solutions of different compositions. The transmission electron microscopy (TEM) of these structures revealed the intensity modulation perpendicular to the growth plane. The authors suggested that these data were indicative of possible spinodal decomposition and, consequently, composition modulation.

In [5], spontaneous formation of a structure called the vertical superlattice by the authors was observed in the growth of $In_xAl_{1-x}As$ films by MOCVD at 565–590°C. The formation of the structure was also attributed to phase separation in the solid solution. TEM and transmission electron diffraction studies of these structures confirmed the existence of periodic vertical regions differing in composition.

Spontaneous modulation of composition in AlGaN layers on sapphire substrates was observed in [6]. However, in this case the composition was modulated in the direction of the film growth.

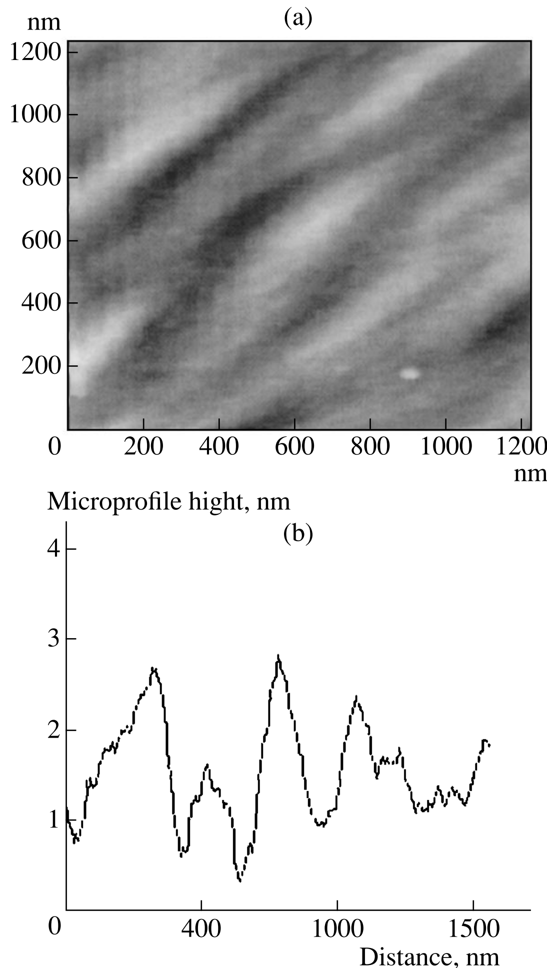

Fig. 1. (a) AFM image of a film free of periodic microprofile and (b) the typical microprofile.

The effect of elastic strains on epilayer growth was discussed in [7–9]. An undulatory surface profile was observed in InGaAs films. It has been suggested that the relationship between the surface energy, which acts as a stabilizer in the formation of a small-period profile, and the elastic strain energy, which destabilizes a surface with a large-period profile, determines the surface formation. As shown in [7], the possibility of composition modulation and morphological stability of the epilayer is determined by the sign of the lattice-mismatch parameter (i.e., depending on whether a film grows under compressive or tensile stress). The composition modulation in the bulk of a film can give rise to anisotropy of transport and optical properties of heterostructures.

Our study of MCT films grown by MBE at elevated (for this method) temperatures (210°C) revealed anomalous electrical properties, which manifested themselves simultaneously in the conductivity anisotropy, a smooth transmission spectrum, and modifications of the transmission and photoconductivity spectra after annealing. Furthermore, a periodic microprofile was always observed on these films. The goal of the present study is to investigate transport and optical processes in MBE-grown MCT films with a periodic surface microprofile.

2. RESULTS AND DISCUSSION

MCT film grown by MBE on (013) GaAs substrates of 50.8 mm in diameter were studied [10]. Substrates had a (011) principal cut. A HgTe buffer layer 5–7 μm thick was grown on the substrate, and further, *n*-type MCT films with $x = 0.21$–0.24, 8–12 μm thick. Films grown at elevated temperatures (~210°C) demonstrated anomalously low carrier mobility (~1000 $cm^2/(V\ s)$), conductivity anisotropy, and features in the transmission spectrum.

A study of the film surface by atomic-force microscopy (AFM) revealed a microprofile on the surface of films grown at 180–200°C (Fig. 1). As seen, the nonuniformities have gentle slopes and are irregular. At a higher growth temperature (up to 210°C), a system of ordered waves appears on the surface in addition to nonuniformities having a gentle slope, as seen in Fig. 2. The characteristic period of this microprofile is 0.1–0.2 μm, and the slope reaches 5°–7°. The direction of waves in respect to the principal cut is the same over the entire film area, with an angle of 30°–45° for different films.

Anisotropy of the in-plane conductivity was observed in MCT films grown at elevated temperatures and exhibiting the periodic surface microprofile, with an anisotropy coefficient of about 10 at a temperature of 77 K. We studied angular dependences of conductivity and established that the conductivity is the lowest in the direction across the surface microprofile waves [11]. The anisotropy is observed at any point of the wafer, and it is not caused by the conductivity gradient over the wafer area. No anisotropy was observed in MCT films free of the periodic surface microprofile. Since the film thickness (~10 μm) is significantly larger than the height of the periodic microprofile (~4 nm), the microprofile itself cannot be the reason for the strong anisotropy of conductivity.

Another specific property of films exhibiting the conductivity anisotropy is weaker spectral dependence of light transmittance near the fundamental absorption edge as compared with that for films with the same thickness and similar composition, but free of the conductivity anisotropy [11]. The annealing of these films at $T = 220$–240°C for several tens of hours results in blue shift of the fundamental absorption edge and steeper spectral dependence. This behavior of the transmission spectrum can be related to the presence in the film of microscopic regions of different composition, which occupy a significant portion of the volume. In this case, the transmission spectrum will be similar to

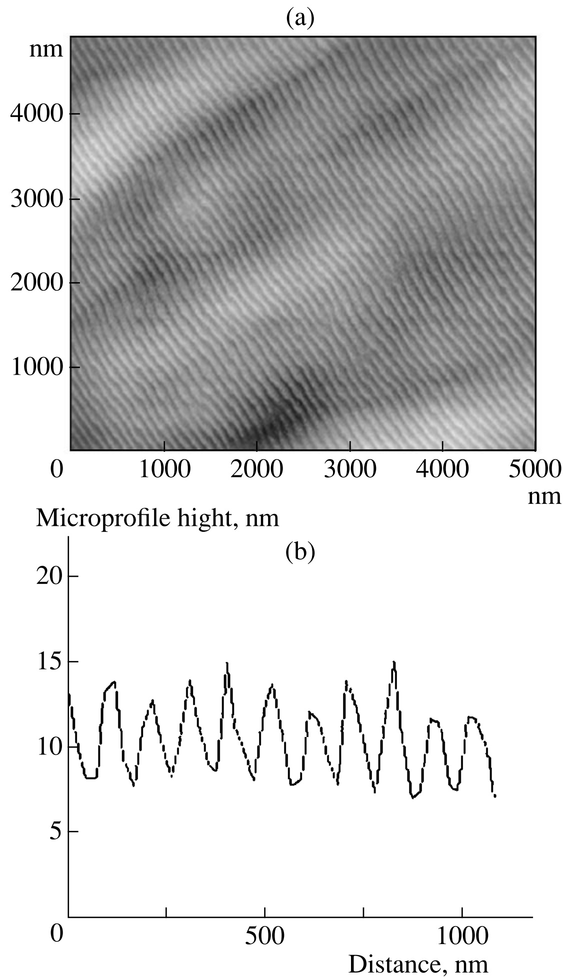

Fig. 2. (a) AFM image of a film with periodic microprofile and the (b) typical microprofile across the waves.

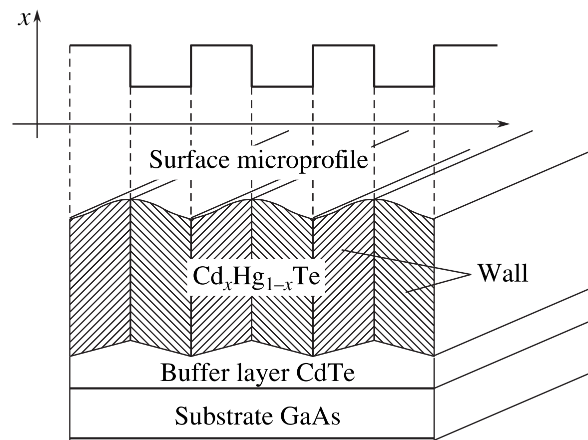

Fig. 3. Schematic cross-section of a structure and the composition distribution across the microprofile waves.

that for an equivalent structure with two layers differing in composition and the slope of the spectral dependence will be lower than for a homogeneous film of the same thickness.

The whole set of the obtained experimental data suggests that the structure of MCT films with anomalous properties is a periodic system of nanowalls with different compositions, arranged along the growth direction, as shown in Fig. 3.

As follows from the literature data, the undulatory profile and composition modulation in epilayers of semiconductor solid solutions can be induced by spinodal decomposition and elastic strains. However, the dependence of the MCT lattice parameter on composition is small. Maximum mismatch between CdTe and HgTe is 0.3%; thus, the elastic strains between the regions with different composition would be small. Moreover, the critical temperature of spinodal decomposition is only 80 K [12]. Thus, it may be suggested that the observed surface morphology and composition modulation stem not from spinodal decomposition or elastic strains, but from some other sources; one of these may be the undulatory profile of the buffer layer. The following mechanism of the wall formation may be suggested. Since the composition of an MCT solid solution can depend on the orientation of the subjacent surface, walls differing in composition and, probably, in carrier density will grow on the opposite slopes of the microprofile waves.

In the presence of nanowalls with different compositions, the modification of spectrum after annealing can be due to the composition equalization by diffusion. We have calculated the thickness of walls that could allow the diffusion equalization of composition under the annealing modes used [11]. This value is ~0.1 μm, which is comparable to the microprofile period.

One should note that after the annealing at T = 240°C, the films become p-type and no conductivity anisotropy is observed.

The presence of compositional microinhomogeneities and composition equalization after annealing is also confirmed by the changes in the photoconductivity spectrum. Figure 4 shows photoconductivity spectra of sample 525 before and after annealing. As seen, the long-wavelength edge of photoconductivity is shifted by ~8 μm to shorter wavelengths after annealing. So large a shift can be attributed only to variation of the composition. Estimates show that for this shift the compositions in adjacent walls must be $x = 0.195$ and $x = 0.270$ before annealing and equalized to $x = 0.233$ after it.

Now we will discuss the possibility that the conductivity anisotropy arises from different conductivities of walls. Our estimates show that, to obtain a ratio of conductivities along and across the walls of ~10 (which has been observed in experiment), it is necessary to have a ratio of conductivities of ~40 in the adjacent walls with different compositions. In this situation, the electron density in the adjacent walls must differ by more than an order of magnitude, since the electron mobility dif-

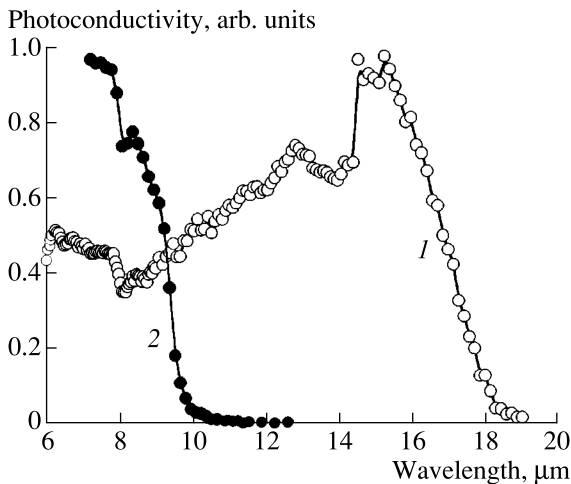

Fig. 4. Photoconductivity spectrum of film 525: (*1*) before annealing; (*2*) after annealing at 220°C for 75 h.

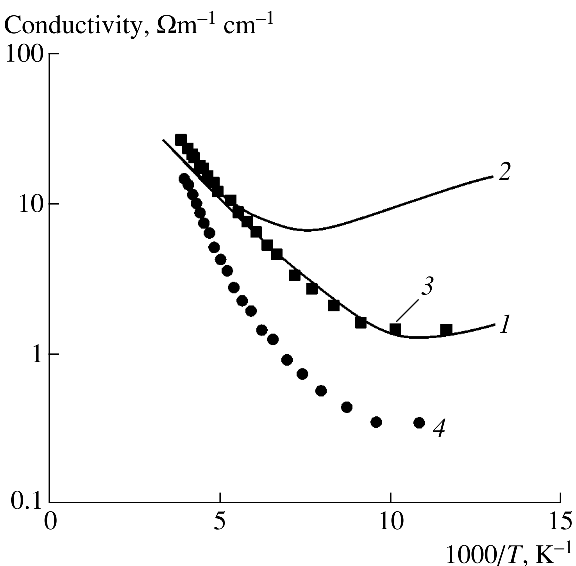

Fig. 5. Temperature dependences of conductivity: (*1*, *2*) calculated for homogeneous materials with donor concentration $N_d = 10^{14}$ and 10^{15} cm^{-3}, respectively; (*3*, *4*) experiment for directions along and across the microprofile waves, respectively.

fers by no more than three times for compositions with $x = 0.2$–0.3. This difference in electron densities in the walls seems hardly probable, because in homogeneous films with different compositions grown under similar conditions, the carrier densities differ only slightly.

To determine the nature of the anisotropy, we studied temperature dependences of conductivity and the Hall factor in the range from 77 to 300 K in the Hall-configuration samples fabricated by photolithography in the directions of maximum and minimum conductivity. Figure 5 shows temperature dependences of conductivity. Solid lines are the calculated dependences for a homogeneous *n*-type material. As seen, the experimental data on conductivity along the microprofile stripes coincide well with the dependence calculated for a homogeneous material with an electron density of 10^{14} cm^{-3}. The temperature dependence for conductivity across the microprofile waves exhibits a steeper slope, and the conductivity value is several times smaller. However, the character of the dependence across the microprofile waves reproduces, on the whole, that along the microprofile stripes.

Temperature dependences of the Hall factor in the samples along and across the microprofile waves are similar, and the Hall factors differ only slightly in the temperature range from 77 to 300 K.

Since the adjacent walls have different compositions, a potential barrier must appear, as in an *n*–*n* heterojunction. In this case, the conductivity must decrease exponentially with decreasing temperature, which is not observed in experiment. This can be due to the large value of the Debye screening length (estimates yield ~0.1 μm), which lowers the barriers between the adjacent walls.

Thus, the anisotropy of conductivity in MCT films under study is most likely due to the difference in the carrier mobilities for carriers moving along and across nanowalls with different compositions. This difference is due to potential barriers between the walls.

3. CONCLUSION

Anomalous electrical properties have been observed in MCT films grown on GaAs substrates by MBE at elevated temperature. The anomalies are the conductivity anisotropy and modifications of the transmission and photoconductivity spectra at low-temperature annealing. All the films with anisotropic conductivity exhibit a periodic undulatory surface microprofile, and the lowest conductivity is observed in the direction across the microprofile waves. It is suggested that an MCT film with anomalous electrical properties represents a spontaneously formed periodic structure in the form of vertical nanowalls differing in composition. The observed specific features in the transmission spectra and the modification of the transmission and photoconductivity spectra after annealing are attributed to the difference in composition between the suggested walls, and to diffusion equalization of the composition under annealing. Most likely, the anisotropy of conductivity is related to the difference in carrier mobility between carriers moving along and across nanowalls with different compositions, due to potential barriers between the walls.

REFERENCES

1. A. I. Vlasenko, A. V. Lyubchenko, and E. A. Sal'kov, Ukr. Fiz. Zh. **25**, 1317 (1980).
2. N. A. Bert, L. S. Vavilova, I. P. Ipatova, *et al.*, Fiz. Tekh. Poluprovodn. (St. Petersburg) **33**, 544 (1999) [Semiconductors **33**, 510 (1999)].

3. I. P. Ipatova, V. G. Malyshkin, A. Yu. Maslov, and V. A. Shchukin, Fiz. Tekh. Poluprovodn. (St. Petersburg) **27**, 285 (1993) [Semiconductors **27**, 158 (1993)].

4. D. Bimerg, I. P. Ipatova, and P. S. Kop'ev, Usp. Fiz. Nauk **167**, 554 (1997).

5. Sung Won, Tae-Yeon Seong, J. H. Lee, and Bun Lee, Appl. Phys. Lett. **68**, 3443 (1996).

6. I. Levin, L. H. Robins, M. D. Vaudin, *et al.*, J. Appl. Phys. **89**, 188 (2001).

7. J. E. Guyer, S. A. Barnett, and P. W. Voorhees, J. Cryst. Growth **217**, 1 (2000).

8. J. E. Guyer and P. W. Voorhees, J. Cryst. Growth **187**, 150 (1998).

9. F. Leonard and R. C. Desai, Phys. Rev. B **57**, 4805 (1998).

10. Yu. G. Sidorov, S. A. Dvoretsky, N. N. Mikhailov, *et al.*, Proc. SPIE **4355**, 228 (2001).

11. P. A. Bakhtin, V. S. Varavin, S. A. Dvoretskiĭ, *et al.*, Avtometriya, No. 2, 83 (2002).

12. S.-H. Wei, L. G. Ferreira, and A. Zunger, Phys. Rev. B **41**, 8240 (1990).

Translated by D. Mashovets

Semiconductors, Vol. 37, No. 11, 2003, pp. 1336–1341. Translated from Fizika i Tekhnika Poluprovodnikov, Vol. 37, No. 11, 2003, pp. 1374–1379.
Original Russian Text Copyright © 2003 by Valakh, Lisitsa, Strelchuk, Vuychik, Ivanov, Toropov, Shubina, Kop'ev.

LOW-DIMENSIONAL SYSTEMS

Excitonic Recombination near the Mobility Edge in CdSe/ZnSe Nanostructures

M. Ya. Valakh*, M. P. Lisitsa*, V. V. Strelchuk*, M. V. Vuychik*, S. V. Ivanov, A. A. Toropov**, T. V. Shubina**, and P. S. Kop'ev****

**Institute of Semiconductor Physics, National Academy of Sciences of Ukraine, Kiev, 03028 Ukraine*
e-mail: valakh@isp.kiev.ua
***Ioffe Physicotechnical Institute, Russian Academy of Sciences, St. Petersburg, 194021 Russia*
Submitted March 11, 2003; accepted for publication March 18, 2003

Abstract—The low-temperature photoluminescence and Raman scattering in CdSe/ZnSe nanostructures with individual CdSe inserts of 1.5 and 3.0 monolayers in nominal thickness were studied. The energy position of the photoluminescene band is governed by interdiffusion of Cd and Zn into the insert regions, whereas the shape of this band is controlled by strong interaction of localized excitons with optical phonons in the $Zn_{1-x}Cd_xSe$ solid-solution insert. Multiphonon processes of excitonic relaxation with involvement of acoustic phonons at the Brillouin zone edges are also important. The results obtained are interpreted in the context of a model for the effective excitonic mobility edge. © *2003 MAIK "Nauka/Interperiodica".*

1. INTRODUCTION

Coherently strained CdSe/ZnSe heterostructures have been intensively studied recently since these structures can be used with good results in fabrication of optoelectronic devices for the visible region of the spectrum. Based on the difference between band gaps (~1 eV) and the mismatch of lattice parameters of the components (~7%), a CdSe/ZnSe system is similar to the well-studied InAs/GaAs heterostructure. Therefore, it has been initially assumed that three-dimensional islands are formed according to the Stranski–Krastanov mechanism (similar to what occurs in an InAs/GaAs system) if the thickness of the deposited CdSe epitaxial layer (epilayer) is close to the critical thickness, which amounts to 3.0–3.5 monolayers (MLs) [1–3]. However, electron microscopy studies have shown that the nucleation of nanoislands (predominantly, of two-dimensional configuration) sets in at a much smaller thickness of the epilayer (0.6–0.7 MLs) [4]. Therefore, structural and compositional disorder can come into existence with resulting random fluctuations of potential in the region of a CdSe insert even at the aforementioned small nominal thickness of the deposited layer. These fluctuations can give rise to spatial localization of energy levels.

The relaxation of localized excitons is typically interpreted on the basis of a model of an exciton that resides in the random potential [5]. The concept of the "mobility edge" suggested by Mott and Anderson [6] is used in the model under consideration; this edge corresponds to the energy that separates the localized and delocalized excitonic states. Two approaches based on the Mott–Anderson model [5, 7] were used to interpret the experimental data obtained for the mixed CdS_xSe_{1-x} crystals [5]. This circumstance was related to the fact that Cohen and Sturge [5] observed a gradual transition (with a width of several millielectronvolts) between the above localized and delocalized states instead of an abrupt mobility edge, which is typically associated with the microscopic nature of disordering. A possible origin of this discrepancy may be related to the existence of macroscopic inhomogeneities in an actual crystal. As a result, the mobility edge can become significantly less steep. In addition, the Mott–Anderson model implies an infinite lifetime of excitations, whereas the lifetime of excitons in direct-gap semiconductors is on the order of 1 ns or shorter. Under conditions of selective excitation, excitons are generated with a well-defined energy and then diffuse over the spectrum. As a result, an "effective" mobility edge (threshold) can arise; the exciton motion for the times on the order of the exciton lifetime becomes possible above this threshold. Therefore, there are no reasons to expect that the corresponding edge will be abrupt (unbroadened).

Excitonic states near the mobility edge affect the efficiency of the transport of photoexcitations; therefore, it is important to gain insight into the origin of these states. Only "hot" excitons are mobile and can be involved in an efficient transport of excitations. If these excitons are generated with an energy above the mobility threshold, they are in the delocalized state; however, when found near the various-origin local fluctuations of potential, these excitons are rapidly thermalized at the aforementioned fluctuations with an accompanying emission of a phonon. Localized excitons are more stable, their dynamics is governed by hopping transport, and they dissociate with emission of a photon whose energy is governed by local levels. Therefore, the lumi-

1063-7826/03/3711-1336$24.00 © 2003 MAIK "Nauka/Interperiodica"

nescence is observed at energies that are lower than the mobility threshold; i.e., spectral diffusion occurs rather rapidly. In contrast, if an exciton is generated with an energy lower than the mobility threshold, this exciton dissociates in the same state (and in the same spatial region) in which it was generated. As a result, the fluorescence line narrows, which is accompanied by a narrowing of the LO-phonon replicas. Such a difference between exciton–phonon interactions for the localized and delocalized states is caused by the fact that a delocalized exciton does not remain at the same site for a long enough time to "sense" the phonon-caused changes in the lattice; as a result, a delocalized exciton interacts more weakly with phonons than does a localized exciton.

In this paper, we report the results of studying the optical properties of CdSe/ZnSe nanostructures with nominal thicknesses of CdSe inserts amounting to 1.5 and 3.0 MLs; these results indicate that local potential fluctuations arise in the course of self-organized growth of nanoislands and modulate spatially the band gap (E_g) on a macroscopic scale comparable to the exciton's diffusion length. This observation may support the notion that nanoislands have sizes that are close to the corresponding excitonic Bohr radius.

2. EXPERIMENTAL

All the samples studied were grown by molecular-beam epitaxy with enhanced migration of atoms on the GaAs(001) substrate at a temperature of 280°C [8]. The thicknesses of the buffer and protective ZnSe layers were 80 and 20 nm, respectively. Individual CdSe inserts were formed between these layers; the thicknesses of these inserts were 1.5 and 3.0 ML, respectively, and were specified by the number of epitaxy runs (0.3 ML in each run) for 135 s with interruption after each run.

The photoluminescence (PL) and Raman spectra at 300 and 5 K were recorded using a DFS-24 double spectrometer in the photon-counting mode. Discrete lines of Ar^+-laser radiation were used to excite the spectra. Some of the PL spectra were excited using a Xe lamp. A high precision of determining the spectral position of recorded lines was ensured by simultaneous detection of the plasma laser lines and was no worse than 0.3 cm^{-1}. The spectral resolution amounted to 0.12 meV when the low-temperature PL spectra were recorded.

3. RESULTS AND DISCUSSION

In Fig. 1, we show the low-temperature (5 K) PL spectrum (the dotted line) for an excitation-photon energy of 2.882 eV and the PL-excitation spectrum with detection at E_{det} = 2.547 eV for a nanostructure with a nominal thickness of CdSe insert of 1.5 MLs. The PL spectrum consists of a single inhomogeneously broadened band which is peaked at 2.567 eV, has a half-width of ~25 meV, and features a low-energy wing. This band corresponds to the excitonic emission from the insert. The position of this band's peak is consistent with published data [9–11]. As for the PL excitation spectra, the high-temperature peak closest to the PL band (in the case under consideration, located at ~2.59 eV) was related previously [11, 12] to an excitonic transition with involvement of a light hole (LH_0) by analogy with the situation for quantum dots (QDs) in the III–V compounds [13]. In the latter case, it was believed that the spectrum of the density of states in a QD was similar to an atomic spectrum (it has a [Delta]-like shape) and that there was no transport between neighboring QDs. It is assumed in this interpretation that the low-energy peak HH_0 in the PL-excitation spectrum is obscured by an intense PL. In this situation, the magnitude of the HH_0–LH_0 splitting for the sample under investigation should not exceed 23 meV (even in the absence of the Stokes shift). However, based on the latest data on the actual shape and size of islands in the CdSe/ZnSe nanostructures obtained using the technology employed in this study, we are inclined to attribute the 2.59-eV peak to the HH_0 transition. In fact, the studies by the method of transmission electron microscopy showed that the shape of nanoislands is far from being spherical and can be approximated by a flat disk with a diameter to height ratio in the range from 5–10 to 1. In this situation, the HH_0–LH_0 splitting is governed not only by a difference in the quantization energies due to dissimilar effective masses but also by the effect of elastic stresses which give rise predominantly to uniaxial (rather than isotropic) strain in the islands. The corresponding estimation for the limiting case of homogeneous pseudomorphic $Zn_{1-x}Cd_xSe$ quantum well yields a splitting magnitude on the order of 100 meV for the

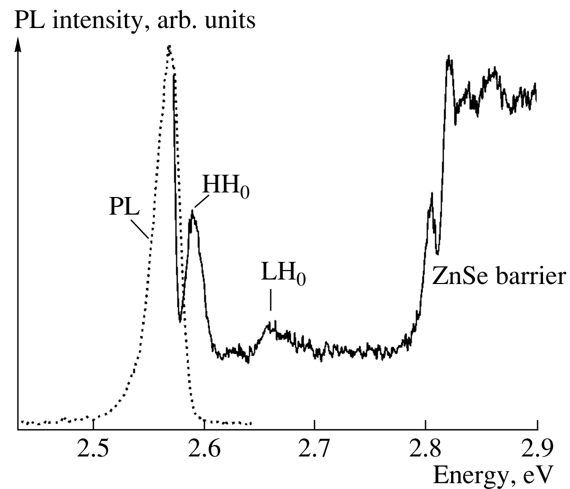

Fig. 1. The PL spectrum of a CdSe/ZnSe nanostructure with a nominal 1.5-ML thickness of the CdSe insert under excitation with a photon energy of 2.882 eV (dotted line) and the luminescence-excitation spectrum at E_{det} = 2.547 eV. T = 5 K.

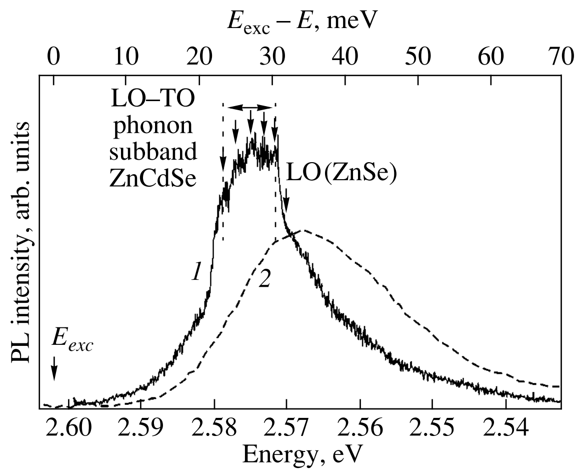

Fig. 2. Photoluminescence spectra of a CdSe/ZnSe structure with a nominal 1.5-ML thickness of the CdSe insert under resonance excitation in the region of excitonic HH_0 transition ($E_{exc} = 2.602$ eV, $P \leq 0.5$ W/cm^2) and under excitation in the absorption region of the ZnSe matrix ($E_{exc} = 2.882$ eV) (dashed line). $T = 5$ K. The spectral resolution is 0.12 meV. The upper scale corresponds to the energy of long-wavelength shift of curve *1* relative to the excitation-photon energy.

Cd atomic fraction $x = 0.3$–0.4 in the solid solution; this composition is found in the sample with a 1.5-ML thick CdSe insert, as will be shown below. This estimate may be slightly inflated for the actual shape of nanoislands; however, in any case, the magnitude of splitting should probably far exceed the aforementioned value of 23 meV. In this case, the latter value is related to the Stokes shift, while the 2.662-eV band in the luminescence-excitation spectrum should be interpreted as originating from the LH_0 transition. The broadening of the LH_0 band is caused by possible fluctuations in the shape of islands and (or) by inhomogeneous stresses.

Two intense peaks at 2.803 and 2.82 eV are also observed in the luminescence-excitation spectrum; these peaks are related to the ZnSe barrier layers and may correspond to excitonic transitions with involvement of the light and heavy holes or to a transition from the higher and lower barriers that differ in stresses. In any case, the observed splitting (~17 meV) indicates that there are appreciable elastic stresses in the barrier layers. Two low-intensity features in the still higher energy portion of the luminescence-excitation spectrum may correspond to spin-related split-off excitonic transitions.

Previous studies of the dynamics of the emission originating from selectively excited CdSe/ZnSe superlattices with a submonolayer-scale thickness of CdSe insert showed [14] that the relaxation of electronic excitations with involvement of LO phonons was dominant in a time interval of 25–30 ps; a broadening of the emission band on the low-energy side and a shift of the band peak to lower energies was observed at longer times. This behavior was related to the spectral diffusion of excitations with involvement of acoustic phonons. In the case of the steady-state measurements under consideration, the PL spectrum depends heavily on the excitation conditions.

Figure 2 (curve *1*) shows the PL spectrum of a sample with a 1.5-ML thick CdSe insert at 5 K under the resonance excitation of nanoislands by photons with an energy of 2.602 eV, which exceeds somewhat the energy of the peak in the luminescence-excitation spectrum; this peak corresponds to the HH_0 excitonic transition. For the sake of comparison, the dashed line *2* in Fig. 2 represents the PL spectrum for nonresonance excitation ($E_{exc} = 2.882$ eV). It can be seen that, in the case of resonance excitation, the emission peak is shifted somewhat to higher energies; as a result, a relatively narrow (~13 meV) distribution of excitons is formed below the effective mobility edge, which is located in the vicinity of ~2.67 eV in a structure with the aforementioned thickness of CdSe insert [11]. The PL intensity under resonance excitation is fairly high. These features of the PL spectrum are related to the fact that the intensity and shape of the emission band depend heavily on the excitation-photon energy if this energy is lower than the excitonic mobility edge. As was mentioned above, this circumstance is caused by the selective filling of localized excitonic states and by the process of their rapid recombination with the predominant involvement of optical phonons without any significant effect of spectral diffusion. The spectral features observed in the case under consideration in the vicinity of the PL peak consist of a group of relatively narrow lines that are separated by 30.8, 29.3, 27.8, 25.8, and 23.7 eV from the excitation-photon energy (these lines are indicated by arrows in Fig. 2). The spectral features are very sensitive to the temperature of measurements and are virtually flattened at $T \geq 10$ K. These features may characterize the optical phonons that are the most important for a specific sample; the rapid and efficient (due to resonance conditions) radiative-recombination channel is formed with the involvement of the above phonons [14–16]. A certain broadening of the emission-band pedestal in the PL spectrum under discussion may be indicative of an appreciable role of multiphonon relaxation mechanisms, including also those with the involvement of acoustic phonons from the edges of the Brillouin zone [11, 17]. The fact that the peak corresponding to the LO phonon of the ZnSe matrix is not observed in the PL spectrum confirms the dominant role of the ZnCdSe-insert phonons in excitonic recombination and indicates that both the ground and the excited states of the islands are localized mainly within the insert.

Using the aforementioned optical-phonon energies, we estimated the range of variations in the composition of a $Zn_{1-x}Cd_xSe$ solid solution in the insert regions. Figure 3 shows the known composition dependence of optical-phonon frequencies for a $Zn_{1-x}Cd_xSe$ solid solution [18, 19]; the energy range for the optical phonons observed in the resonance PL is indicated. It can be seen that the width of the LO–TO phonon sub-

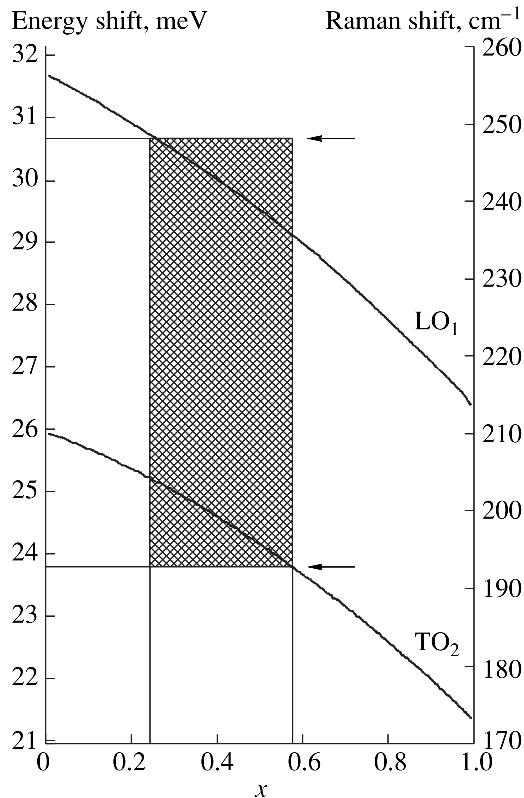

Fig. 3. The composition dependence of the optical-phonon frequency at the center of the $Zn_{1-x}Cd_xSe$ Brillouin zone. The solid lines represent the data reported by Alonso *et al.* [18]. The vertical scale on the left corresponds to experimental values within the energy range of optical phonons; this range was obtained from the resonance PL spectra (see Fig. 2). The hatched area corresponds to the correlation between the experimental values of photon energies and the Cd content in $Zn_{1-x}Cd_xSe$. $T = 5$ K.

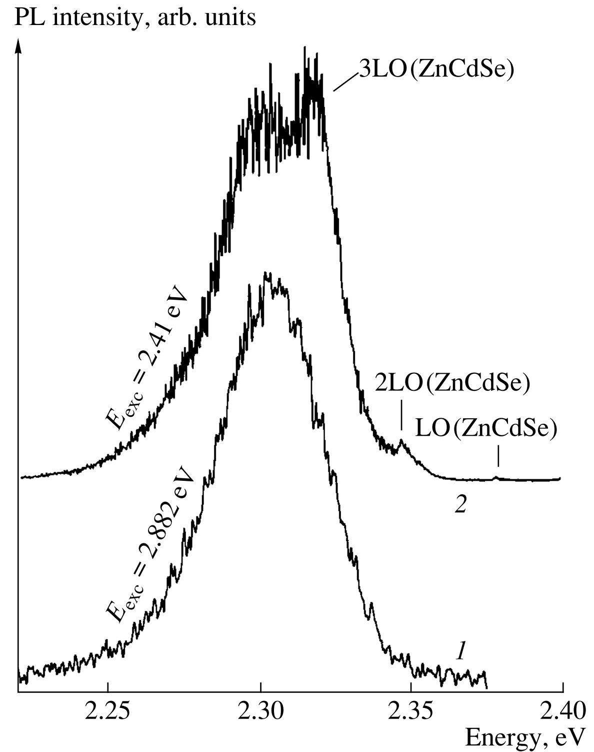

Fig. 4. Photoluminescence spectra of a CdSe/ZnSe nanostructure with a nominal 3.0-ML thickness of the CdSe insert at various excitation-photon energies. $T = 5$ K.

band corresponds to the Cd content in the range $x \approx 22$–58%. The values of x obtained may be both overestimated due to the effect of the dimensional confinement and the contribution of interfacial vibrations and underestimated if the insert-compression effect is dominant. In any case, the determined range of compositions is consistent with the values of x estimated previously [20, 21]; this fact substantiates once again the important role of possible processes of interdiffusion and segregation of Cd and Zn in the course of the growth of the structure.

The PL spectrum for the sample with a nominally 3.0-ML-thick CdSe insert is shown in Fig. 4. As can be seen, if the ZnSe-barrier region is excited ($E_{exc} = 2.882$ eV, curve *1*), a single PL band which is peaked at 2.306 eV and has a half-width of ~41 meV is detected; this band features an insignificant asymmetry on the low-energy side (curve *1*). The shift of this band to lower energies compared to what is observed in the sample with a 1.5-ML-thick CdSe insert is mainly caused by an increase in the Cd content in the insert. The simultaneous increase in the island density [20] brings about an increase in the contribution of the islands to PL and accounts for a decrease in the emission-band asymmetry [9, 22, 23]. An appreciable increase in the half-width of this band (41 meV, to be compared with 24 meV for the sample with a 1.5-ML-thick CdSe insert) is consistent with the previously ascertained [20] fact of an increase in the spread of the composition (stoichiometric coefficients x) in the islands for larger nominal thickness of the CdSe insert. It is worth noting that the actual intensity of the recorded PL band decreases approximately by a factor of 2 when we pass from the sample with a 1.5-ML-thick CdSe insert to the sample with a 3.0-ML-thick CdSe insert if the excitation power remains unchanged. If we take into account the increase in the island density, the above means that the emission efficiency is much lower in a sample with a thicker CdSe insert. This behavior may be caused by an appreciable increase in the role of structural defects, in particular, by a high concentration of cationic vacancies formed as a result of nonequilibrium conditions of molecular-beam epitaxy [20].

A different situation arises when we realize the resonance conditions ($E_{exc} = 2.41$ eV), when the energy spacing between the excitation photon and the position of the PL band peak is close to the triple LO-phonon energy in the insert (Fig. 4, curve *2*). In this case, the

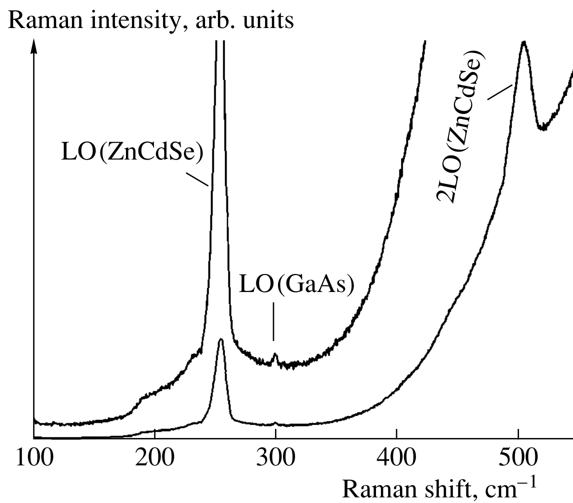

Fig. 5. The resonance Raman spectrum of a CdSe/ZnSe nanostructure with a nominal 3.0-ML thickness of the CdSe insert. $T = 5$ K. $\lambda_{exc} = 514.5$ nm.

wider low-energy PL band (2.306 eV) corresponds to the emission of thermalized excitons, and the energy position of this band coincides with that observed when we have a high-energy nonresonance excitation (Fig. 4, curve *1*). An additional band that was peaked at 2.319 eV and had a comparable intensity appeared in the high-energy portion of the spectrum. Kim *et al.* [9] simulated the PL spectrum for a similar structure by two Gaussian lines; the high-energy line was attributed to the 2D-like excitons in the wetting layer, whereas the low-energy line was attributed to the emission of 0D excitons in the islands. The fact that, in the case under consideration, the peak of the high-energy band is separated from the excitation-photon energy by the triple energy of phonons in the insert suggests the following: this band may be attributed to emission from localized excitons in the region below the effective excitonic mobility edge with the involvement of three LO phonons (similarly to the case considered above for the sample with a 1.5-ML-thick CdSe insert). The LO-phonon energy in the insert corresponds to the $Zn_{1-x}Cd_xSe$ solid solution with $x \approx 0.38$–0.40 [18, 19] (disregarding the effect of stress; this effect becomes more profound with increasing insert thickness and leads to an underestimation of x).

The process of resonance Raman scattering also manifested itself in the case of resonance excitation of the sample with a 3.0-ML-thick CdSe insert. The Raman spectrum is shown in Fig. 5 in detail. In this spectrum, we can see that the LO- and 2LO-phonon lines peaked at 251 and 500 cm^{-1}, respectively, which corresponds to the $Zn_{1-x}Cd_xSe$ solid solution with $x \approx 0.18$–0.20 [18, 19]. According to the data reported in [20], this value of x corresponds to the 2D layer of the $Zn_{1-x}Cd_xSe$ insert. The spectrum also includes a low-intensity LO-phonon line of the GaAs substrate ($\nu \approx 293$ cm^{-1}). Furthermore, an additional Raman scattering is clearly detected in the region of 160–350 cm^{-1}; this scattering is caused by activation of the entire phonon density of states in the Raman spectrum of the $Zn_{1-x}Cd_xSe$ insert. This effect is due to a violation in the translational symmetry of the crystal structure and is caused by nonuniformity in the insert composition. Such an effect was also observed in the luminescence-excitation spectra of similar structures [17].

Thus, two independent processes can be recognized in the PL and resonance Raman spectra of the sample with a 3.0-ML-thick CdSe insert exposed to the resonance excitation. First, we have fast recombination of excitons localized in the nanoisland regions enriched with the cadmium. This recombination occurs with the involvement of three LO phonons and gives rise to the high-energy PL peak. Spectral diffusion to deeper states in the band tails due to interaction with acoustic phonons gives rise to the low-energy PL component, similarly to the mechanism discussed previously [14]. Second, the Raman process takes place. For this process, conditions for the output resonance with the high-energy PL edge are fulfilled; this edge is defined by the insert regions with the lowest Cd content (the 2D layer [20, 21]).

Summarizing the above results, we may conclude that the spectral shape of the band for the emission from nanoislands in the CdSe/ZnSe nanostructure with a 1.5-ML-thick CdSe insert subjected to resonance excitation in the region of the main excitonic transition differs from that in the case of nonresonance excitation. The fairly small spectral width of the corresponding emission band with a phonon-related structure and its high efficiency are indicative of very fast relaxation processes with the predominant interaction of localized excitons with optical phonons. Energies of optical phonons involved in the relaxation process corroborate an appreciable compositional disordering of the CdSe insert. The observed low-energy broadening of the emission band at its pedestal is indicative of the important role of multiphonon processes in exciton relaxation, including those with the involvement of acoustic phonons at the Brillouin zone edges.

When the sample with the 3.0-ML-thick CdSe insert was subjected to the resonance excitation, we observed an emission band with an additional peak caused by the interaction of localized excitons with three LO phonons of nanoislands. The resonance Raman scattering was controlled by the composition of the 2D layer in the insert.

The above-reported experimental data can be interpreted in the context of a model that implies the presence of both weakly localized states in the vicinity of the effective excitonic mobility edge (these states are initiated by slight fluctuations and (or) stresses in the 2D layer) and more strongly localized deep tails of the states caused by appreciable compositional disorder in the nanoislands.

ACKNOWLEDGMENTS

This study was supported by the Russian Foundation for Basic Research (project no. 03-02-17563) and by the joint Russia–Ukraine research program.

REFERENCES

1. S. H. Xin, P. D. Wang, A. Yin, *et al.*, Appl. Phys. Lett. **69**, 884 (1996).
2. F. Flack, N. Samarth, V. Nikitin, *et al.*, Phys. Rev. B **54**, 17312 (1996).
3. K. Leonardi, H. Heinke, K. Ohkawa, *et al.*, Appl. Phys. Lett. **71**, 1510 (1997).
4. A. A. Toropov, S. V. Ivanov, T. V. Shubina, *et al.*, Jpn. J. Appl. Phys. **38**, 566 (1999).
5. E. Cohen and M. D. Sturge, Phys. Rev. B **25**, 3828 (1982).
6. N. F. Mott and E. A. Davis, *Electronic Processes in Non-Crystalline Materials*, 2nd ed. (Clarendon Press, Oxford, 1979; Mir, Moscow, 1982), Vol. 2.
7. J. Hegarty, L. Goldner, and M. D. Sturge, Phys. Rev. B **30**, 7346 (1984).
8. S. Sorokin, T. Shubina, A. Toropov, *et al.*, J. Cryst. Growth **200–201**, 461 (1999).
9. C. S. Kim, M. Kim, S. Lee, *et al.*, J. Cryst. Growth **214–215**, 761 (2000).
10. S. V. Ivanov, A. A. Toropov, T. V. Shubina, *et al.*, J. Appl. Phys. **83**, 3168 (1998).
11. A. Resnitsky, A. Klochikhin, S. Permogorov, *et al.*, in *Proceedings of 10th International Symposium on Nanostructures: Physics and Technology* (St. Petersburg, 2002).
12. I. L. Krestnikov, M. V. Maximov, A. V. Sakharov, *et al.*, J. Cryst. Growth **184–185**, 545 (1998).
13. N. N. Ledentsov, V. M. Ustinov, V. A. Shchukin, *et al.*, Fiz. Tekh. Poluprovodn. (St. Petersburg) **32**, 385 (1998) [Semiconductors **32**, 343 (1998)].
14. A. A. Toropov, T. V. Shubina, S. V. Sorokin, *et al.*, J. Cryst. Growth **214–215**, 806 (2000).
15. F. Gindele, K. Hild, W. Langbein, *et al.*, J. Lumin. **83–84**, 305 (1999).
16. R. Heitz, M. Grundmann, N. N. Ledentsov, *et al.*, Appl. Phys. Lett. **68**, 361 (1996).
17. S. Permogorov, A. Resnitsky, A. Klochikhin, *et al.*, J. Lumin. **87–89**, 435 (2000).
18. R. G. Alonso, E.-K. Suh, A. K. Ramdas, *et al.*, Phys. Rev. B **40**, 3720 (1989).
19. M. Ya. Valakh, M. P. Lisitsa, G. S. Pekar, *et al.*, Phys. Status Solidi B **113**, 635 (1982).
20. N. Peranio, A. Rosenauer, D. Gerthsen, *et al.*, Phys. Rev. B **61**, 16015 (2000).
21. D. Litvinov, A. Rosenauer, D. Gerthsen, and N. N. Ledentsov, Phys. Rev. B **61**, 16819 (2000).
22. M. Ya. Valakh, V. V. Strelchuk, A. A. Toropov, *et al.*, Semicond. Sci. Technol. **17**, 173 (2002).
23. T. V. Shubina, M. Ya. Valakh, V. V. Strelchuk, *et al.*, in *Proceedings of 10th International Conference on II–VI Compound* (Bremen, Germany, 2001), Mo-P60.

Translated by A. Spitsyn

Semiconductors, Vol. 37, No. 11, 2003, pp. 1342–1344. Translated from Fizika i Tekhnika Poluprovodnikov, Vol. 37, No. 11, 2003, pp. 1380–1382.
Original Russian Text Copyright © 2003 by Tetelbaum, Ezhevskiĭ, Mikhaylov.

Extremal Dependence of the Concentration of Paramagnetic Centers Related to Dangling Bonds in Si on Ion-Irradiation Dose as Evidence of Nanostructuring

D. I. Tetelbaum*, A. A. Ezhevskiĭ, and A. N. Mikhaylov

Research Physicotechnical Institute, Lobachevskiĭ State University, Nizhni Novgorod, 603950 Russia

**e-mail: tetelbaum@phys.unn.ru*

Submitted January 28, 2003; accepted for publication March 4, 2003

Abstract—Dose dependences of the concentration of paramagnetic centers with $g = 2.0055$ under irradiation of silicon with Ge^+, Ar^+, and Ne^+ ions have been studied in detail. It is shown that, in all cases, the dependences are characterized by the previously unnoticed presence of maxima at doses corresponding to transition to complete amorphization. This feature is explained in terms of a model assuming an additional contribution to electron spin resonance from dangling bonds at the interface between nanocrystals and the amorphous matrix. *© 2003 MAIK "Nauka/Interperiodica".*

1. INTRODUCTION

It is known that ion irradiation of silicon leads to formation in its crystal lattice of defects whose electron spin resonance (ESR) spectrum is characterized by a g-factor of 2.0055 [1]. This type of defect is commonly described as a center of vacancy nature (*VV* center) [2] or as a dangling bond (*D* center) [1]. Accumulation of defects of this kind leads to amorphization, with the centers preserved in the amorphous phase.

Until now, there have been no published evidence concerning any anomaly in the dose dependence of the concentration of these centers in transition to the amorphous state: their concentration grows gradually, then levels off [2, 3] and starts to decrease only at ultrahigh doses under certain conditions ("high-dose effect") [3]. However, the authors of the present study have found, in a more detailed study of dose dependences, a systematic, previously unnoticed feature at doses corresponding to transition to complete amorphization [4, 5].

In [4, 5], this phenomenon was discussed with the aim of explaining the luminescent properties of silicon in which a composite amorphous-nanocrystalline system (a-Si:nc-Si) is formed under ion irradiation. Here, the structural aspect of the problem is discussed and the above feature is accounted for.

2. EXPERIMENTAL

As starting material we used (100)Si samples of KDB Si (p-Si:B) with a resistivity of 2000 Ω cm. The wafers were subjected to standard chemical–mechanical treatment with subsequent etching off of the disrupted layer (~20 μm). Irradiation was performed at room temperature with 80 keV Ge^+ ions at doses of $(2–50) \times 10^{13}$ cm^{-2}, 150 keV Ar^+ ions at $(4–500) \times 10^{13}$ cm^{-2}, and 150 keV Ne^+ ions at $(5–500) \times 10^{14}$ cm^{-2}. The ion current density did not exceed 5 μA/cm^2 in all cases. The ESR was studied at liquid nitrogen temperature on an RE-1306 spectrometer. The concentration of the centers with a g-factor of 2.0055 was determined by double integration of differential curves. Reduction to the common scale was done using Mn^{2+}:MgO as a reference.

3. RESULTS AND DISCUSSION

Figure 1 shows dose dependences of the concentration of ESR centers with a g-factor of 2.0055 under irradiation of Si with ions with different masses. It can be seen that, in all cases, the dependences pass through a maximum. The positions of the peaks in the curves are in satisfactory agreement with published data on amorphization doses [6, 7]. Since the amorphization doses have not been determined precisely, it seems reasonable to assume that such a behavior characterizes the dose range immediately preceding the formation of a continuous amorphous layer at depths close to that of the maximum ion energy loss.

What is the reason for the appearance of peaks in the dose curves? Amorphization under ion irradiation is not an instantaneous event occurring in the entire irradiated region. This is manifested the most clearly under irradiation with heavy ions, when amorphization first occurs in the regions of displacement cascades produced by separate ions [8] and only merging of such local amorphous regions with increasing dose leads to formation of a continuous amorphous layer. Therefore, there must exist a certain intermediate range of doses in which the structure of the irradiated layer is of composite nature, i.e., having the form of a mixture of amorphous and crystalline regions. This circumstance underlies the

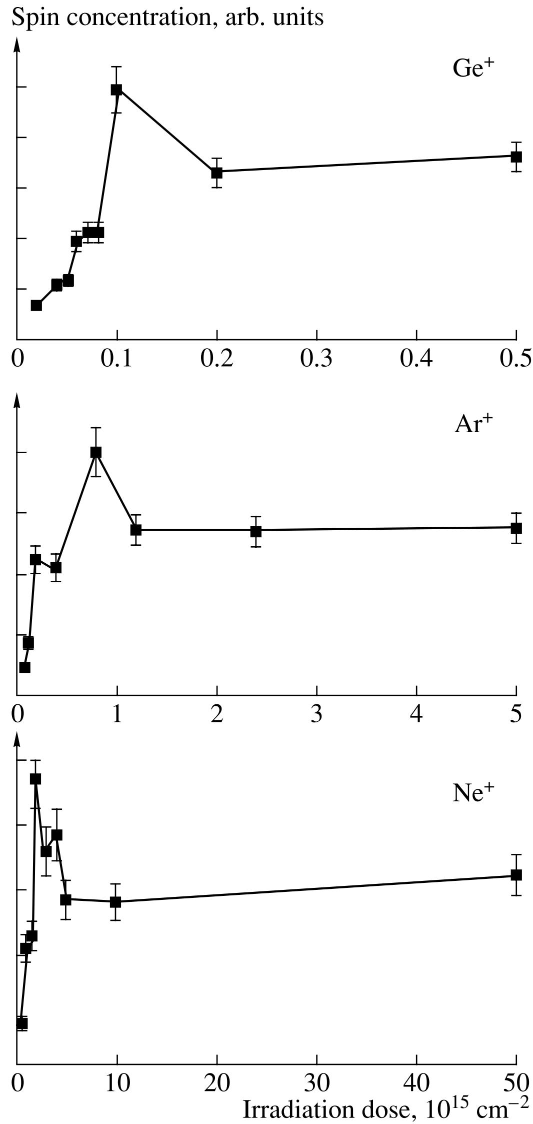

Fig. 1. Dose dependence of the concentration of ESR centers with $g = 2.0055$ for silicon samples irradiated with Ge^+, Ar^+, and Ne^+ ions.

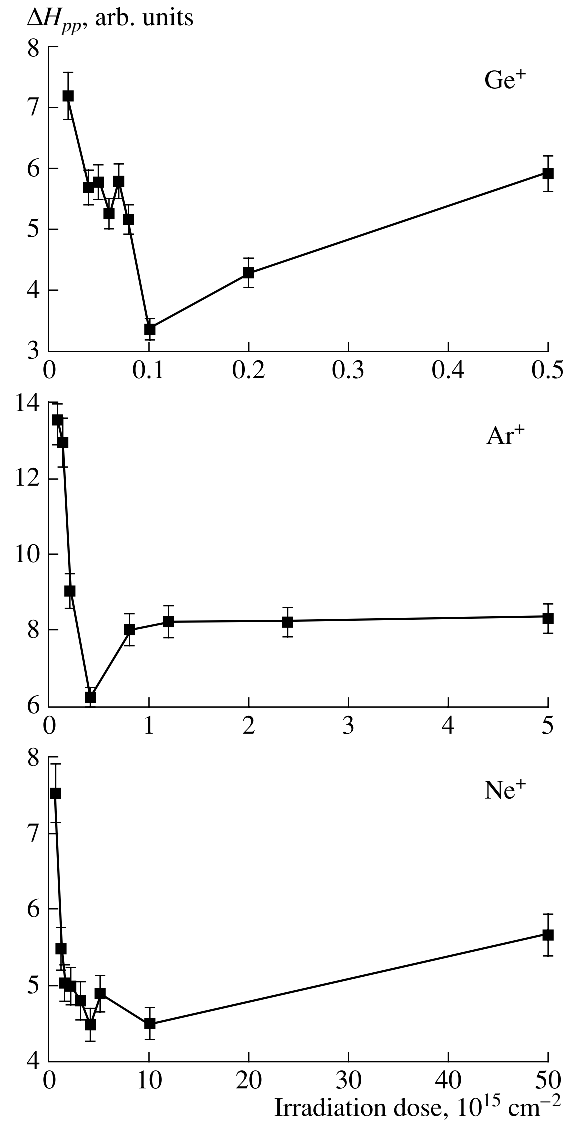

Fig. 2. Dose dependences of the ESR linewidth ($g = 2.0055$) for silicon samples irradiated with Ge^+, Ar^+, and Ne^+ ions.

method first suggested by the authors for obtaining the system *a*-Si:*nc*-Si [5, 9–12], exhibiting, in contrast to single-crystal (*c*-Si) and amorphous (*a*-Si) silicon, room-temperature luminescence related to Si nanocrystals in the amorphous matrix (quantum-confinement effect).

Amorphous silicon is characterized by somewhat longer interatomic distances (bond lengths) as compared with *c*-Si [1]. Therefore, mechanical stresses exist at interfaces between crystalline and amorphous regions and a high concentration of dangling bonds should be expected at these interfaces. Thus, in the transitional (to that corresponding to complete amorphization) dose range in which crystalline inclusions are present in the amorphous matrix, the total concentration of dangling bonds contributing to the ESR signal with $g = 2.0055$ exceeds that at higher doses corresponding to the existence of continuous amorphous layer. In the latter case, the overwhelming majority of dangling bonds are situated in the amorphous phase.

The adequacy of the above assumption concerning the nature of peaks in the dose curves (Fig. 1) is confirmed by the following estimate. According to calculations performed using the Monte Carlo method [9, 10, 12], the fraction of the volume occupied by Si nanocrystals in the amorphous layer is ~10% for Ar^+ ions (close in mass to Ge^+ ions) at a dose of 8×10^{13} cm^{-2}, and the average diameter of crystalline islands at the same dose is ~10 nm. Hence, it follows that the average number of Si atoms on the nanocrystal surface (assumed to be spherical) is 3×10^3. If each atom of this kind had a single broken bond with the surrounding amorphous matrix, then, as readily obtained taking into account the fraction of the crystalline phase, the concentration of additional dangling bonds of silicon at the *nc*-Si/*a*-Si

interfaces would be 6×10^{20} cm^{-3}. The density of spins with $g = 2.0055$ in Si amorphized by ion irradiation is ~10^{20} cm^{-3} [2, 3]. It may be assumed that the rise of the curve peak over the plateau level in Fig. 1 is determined by the relative amount of spins localized on the surface of nanocrystals. Then, agreement between the calculation and the experimental data (averaged over three kinds of ions) can be achieved if every 20th Si atom on the nanocrystal surface has a broken bond with atoms of the amorphous matrix. This value is quite reasonable.

The dose dependence of the ESR linewidth ΔH_{pp} (Fig. 2) shows its decrease in the transition region, which, on the whole, correlates with the dose dependence of the signal amplitude. The decrease in linewidth can be attributed to exchange narrowing of the absorption line with increasing concentration of paramagnetic centers [2]. Since there is no reason to believe that the spin density is increased in the transition dose range for centers localized within amorphous regions, it seems natural to relate the additional narrowing observed in this range to centers localized just at interfaces, where the average distances between paramagnetic centers are shorter than those within the amorphous phase.

4. CONCLUSION

Specific features have been revealed in the dose dependences of the concentration of paramagnetic centers with $g = 2.0055$ and in the behavior of the linewidth of the corresponding signal under ion irradiation of silicon. These features are interpreted in terms of a model assuming an additional contribution to electron spin resonance from dangling bonds situated at the interface between nanocrystals and the amorphous matrix. The results indicate that a more detailed study is needed of the structural and physical properties of Si in the dose range transitional to one corresponding to amorphization (and also in the intermediate range of depths, between the amorphous *a*-Si layer and *nc*-Si). It is in this range that specific features of scientific and practical interest would be expected to appear, which is also indicated by photoluminescence [4, 5, 12] and electrical conductivity data [9]. Detailed measurements of the dose dependence of ESR can be used for detecting nanocrystalline inclusions in the amorphized layer.

ACKNOWLEDGMENTS

We thank V.K. Vasil'eva and A.Yu. Yuzova for assistance in performing ion implantation, and also S.E. Akis and A.Kh. Mukhamatulina for help in ESR studies.

This study was supported by the program of the Ministry of Education of the Russian Federation "Higher School Research in Priority Fields of Science and Technology" (subprogram no. 205).

REFERENCES

1. *Amorphous Semiconductors*, Ed. by M. H. Brodsky (Springer, Berlin, 1979; Mir, Moscow, 1982).
2. N. N. Gerasimenko, A. V. Dvurechenskiĭ, and L. S. Smirnov, Fiz. Tekh. Poluprovodn. (Leningrad) **6**, 1111 (1972) [Sov. Phys. Semicond. **6**, 965 (1972)].
3. *Physical Processes in Irradiated Semiconductors*, Ed. by L. S. Smirnov (Nauka, Novosibirsk, 1977).
4. S. A. Trushin, A. N. Mikhaylov, A. A. Ezhevskiĭ, *et al.*, Vestn. Nizhegorod. Univ. im. N.I. Lobachevskogo, Fiz. Tverd. Tela **2** (5), 37 (2001).
5. D. I. Tetelbaum, A. A. Ezhevskii, S. A. Trushin, *et al.*, Mater. Sci. Eng. B **101**, 279 (2003).
6. E. I. Zorin, P. V. Pavlov, and D. I. Tetelbaum, *Ion-Implantation Doping of Semiconductors* (Énergiya, Moscow, 1975).
7. H. Ryssel and I. Ruge, *Ionenimplantation* (Teubner, Stuttgart, 1978; Nauka, Moscow, 1983), p. 304.
8. J. F. Gibbons, Proc. IEEE **60**, 1062 (1972).
9. D. I. Tetelbaum, V. G. Shengurov, D. V. Shengurov, *et al.*, Poverkhnost, No. 5, 34 (1988) [Surf. Invest. **14**, 605 (1998)].
10. D. I. Tetelbaum, S. A. Trushin, and A. V. Pitirimov, Izv. Ross. Akad. Nauk, Ser. Fiz. **64**, 2168 (2000).
11. A. V. Pitirimov, E. A. Pitirimova, D. I. Tetelbaum, *et al.*, Poverkhnost, Nos. 5–6, 11 (1999) [Surf. Invest. **15**, 701 (2000)].
12. D. I. Tetelbaum, S. A. Trushin, Z. F. Krasil'nik, *et al.*, Opt. Mater. **17** (1–2), 57 (2001).

Translated by M. Tagirdzhanov

Semiconductors, Vol. 37, No. 11, 2003, pp. 1345–1349. Translated from Fizika i Tekhnika Poluprovodnikov, Vol. 37, No. 11, 2003, pp. 1383–1388.
Original Russian Text Copyright © 2003 by Yakimov, Dvurechenskiĭ, Nikiforov, Chaĭkovskiĭ, Tiĭs.

PHYSICS OF SEMICONDUCTOR DEVICES

Ge/Si Photodiodes with Embedded Arrays of Ge Quantum Dots for the Near Infrared (1.3–1.5 μm) Region

A. I. Yakimov*, A. V. Dvurechenskiĭ, A. I. Nikiforov, S. V. Chaĭkovskiĭ, and S. A. Tiĭs

Institute of Semiconductor Physics, Siberian Division, Russian Academy of Sciences, Novosibirsk, 630090 Russia

**e-mail: yakimov@isp.nsc.ru*

Submitted January 10, 2003; accepted for publication January 21, 2003

Abstract—A method has been devised for MBE fabrication of *p–i–n* photodiodes for the spectral range of 1.3–1.5 μm, based on multilayer Ge/Si heterostructures with Ge quantum dots (QDs) on a Si substrate. The sheet density of QDs is 1.2×10^{12} cm^{-2}, and their lateral size is ~8 nm. The lowest room-temperature dark current reported hitherto for Ge/Si photodetectors is achieved (2×10^{-5} A/cm^2 at 1 V reverse bias). A quantum efficiency of 3% at 1.3 μm wavelength is obtained. © *2003 MAIK "Nauka/Interperiodica".*

1. INTRODUCTION

The efforts in the design of quantum dot (QD) photodetectors began only in the late 1990s, based mainly on InAs/GaAs and Ge/Si heterostructures, and all of them have been concentrated as yet on the production of high-efficiency single elements. QD photodetectors are in a position to cover a significant section of the IR range actual for multiple applications, from the near-IR telecommunication wavelength range (1.3–1.5 μm) to the far-IR spectral range (20–200 μm).

An additional restriction of the carrier motion in the structure plane and discrete energy spectrum of carriers offers a number of significant advantages of QD photodetectors over quantum well (QW) structures and bulk layers [1]:

(i) optical transitions polarized in the photodetector plane become allowed, which opens the possibility for device operation at a normal incidence of light without additional gratings or reflectors;

(ii) oscillator strength (and, consequently, the light absorption coefficient) for intraband and exciton transitions is high owing to localization of the carrier wave function along all three spatial coordinates;

(iii) the lifetime of photoexcited carriers is long ($>10^{-11}$ s) [2], with the result that the photoelectric gain is high owing to the low capture rate of carriers in a QD. The capture rate is low either because of the absence of allowed energy states between the level in QD and the band of delocalized states or because of the suppression of carrier scattering on optical phonons under the conditions when the energy spacing between the quantum confinement levels exceeds the optical phonon energy.

(iv) dark currents are small (and, consequently, the operating temperature of the photodetector is high). The latter circumstance is a consequence of noninvolvement of excited states in a QD in the processes of thermal generation of carriers in allowed bands in the case when the energy spacings between the QD levels are sufficiently large.

The most important disadvantages of photodetectors with QD sheets are as follows:

(a) inevitable spread of QD sizes in the array, which results in inhomogeneous broadening of the absorption spectrum and a decrease in the absolute intensity of the photoresponse [2];

(b) low sheet density of QDs (10^9–10^{10} cm^{-2}), which is usually by two to three orders of magnitude smaller than the typical electron density in 2D subbands in QW photodetectors (10^{11}–10^{12} cm^{-2}).

2. FORMULATION OF THE PROBLEM

The elaboration of optical fiber communication lines and related photonic devices operating in the near-IR atmospheric window (1.3–1.5 μm) is one of the most important directions in the development of promising methods for information transmission. It seems necessary to fabricate in one and the same chip the entire set of components of an optical fiber communication line: modulators, demodulators, multiplexers, light emitters, and, naturally, photodetectors. To reduce the cost of such systems it is necessary that all the components be integrated into modern VLSI silicon technology and formed on Si substrates. However, silicon itself is transparent to photons having a wavelength that exceeds 1.1 μm. Germanium photodetectors have a high sensitivity at ~1.5 μm. This poses the problem of designing Ge/Si heterostructures photosensitive in a range of communication wavelengths of 1.3–1.5 μm at room temperature.

At the first stage, the problem was resolved either by depositing bulk dislocated Ge layers onto Si [3] or by growing multilayer strained superlattices Ge_xSi_{1-x}/Si [4–6]. Standard performance criteria for these photodetectors are the quantum efficiency, and a dark current at

1063-7826/03/3711-1345$24.00 © 2003 MAIK "Nauka/Interperiodica"

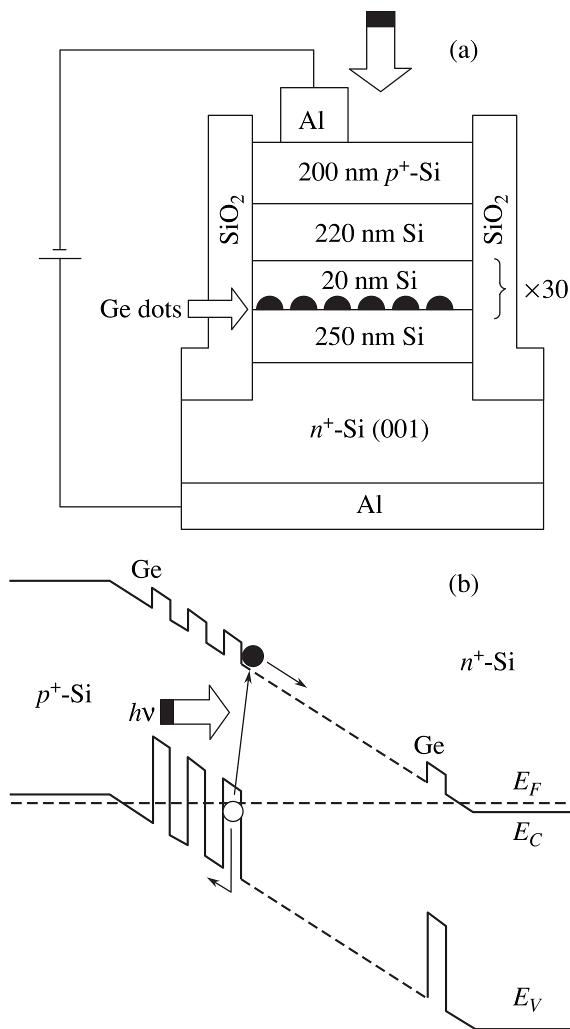

Fig. 1. (a) Sketch of the cross-section of a silicon *p–i–n* photodiode with Ge QDs; (b) the energy diagram of the diode under zero bias.

a bias of 1 V or the saturation current in diode structures. Similar to the case of long-wavelength photodetectors, a low dark current is necessary to provide low threshold power for the detector.

It was shown that for a photon wavelength of λ = 1.3 μm, the quantum efficiency of such devices is η = 1–4.2% under normal incidence of light onto the detector, and it can reach η = 11% if the end face of planar waveguides formed on the same Si substrate is illuminated. In the latter case, the transmission of light along GeSi layers and multiple reflection from the waveguide walls made it possible to obtain high η. In spite of the relatively high quantum efficiency, the dark current in bulk and multilayer Ge_xSi_{1-x}/Si heterostructures appeared to be too high. For example, typical dark current densities under a bias of 1 V at room temperature were 10^{-4}–10^{-3} A/cm^2, and the saturation current density was ~10^{-2} A/cm^2, which strongly exceeded currents in Si or Ge *p–n* diodes.

The next step in the design of high-efficiency Ge/Si photodetectors was the replacement of continuous GeSi layers with sheets of Ge QDs. In view of the prospects for incorporating these elements into Si VLSI circuits, Ge/Si heterostructures with coherently introduced Ge nanoclusters seem the most attractive, since there is the possibility of overgrowing elastically strained Ge layers with structurally perfect Si layers on which other components of a VLSI circuit can be then formed.

The production of waveguide structures based on Si *p–i–n* diodes with sheets of Ge islands introduced into the diode base was reported in [7, 8]. A quantum efficiency of η = 2.3% was obtained for λ = 1.3 μm and a dark current density of $J = 4.2 \times 10^{-4}$ A/cm^2 under 1-V reverse bias.[1] The authors of [9] reported the production of *p–i–n* diodes based on Si with Ge nanoclusters, where a maximum quantum efficiency of 8% at a wavelength of λ = 1.46 μm and a record-breaking low dark current of $J = 3 \times 10^{-5}$ A/cm^2 were reached. It is necessary to note that, in the above-cited studies, the density of Ge islands was ~10^9 cm^{-2} and the islands had a lateral size of about 100 nm and a height of about 10 nm. At so large a size, the splitting of energy levels in the growth plane (~ 1 meV), caused by quantum confinement, is much smaller than the room-temperature thermal energy, and, therefore, all the advantages of QD photodetectors over systems of higher dimensionality (e.g., small dark currents) could not be actualized to the fullest extent. It became evident that further improvement of the device parameters demands reduction of the QD size to less than 10 nm with a simultaneous increase in the QD sheet density in order to make the dark current as small as possible without impairing the quantum efficiency of photoconversion.

The goal of the present study was to produce a Ge/Si photodetector containing arrays of Ge QDs with a sheet density at a level of 10^{12} cm^{-2} and a dot size of less than 10 nm, with small dark current and high sensitivity to light at a wavelength of 1.3–1.5 μm.

3. THE TECHNOLOGY OF PHOTODETECTOR FABRICATION

Photodetectors were Si *p–i–n* diodes, with 30 sheets of Ge QDs, separated by Si spacers 20 nm thick, incorporated into the base (Fig. 1). To reduce the size and increase the density of islands, they were formed on a preliminarily oxidized Si surface.

The samples were MBE-grown on As-doped (001) n^+-Si substrates with a resistivity of 0.01 Ω cm. The growth temperature was 500°C for both Si and Ge layers. The growth rate was 0.3 nm s^{-1} for Si and 0.03 nm s^{-1} for Ge. After a standard cleansing of the Si surface, Si buffer layer 250 nm thick was grown. Then oxygen gas was fed into the growth chamber, and Si surface was oxidized for 10 min at an oxygen pressure of 10^{-4} Pa

[1] Here and below the room-temperature parameters of photodetectors are presented.

and a substrate temperature of 500°C. In this process, a SiO_x layer of several angstroms in thickness was formed (not shown in Fig. 1). Further, the chamber was evacuated to a residual oxygen pressure of 10^{-7} Pa, a 0.5-nm-thick Ge layer was deposited, and germanium was overgrown with a 20-nm-thick Si layer. The last three procedures (oxidation, deposition of 0.5-nm Ge, deposition of 20-nm Si) were repeated 30 times successively. The multilayer Ge/Si structure was covered with 220-nm Si. The background concentration of B impurity in intentionally undoped Si was $(7–8) \times 10^{15}$ cm^{-3}. The fabrication of $p–i–n$ diode was done by growth of 200-nm p^+-Si (B concentration in the layer 2×10^{18} cm^{-3}) and 10-nm p^{++}-Si (B concentration 10^{19} cm^{-3}, not shown in Fig. 1).

Aluminum films deposited in a high-vacuum chamber were used to fabricate ohmic contacts to heavily doped Si layers. Columnar diodes were formed by standard photolithography and reactive ion etching of the structures to a depth of ~1.7 μm. The cross-sectional area of mesa-structures varied from 150×150 to 700×700 μm^2. The dimensions of Al contact pads on the top p^+-Si layer were 80×80 μm^2. The diode surface was passivated by depositing a 0.5-μm-thick SiO_2 film from an oxygen–monosilane mixture in a special reactor.

The formation of Ge islands and the quality of Si layers were monitored in situ by reflection high-energy electron diffraction (RHEED) (see Fig. 2). After the Si buffer layer growing, the diffraction pattern exhibits reflections from (2×1) superstructure typical of atomically clean (001) Si surface. Oxidation changes the diffraction pattern significantly. All the superstructure-related reflections disappear, the bulk reflections become less pronounced, and the diffusion background is more intense. This indicates the formation of a solid SiO_x film on the Si surface. After deposition of Ge onto an oxidized surface, the diffraction pattern typical of 3D Ge islands is observed, with the islands having the same crystallographic orientation as the silicon substrate, indicative of epitaxial growth. Furthermore, it was found that Ge islands are formed in this case after deposition of one Ge monolayer (ML) without the formation of the underlayer typical of the Stranski–Krastanow growth mechanism. Therefore, Ge nanoclusters in this system are completely isolated from one the other. This fact seems especially important, since the presence of 2D states in the underlayer can significantly accelerate capture of carriers in QDs [10, 11].

The mechanism of the formation of Ge islands in $Ge/SiO_x/Si$ system has yet to be explained. The most probable hypothesis is that, at the early stage of growth, GeO and SiO molecules are formed in the reaction of Ge adatoms with a SiO_2 film; leaving the surface, these molecules uncover Si areas on which Ge nanoclusters are then nucleated [12].

Figure 3a shows an SEM image of a (001) Ge/Si surface formed after deposition of a single Ge layer of 0.5 nm in thickness. As seen, the surface represents an array of islands, and Figure 3b shows their profile in the direction marked by the line in Fig. 3a. Statistical processing of the surface profiles yielded an average lateral size of Ge islands of ~8 nm and a density of ~1.2×10^{12} cm^{-2}.

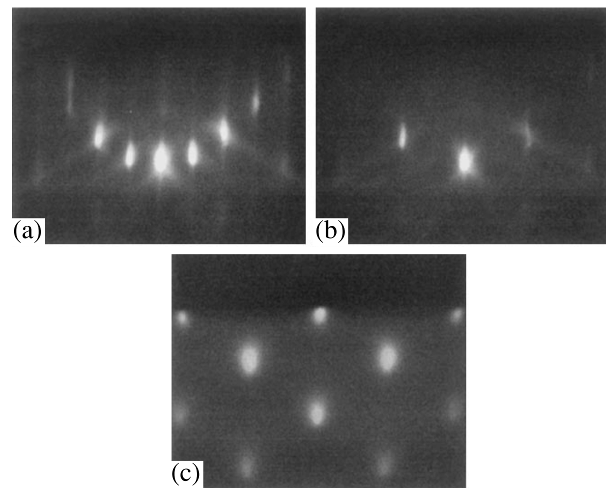

Fig. 2. RHEED pattern from the sample surface at different growth stages: (a) (001) Si (2×1) after growth of an Si buffer layer; (b) (001) Si (1×1) after oxidation in O_2 flow; (c) 3D diffraction after deposition of 0.5-nm Ge.

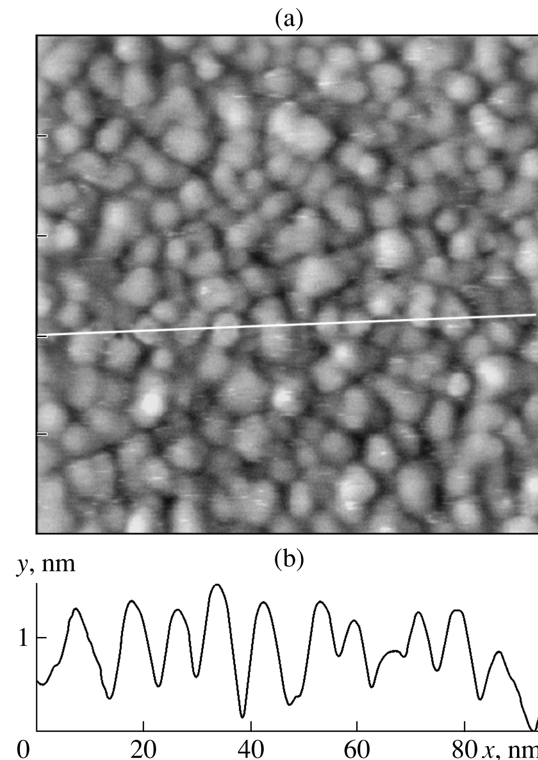

Fig. 3. (a) SEM image of the Si surface after deposition of a 0.5-nm Ge layer. An image size of 100×100 nm^2; (b) The surface profile along the line is marked in Fig. 3a.

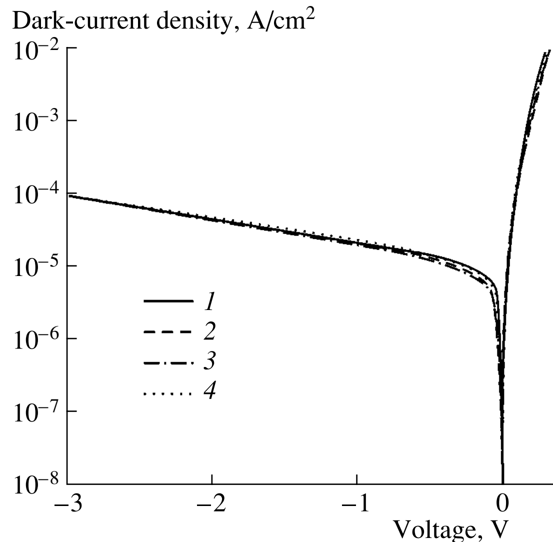

Fig. 4. Dark *J–V* characteristics of photodiodes with cross-sectional areas of (*1*) 700 × 700, (*2*) 500 × 500, (*3*) 300 × 300, and (*4*) 150 × 150 μm^2. Recorded at $T = 300$ K.

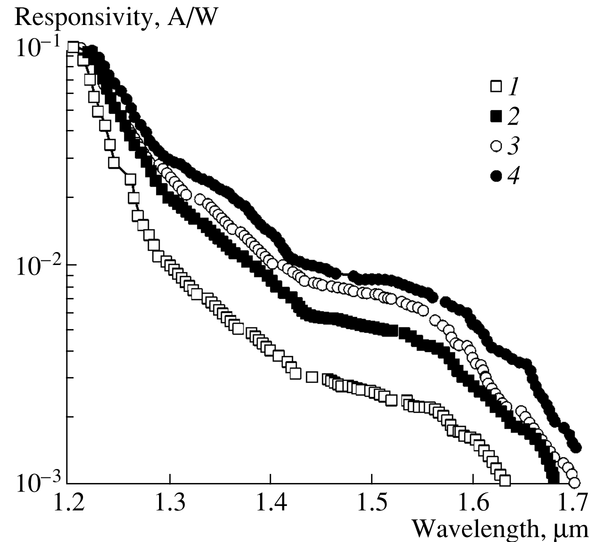

Fig. 5. Current responsivity spectra at varied reverse bias on the photodiode $|U|$: (*1*) 0 (short-circuit mode), (*2*) 0.2, (*3*) 0.5, and (*4*) 2 V. Recorded at room temperature.

4. DARK-CURRENT–VOLTAGE CHARACTERISTICS

Figure 4 shows the dark current density vs. voltage (*J–V* characteristics) at room temperature for diodes differing in area. The current density is virtually independent of the diode area, which is indicative of small surface leakage and predomination of bulk processes in the charge transport. A ideality factor of $n = 1.02$ and a saturation current density of $J_S = 6 \times 10^{-6}$ A/cm^2 were determined from *J–V* characteristics. The ideality factor is close to unity, which indicates the absence of any considerable contribution of tunneling and recombination currents related to possible deep centers in the diode base. The saturation current density is one to two orders of magnitude smaller than that in *p*–- and *p–i–n* diodes (10^{-4}–10^{-3} A/cm^2) [13], which implies that the energy gap in a QD Ge/Si heterostructure is wider than in bulk Ge, to all appearances due to confinement-induced quantization of the energy spectrum of holes in the Ge valence band.

The dark current density at 1-V reverse bias was 2×10^{-5} A/cm^2. To our knowledge, this is the lowest value achieved hitherto for Ge/Si photodetectors.

5. PHOTOELECTRIC PROPERTIES

Figure 5 shows typical current responsivity spectra at different reverse biases under normal incidence of light onto the photodetector surface. The measurements were made at room temperature. The photocurrent in the short-circuit mode (a bias of $U = 0$) was measured directly with a Keithley electrometer. The photoresponse of reverse-biased photodiodes was measured using a lock-in nanovoltmeter at a light-modulation frequency of 560 Hz. The spectral characteristics of illumination intensity were obtained using a cooled CdHgTe photoresistor. As seen, the photosensitivity of a QD Ge/Si *p–i–n* diode in near-IR range extends to wavelengths of 1.6–1.7 μm.

Figure 6 shows the dependence of quantum efficiency η at a wavelength of $\lambda = 1.3$ μm on the reverse bias. The value of η was calculated from the known relation between the sensitivity R, photon energy $h\nu$, and elementary charge: $R = (e/h\nu)\eta$. With increasing bias, the quantum efficiency increases and levels off at $|U| \approx 2$ V. Study of capacitance–voltage (*C–V*) characteristics of diodes has shown that the device capaci-

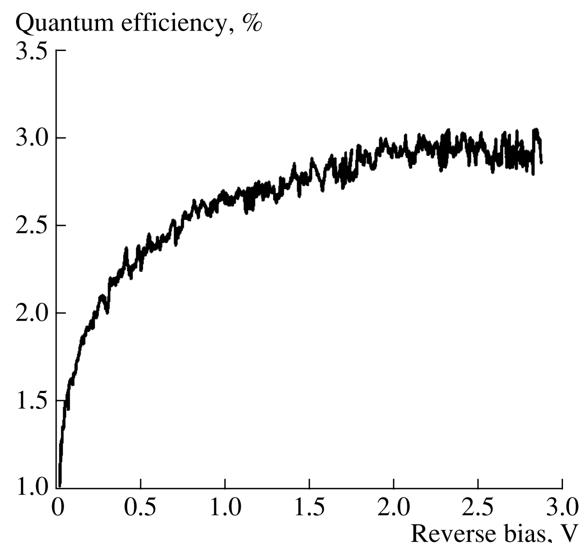

Fig. 6. The quantum efficiency of a photodiode at a wavelength of 1.3 μm vs. reverse bias.

tance remains unchanged within a 5% accuracy in the reverse bias range |0–5| V. This means that the entire *i*-layer lies within the space-charge region of ionized residual boron impurities and QDs do not contain holes (otherwise, the recharging of QDs with increasing $|U|$ would give rise to features in the *C–V* characteristics [14]). Consequently, all 30 sheets of Ge QDs can be involved in the band-to-band absorption of light even in the unbiased state, and it might seem that further rise of the reverse bias must not lead to any increase in η.

The increase in the quantum efficiency in electric field can be explained as follows. It is known that the Ge/Si heterojunction is of type II, since the lowest energy state for electrons lies in the Si conduction band, and the lowest state for holes, in the Ge conduction band (Fig. 1b) [14]. The absorption of photons with energy lower than the energy gap of Si gives rise to electron transitions from the Ge valence band to the Si conduction band. In this process, free electrons appear in the Si conduction band, and holes, in Ge islands. Since holes are localized in Ge QDs, electrons make the major contribution to photocurrent at low electric field. At high voltage, holes can effectively tunnel from localized states in QDs to the Si valence band; thus, the photocurrent increases. Evidently, in a sufficiently strong electric field, when all the photoholes can move away from QDs, the photoresponse levels off.

Maximum quantum efficiency of detectors was 3%, which is close to the values obtained for photodetectors based on strained multilayer Ge_xSi_{1-x}/Si superlattices. Further increase in quantum efficiency can be reached by designing a detector with a waveguide structure which uses the effect of multiple internal reflection, e.g., on a silicon-on-insulator substrate.

6. CONCLUSIONS

The main results of this study are as follows.

(1) A method has been devised for fabrication of silicon *p–i–n* photodiodes for the near-IR (1.3–1.5 μm) range with incorporated sheets of Ge QDs; with a sheet density of QDs higher than 10^{12} cm^{-2}, the dot size less than 10 nm.

(2) The lowest reported dark current density, 2×10^{-5} A/cm^2 under reverse bias of 1 V at room temperature, has been achieved in these detectors.

(3) Quantum efficiency under normal incidence of light onto photodiode reaches 3%, which is close to the values obtained for photodetectors based on strained multilayer Ge_xSi_{1-x}/Si superlattices.

ACKNOWLEDGMENTS

We are grateful to N.P. Stepina for her assistance in the preparation of samples, and to A.E. Klimov and I.B. Chistokhin for technical assistance.

The study was supported by the program of the Ministry of Industry, Science, and Technology of the Russian Federation (project no. 01.200.113897), INTAS (project no. 2001-0615), and the Russian Foundation for Basic Research (project no. 03-02-16526).

REFERENCES

1. V. Ryzhii, Semicond. Sci. Technol. **11**, 759 (1996).
2. J. Phillips, J. Appl. Phys. **91**, 4590 (2002).
3. L. Colace, G. Masini, G. Assanto, *et al.,* Appl. Phys. Lett. **76**, 1231 (2000).
4. F. Y. Huang, X. Zhu, M. O. Tanner, and K. Wang, Appl. Phys. Lett. **67**, 566 (1995).
5. H. Presting, Thin Solid Films **321**, 186 (1998).
6. C. Li, C. J. Huang, B. Cheng, *et al.,* J. Appl. Phys. **92**, 1718 (2002).
7. M. Elcurdi, P. Boucaud, S. Sauvage, *et al.,* Appl. Phys. Lett. **80**, 509 (2002).
8. M. Elcurdi, P. Boucaud, S. Sauvage, *et al.,* J. Appl. Phys. **92**, 1858 (2002).
9. S. Tong, J. L. Wan, and K. Wang, Appl. Phys. Lett. **80**, 1189 (2002).
10. D. Morris, N. Perret, and S. Fafard, Appl. Phys. Lett. **75**, 3593 (1999).
11. Y. Yoda, O. Moriwaki, M. Nishioka, and Y. Arakawa, Phys. Rev. Lett. **82**, 4114 (1999).
12. A. A. Shklyaev, M. Shibata, and M. Ichikawa, Phys. Rev. B **62**, 1540 (2000).
13. G. E. Pikus, *Fundamentals of the Theory of Semiconductor Devices* (Nauka, Moscow, 1965), p. 207.
14. A. I. Yakimov, N. P. Stepina, A. V. Dvurechenskii, *et al.,* Semicond. Sci. Technol. **15**, 1125 (2000).

Translated by D. Mashovets

Semiconductors, Vol. 37, No. 11, 2003, pp. 1350–1355. Translated from Fizika i Tekhnika Poluprovodnikov, Vol. 37, No. 11, 2003, pp. 1389–1393.
Original Russian Text Copyright © 2003 by Ashcheulov, V. Okhrem, E. Okhrem.

Thermoelements with Side Heat Exchange

A. A. Ashcheulov*, V. G. Okhrem, and E. A. Okhrem***

Institute of Thermoelectricity, Chernovtsy, 58027 Ukraine

***Fedkovich National University, Chernovtsy, 58012 Ukraine*

e-mail: oe-dpt@chnu.cv.ua

Submitted February 26, 2003; accepted for publication March 28, 2003

Abstract–Thermoelements with side heat exchange are studied. These thermoelements differ from conventional thermoelements in the position of their arms: one pair of end sides is in ideal thermal and electrical contact, whereas the other pair is in isothermal contact with a thermostat; thermal flux is incident on one of the side faces, while the three other sides are adiabatically isolated from the environment. Thermoelectric power and efficiency under steady-state conditions are investigated. The results obtained are analyzed, and possible applications are suggested. © *2003 MAIK "Nauka/Interperiodica"*.

1. INTRODUCTION

In this paper, we report the results of studying thermoelements with side heat exchange (TSHEs), which differ from conventional thermoelements in the arrangement of their arms; specifically, the first and second arms are brought into an ideal thermal and electrical contact by one pair of ends, while the second pair of ends of these arms are in isothermal contact with a thermostat at a temperature T_0. Steady-state thermal flux with density q is incident on one of the side faces, whereas the three remaining side faces are adiabatically isolated from the environment.

We will consider the thermoelectric emf and current mode of a TSHE under steady-state conditions. Since a TSHE represents a zonally inhomogeneous medium (ZIM), electrical isolation of its side faces gives rise to Hirose currents in the bulk [1, 2]. We will calculate first the thermoelectric emf caused by the above currents and then the efficiency of a TSHE. Finally, we will analyze the results obtained.

2. THE HIROSE CURRENTS AND TRANSVERSE THERMOELECTRIC EMF IN A THERMOELEMENT WITH SIDE HEAT EXCHANGE

Complex thermoelectric processes are characteristic of a ZIM. For example, closed thermoelectric currents arise in a ZIM if there is a temperature gradient over the boundary between contacting media 1 and 2 under the condition that the side faces are electrically isolated [1–5]. These currents were first referred to as eddy thermoelectric currents [2], and then, as bulk Seebeck currents or Hirose currents [3–5]. It was suggested that the phenomenon of origination of Hirose currents be used to determine the thickness of metal layers in bimetallic structures [1] and that the thermal emf, which is transverse to the temperature gradient, be used to reveal inhomogeneities in the contacting media [2]. It is also known that a ZIM may be considered as the source of emf [6, 7]. The emf of a short-circuited thermoelement made of a ZIM has been calculated previously [8].

In this section, we substantiate analytically the possibility of fabricating a photoelement whose operation is based on the phenomenon of the Hirose currents. The zonally inhomogeneous medium consists of two isotropic thermoelectric plates 1 and 2 (with temperature- and coordinate-independent kinetic coefficients); these plates are in an ideal thermal and electric contact (Fig. 1).

A uniform thermal flux with the density q is incident on the upper surfaces of the plates, whereas the lower surfaces are adiabatically isolated from the environment; the side faces ($x = -c$ and $x = a$) are in isothermal contact with a thermostat at a temperature T_0. It is assumed (as in [1, 2]) that the ZIM is electrically isolated. In this case, the heat-conduction equation can be written as

$$\frac{\partial^2 T_i}{\partial x^2} + \frac{\partial^2 T_i}{\partial y^2} = 0, \quad (1)$$

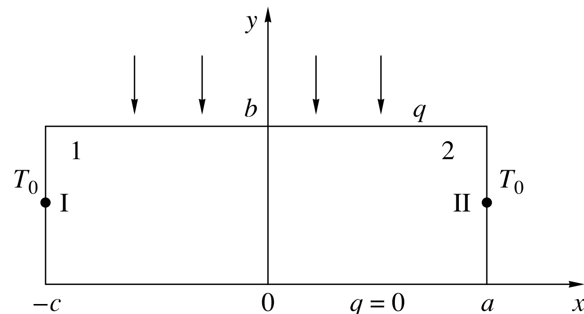

Fig. 1. Schematic representation of a thermoelement with side heat exchange.

1063-7826/03/3711-1350$24.00 © 2003 MAIK "Nauka/Interperiodica"

where $T_i = T_i(x, y)$ is the temperature of the point (x, y) in the ith region ($i = 1, 2$). The boundary conditions

$$\kappa_i \frac{\partial T_i(x, 0)}{\partial y} = 0 \quad (2)$$

account for the adiabatic isolation of the lower ZIM face; the relation

$$T_1(-c, y) = T_2(a, y) = T_0 \quad (3)$$

expresses isothermal contact of the side face with the thermostat at a temperature T_0; and expression

$$q = \kappa_i \frac{\partial T_i(x, b)}{\partial y} \quad (4)$$

describes the density of thermal flux that is incident on the face $y = b$. Continuity of the thermal flux and temperature at the interface between regions 1 and 2 ($x = 0$) can be represented as

$$\kappa_1 \frac{\partial T_1(0, y)}{\partial x} = \kappa_2 \frac{\partial T_2(0, y)}{\partial x}, \quad (5)$$

$$T_1(0, y) = T_2(0, y), \quad (6)$$

where κ_1 and κ_2 are the thermal conductivities of materials in arms 1 and 2. It is noteworthy that the formulated thermal part of the problem is approximate: in Eq. (1), we disregarded the Joule heat generated by the Hirose currents as a negligible quantity; in Eq. (5), we disregarded the Peltier heat on the same grounds. This approximation was substantiated and used as applied to modern thermoelectric materials, e.g., in [3–6].

Equation (1) is solved by the Fourier method. The solution is given by

$$T_i(x, y) = T_0 + D_{i0} + \frac{q}{2\kappa_i b}\sum_{n=1}^{\infty} F_n \cos(\delta_n y) - \frac{q}{2\kappa_i}x^2 + B_{i0}x + \sum_{n=1}^{\infty} f_{in}(x)\cos(\delta_n y),$$

where

$$\delta_n = n\pi/b, \quad f_{in}(x) = A_{in}\exp(\delta_n x) + B_{in}\exp(-\delta_n x),$$

$$D_{i0} = \frac{qac}{2b}\frac{c + a}{c\kappa_2 + a\kappa_1}, \quad F_n = (-1)^n b^2/(n\pi)^2,$$

$$B_{i0} = -\frac{q}{2b\kappa_1}\frac{c^2 k_2 - a^2\kappa_1}{c\kappa_2 + a\kappa_1},$$

and A_{in} and B_{in} are the integration constants, which can be determined from boundary conditions (2)–(6). These constants are expressed as

$$A_{in} = -\frac{q}{2\kappa_1 b}F_n \exp(\delta_n c) - B_{1n}\exp(2\delta_n c),$$

$$A_{2n} = -\frac{q}{2\kappa_2 b}F_n \exp(-\delta_n a) - B_{2n}\exp(-2\delta_n a),$$

$$B_{1n} = \frac{q}{2b}F_n \times \frac{[1 - \exp(-\delta_n a)]^2 - (\kappa_2/\kappa_1)[1 - \exp(\delta_n c)][1 + \exp(-2\delta_n a)]}{C} + \frac{\exp(\delta_n c)[1 - \exp(-2\delta_n a)]}{C},$$

$$B_{2n} = -\frac{q}{2b}F_n \times \frac{[1 - \exp(-\delta_n a)]^2 - (\kappa_1/\kappa_2)[1 - \exp(\delta_n c)][1 + \exp(2\delta_n a)]}{C} + \frac{\exp(-\delta_n c)[1 - \exp(2\delta_n a)]}{C},$$

$$C = \kappa_2[1 - \exp(2\delta_n c)][1 + \exp(-2\delta_n a)] - \kappa_1[1 + \exp(2\delta_n c)][1 - \exp(-2\delta_n a)].$$

Let us now formulate the electrical part of the problem. The density of the Hirose currents is described by the following components:

$$j_1^{(i)} = -\sigma_i \frac{\partial}{\partial x}(\psi_i + \alpha_i T_i), \quad j_2^{(i)} = -\sigma_1 \frac{\partial}{\partial y}(\psi_i + \alpha_i T_i). \quad (7)$$

Equations for the potential are written as

$$\frac{\partial^2 \psi_i}{\partial x^2} + \frac{\partial^2 \psi_i}{\partial y^2} = 0, \quad (8)$$

where $\psi_i = (1/e)\mu_i$, e is the elementary charge, and μ_i is the electrochemical potential. In Eqs. (7), σ_i is the electrical conductivity and α_i is the thermoelectric power. We solve Eq. (8) by the Fourier method; as a result we obtain

$$\psi_i(x, y) = -\alpha_i T_i + \varphi_{i0}(x) + \sum_{n=1}^{\infty} \varphi_{in}(x)\cos\delta_n y, \quad (9)$$

where

$$\varphi_{i0}(x) = K_{i0}x + L_{i0},$$

$$\varphi_{in}(x) = G_{in}\exp(\delta_n x) + H_{in}\exp(-\delta_n x), \quad n \ge 1;$$

K_{i0}, L_{i0}, G_{in}, and H_{in} are the integration constants, which can be determined from the boundary conditions

$$\left.\frac{\partial \psi_i}{\partial y}\right|_{y=0} = 0, \quad (10)$$

$$\left.\frac{\partial \psi_i}{\partial y}\right|_{y=b} = -\frac{\alpha_i}{\kappa_i}q, \quad (11)$$

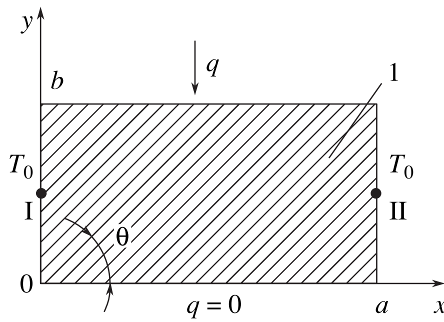

Fig. 2. Schematic representation of a thermoelement made of a thermoelectrically anisotropic crystal. Line *1* represents the crystal axis.

$$\frac{\partial}{\partial x}(\psi_1 + \alpha_1 T_1)\bigg|_{x=-c} = 0, \quad \frac{\partial}{\partial x}(\psi_2 + \alpha_2 T_2)\bigg|_{x=a} = 0, \tag{12}$$

$$\sigma_1 \frac{\partial}{\partial x}(\psi_1 + \alpha_1 T_1)\bigg|_{x=0} = \sigma_2 \frac{\partial}{\partial x}(\psi_2 + \alpha_2 T_2)\bigg|_{x=0}, \tag{13}$$

$$\psi_1|_{x=0} = \psi_2|_{x=0}. \tag{14}$$

The boundary conditions (10) and (11) signify that the bottom and top ZIM faces are electrically isolated; condition (12) signifies electrical isolation of the side faces ($x = -c$ and $x = a$); and conditions (13) and (14) express the continuity of electric current and potential at the $x = 0$ boundary. Using conditions (10)–(14), we obtain expressions for the integration constants; i.e., $K_{10} = K_{20} = 0$, while L_{10} and L_{20} are related by the expression

$$L_{10} = L_{20} + (\alpha_1 - \alpha_2)(T_0 + D_{10}).$$

We also have

$$G_{1n} = -\sigma_2 \Delta_n [\exp(-2\delta_n a) - 1]\exp(2\delta_n c)/P_n,$$

$$G_{2n} = -\sigma_1 \Delta_n [\exp(2\delta_n c) - 1]\exp(-2\delta_n a)/P_n,$$

$$H_{1n} = -\sigma_2 \Delta_n [\exp(-2\delta_n a) - 1]/P_n,$$

$$H_{2n} = -\sigma_1 \Delta_n [\exp(2\delta_n c) - 1]/P_n,$$

where

$$P_n = \sigma_2[\exp(-2\delta_n a) - 1][\exp(2\delta_n c) + 1] - \sigma_1[\exp(-2\delta_n a) + 1][\exp(2\delta_n c) - 1],$$

$$\Delta_n = -(\alpha_1 - \alpha_2)\left[\frac{q}{2\kappa_1 b} F_n + f_{1n}(0)\right].$$

Consequently, the Hirose currents appear in a ZIM under the above thermal and electrical boundary conditions; the components of these currents are given by expressions (7).

Let us now determine the potential difference between points I and II (Fig. 1) $\Delta\psi_{\mathrm{I,\,II}} = \varepsilon$, which can be interpreted as the thermoelement's emf. The expression for ε is written as

$$\varepsilon = -\Delta\alpha T_0 + L_{10} - L_{20} + 2\sum_{n=1}^{\infty} \Delta_n \left\{ \frac{\sigma_2[\exp(-2\delta_n c) - 1]\exp(\delta_n c)}{D} - \frac{\sigma_1[\exp(2\delta_n c) - 1]\exp(-\delta_n c)}{D} \right\} \cos\frac{\delta_n b}{2}, \tag{15}$$

$$D = \sigma_2[\exp(-2\delta_n a) - 1]\exp(2\delta_n c) + 1] - \sigma_1[\exp(-\delta_n a) + 1][\exp(\delta_n c) - 1],$$

where $\Delta\alpha = \alpha_1 - \alpha_2$.

If $\exp(\delta_n c) \gg 1$ and $\exp(\delta_n a) \gg 1$, the sum in (15) is a small quantity and can be disregarded. For example, the second and third terms of the sum are smaller by a factor on the order of 10^3 than the first term in (5) if $\Delta\alpha = 500$ μV/K, $\kappa_1 \approx \kappa_2 \approx 10^{-2}$ W/(cm K), $a = c = 3$ cm, $b = 0.2$ cm, and $q = 1$ W/cm^2. In this case, the quantity ε is given by

$$\varepsilon = \frac{\Delta\alpha q}{2b} \frac{ac(a+c)}{a\kappa_1 + c\kappa_2}.$$

It can be seen that the emf is independent of the thermostat temperature and electrical conductivities σ_1 and σ_2; rather, the emf is controlled by differences in thermoelectric emfs, thermal conductivities κ_1 and κ_2, and the density of the incident thermal flux, and it depends on the dimensions a, b, and c of plates 1 and 2. The numerical value of ε is equal to 1.15 V for the above values of the other parameters.

Let us compare the calculated emf with the emf of an anisotropic thermoelement that operates under identical thermal and electrical conditions. The potential difference $\Delta\psi_{\mathrm{I,\,II}}$ transverse with respect to the incident thermal flux (Fig. 2) was calculated previously [6]. A thermoelectrically anisotropic material with constant kinetic coefficients was chosen as the basis for an anisotropic thermoelement. It is assumed that κ and σ are isotropic quantities and the thermoelectric power $\alpha_{12} = (\alpha_\parallel - \alpha_\perp)/2$ (i.e., $\theta = 45°$), where $\alpha_\parallel$ and $\alpha_\perp$ are the longitudinal and transverse (with respect to the crystal axis) components of thermoelectric power, which are independent of the coordinates and temperature. The potential difference between points I and II is equal to $\Delta\varphi_{\mathrm{I,\,II}} = 0.05$ V at $\alpha_{12} = 150$ μV/K, $\kappa \sim 10^{-2}$ W/(K cm), $a = 2$ cm, $b = 4$ cm, and $q = 1$ W/cm^2 (see [6]). Numerical calculation yields $\Delta\varphi_{\mathrm{I,\,II}} = 0.12$ V for the same material constants and for $a = 3$ cm and $b = 0.2$ cm.

Consequently, we may state that the transverse emf of a zonally inhomogeneous medium (or a thermoelement with side heat exchange) is much larger than the emf of an anisotropic thermoelement. The scheme under consideration also has the advantage over an

anisotropic thermoelement, which is subjected to a thermal effect using two thermostats [3, 5].

To conclude this section, we note that the emf under investigation is not passive; i.e., this emf cannot be used to generate current: if an external circuit is connected to points I and II (Fig. 1), the condition for electrical insulation is violated and the above-derived expressions become invalid.

3. THERMOELEMENTS WITH SIDE HEAT EXCHANGE IN THE MODE OF ELECTRICAL–ENERGY GENERATION

The circuit design of a loaded TSHE differs from that of a TSHE that operates in the mode of thermal emf (Fig. 1) in that there is a current with density j along the x axis. As an addition to the above-described design, we mention that the size of the TSHE along the z axis is denoted by h. The ends at $x = -c$ and $x = a$ are in ideal thermal and electrical contact with a thermostat at a temperature T_0. The thermostat is made of a material with high electrical and thermal conductivities (for example, copper), so that the conditions for constancy of both the temperature at the end faces and the electric current are satisfied. The latter approximation was used, for example, in [9, 10].

Under the aforementioned thermal conditions of TSHE, both the thermal flux and the temperature distribution are two-dimensional. Consequently, the problem primarily consists in determining the temperature distribution.

3.1. The Temperature Distribution

The generalized heat-conduction equation is written as

$$\frac{\partial^2 T_i}{\partial x^2} + \frac{\partial^2 T_i}{\partial y^2} + \gamma_i = 0. \tag{16}$$

Here, $\gamma_i = \rho_i j^2/\kappa_i$, where ρ_i is the resistivity and j is the current density.

The boundary conditions are given by

$$\kappa_i \frac{\partial T_i(x, b)}{\partial y} = q, \tag{17}$$

$$\frac{\partial T_i(x, 0)}{\partial y} = 0, \tag{18}$$

$$T_1(-c, y) = T_0, \quad T_2(a, y) = T_0, \tag{19}$$

$$\begin{aligned} &-\kappa_1 \frac{\partial T_1(0, y)}{\partial x} + \alpha_1 j T_1(0, y) \\ &= -\kappa_2 \frac{\partial T_2(0, y)}{\partial x} + \alpha_2 j T_2(0, y), \end{aligned} \tag{20}$$

$$T_1(0, y) = T_2(0, y). \tag{21}$$

The solution to Eq. (16) is written as

$$\begin{aligned} T_i(x, y) &= -\frac{q}{2\kappa_1 b}(x^2 - y^2) + A_i x + B_i - \frac{\gamma_i x^2}{2} \\ &+ \sum_{n=1}^{\infty} [A_{in}\exp(\delta_n x) + B_{in}\exp(-\delta_n x)]\cos\delta_n y, \end{aligned} \tag{22}$$

where $\delta_n = n\pi/b$; and A_i, B_i, A_{in}, and B_{in} are the integration constants, which can be determined from conditions (17)–(21). These constants are given by

$$A_1 = \frac{1}{c}B_1 - \frac{1}{c}T_0 - \frac{1}{2}\gamma_1 c + \frac{q}{2\kappa_1 cb}(D_0 - c^2),$$

$$A_2 = -\frac{1}{a}B_1 + \frac{1}{a}T_0 + \frac{1}{2}\gamma_2 a - \frac{q}{2\kappa_1 ab}\left(D_0 - \frac{\kappa_1}{\kappa_2}a^2\right),$$

$$B_2 = B_1 + \frac{qD_0}{2\kappa_1}\frac{\kappa_2 - \kappa_1}{\kappa_2}, \quad D_0 = (2/3)b^2,$$

$$B_1 = \frac{(a\kappa_1 + c\kappa_2)T_0 + (1/2)(\rho_1 c + \rho_2 a)j^2 ac}{a\kappa_1 + c\kappa_2 - \Delta\alpha jac} + \frac{(a/2b)ac(a+c) - (qD_0/2\kappa_1 b)(a\kappa_1 + c\kappa_2 - \Delta\alpha jac)}{a\kappa_1 + c\kappa_2 - \Delta\alpha jac},$$

$$A_{1n} = -\frac{E_{1n}}{L_n}\exp(2\delta_n c) - \frac{q}{2\kappa_1 b}D_n\exp(\delta_n c),$$

$$A_{2n} = -\frac{E_{2n}}{L_n}\exp(-2\delta_n a) - \frac{q}{2\kappa_2 b}D_n\exp(\delta_n a),$$

$$B_{1n} = \frac{E_{1n}}{L_n}, \quad B_{2n} = \frac{E_{2n}}{L_n},$$

where

$$\begin{aligned} E_{1n} = \Bigg\{ &\frac{q\delta_n}{2b}D_n[\exp(-\delta_n c) - \exp(\delta_n c)] \\ &- \frac{\Delta\alpha jq}{2\kappa_1 b}D_n\left[\frac{\kappa_1}{\kappa_2} - \exp(\delta_n c)\right]\Bigg\}[1 - \exp(-2\delta_n a)] \\ &+ \frac{q\kappa_2\delta_n}{2\kappa_1 b}\left[1 - \exp(\delta_n c) - \kappa_1\frac{1 - \exp(-\delta_n a)}{\kappa_2}\right] \\ &\times [1 + \exp(-2\delta_n a)], \end{aligned}$$

$$\begin{aligned} E_{2n} = \Bigg\{ &-\frac{q}{2\kappa_1 b}D_n(\kappa_1\delta_n - \Delta\alpha j)\exp(\delta_n c) \\ &+ \frac{q}{2\kappa_2 b}D_n[\kappa_2\delta_n\exp(-\delta_n c) - \Delta\alpha j]\Bigg\} \end{aligned}$$

$$\times[1-\exp(2\delta_n c)] + \frac{q}{2b}D_n\left[\frac{1-\exp(\delta_n c)}{\kappa_1}\right.$$

$$\left.-\frac{1-\exp(-\delta_n a)}{\kappa_2}\right]\{\kappa_1\delta_n[1+\exp(2\delta_n c)]$$

$$+\Delta\alpha j[1-\exp(2\delta_n c)]\},$$

$$L_n = -\kappa_2\delta_n[1-\exp(-\delta_n a)][1-\exp(2\delta_n c)]$$

$$+\{\kappa_1\delta_n[1+\exp(2\delta_n c)]+\Delta\alpha j[1-\exp(2\delta_n c)]\}$$
$$\times[1-\exp(-2\delta_n c)],$$

$$\Delta\alpha = \alpha_1-\alpha_2, \quad D_n = [(-1)^n-1]4b^2/(\pi n)^2.$$

Consequently, there is a two-dimensional temperature distribution in the loaded TSHE under consideration. This thermoelement can operate both in the mode of electrical-energy generation (in which case, the intensity of the current that flows through the external resistance $R_e$is equal to $I = jbh$) and in the mode of cooling (in which case, I is the current intensity that is generated in the thermostat by an external source).

3.2. The Efficiency of a Thermoelement with Side Heat Exchange

The most important characteristic of a loaded TSHE is the efficiency

$$\eta = \frac{q(a+c)h-Q_0}{q(a+c)},$$

where $q(a+c)h$ is the heat supplied to the upper face of the TSHE and Q_0 is the heat released to the thermostat. If the temperature distribution is known, we can calculate Q_0; i.e.,

$$Q_0 = -h\int_0^b q_1^{(1)}(-c,y)dy + h\int_0^b q_1^{(2)}(a,y)dy,$$

where

$$q_1^{(i)} = -\kappa_i\frac{\partial T_i(x,y)}{\partial x}+\alpha_i T_i(x,y)j.$$

Performing mathematical transformations, we obtain

$$Q_0 = q(a+c)h+\Delta\alpha j\left(\frac{q}{2\kappa_1 b}D_0+B_1\right)bh$$
$$+(\rho_1 c+\rho_2 a)j^2bh-\Delta\alpha jT_0bh.$$

We then use the expressions for B_i and η to obtain

$$\eta = \frac{b}{q(a+c)}$$
$$\times\left\{\frac{\Delta\alpha jac[q(a+c)/2b]-\Delta\alpha jT_0-(1/2)(\rho_1 c+\rho_2 a)j^2}{(a\kappa_1+c\kappa_2+\Delta\alpha jac)}\right.$$
$$\left.-\frac{(\rho_1 c+\rho_2 a)(a\kappa_1+c\kappa_2)j^2}{(a\kappa_1+c\kappa_2+\Delta\alpha jac)}\right\},$$

here, we took into account that the current flows in the negative direction of the x axis (Fig. 1). It can be seen from the above expression that the value of η primarily depends on the term $q(a+c)/2b$. Therefore, the TSHE height should be small, whereas the value of q should be large. Let us assume that the condition $q(a+c)/2b \gg \Delta\alpha jT_0 + (1/2)(\rho_1 c+\rho_2 a)j^2$ can be satisfied if the values of j are sufficiently small. Then, assuming also that

$$\Delta\alpha jac\frac{q(a+c)}{2b} \gg (\rho_1 c+\rho_2 a)(a\kappa_1+c\kappa_2)j^2,$$

we find that the efficiency is given by

$$\eta = \frac{1}{2}\frac{\Delta\alpha jac}{a\kappa_1+c\kappa_2+\Delta\alpha ac}.$$

The above conditions are satisfied if, for example, $a = c = 1$ cm, $b = 0.1$ cm, $\kappa_1 = \kappa_2 = 10^{-2}$ W/(cm K), $\Delta\alpha = 10^{-4}$ V/K, $\rho_1 = \rho_2 = 10^{-3}$ Ω cm, and $q = 2$ W/cm^2. Here, it should be taken into account that the value of j is limited by the TSHE internal resistance. Let us estimate the largest attainable value of j. To this end, we write the equation

$$\rho_i jdx = d(\mu_i+\alpha_i T_i)$$

(where μ_i is the electrochemical potential), which follows from Ohm's law. Integrating this equation with respect to x between $-c$ and a and taking into account that the voltage drop across the thermoelement is equal to jR_ebh, we obtain

$$j(y) = \frac{\Delta\alpha[T_1(0,y)-T_0]}{\rho_1 c+\rho_2 a+R_2bh} = \frac{\Delta\alpha\Delta T}{\rho_1 c+\rho_2 a+R_ebh}.$$

Notably, if the TSHE height b is small, we may assume that $\Delta T = \text{const}$. If $R_e = 0$ (the short-circuit conditions), the value of j is the largest; i.e.,

$$j_{\max} = \frac{\Delta\alpha\Delta T}{\rho_1 c+\rho_2 a},$$

where the value of ΔT is controlled by the value of the thermal-flux density q. For example, if $\Delta T = 20$ K, we have $j_{\max} = 5$ A/cm^2. We find that the highest efficiency is equal to 6% for the aforementioned material and dimensional constants.

The loaded TSHE considered in this study can be used as a sensor of thermal radiation or as a current generator.

REFERENCES

1. A. J. Hirose, J. Inst. Electron. Eng. Jpn. **74**, 1056 (1954).
2. L. I. Anatychuk and O. Ya. Luste, Izv. Vyssh. Uchebn. Zaved. Fiz., No. 6, 134 (1969).
3. S. L. Korolyuk, I. M. Pilat, A. G. Samoĭlovich, *et al.*, Fiz. Tekh. Poluprovodn. (Leningrad) **7**, 725 (1973) [Sov. Phys. Semicond. **7**, 502 (1973)].
4. A. G. Samoĭlovich, in *Problems in Modern Physics* (Nauka, Leningrad, 1980), p. 304.
5. A. A. Snarskiĭ, Candidate's Dissertation (Chernovtsy, 1975).
6. A. A. Ashcheulov and V. G. Okhrem, Termoélektrichestvo, No. 4, 17 (2001).
7. L. I. Anatychuk, *Thermoelements and Thermoelectric Devices* (Naukova Dumka, Kiev, 1979).
8. E. A. Okhrem and I. V. Prots, Termoélektrichestvo, No. 3, 16 (2000).
9. V. G. Okhrem, Inzh.–Fiz. Zh. **40**, 75 (1981).
10. V. G. Okhrem and E. A. Okhrem, Inzh.–Fiz. Zh. **73**, 650 (2000).

Translated by A. Spitsyn

Semiconductors, Vol. 37, No. 11, 2003, pp. 1356–1362. Translated from Fizika i Tekhnika Poluprovodnikov, Vol. 37, No. 11, 2003, pp. 1394–1401.
Original Russian Text Copyright © 2003 by Lyutetskiĭ, Pikhtin, Slipchenko, Sokolova, Fetisova, Leshko, Shamakhov, Andreev, Golikova, Ryaboshtan, Tarasov.

PHYSICS OF SEMICONDUCTOR DEVICES

1.7–1.8 μm Diode Lasers Based on Quantum-Well InGaAsP/InP Heterostructures

A. V. Lyutetskiĭ*, N. A. Pikhtin*^, S. O. Slipchenko*, Z. N. Sokolova*, N. V. Fetisova*, A. Yu. Leshko*, V. V. Shamakhov*, A. Yu. Andreev, E. G. Golikova**, Yu. A. Ryaboshtan**, and I. S. Tarasov***

**Ioffe Physicotechnical Institute, Russian Academy of Sciences, Politekhnicheskaya ul. 26, St. Petersburg, 194021 Russia*

^e-mail: nike@hpld.ioffe.ru

***Sigm Plus, Moscow, 117342 Russia*

Submitted May 19, 2003; accepted for publication May 20, 2003

Abstract—Separate-confinement InGaAsP/InP heterostructures with highly strained quantum wells are grown by metal–organic vapor-phase epitaxy (MOVPE). The properties of InGaAsP and InGaAs quantum wells are studied, and the influence of the heterostructure parameters on the lasing wavelength is analyzed. The grown structures are used for designing high-intensity multimode and single-mode mesa-stripe laser diodes operating in the range λ = 1.7–1.8 μm. The maximum continuous-wave lasing power achieved at room temperature is 1.6 W and 150 mW for multimode and single-mode laser diodes, respectively. Single-mode lasing is retained up to 100 mW. © *2003 MAIK "Nauka/Interperiodica".*

INTRODUCTION

The operating wavelength range of semiconductor lasers available for commercial production is becoming greater every year. This progress is caused by the rapid development of techniques for epitaxial growth of solid solutions. The interest in long-wavelength (λ = 1.7–2.0 μm) diode lasers is due to the great number of their possible applications. For example, high-power multimode lasers emitting in the range 1.7–2.0 μm are widely used in medicine and for pumping holmium-doped crystals. Single-mode lasers operating in the same spectral range are promising for communication systems with ultra low optical loss [1], as well as for ecological monitoring [2] and spectroscopic analysis of industrial gases [3].

The design and fabrication of such lasers are in progress in a number of laboratories where a high technological level of metal–organic vapor-phase epitaxy (MOVPE) and molecular-beam epitaxy (MBE) is achieved [4–9].

At present, there are several possible approaches to producing laser diodes emitting in the medium infrared range. In particular, solid-solution systems AlInGaAsSb/GaSb [10, 11] and InGaAsP/InP [2, 12, 13] can be used. For a number of reasons, the InGaAsP/InP system is more convenient from a processing point of view for the production of laser diodes with wavelengths up to 2 μm [14]. We investigated the optical properties of highly strained $In_{1-x}Ga_xAs/In_{0.53}Ga_{0.47}As$ quantum wells grown on InP substrates [15–17]. The maximum photoluminescence (PL) wavelength obtained was 1.66 μm at 77 K (1.85 μm at room temperature) [16]. Such structures are known to forma type-II heterojunction (wide-gap barrier layer–strained quantum well) [17]; because of this fact, the luminescence efficiency was low.

Emission from InAs quantum dots grown on InP substrates also falls in the range 1.7–2.0 μm. Structures with quantum dots were fabricated both by MOVPE [17–19] and MBE [20–22]. However, the efficiency of luminescence from InAs quantum dots still remained low [19]. One of the reasons for this may be that the electron–hole overlapping integral is small in such dots [23]. The best result obtained was a lasing threshold of 11 A/cm^2 at liquid-nitrogen temperature; however, at 200 K, the threshold value was as high as 2 kA/cm^2 [24]. No lasing was observed at room temperature. No advantages of quantum-dot structures over quantum-well structures were revealed in the spectral range considered.

Another candidate for designing 1.7 to 2.0-μm lasers is the InAsN solid solution [25, 26]. However, studies in this area are still prospective and do not give a clear idea of how promising systems based on this solid solution are.

In this paper, we report on the fabrication and investigation of highly efficient 1.7–2.0 μm semiconductor lasers grown by MOVPE technique in the system of InGaAsP/InP solid solutions.

The structure of this paper is as follows: Section 2 contains analysis of the possibility of obtaining the maximum lasing wavelength in heterostructures with active regions based on InGaAsP/InP solid solutions. Sections 3 and 4 contain the results of experimental optimization of the composition of the active region in

order to obtain the highest efficiency of lasing. Analysis of these results is performed in Section 4.

OPTIMIZATION OF HETEROSTRUCTURES

With the aim of extending the operating range of InGaAsP/InP heterolasers with strained quantum wells (QWs) to long wavelengths as far as possible, we searched for the optimal heterostructure parameters. In the entire range of compositions, the band gap (E_g) of ternary solid solutions $In_{1-x}Ga_xAs$ is narrower than that of quaternary solid solutions $In_{1-x}Ga_xAs_yP_{1-y}$ with the same lattice constant a. Therefore, the use of InGaAs quantum wells for active regions is preferable. Despite this fact, the optimization was carried out both for the structures based on $In_{1-x}Ga_xAs$ and $In_{1-x}Ga_xAs_yP_{1-y}$ quantum wells (the latter had a low phosphorous content: $y = 0.93$).

The lasing wavelength was calculated as a function of the lattice mismatch ($\Delta a/a$), the QW width d, and the composition of the wide-gap barrier layers enclosing the QW. Figure 1 shows the wavelengths corresponding to the peak of PL from QWs formed by quaternary InGaAsP and ternary InGaAs solid solutions, calculated as functions of d for two values of $\Delta a/a$ (1% and 1.5%). In all cases, InGaAsP, which is isoperiodic with InP, was chosen as a wide-gap barrier (E_g = 1 eV). According to our calculation, the maximum wavelength is obtained for the widest QWs subjected to maximum compression. The maximum allowable strain is related to the critical QW width d_c. In QWs whose width exceeds the critical value, misfit dislocations appear and the PL intensity drops. One can determine the critical width both experimentally and theoretically. This value depends on a number of factors, in particular, the material of the QW and the wide-gap barrier, the growth temperature, the substrate orientation, and the quality of the layers. Hence, the theoretically predicted value of d_c may differ appreciably from the QW width at which the PL efficiency drops in the experiment. For a given mismatch in the lattice constants of the materials in contact a_c–a_b (a_c and a_b are the lattice constants of the active region and the wide-gap barrier layer, respectively), the critical width of an active region can be estimated as

$$d_c = b/(2f),$$

where

$$f = (a_c - a_b)/a_c, \quad b = a_c/\sqrt{2}. \tag{1}$$

This simplified expression, which is derived from Matthew's universal formula [27], yields an overestimated value. For the structures under study, formula (1) yields d_c = 207 and 140 Å at a mismatch of 1% and 1.5%, respectively. The constants a_c and a_b are determined in (1) at the growth temperature (700 K).

As can be seen from Fig. 1, with a fixed lattice mismatch, the lasing wavelength is larger for InGaAs quantum wells. An increase in mismatch, which results in a red shift of the PL-band peak, is due to the increasing mole fraction of InAs in the ternary solid solution InGaAs. However, an increase in the InAs mole fraction leads to a decrease in the QW maximum width, which is limited by the critical value d_c. From below, the QW width is limited by the requirement to provide the threshold lasing conditions.

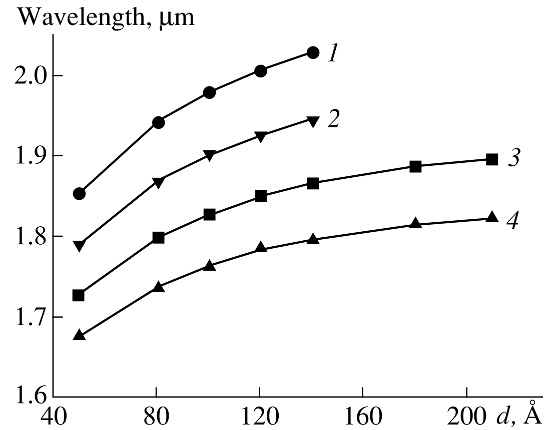

Fig. 1. The calculated wavelengths of the peak of PL from QWs formed by (*2*, *4*) quaternary InGaAsP and (*1*, *3*) ternary InGaAs solid solutions vs. the QW depth for the lattice mismatch $\Delta a/a$ = (*1*, *2*) 1.5% and (*3*, *4*) 1%.

The calculation performed for the strained quantum wells (Fig. 1) includes the following stages. First, we determine the lattice constant a_c that corresponds to the compression $\varepsilon_p = (a_c - a_b)/a_c$ for a given a_b of the wide-gap barrier material. Then, using Vegard's rule

$$a_c = a_{InP}(1-x)(1-y) + a_{InAs}(1-x)y + a_{GaP}(1-y)x + xya_{GaAs}, \tag{2}$$

for a solid solution with a known phosphorous content y and a lattice constant that is different from that of InP, we find the value of x and the band gap E_g [28]:

$$E_g = 1.35 + 0.668x - 1.17y + 0.758x^2 + 0.18y^2 - 0.069xy - 0.322x^2y + 0.03xy^2. \tag{3}$$

Here, a_{InP}, a_{InAs}, a_{GaP}, and a_{GaAs} are the lattice constants of binary compounds.

The corresponding constants for the $In_{1-x}Ga_xAs_yP_{1-y}$ solid solutions and, then, the value of the band gap for the strained solid solution (E_g^s) were calculated with the use of linear approximation of the deformation potentials and elastic moduli of binary compounds [29, 30].

In order to calculate the wavelength of emission from a strained active region, one should determine the effective band gap with regard to the electron and hole quantum-confined levels in the QW (with the corresponding depths ΔE_c^s and ΔE_v^s). For this purpose, we

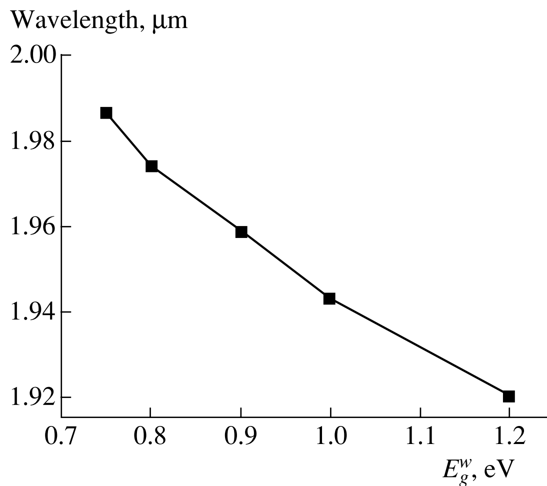

Fig. 2. The calculated wavelength of the peak of PL from an 80-Å-thick strained ($\Delta a/a = 1.5\%$) InGaAs QW vs. the band gap of InGaAsP barrier layers.

first determined in terms of the model [31] the values of band discontinuities characterizing the QW depths ΔE_c and ΔE_v in an unstrained solid solution. It turned out that, for unstrained solid solutions, the difference $\Delta E_g = E_g^b - E_g$ (E_g^b and E_g are the band gaps of the barrier layer and QW, respectively) is distributed nearly equally between the conduction and valence bands; i.e., the value of ΔE_c amounts to approximately 50% of ΔE_g. For strained solid solutions, ΔE_c was equal to 37% of ΔE_g; the QW depth ranged between 122 and 154 meV for electrons and between 211 and 261 meV for holes.

Our calculations show that, with an increase in compressive strain, the difference ($E_g^s - E_g$) increases, but the absolute value of E_g^s diminishes due to a decrease in E_g of solid solutions with larger lattice constant a_c and correspondingly longer emission wavelengths (Fig. 1).

Using InGaAsP with a narrower gap as a wide-gap barrier layer makes the electron QW shallower and, thus, increases the emission wavelength (Fig. 2). However, a considerable narrowing of the barrier band gap (with the aim of maximizing the emission wavelength) enhances the escape of electrons from the active region. In this study, we chose an optimal barrier band gap of 1 eV.

When the QW material contains phosphorous, the PL-band peak shifts to shorter waves. For example, with a constant mismatch, the addition of 7% of phosphorous to a ternary solid solution forming a QW decreases the PL-peak wavelength by 65 nm on average (Fig. 1).

Furthermore, regardless of the composition of a strained QW, an increase in its width from 50 to 100 Å decreases the band gap by about 40 meV (~100 nm) due to the shift of the quantum-confined levels.

Our theoretical analysis suggests the following. The maximum available emission wavelength (2 μm) can be attained only with InGaAs quantum wells under the condition that their width does not exceed 120 Å and the lattice mismatch is within 1.5%. A quantum well with a band gap corresponding to an emission wavelength of 1.8 μm can be fabricated using either a ternary solid solution InGaAs or a quaternary solid solution InGaAsP as an active-region material. The latter variant is less preferable from the viewpoint of maximizing the emission wavelength, because its implementation requires a larger mismatch between the lattice parameters of a QW and a barrier.

EXPERIMENT: GROWTH OF STRAINED ACTIVE REGIONS

As we demonstrated in the previous section, there are two ways to implement a quantum well with a band gap corresponding to an emission wavelength of 1.8 μm. For the experimental study of these two ways, we fabricated a series of photoluminescence structures. All the samples consisted of wide-gap undoped InGaAsP barrier layers of the same composition and a narrow-gap quantum well.

When elaborating the growth technique for structures with strained QWs 90 Å wide based on the quaternary solid solution InGaAsP, we made an attempt to increase the PL wavelength above 1.8 μm by reducing the phosphine partial pressure by 20% at a constant partial pressure of arsine with equal consumption of the metalorganic material. As a result of this, the PL-band peak completely vanished. This result evidently stems from the fact that the considerable lattice mismatch between the materials of a QW and a barrier leads to an increase in the compressive strain above the critical value, which results in an avalanche formation of dislocations in the active region.

When strained QW structures with the PL-peak wavelength exceeding 1.8 μm were based on the ternary solid solution InGaAs, an increase in the indium content to 20% did not increase the compressive strain above the critical value; therefore, the PL band was retained. However, in structures emitting at a wavelength of 1.74 μm, an appreciable broadening of the PL line was observed (Fig. 3), which, in our opinion, is related to the deterioration of the quality of the InGaAs/InGaAsP heterojunction as compared to that of the InGaAsP/InGaAsP heterojunction.

For structures emitting at a wavelength of 1.8 μm, with an active region formed of InGaAsP, the PL line was narrower than that of the structures with an InGaAs active region (the QWs had identical widths and band gaps) (Figs. 3a, 3b).

LASER HETEROSTRUCTURES: GROWTH AND PROPERTIES

Multimode Laser Diodes

Research into the PL properties of QW structures based on InGaAsP and InGaAs solid solutions has shown that both of them can be used to form active regions in semiconductor heterolasers. In order to optimize the composition of the active region, we fabricated a number of QW separate-confinement heterostructures with an active region based on either InGaAsP or InGaAs. The structures under study included the following epitaxial layers: heavily doped n-InP (Si, $N = 6 \times 10^{17}$ cm^{-3}) and p-InP (Zn, $P = 7.8 \times 10^{17}$ cm^{-3}) emitters and a nominally undoped waveguide based on a InGaAsP solid solution 0.5 μm thick (E_g = 1.03 eV) [31]. The active region was formed of either two strained InGaAs QWs (a heterostructure of the KR1274 type) or two strained InGaAsP QWs (a heterostructure of the KR1278 type). The QWs, both of which were 90 Å thick, were separated by an InGaAsP 200-Å-thick barrier layer (E_g = 1.03 eV). Then, mesastripes with a width of W = 100 μm were formed by photolithography in the insulating SiO_2 layer. Then we formed with Au/Te and Au/Zn ohmic contacts to the structures. After that, each structure was divided into laser diodes with a cavity length L = 500–4000 μm. By magnetron deposition, the cavity edges were covered with Si/SiO_2 mirrors with the reflection coefficient $R >$ 0.95 and antireflection coatings with $R < 0.04$. These samples of laser diodes were mounted on copper heat sinks using indium solder.

The current–power (I–P) characteristics of the samples were measured in continuous-wave (cw) mode with a heatsink temperature of 20°C. These data were used to determine the external differential quantum efficiency η_d and the threshold current densities for lasers based on the structures of both types with cavities of different lengths. The inverse value of η_d versus the cavity length L is plotted in Fig. 4. Using the well-known formula relating η_d to the characteristic parameters of the heterostructure,

$$\eta_d = \eta_i \frac{\alpha_{ext}}{(\alpha_i + \alpha_{ext})} \quad (4)$$

(here, η_i is the internal quantum yield of stimulated emission, α_i is the internal optical loss, and α_{ext} is the optical loss at the output), we determined the values of η_i and α_i for the heterostructures of both types. They turned out to be η_i = 58% and α_i = 9.5 cm^{-1} (KR1274 series) and η_i = 50% and α_i = 5.6 cm^{-1} (KR1278 series). It can be seen that using InGaAsP as a material for the active region allows us to considerably reduce the internal optical loss. This fact suggests that the internal loss in these heterostructures is primarily governed by the characteristics of the active region. One of the causes of such a significant difference in the internal optical losses may be the deteriorated quality of the heterojunction between the quaternary solid solution of the waveguide and the ternary solid solution of the active region.

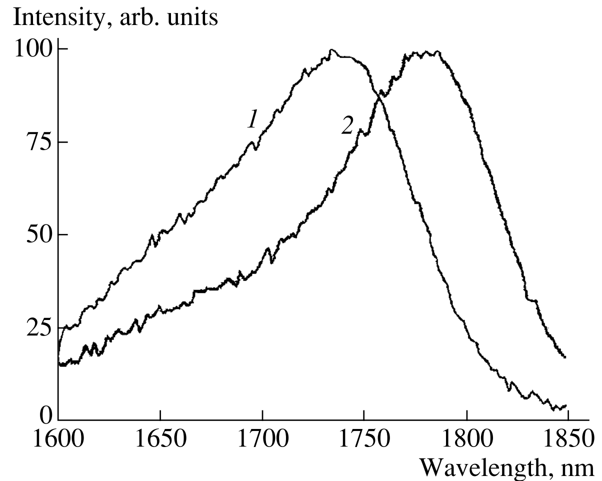

Fig. 3. PL spectra of (*1*) InGaAs and (*2*) InGaAsP QWs at room temperature.

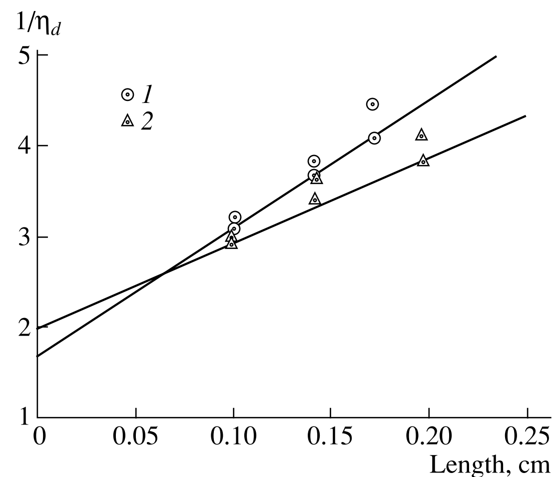

Fig. 4. The experimental dependences of the inverse external differential quantum efficiency $1/\eta_d$ on the cavity length for (*1*) InGaAs/InGaAsP/InP laser diodes (KR1274 series) and (*2*) InGaAsP/InGaAsP/InP laser dioder (KR1278 series).

The internal quantum yield of stimulated emission η_i remained low for both InGaAsP and InGaAs heterostructures. However, the value of η_i for InGaAsP hetorostructures emitting in the range between 1.3 and 1.6 μm was close to 100% [32]. The decrease in η_i we observed could have been caused by the higher threshold density of free carriers in QWs, which is primarily due to the high intensity of nonradiative Auger recombination [33]. Another factor that increases the threshold density is the ejection of electrons from QWs into barrier layers [34].

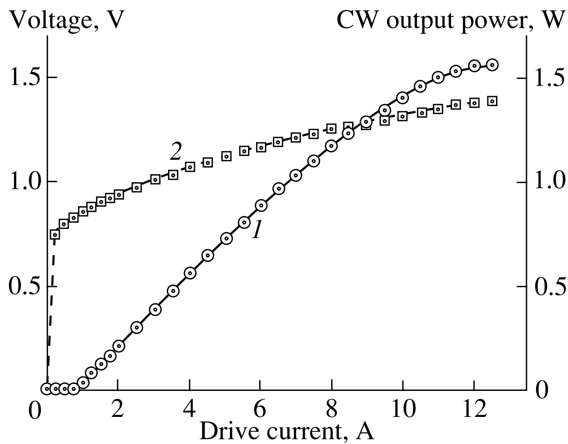

Fig. 5. (*1*) Current–power and (*2*) current–voltage characteristics of a laser diode based on a KR1278 structure with $W = 100$ μm and cavity length $L = 2$ mm, coated with antireflection (5%) and high-reflective(95%) dielectric layers.

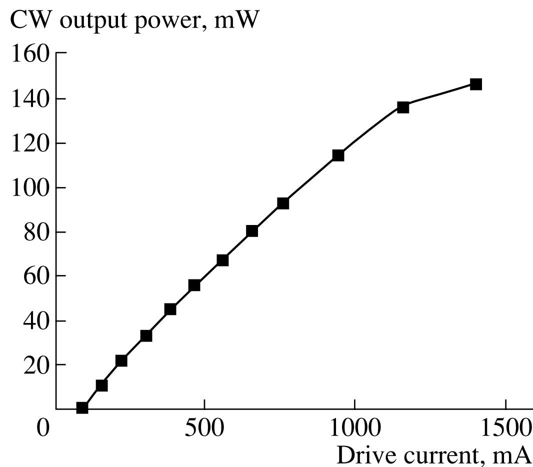

Fig. 6. Current–power characteristic of a laser diode based on a KR1278 structure with cavity length $L = 2$ mm and stripe width $W = 4.5$ μm, coated with antireflection (5%) and high-reflective (95%) dielectric layers. Lasing in cw mode with a heatsink temperature of 20°C.

Figure 5 shows a typical *I–P* characteristic of lasers based on KR1278 structures. The peak output power attained in continuous-pumping mode at room temperature was as high as 1.6 W. The corresponding external differential quantum efficiency remained at a constant level of 0.18 W/A until the drive current reached 4.5 A. It should be noted that the output power of the laser diodes with a cavity length of 1.4–2 mm tended to a constant value at a drive current of 11–12 A, respectively. In our opinion, this phenomenon is related to the low internal quantum yield of stimulated emission, the high internal optical loss, and the high effective differential resistance $\sigma_s = 1.2 \times 10^{-4}\ \Omega\ \text{cm}^2$. There is no point in increasing the cavity length above 2 mm, since a high internal loss would result in the reduction of η_d in this case.

The threshold current densities in four cleaved samples ranged between 300 and 350 A/cm^2, which is twice as high as that for lasers emitting at 1.3 μm [9, 35]. This fact may be explained by the low efficiency of the internal quantum yield of stimulated emission [36].

We also studied the temperature dependences of the threshold current density of the laser diodes under consideration. An increase in the temperature of the active region impairs their radiative characteristics [37]. One of the reasons for such behavior is the increase in the threshold concentration of charge carriers in a QW [38], which primarily affects the threshold current. In order to characterize the temperature sensitivity of the threshold current, we measured the *I–P* characteristics of laser diodes in pulsed mode at different heat sink temperatures. Exponential approximation of the experimental temperature dependences of the threshold current I_{th} in the range 10–70°C by the empirical expression

$$I_{th}(T) = I_{th}(300\text{ K})\exp(T - 300\text{ K}/T_0)$$

yields the characteristic parameter $T_0 = 50$–60 K for the laser diodes with a cavity length of 1–2 mm. This value of T_0 is minimum for laser diodes based on InGaAsP/InP heterostructures with an operational range of 1.3–1.55 μm [39]. The increase in the temperature sensitivity may be attributed to the fact that the Auger recombination in the active region becomes more intensive with increasing lasing wavelength. This circumstance does not mean, however, that a further increase in the QW depth is ineffective for improving the temperature stability of the radiative characteristics [38, 40]. For example, the use of the AlInGaAs/InP solid-solution system with a deeper QW for laser dioder emitting at 1.8 μm made it possible to increase the characteristic parameter T_0 by more than a factor of 1.5 [40, 41] compared to the conventional InGaAsP/InP solid-solution system.

Single-Mode Laser Diodes

Single-mode laser diodes of mesastripe type were fabricated on the basis of heterostructures with an InGaAsP active region [39]. In the mesastripe construction, single-mode lasing is attained due to the step in the effective refractive index in the plane parallel to the *p–n* junction (Δn_L). As we showed in [31], there are many factors that affect the value of Δn_L. The most important of them are the concentration of free charge carriers and temperature. These factors are difficult to take into consideration because both the concentration of free carriers in the waveguide and in the active region and the temperature of the layers vary with the drive current.

With the aim of maximizing the power of single-mode lasing, we calculated the parameters of the studied structure in terms of the passive-waveguide model [42]. The parameters to be determined were the etching depth and the stripe width, with the specified parame-

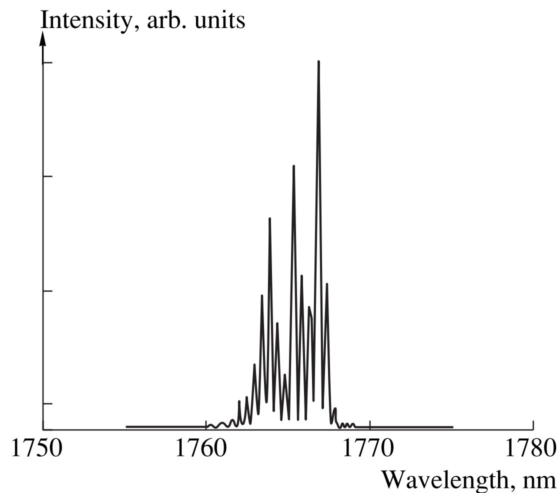

Fig. 7. Emission spectrum of a laser diode based on a KR1278 structure with cavity length $L = 2$ mm and stripe width $W = 4.5$ μm with a drive current of $1.5I_{th}$.

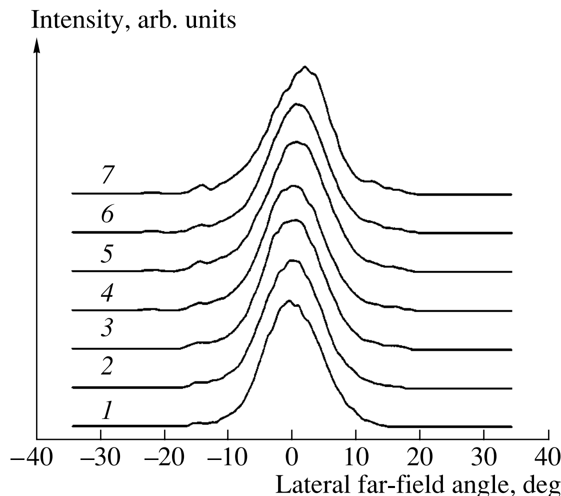

Fig. 8. The distribution of the intensity of far- field emission in the plane parallel to the *p–n* junction at different values of output optical power of a laser based on a KR1278 structure with cavity length $L = 2$-mm and stripe width $W = 4.5$ μm; lasing in cw mode. Field width at half-maximum $\Theta_{\|}$, deg: (*1*) 10.5, (*2*) 10.6, (*3*) 10.9, (*4*) 10.7, (*5*) 11.1, (*6*) 10.6, and (*7*) 10.1. Output power in cw mode, mW: (*1*) 5, (*2*) 20, (*3*) 40, (*4*) 60, (*5*) 80, (*6*) 100, and (*7*) 120.

ters of the grown heterostructure. When forming a mesastripe of required height, a 70-Å-thick InGaAsP stop layer was grown in the *p*-InP emitter to stop the selective etching. Taking into account the results of calculations, we applied the conventional postgrowth treatment [39, 31] to the described structure to fabricate mesastripe heterolasers with the stripe width $W = 4.5$ μm and different lengths of the Fabry–Perot cavity $L = 200$–2000 μm. The diodes obtained were soldered stripe down on copper heatsinks using indium solder.

The *I–P* characteristics of the fabricated devices were measured in CW mode with a heatsink temperature of 20°C. Figure 6 shows a typical dependence of the output power on the drive current for the laser diodes with the cavity length $L = 2000$ μm and antireflection and reflective dielectric layers (the respective power reflection coefficients are 5 and 95%) deposited on the cavity edges. The peak output power of such lasers attained 150 mW and was limited by the heating of the active region.

Figure 7 shows the output spectrum of the single-mode laser operating in cw mode with a drive current of $1.5I_{th}$. The separation between neighboring modes in the spectrum corresponds to the distance between zero longitudinal modes of a Fabry–Perot cavity. This observation confirms the fact that the laser diode operates in the fundamental optical mode.

Our experimental data on the lasing wavelength versus the drive current in cw mode are indicative of a smooth red shift of the emission spectrum with an increase in the injection level. This shift occurs at a constant rate of 0.375 Å/mA. This corroborates the fact that the active region heats up under continuous pumping.

The distribution of the intensity of the far-field emission of a laser diode in the plane parallel to the *p–n* junction at different drive currents is shown in Fig. 8. It can be seen that the width of the peak at half-maximum is the same up to the drive current equal to $9I_{th}$, which indicates single-mode lasing. A further increase in the drive current results in a shift of the far-field pattern (Fig. 8). In our opinion, this circumstance is related to the beam steering effect [31]. The peak power of single-mode cw lasing at maximum drive current was as high as 100 mW, which is a record value for single-mode lasers operating in the range $\lambda = 1.7$–1.8 μm [13, 14, 43].

CONCLUSIONS

(1) We showed both experimentally and theoretically the possibility of obtaining with the use of MOVPE InGaAsP/InP heterostructures with QWs formed from highly strained InGaAs or InGaAsP epitaxial layers emitting at 1.7–1.8 μm.

(2) It is established that the quaternary solid solution InGaAsP is preferable for use as an active region in separate-confinement InGaAsP/InP heterostructures: the internal optical loss in such structures can be reduced to 5.6 cm^{-1}.

(3) On the basis of the heterostructures developed, we designed a multimode and a single-mode laser emitting in cw mode at 1.76 μm with a peak power at room temperature of 1.6 W and 150 mW, respectively. Despite the enhanced effect of Auger recombination in the fabricated diode lasers with highly strained active regions, we managed to obtain the value $T_0 = 60$ K.

ACKNOWLEDGMENTS

This study was supported in part by the Russian Foundation for Basic Research, project no. 01-02-17851, and the Interdisciplinary Scientific and Technical Program of the Russian Federation "Physics of Solid Nanostructures."

REFERENCES

1. J. S. Wang, H. H. Lin, and L. W. Sung, IEEE J. Quantum Electron. **34**, 1959 (1998).
2. J. Dong, A. Ubukata, and K. Matsumoto, Jpn. J. Appl. Phys. **36**, 5468 (1997).
3. M. Mitsuhara, M. Ogasawara, M. Oishi, *et al.*, IEEE Photonics Technol. Lett. **11**, 33 (1999).
4. S. O'Brien, W. Plano, J. Major, *et al.*, Electron. Lett. **31**, 105 (1995).
5. X. He, D. Xu, A. Ovtchinnikov, *et al.*, Electron. Lett. **35**, 1343 (1999).
6. J. S. Major, D. W. Nam, J. S. Osinski, and D. F. Welch, IEEE Photonics Technol. Lett. **5**, 594 (1993).
7. H. K. Choi and S. J. Eglash, IEEE J. Quantum Electron. **27**, 1555 (1991).
8. H. K. Choi and S. J. Eglash, Appl. Phys. Lett. **61**, 1154 (1992).
9. D. A. Livshits, I. V. Kochnev, V. M. Lantratov, *et al.*, Electron. Lett. **36**, 1848 (2000).
10. H. K. Choi, G. W. Turner, and S. I. Eglash, IEEE Photonics Technol. Lett. **6**, 7 (1994).
11. D. Z. Garbuzov, H. Lee, V. Khalfin, *et al.*, IEEE Photonics Technol. Lett. **11**, 794 (1999).
12. R. U. Martinelli, T. J. Zameroswski, and P. A. Longeway, Appl. Phys. Lett. **54**, 277 (1989).
13. R. U. Martinelli, R. J. Menna, A. Triano, *et al.*, Electron. Lett. **30**, 324 (1994).
14. J. S. Major, D. W. Nam, J. S. Osinski, and D. F. Welch, IEEE Photonics Technol. Lett. **5**, 733 (1993).
15. A. D. Bondarev, D. A. Vinokurov, V. A. Kapitonov, *et al.*, Pis'ma Zh. Tekh. Fiz. **24** (22), 46 (1998) [Tech. Phys. Lett. **24**, 886 (1998)].
16. Z. N. Sokolova, O. V. Kovalenkov, D. A. Vinokurov, *et al.*, in *Abstracts of 6th International Symposium on Nanostructures: Physics and Technology* (St. Petersburg, 1998), p. 410.
17. Z. N. Sokolova, D. A. Vinokurov, I. S. Tarasov, *et al.*, Fiz. Tekh. Poluprovodn. (St. Petersburg) **33**, 1105 (1999) [Semiconductors **33**, 1007 (1999)].
18. O. V. Kovalenkov, I. S. Tarasov, D. A. Vinokurov, and V. A. Kapitonov, in *Abstracts of 6th International Symposium on Nanostructures: Physics and Technology* (St. Petersburg, 1998), p. 268.
19. D. A. Vinokurov, V. A. Kapitonov, O. V. Kovalenkov, *et al.*, Fiz. Tekh. Poluprovodn. (St. Petersburg) **33**, 858 (1999) [Semiconductors **33**, 788 (1999)].
20. V. M. Ustinov, A. E. Zhukov, A. F. Tsatsul'nikov, *et al.*, Fiz. Tekh. Poluprovodn. (St. Petersburg) **31**, 1256 (1997) [Semiconductors **31**, 1080 (1997)].
21. M. Taskinen, M. Sopanen, H. Lipsanen, *et al.*, Surf. Sci. **376**, 60 (1997).
22. N. N. Ledentsov, V. M. Ustinov, V. A. Shchukin, *et al.*, Fiz. Tekh. Poluprovodn. (St. Petersburg) **32**, 385 (1998) [Semiconductors **32**, 343 (1998)].
23. L. V. Asryan, M. Grundmann, N. N. Ledentsov, *et al.*, Proc. SPIE **3944**, 823 (2000).
24. A. E. Zhukov, A. Yu. Egorov, A. R. Kovsh, *et al.*, Fiz. Tekh. Poluprovodn. (St. Petersburg) **32**, 892 (1998) [Semiconductors **32**, 795 (1998)].
25. M. Kondow, K. Uomi, T. Kitatani, *et al.*, J. Cryst. Growth **164**, 175 (1996).
26. H. Naoi, Y. Naoi, and S. Sakai, Solid-State Electron. **41**, 319 (1997).
27. J. W. Matthews, *Epitaxial Growth*, Ed. by J. W. Matthews (Academic, New York, 1975), Part B.
28. R. E. Nahory, M. A. Pollack, W. D. Johnston, Jr., and R. L. Barns, Appl. Phys. Lett. **33**, 659 (1978).
29. S. L. Chuang, Phys. Rev. B **43**, 9649 (1991).
30. M. Krijn, Semicond. Sci. Technol. **6**, 27 (1991).
31. E. G. Golikova, V. A. Kureshov, A. Yu. Leshko, *et al.*, Pis'ma Zh. Tekh. Fiz. **28** (3), 66 (2002) [Tech. Phys. Lett. **28**, 113 (2002)].
32. A. Yu. Leshko, A. V. Lyutetskiĭ, N. A. Pikhtin, *et al.*, Fiz. Tekh. Poluprovodn. (St. Petersburg) **36**, 1393 (2002) [Semiconductors **36**, 1308 (2002)].
33. Z. N. Sokolova, D. I. Gurylev, N. A. Pikhtin, and I. S. Tarasov, in *Abstracts of 10th International Symposium on Nanostructures: Physics and Technology* (St. Petersburg, 2002), p. 252.
34. A. Yu. Leshko, A. V. Lyutetskiĭ, N. A. Pikhtin, and G. V. Skrynnikov, Fiz. Tekh. Poluprovodn. (St. Petersburg) **34**, 1457 (2000) [Semiconductors **34**, 1397 (2000)].
35. D. A. Livshits, A. Yu. Egorov, I. V. Kochnev, *et al.*, Fiz. Tekh. Poluprovodn. (St. Petersburg) **35**, 380 (2001) [Semiconductors **35**, 365 (2001)].
36. N. A. Pikhtin, S. O. Slipchenko, Z. N. Sokolova, and I. S. Tarasov, Fiz. Tekh. Poluprovodn. (St. Petersburg) **36**, 364 (2002) [Semiconductors **36**, 344 (2002)].
37. E. G. Golikova, V. A. Kureshov, A. Yu. Leshko, *et al.*, Fiz. Tekh. Poluprovodn. (St. Petersburg) **34**, 886 (2000) [Semiconductors **34**, 853 (2000)].
38. G. G. Zegrya, N. A. Pikhtin, G. V. Skrynnikov, *et al.*, Fiz. Tekh. Poluprovodn. (St. Petersburg) **35**, 1001 (2001) [Semiconductors **35**, 962 (2001)].
39. E. G. Golikova, V. A. Gorbylev, Yu. V. Il'in, *et al.*, Pis'ma Zh. Tekh. Fiz. **26** (7), 57 (2000) [Tech. Phys. Lett. **26**, 295 (2000)].
40. S. O. Slipchenko, A. V. Lyutetskiĭ, N. A. Pikhtin, *et al.*, Pis'ma Zh. Tekh. Fiz. **29** (3), 65 (2003) [Tech. Phys. Lett. **29**, 115 (2003)].
41. G. K. Kuang, G. Bohm, N. Graf, *et al.*, IEEE Photonics Technol. Lett. **13**, 275 (2001).
42. S. L. Chuang, *Physics of Optoelectronic Devices* (Wiley, New York, 1995).
43. M. Ochiai, H. Temkin, S. Forouhar, and R. A. Logan, IEEE Photonics Technol. Lett. **7**, 825 (1995).

Translated by A. Sidorova